PARTICLES AND BLACK HOLES: TIME-DOMAIN INTEGRATION OF THE EQUATIONS OF BLACK-HOLE PERTURBATION THEORY

A Thesis

Presented to

The Faculty of Graduate Studies

of

The University of Guelph

by

KARL MARTEL

In partial fulfilment of requirements

for the degree of

Doctor of Philosophy

December, 2003

Your file Votre référence
ISBN: 0-612-89262-X
Our file Notre référence
ISBN: 0-612-89262-X

ABSTRACT

PARTICLES AND BLACK HOLES: TIME-DOMAIN INTEGRATION OF THE EQUATIONS OF BLACK-HOLE PERTURBATION THEORY

Karl Martel
University of Guelph, 2003

Advisor:
Professor Eric Poisson

Binary systems consisting of a solar mass compact object orbiting a supermassive black hole are a promising source of gravitational waves for space-based laser interferometers. Because of the small mass ratio involved, the system is amenable to a treatment using black hole perturbation theory. We present a covariant and gauge invariant formalism for the metric perturbations of a Schwarzschild black hole that accounts for the radiation emitted by a small orbiting object. The perturbations are simply described in terms of the Zerilli-Moncrief and Regge-Wheeler functions, and these obey simple inhomogeneous one-dimensional wave equations.

The partial differential equations governing the evolution of these two functions are integrated numerically in the time domain using a corrected Lousto-Price algorithm. In this manner we obtain the gravitational waveforms associated with the motion of the small compact object, which is assumed to follow a geodesic of the Schwarzschild spacetime. We present a method for obtaining, from the gravitational waveforms, the fluxes of energy and angular momentum at infinity and through the event horizon.

Astrophysical black holes, such as the ones residing at the centre of many galaxies, are likely to be rapidly rotating. To deal with these situations, we present a

time-domain method of integration of the Teukolsky equation governing the evolution of the curvature perturbations of the Kerr black hole. We show that our method is both stable and quadratically convergent, and that it reproduces known predictions of the Teukolsky equation. We also comment on the difficulty of incorporating orbiting particles in the method.

Acknowledgments

I would like to acknowledge first and foremost my supervisor Eric Poisson. Without his help and guidance this dissertation would have never seen the light of day. The time and effort he spent reading and commenting on the content of the dissertation is invaluable. His ability to motivate and teach me, was incredibly precious as a graduate student. I hope that this dissertation has made it worthwhile.

I would like to thank my advisory committee Eric Poisson, Bernie Nickel, Rob Mann, and Ernie MacFarlane. They each took time to give the dissertation a thorough reading. They have also been a source of support over the years during my doctoral studies. I also would like to acknowledge my examining committee: Eric Poisson, Bernie Nickel, David Garfinkle, Don E. Sullivan, as well as my external examiner Richard H. Price. I hope they enjoyed reading my dissertation.

Every member of family deserves a very special thank you: my father for giving me an "ideal" to thrive for by being the man he is; my mother for listening and understanding me so well; my sisters for taking time from their busy schedule to listen, talk to me, and take my mind off work for short, but precious, moments.

I would like to thank the people in Guelph who touched my life and whose friendship I treasure. They know who they are.

Most importantly I would like to dedicate this dissertation to my dear Hitomi.

She is my light in the night and my shelter in the storm.

She gives me strength by shining deep inside me...

Contents

List of Tables

List of Figures

Chapter 1

Introduction and overview

1.1 Black holes in the universe

The theory of general relativity predicts the existence of black holes, objects so massive that even light cannot escape their gravity. Direct observation of these objects would be a great confirmation of the general theory of relativity in a regime that has never been tested before: strong gravitational fields. Because black holes are dark, conventional astronomy that detects electromagnetically active sources is not able to detect black holes directly.

The best, albeit indirect, evidence of the existence of black holes comes from measurements of the proper motion and radial velocities of luminous objects near the galactic core of many galaxies. These measurements point to the presence of very massive objects at the center of most galaxies at low redshifts [1, 2, 3, 4], the Milky Way being the best example: it harbours a dense compact object of mass $3.6 \times 10^6 M_\odot$ [5, 6, 3, 4]. (The evidence at high redshift ($z \gtrsim 6$) is more circumstantial [7, 8].) Determining whether these objects truly are black holes or some more exotic objects requires direct observation of their physical properties.

Isolated black holes are described by three parameters: their mass, their angular momentum and their charge [9]. Classically, these black holes do not radiate, but as a result of interaction with matter fields, astrophysical black holes can emit gravitational waves. The waves emitted by the black hole in such situations contain clear signatures that allows it to be identified as a black hole. For instance, distorted black holes should radiate at quasi-normal frequencies, and measuring these modes would provide a direct means of identifying black holes [10]. So where conventional astronomy fails, gravitational-wave astronomy offers a chance of success: black holes will be identified by their unique gravitational waves.

At the centre of a galaxy, the black hole may interact with much lighter compact objects such as neutron stars and/or solar mass black holes. They migrate toward the galactic centre by dynamical friction, and the heavy black hole is soon surrounded by a rich cluster of compact objects [11]. The motion of these compact objects is then dominated by the gravity of the central black hole. The resulting binary systems are promising sources of gravitational waves. Binary systems consisting of a small compact object orbiting a much heavier central black holes are amenable to a treatment using black hole perturbation theory: they are the focus of the work presented here.

The remainder of this chapter is organized in three main sections. In Sec. 1.2 we present the connection between gravitational-wave detectors and binary systems. Specifically, in Sec. 1.2.1 we discuss the laser interferometers under construction and in Sec. 1.2.2 we discuss circular binary systems in the quadrupole approximation. In Sec. 1.3 we discuss the scope of this thesis and in Sec. 1.4 we provide a detailed overview of the content of each chapter .

1.2 Compact binary systems

1.2.1 Laser interferometers

Much effort has been devoted in recent years to the construction of laser interferometers sufficiently sensitive to measure the small changes induced in the length of the arms by the passage of a gravitational wave.

Laser interferometers can be divided in two categories. Earth-based detectors, such as the Laser Interferometer Gravitational-wave Observatory (LIGO), will be sensitive to frequencies in the the range 10 Hz $< f_{GW} <$ 10^4 Hz, while space-based detectors, such as the Laser Interferometer Space Antenna (LISA), will be monitoring gravitational waves with frequencies lying between 10^{-4} Hz and 10^{-1} Hz. The interferometers should be sensitive to strains, $\Delta L/L$, of the order of 10^{-22} to 10^{-23}. (See [12, 13] and references therein.)

Recently there has been a significant change of tone in discussing the prospects of detecting gravitational waves. The first phase of the earth-based Laser Interferometer Gravitational-wave Observatory has been completed and the LIGO collaboration has started performing scientific runs [14]. While the sensitivity of the detectors is not good enough yet for detection of gravitational-wave signals, the data have been used to improve upper limits on the number of neutron stars binary mergers (of masses ranging from 1 to $3M_{\odot}$): they found an upper limit of 170 mergers/yr per Milky Way equivalent galaxy with 90% confidence [14].

The ultimate goal is direct detection of gravitational-wave signals, but these upper-limit results constitute a huge first step in this direction. The advanced LIGO and LISA are both expected to be completed by 2012 and both interferometers will be

sensitive enough to hopefully make detection of gravitational waves a common occurrence. A conservative estimate yields detection of gravitational waves from one extreme mass ratio binary system per year at one gigaparsec [15].

1.2.2 Quadrupole approximation for circular orbits

The interferometers should be able to detect a large variety of gravitational wave sources. This includes, for example, pulsars, supernovae and compact binary systems [12]. Compact binary systems are promising sources of gravitational waves because they strongly emit gravitational waves as the companions spiral toward each other. In their lifetime, they span the broad frequency range to which the laser interferometers are sensitive, and, by following the "chirp" signals over the whole frequency range, high signal-to-noise ratios can be achieved. In order to successfully detect the gravitational waves and extract information about the binary systems (mass, angular momentum, distance, position), it is necessary to have a good theoretical understanding of the radiation they emit, so that the phase of the signal can be closely matched by theoretical gravitational waveforms.

To illustrate the importance of this point, we consider a binary system consisting of two companions in circular orbit around each other. In a weak-field and slow-motion approximation, the binary system emits quadrupolar radiation whose frequency f_{GW} is twice the orbital frequency:

$$f_{GW} = \frac{6.4 \times 10^{-2}}{p^{3/2}} \left(\frac{10^6 M_\odot}{M} \right) \text{ Hz},$$

where M is the total mass of the binary, $p = (c^2/G)(r_p/M)$, and r_p is the radius of the orbit. For binary systems composed of 10 $M_\odot$ compact objects in orbit at the last stable circular orbit ($p \approx 6$), we get $f_{GW} \approx 200$ Hz. For a small compact object

in orbit around a $10^6\ M_\odot$ black hole at $p \approx 6$, we have instead $f_{GW} \approx 4 \times 10^{-3}$ Hz. The first type of binary is then a good candidate for observation by LIGO, while the second type is in the appropriate frequency range for detection by LISA. The total mass determines the range of frequencies into which binary systems dominantly radiate. We shall consider extreme mass ratio binary systems, treat them using black hole perturbation theory, and the work presented in this thesis is most relevant for LISA.

As a result of the emission of gravitational waves, the system loses orbital energy and the two companions slowly spiral down toward each other. The rate at which the total energy $E_{bin} = -\mu c^2/(2p)$ changes is given, in the quadrupole approximation, by [16]

$$\frac{d}{dt}E_{bin} = -\frac{32}{5}\left(\frac{c^5}{G}\right)\left(\frac{\mu}{M}\right)^2 p^{-5},$$

where μ is the reduced mass of the system. It is then an easy task to approximate the time spent in the frequency band of the detector as well as the number of wave cycles emitted in that time:

$$\begin{aligned} T &= \int dt = \int_{p_o}^{p_f} dp\, \frac{dE_{bin}/dp}{dE_{bin}/dt}, \\ N_{cycle} &= 2\pi \int dt\, f_{GW} = 4\int_{p_o}^{p_f} dp\, \Omega(p) \frac{dE_{bin}/dp}{dE_{bin}/dt} \end{aligned} \tag{1.1}$$

where $\Omega(p) = 2(c^3/G)M^{-1}p^{-3/2}$, and p_o and p_f is the dimensionless radius of the orbit when the binary enters and exits the frequency band of the interferometer, respectively. For an extreme mass ratio binary, we have roughly that $p_o \approx 20$ and $p_f \approx 6$, which yields

$$\begin{aligned} T &\approx 10^8 \left(\frac{M}{10^6 M_\odot}\right)^2 \left(\frac{M_\odot}{\mu}\right)\ \text{s}, \\ N_{cycle} &\approx 10^7 \left(\frac{M}{10^6 M_\odot}\right)\left(\frac{\mu}{M_\odot}\right). \end{aligned} \tag{1.2}$$

For compact binaries composed of two solar mass objects, the observation time is of the order of a few minutes, during which the binary goes through a few thousands of orbits. Similarly, for a small compact object orbiting a supermassive black hole, we get that the binary evolves over a time scale of years, and that during this period the small object orbits the black hole a few hundred thousand times. This suggests that the theoretical gravitational waveforms will need to be of excellent quality in order to detect the waves emitted by the binary, as well as extract information about the companions. Detection and information extraction will use the method of matched filtering, in which the detector's output is cross-correlated with theoretical waveforms in order to build a high signal-to-noise ratio. The method relies on the fact that the theoretical waveform will keep phase with the astrophysical signal, and this can only be achieved with an accurate theoretical model.

In this thesis we present tools for the accurate calculation of gravitational waves emitted by compact binary systems in the extreme mass ratio limit. Our tools rely on black hole perturbation theory and do not rely on weak-field, or slow-motion assumptions.

1.3 Scope

The LISA mission will be sensitive to gravitational waves emitted by a solar mass compact object orbiting a supermassive black hole. Because of the number of orbits and the length of time over which LISA will follow the gravitational wave signal from these binary systems, there is a need to develop a thorough understanding of the radiation process, from which we shall then be able to develop accurate gravitational waveforms. This is a very complicated problem, because the correct treatment will

have to incorporate radiation reaction effects on the motion of the compact object. In a slow-motion and weak-field approximation this a tractable problem, but the general relativistic treatment is much more complicated.

For the values of p considered, the weak-field and slow-motion approximations are not adequate, and a relativistic treatment is necessary. Part of the material covered in this dissertation is aimed at providing efficient means of numerically computing gravitational waveforms associated with the motion of a small compact object around a supermassive black hole. But we shall neglect radiation reaction effects and assume that the small object is in geodesic motion.

For most of this work we concentrate on gravitational waves produced by a small particle orbiting a Schwarzschild black hole. An important reason for this restriction is that the perturbations are then described by simple, one-dimensional, wave equations for which accurate numerical time domain methods can be devised. Gravitational waveforms for arbitrary geodesic motion of the point particle will be produced, and these are used to obtain the energy and angular momentum fluxes carried by the waves at infinity and through the event horizon.

The advantages of time domain methods are twofold. First, LISA will be detecting gravitational waves from highly eccentric motion of the compact object. For this type of motion, gravitational waves are predominantly emitted in bursts at periastron: time domain methods are very good at capturing this type of behaviour. Second, radiation reaction schemes are not fully developed yet, but prescriptions will be most easily implemented in the time domain. It is beyond the scope of this thesis to implement such radiation reaction schemes, but it is hoped that our time domain methods can be easily extended to incorporate this important effect.

Astrophysical black holes are likely to be rotating [17], and in later chapters of the

dissertation we will consider the perturbations of a Kerr black hole, whose evolution is governed by the Teukolsky equation [18]. We shall discuss the time domain integration of the homogeneous Teukolsky equation, but we shall not incorporate a source term associated with an orbiting compact object.

1.4 Overview

We now provide a detailed outline of the content of the work presented in this dissertation.

In Chapter 2, we present a covariant and gauge-invariant formalism for the metric perturbations of a Schwarzschild black hole. In the formalism, information about the gravitational-wave content of the spacetime is encoded in two scalar functions: the Zerilli-Moncrief and the Regge-Wheeler functions [19, 20, 21, 22]. We derive simple inhomogeneous wave equations that govern the evolution of these two functions. The formalism allows for the possibility that the perturbations are produced by an arbitrary stress-energy tensor.

In order to solve the perturbation equations, specific coordinates need to be introduced. We work in Schwarzschild coordinates and we begin Chapter 3 by expressing the perturbation equations of Chapter 2 in these coordinates. We also establish the relation between the two gravitational-wave polarizations and the Zerilli-Moncrief and Regge-Wheeler functions, both in the radiation zone and near the event horizon. These relations are then used to establish the connection between the Zerilli-Moncrief and the Regge-Wheeler functions, and the rate at which gravitational-waves carry energy and angular momentum to infinity and through the event horizon.

In Chapter 4 and Chapter 5, we numerically solve the equations presented in

Chapter 3. This allows us to obtain gravitational waveforms associated with arbitrary geodesic motion of a particle around a Schwarzschild black hole. In the work presented in these chapters, we include a study of the effects of the choice of initial data on the evolution of the metric perturbation during the radial infall of the point particle. This type of study is useful in determining in which situation gravitational waves contained in the initial data strongly contaminate gravitational waves emitted by a binary system consisting of a small object and a much heavier black hole. We also obtain gravitational waveforms associated with circular, eccentric and parabolic motion of a point particle around a Schwarzschild black hole. These waveforms are then used to calculate the energy and angular momentum radiated by the system, both at infinity and through the event horizon. We show that the contribution of black hole absorption to the total energy and angular momentum radiated can be as large as 5% when the orbital separation between the small object and the black hole is less than $5GM/c^2$.

The long term goal is to obtain waveforms from a particle orbiting a rotating black hole. This requires the numerical integration of the inhomogeneous Teukolsky equation. In Chapter 6, we develop an independent numerical method for the time domain integration of the homogeneous Teukolsky equation. We show that the method is stable and quadratically convergent. It also reproduces well-known physical predictions of the Teukolsky equation, such as angular profiles for $a = 0$, and quasi-normal modes for various values of the angular momentum of a Kerr black hole. We do not treat the inhomogeneous Teukolsky equation in this dissertation, but near the end of Chapter 6, we comment on the possibility of incorporating a singular source term in the time domain.

In chapter 7, we offer some concluding remarks, summarize our findings and offer

some possible directions for extending the work presented in this dissertation.

Throughout the dissertation we adhere to the Misner, Thorne and Wheeler conventions for the metric signature and the definition of the Riemann tensor [23]. We also use geometrical units in which G and c are set to one.

Chapter 2

Perturbations of a Schwarzschild black hole: covariant formulation of the equations

The prospect of detecting gravitational waves has motivated many groups to attempt solving numerically the Einstein field equations [24, 25, 26, 27, 28, 29, 30, 31, 32, 33]. The problem is difficult and, so far, progress has been slow. Perturbation theory cannot provide clues as to the nature of the instabilities associated with the full Einstein field equations [25, 31, 34], but, in the limit where both approaches agree, it can provide a useful benchmark against which to test solutions of full numerical relativity.

In this chapter, we derive the differential equations obeyed by the metric perturbations. The equations describing the metric perturbation of a Schwarzschild black hole have been derived a number of times, but in most cases the derivation concentrated on vacuum perturbations [19, 22, 35], or relied on a spectral decomposition of the metric

perturbation [20, 21]. Here we derive covariant Zerilli-Moncrief and Regge-Wheeler equations, including source terms from an arbitrary stress-energy tensor. The source term for the perturbation has been derived in the past in Schwarzschild coordinates and assuming a harmonic time dependence for the perturbations [20]. U.H. Gerlach and U.K. Sengupta [36, 37] considered the more general case of the perturbations of a general spherically symmetric spacetime, but they were unable to provide decoupled equations for the perturbations. By introducing the Zerilli-Moncrief and Regge-Wheeler functions, the perturbation equations can be decoupled covariantly. These functions were first introduced in Schwarzschild coordinates [20, 22, 19], and later covariantly for vacuum perturbations [35]. Our derivation can be considered an extension of the work found in [35] for perturbations produced by an arbitrary perturbing stress-energy tensor.

To derive the perturbation equations we follow the approach of U.H. Gerlach and U.K. Sengupta for a general spherically symmetric spacetime [36, 37]: the spacetime is split into a spherically symmetric subspace and a two-dimensional Lorentzian manifold. The spherical symmetry of the Schwarzschild spacetime can be used to simplify the expressions, while avoiding the explicit use of coordinates in the two-dimensional Lorentzian space. In section Sec. 2.1.1, we introduce the notation used in this chapter. Sec. 2.1.2 contains the line-element used in deriving the perturbation equations, while the Christoffel symbols, the Ricci tensor and scalar are listed in Sec. 2.1.4. These can be used to derive simple geometric relations useful in simplifying the appearance of the perturbation equations of a Schwarzschild black hole. Sec. 2.2 contains material that pertains to the derivation of the perturbation equations themselves. The equations are derived in the Regge-Wheeler gauge, which is introduced in Sec. 2.3.1. In this section, the connection between the Regge-Wheeler gauge and gauge invariant

quantities is also established. The angular dependence of the metric perturbations is then separated using tensorial spherical harmonics: the resulting equations are presented in Sec. 2.3.2 and Sec. 2.3.3. Sec. 2.4 presents the (contracted) Bianchi identities for the Schwarzschild spacetime. These provide a sufficient number of relations between the perturbation equations to insure that the resulting system of equations is not overdetermined. The final result is a set of two-dimensional covariant partial differential equations for gauge invariant quantities, including the source term from an arbitrary perturbing stress-energy tensor.

After having formulated the perturbation equations for the Schwarzschild spacetime, we show that they can be decoupled by introducing the Zerilli-Moncrief [20, 22, 38], and the Regge-Wheeler [19] scalar functions. In Sec. 2.5, we provide covariant definitions of these functions, which, in Schwarzschild coordinates reduce to the usual expressions. In Sec. 2.5.1 and Sec. 2.5.2, we give a *covariant* derivation of the inhomogeneous master equations governing the evolution of the Zerilli-Moncrief and Regge-Wheeler functions, respectively. This is one of the main results of this chapter and, to the best of our knowledge, this has never appeared before in the literature.

2.1 Notation and basic geometrical relations

2.1.1 Notation

Every point of a spherically symmetric spacetime belongs to a sphere of area $4\pi r^2$, where r is a positive function of the two coordinates that designate the sphere; we refer to this two-dimensional space as the spherical space, and denote its coordinates by $\theta^A = (\theta, \phi)$. These spheres are orthogonal to a Lorentzian two dimensional space; its coordinates are denoted by $x^a = (x^0, x^1)$. Throughout this chapter we adhere to the

following convention: lower-case roman indices are reserved for coordinates spanning the Lorentzian space, while capital roman indices are used to denote coordinates on the two-spheres. As usual, Greek indices denote the coordinates of the four-dimensional spacetime. Finally, symmetrization with respect to a group of indices is denoted by parenthesis:

$$T_{(\mu\nu)} = \frac{1}{2}\left(T_{\mu\nu} + T_{\nu\mu}\right),$$

where $T_{\mu\nu}$ is an arbitrary tensor. Generalization of this relation to tensors of higher ranks is obvious.

2.1.2 The line-element

In all generality, the line-element of the Schwarzschild spacetime can be written as [23]:

$$ds^2 = g_{ab}\, dx^a\, dx^b + r^2 \Omega_{AB}\, d\theta^A\, d\theta^B, \tag{2.1}$$

where $g_{ab} \equiv g_{ab}(x^c)$ is the metric of the two-dimensional Lorentzian space, $r = r(x^a)$ is an areal radius of a two-sphere at constant x^a, and $\Omega_{AB} \equiv \Omega_{AB}(\theta^C)$ is the metric on the unit two-sphere; we use $\Omega_{AB}\, d\theta^A\, d\theta^B = d\theta^2 + \sin^2\theta\, d\phi^2$.

2.1.3 Covariant derivatives

Covariant derivatives can be defined with respect to any of $g_{\mu\nu}$, g_{ab}, and Ω_{AB}:

$$g_{\mu\nu;\beta} = 0, \qquad g_{ab:c} = 0, \qquad \text{and } \Omega_{AB|C} = 0. \tag{2.2}$$

These three relations uniquely define " ; ", " : ", and " | ". Because the covariant derivative of Ω_{AB} involves no factors of r, it commutes with the covariant derivative of g_{ab}. This is a useful property that is exploited in deriving the perturbation equations.

2.1.4 Basic Geometrical relations and covariant derivatives

The metric of Eq. (2.1) can be used to calculate the Christoffel symbols as well as the Ricci tensor and scalar. For completeness, we list the results found in the doctoral dissertation of E. Poisson [39]. Quantities defined with respect to $g_{\mu\nu}$ are identified with the superscript "4", while quantities defined with respect to g_{ab} or Ω_{AB} are free of superscripts.

Christoffel symbols

The calculation of the Christoffel symbols, ${}^4\Gamma^{\mu}_{\alpha\beta}$, is straightforward and yields

$$\begin{aligned}
{}^4\Gamma^a_{bc} &= \Gamma^a_{bc}, \\
{}^4\Gamma^a_{AB} &= -\frac{1}{2}g^{ac}g_{AB,c} = -rr_{,}{}^a\Omega_{AB}, \\
{}^4\Gamma^A_{aB} &= \frac{1}{2}g^{AC}g_{BC,a} = \frac{r_{,a}}{r}\delta^A_B, \\
{}^4\Gamma^A_{BC} &= \Gamma^A_{BC},
\end{aligned} \tag{2.3}$$

${}^4\Gamma^a_{bA} = 0$, and ${}^4\Gamma^A_{ab} = 0$. The only non-vanishing components of Γ^A_{BC} are $\Gamma^{\theta}_{\phi\phi} = -\sin\theta\cos\theta$, and $\Gamma^{\phi}_{\theta\phi} = -\cot\theta$, and an explicit expression for Γ^a_{bc} can be calculated once g_{ab} is specified.

Ricci tensor and Ricci scalar

The Ricci tensor is [39]:

$$\begin{aligned}
{}^4R_{ab} &= \frac{1}{2}\mathcal{R}g_{ab} - \frac{2}{r}r_{:ab}, \\
{}^4R_{AB} &= \left(1 - r\tilde{\Box}r - r_{,}{}^a r_{,a}\right)\Omega_{AB},
\end{aligned} \tag{2.4}$$

where $\mathcal{R}$ is the Ricci scalar of g_{ab}, and $\tilde{\Box} r = g^{ab} r_{:ab}$. The four-dimensional Ricci scalar is obtained by taking the trace of Eq. (2.4):

$$ {}^4R = \mathcal{R} + \frac{2}{r^2}\left(1 - 2r\tilde{\Box} r - r^{,a} r_{,a}\right). \tag{2.5} $$

The fact that the Schwarzschild spacetime is Ricci flat can now be used to derive covariant relations for $r^{,a} r_{,a}$, $\mathcal{R}$ and $r_{:ab}$. The scalar $r^{,a} r_{,a}$ can be evaluated explicitly in a specific coordinates system. We do it in Schwarzschild coordinates, for which the metric of the Lorentzian space is

$$ g_{ab} dx^a dx^b = -f dt^2 + f^{-1} dr^2, \tag{2.6} $$

where $f = 1 - 2M/r$, and M is the mass of the black hole. In these coordinates,

$$ r^{,a} r_{,a} = g^{rr} = f, \tag{2.7} $$

where the last equality holds in any coordinate system.

Next, setting ${}^4R_{AB} = 0$ in Eq. (2.4), and using Eq. (2.7) yields

$$ \tilde{\Box} r = \frac{2M}{r^2}, \tag{2.8} $$

while setting ${}^4R = 0$, combined with Eq. (2.7) and Eq. (2.8), reveals that

$$ \mathcal{R} = \frac{4M}{r^3}. \tag{2.9} $$

Finally, this expression for $\mathcal{R}$ can be inserted into Eq. (2.4) for ${}^4R_{ab}$ to yield an expression for $r_{:ab}$:

$$ r_{:ab} = \frac{M}{r^2} g_{ab}. \tag{2.10} $$

These relations for $r^{,a} r_{,a}$, $r_{:ab}$ and $\mathcal{R}$ will be used in simplifying the equations describing the covariant metric perturbations of a Schwarzschild black hole.

Riemann tensor of the Lorentzian and spherical submanifolds

The full spacetime is the product of a two-sphere and a two-dimensional Lorentzian manifold. Their respective Riemann tensors are

$$\mathcal{R}_{abcd} = \frac{1}{2}\mathcal{R}\left(g_{ac}g_{bd} - g_{ad}g_{bc}\right), \tag{2.11}$$

$$R_{ABCD} = \Omega_{AC}\Omega_{BD} - \Omega_{AD}\Omega_{BC}. \tag{2.12}$$

We stress that these curvature tensors are *not* associated with $g_{\mu\nu}$. They purely describe the curvature of the Lorentzian manifold and of the two-sphere, without considering that they belong to a higher dimensional space. The Riemann tensor of g_{ab} is used below, while that of Ω_{AB} is used in Appendix A: they appear whenever two covariant derivatives belonging to the same submanifold are commuted.

2.2 Metric Perturbations of a Schwarzschild black hole

We now derive the field equations obeyed by the metric perturbations. First, we write down the covariant perturbation of the Einstein tensor, produced by a small arbitrary perturbing stress-energy tensor $T_{\mu\nu}$. This step requires no assumption about the spacetime. The angular dependence is then removed from the metric perturbations by using tensorial spherical harmonic functions. Finally, we introduce the Regge-Wheeler gauge to perform the calculations and derive the covariant and gauge invariant perturbation equations.

2.2.1 Variation of the Einstein tensor

We are interested in deriving the equations governing the perturbations of a Schwarzschild black hole of mass M. Later on we will assume that the perturbations arise from the motion of a point-particle of mass $\mu \ll M$ traveling on a geodesic of a Schwarzschild black hole. The perturbing stress-energy tensor is then given by

$$T_{\mu\nu} = \mu \int d\tau \, (-g)^{-1/2} \, u_\mu u_\nu \delta^4 \left(x^\alpha - z^\alpha(\tau)\right), \tag{2.13}$$

where τ is the proper time along the particle's geodesic z^ν, $u^\nu \equiv dz^\nu/d\tau$ is the four-velocity, tangent to the geodesic, and $g = \det(g_{\mu\nu})$. For the moment, we place no restriction on $T_{\mu\nu}$.

The background spacetime satisfies Einstein's field equations $G_{\mu\nu} = 0$. The introduction of a small stress-energy tensor generates perturbations of the spacetime. To obtain a formalism describing covariantly the metric perturbations of a Schwarzschild black hole, we write the perturbed metric as

$$g^p_{\mu\nu} = g_{\mu\nu} + h_{\mu\nu}, \tag{2.14}$$

where $g_{\mu\nu}$ is the background metric of Eq. (2.1), and $h_{\mu\nu}$ is a small perturbation. To linear order in the perturbation, the inverse metric is $g^{p\,\mu\nu} = g^{\mu\nu} - h^{\mu\nu}$, where indices on $h^{\mu\nu}$ are raised and lowered with the background metric. Perturbations of the Einstein field equations are then described by

$$\delta G_{\mu\nu} \;=\; 8\pi T_{\mu\nu}, \tag{2.15}$$

where

$$\delta G_{\mu\nu} \;=\; \delta R_{\mu\nu} - \frac{1}{2} g_{\mu\nu} g^{\alpha\beta} \delta R_{\alpha\beta}. \tag{2.16}$$

The next step is to get an expression for $\delta R_{\mu\nu}$ in terms of the perturbation tensor $h_{\mu\nu}$ and its derivatives. The calculation is most conveniently performed in a locally

inertial system of coordinates. In such coordinates, $R_{\mu\nu} \doteq \Gamma^{\beta}_{\mu\nu\,,\beta} - \Gamma^{\beta}_{\mu\beta\,,\nu}$, where $\Gamma^{\beta}_{\mu\nu}$ is the affine connection and $\doteq$ indicates that the equality is valid only in these coordinates. Variation of this expression yields the Palatini identity [40]

$$\begin{aligned} \delta R_{\mu\nu} &\doteq \delta\Gamma^{\beta}_{\mu\nu\,,\beta} - \delta\Gamma^{\beta}_{\mu\beta\,,\nu} \\ \delta R_{\mu\nu} &= \delta\Gamma^{\beta}_{\mu\nu\,;\beta} - \delta\Gamma^{\beta}_{\mu\beta\,;\nu} \ . \end{aligned} \tag{2.17}$$

To go from the first line to the second line, we used the fact that in these coordinates covariant derivatives are identical to partial derivatives. The last equality is a tensorial equality and holds in all coordinates. Calculation of the variation of the affine connection is again most conveniently accomplished in this coordinates system:

$$\begin{aligned} \delta\Gamma^{\beta}_{\mu\nu} &\doteq \frac{1}{2}g^{\beta\alpha}\left(h_{\mu\alpha\,,\nu} + h_{\nu\alpha\,,\mu} - h_{\mu\nu\,,\alpha}\right) \\ \delta\Gamma^{\beta}_{\mu\nu} &= \frac{1}{2}g^{\beta\alpha}\left(h_{\mu\alpha\,;\nu} + h_{\nu\alpha\,;\mu} - h_{\mu\nu\,;\alpha}\right) \ , \end{aligned} \tag{2.18}$$

where, again, the last equality is a tensorial equality and must hold in any coordinate system. Substituting Eq. (2.17) and Eq. (2.18) into Eq. (2.16) for $\delta G_{\mu\nu}$ yields

$$\begin{aligned} \delta G_{\mu\nu} &= -\frac{1}{2}\Box h_{\mu\nu} + h_{\beta(\mu;\nu)}{}^{\beta} - \frac{1}{2}h^{\beta}{}_{\beta;\mu\nu} \\ &- \frac{1}{2}g_{\mu\nu}\left(h_{\alpha\beta}{}^{;\alpha\beta} - \Box h^{\beta}_{\beta}\right). \end{aligned} \tag{2.19}$$

2.3 Covariant and gauge invariant perturbation equations

At this stage, no advantage was taken of the spherical symmetry, and Eq. (2.19) could be applied to any vacuum spacetime. The task at hand is to evaluate Eq. (2.15) with the aid of the spherically symmetric metric of Eq. (2.1).

To do this, we first express the metric perturbations as multipole expansions. This is accomplished by using tensorial spherical harmonics, which are introduced in Appendix A, Sec. A.1, Sec. A.2, and Sec. A.3. Such a decomposition introduces two types of perturbations: even and odd parity modes. This is a reflection of the fact that tensorial spherical harmonics come with these two parities. This is discussed in more detail in Appendix A. The advantage of this separation is the following: spherical symmetry prevents different parity modes from mixing, and the perturbation equations can be derived for each parity separately. This is done in Sec. 2.3.2 and Sec. 2.3.3, for even and odd parity modes, respectively. In arriving at the perturbation equations, we use, for even parity modes, the expansion

$$\begin{aligned} h_{ab}(x^c,\theta^C) &= p_{ab}(x^c)\ Y^{lm}(\theta^C), \\ h_{aA}(x^c,\theta^C) &= q_a(x^c)\ Z^{lm}_A(\theta^C), \\ h_{AB}(x^c,\theta^C) &= r^2\Big[K(x^c)\ U^{lm}_{AB}(\theta^C) + G(x^c)\ V^{lm}_{AB}(\theta^C)\Big], \end{aligned} \tag{2.20}$$

while for odd parity modes, we use

$$\begin{aligned} h_{aA}(x^c,\theta^C) &= h_a(x^c)\ X^{lm}_A(\theta^C), \\ h_{AB}(x^c,\theta^C) &= h_2(x^c)\ W^{lm}_{AB}(\theta^C), \end{aligned} \tag{2.21}$$

where p_{ab}, q_a, K, G, h_a, and h_2 are understood to have indices l and m, and summation over l and m is implicit.

2.3.1 Regge-Wheeler gauge

To obtain the perturbation equations, we use the gauge freedom inherent to the theory to eliminate four (three even parity modes and one odd parity mode) components of the metric perturbations. The gauge fixed expansions are then inserted back into

Eq. (2.15) to obtain a set of ten coupled partial differential equations. Although the equations are derived in a specific gauge, the Regge-Wheeler gauge, it is possible, as we explain below, to reinstate gauge invariance of the perturbation equations *a posteriori*. This is possible by virtue of the fact that in a vacuum background spacetime the perturbed Einstein tensor is gauge invariant.

Under an infinitesimal coordinate transformation, $x^\mu \to x^\mu + \xi^\mu$, the perturbation field $h_{\mu\nu}$ transforms as

$$h^n_{\mu\nu} = h^o_{\mu\nu} - 2\xi_{(\mu;\nu)}, \tag{2.22}$$

where "n" labels the field obtained after the infinitesimal transformation, and "o" is assigned to the field before the transformation.

The most general vector ξ^μ can be decomposed into even and odd parity vectors. The even parity component is given by $\xi^{(even)}_\mu dx^\mu = \alpha_a(x^b)Y^{lm}dx^a + r^2\beta(x^b)Z^{lm}_A d\theta^A$, while the odd parity part is $\xi^{(odd)}_\mu dx^\mu = r^2\gamma(x^b)X^{lm}_A d\theta^A$. Since $\xi^{(even)}_\mu$ contains three arbitrary functions, it can be used to fix three of the metric perturbations. On the other hand, $\xi^{(odd)}_\mu$ contains a single freely specifiable function, and only one of the odd parity metric perturbations can be gauged away. With the help of Eq. (2.3), it is trivial to calculate the transformation laws for both even and odd parity modes. Then, multiplying by the appropriate tensorial spherical harmonic function and integrating over the sphere yields the transformation laws for each multipole moment of the metric perturbations. Even parity modes transform as

$$p^n_{ab} = p^o_{ab} - 2\alpha_{(a:b)}, \tag{2.23}$$

$$q^n_a = q^o_a - \alpha_a - r^2\beta_{,a}, \tag{2.24}$$

$$K^n = K^o - 2\frac{r^{,a}}{r}\alpha_a + l(l+1)\beta, \tag{2.25}$$

$$G^n = G^o - 2\beta, \tag{2.26}$$

while odd parity modes transform according to

$$h_a^n = h_a^o - r^2\gamma_{,a}, \tag{2.27}$$

$$h_2^n = h_2^o - 2r^2\gamma. \tag{2.28}$$

Gauge invariant quantities for even and odd parity modes are obtained by forming linear combinations of the transformation equations given above. The combinations must be chosen to eliminate the functions α_a, β and γ from the right hand side of Eqs. (2.23)-(2.28). For even parity modes, there are four independent gauge invariant quantities (denoted by a " ~ "):

$$\begin{aligned} \tilde{p}_{ab} &= p_{ab} - 2v_{(a:b)} \\ \tilde{K} &= K + \frac{l(l+1)}{2}G - 2\frac{r^{,a}}{r}v_a, \end{aligned} \tag{2.29}$$

where $v_a = q_a - \frac{1}{2}r^2G_{,a}$. For odd parity modes, there are two gauge invariant quantities:

$$\tilde{h}_a = h_a - \frac{1}{2}h_{2,a} - \frac{r_{,a}}{r}h_2. \tag{2.30}$$

We note that any linear combination of gauge invariant quantities is itself gauge invariant. This property is used in Sec. 2.5 to provide decoupled covariant equations for the metric perturbations of the Schwarzschild spacetime.

A specific choice of gauge is known in the literature as the Regge-Wheeler gauge. It was introduced by T. Regge and J.A. Wheeler for the purpose of studying the stability of the Schwarzschild black hole [19]. In this gauge, the functions α_a, β and γ appearing in Eqs. (2.23)-(2.28) are chosen such that $q_a = 0$, $G = 0$ and $h_2 = 0$. In this gauge, $\tilde{p}_{ab} = p_{ab}$, $\tilde{K} = K$, and $\tilde{h}_a = h_a$. The power of this gauge resides in the following observation: gauge invariance can be recovered in any result obtained in the Regge-Wheeler gauge simply by substituting the gauge invariant quantities of Eq. (2.29) and Eq. (2.30) in place of the Regge-Wheeler quantities.

2.3.2 Perturbation equations for even parity modes

The variation of the Einstein tensor (Eq. (2.16)), calculated in the Regge-Wheeler gauge, can be found in Appendix B. In that Appendix, the covariant derivatives of the perturbation tensor are calculated for the Schwarzswchild spacetime. We also use Eq. (2.7), Eq. (2.9) and Eq. (2.10) to simplify the appearance of these equations.

There are seven coupled differential equations describing the even parity perturbation modes. Three can be obtained by calculating $\int d\Omega\ \delta G_{ab}\ Y^{*lm}$, two more from $\int d\Omega\ \delta G_{aA}\ Z^{A*}_{lm}$, and the last two from $\int d\Omega\ \delta G_{AB}\ U^{AB*}_{lm}$, and $\int d\Omega\ \delta G_{AB}\ V^{AB*}_{lm}$. The quantities δG_{ab}, δG_{aA}, and δG_{AB} are found, with the replacements mentioned above, in Eq. (B.13), Eq. (B.14), and Eq. (B.15), respectively. The angular integrals are evaluated with the use of Eq. (A.3), Eq. (A.6), and Eq. (A.9). Explicitly, the even parity perturbation equations are

$$\begin{aligned}
Q_{ab} &= \tilde{p}^{c}{}_{(a:b)c} - \frac{1}{2}g_{ab}\tilde{p}^{cd}{}_{:cd} - \frac{1}{2}\tilde{p}^{c}{}_{c:ab} - \frac{1}{2}\left(\tilde{\Box}\tilde{p}_{ab} - g_{ab}\tilde{\Box}\tilde{p}^{c}{}_{c}\right) \\
&+ \frac{2}{r}r_{,c}\left(\tilde{p}^{c}{}_{(a:b)} - g_{ab}\tilde{p}^{cd}{}_{:d}\right) - \frac{r^{,c}}{r}\left(\tilde{p}_{ab:c} - g_{ab}\tilde{p}^{d}{}_{d:c}\right) + \frac{l(l+1)}{2r^2}\tilde{p}_{ab} \\
&- \frac{1}{r^2}g_{ab}r^{,c}r^{,d}\tilde{p}_{cd} - \frac{1}{2r^2}g_{ab}\left[l(l+1) + \frac{2M}{r}\right]\tilde{p}^{c}{}_{c} \\
&- \tilde{K}_{:ab} + g_{ab}\tilde{\Box}\tilde{K} - \frac{2}{r}r_{(,a}\tilde{K}_{,b)} + \frac{3}{r}g_{ab}r^{,c}\tilde{K}_{,c} - \frac{(l+2)(l-1)}{2r^2}g_{ab}\tilde{K}\ , \qquad (2.31) \\
Q_{a} &= \tilde{p}^{b}{}_{a:b} - \tilde{p}^{b}{}_{b:a} + \frac{r_{,a}}{r}\tilde{p}^{b}{}_{b} - \tilde{K}_{,a}\ , \qquad (2.32) \\
Q^{\flat} &= \tilde{\Box}\tilde{p}^{a}{}_{a} - \tilde{p}^{ab}{}_{:ab} - \frac{2}{r}r^{,b}\tilde{p}^{a}{}_{b:a} + \frac{r^{,a}}{r}\tilde{p}^{b}{}_{b:a} - \frac{1}{2}\frac{l(l+1)}{r^2}\tilde{p}^{a}{}_{a} + \frac{2}{r}r^{,a}\tilde{K}_{,a} + \tilde{\Box}\tilde{K}, \qquad (2.33) \\
Q^{\sharp} &= -\tilde{p}^{a}{}_{a}, \qquad (2.34)
\end{aligned}$$

where the source terms are defined as

$$\begin{aligned}
Q^{ab} &= 8\pi\int d\Omega\ T^{ab}\ Y^{lm*} \\
Q^{a} &= \frac{16\pi}{l(l+1)}r^2\int d\Omega\ T^{aA}\ Z^{lm*}_{A} \\
Q^{\flat} &= 8\pi r^2\int d\Omega\ T^{AB}\ U^{lm*}_{AB}
\end{aligned}$$

$$Q^{\sharp} = 32\pi\frac{(l-2)!}{(l+2)!}r^4\int d\Omega\; T^{AB}\; V^{lm*}_{AB}\;. \tag{2.35}$$

This complete the derivation of the covariant and gauge invariant even perturbation equations of a Schwarzschild black hole. The expressions above agree with those found in [36, 37], once their expressions are specialized to the vacuum perturbations of a Schwarzschild black hole.

2.3.3 Perturbation equations for odd parity modes

Again, the various quantities needed to evaluate Eq. (2.15) are given in Appendix B and are specialized a Schwarzschild spacetime by using Eq. (2.7), Eq. (2.9) and Eq. (2.10).

There are three odd parity perturbation equations; of these three equations, two are obtained from $\int d\Omega\; \delta G_{aA}\; X^{A*}_{lm}$, and the third one from $\int d\Omega\; \delta G_{AB}\; V^{AB*}_{lm}$. The expressions needed for δG_{aA} and δG_{AB} can be found in Eq. (B.14) and Eq. (B.15), respectively, and the angular integrals are evaluated by making use of Eq. (A.6) and Eq. (A.9).

Explicitly, the odd parity perturbation equations are

$$\begin{aligned} P_a &= -\tilde{\Box}\tilde{h}_a + \tilde{h}^{b}{}_{:ab} + \frac{2}{r}\left(r^{,b}\tilde{h}_{b:a} - r_{,a}\tilde{h}^{b}{}_{:b}\right) \\ &+ \frac{1}{r^2}\left(l(l+1) - \frac{2M}{r}\right)\tilde{h}_a - \frac{2}{r^2}r_{,a}r^{,b}\tilde{h}_b\;, \qquad (2.36) \\ P &= \tilde{h}^{a}{}_{:a}\;. \qquad (2.37) \end{aligned}$$

where the source terms are

$$\begin{aligned} P^a &= \frac{16\pi}{l(l+1)}r^2\int d\Omega\; T^{aA}\; X^{lm*}_{A}\;, \\ P &= 16\pi\frac{(l-2)!}{(l+2)!}r^4\int d\Omega\; T^{AB}\; W^{lm*}_{AB}\;. \qquad (2.38) \end{aligned}$$

This completes the derivation of the covariant and gauge invariant odd parity perturbation equations of a Schwarzschild black hole. Our expressions agree with expression found in [36, 37], once their expressions are specialized to the vacuum perturbations of a Schwarzschild black hole.

The expressions governing the perturbations of the Schwarzschild spacetime, derived in the previous section and in this section can, in principle, be expanded using a specific coordinate system and then solved as a set of coupled partial differential equations. However, we show below that these equations can be decoupled by introducing the Zerilli-Moncrief and Regge-Wheeler scalar functions.

2.4 Bianchi identities

It seems at first glance that the system of equations above is overdetermined, since we now have ten coupled perturbation equations and only six gauge invariant quantities. However, this is not the case, for the well known reason that the contracted Bianchi identities provide an additional four relations among the perturbation equations. The number of independent equations is thus reduced to six.

From the definition of the source terms, Eq. (2.35), and Eq. (2.38), the perturbing stress-energy tensor can be expanded as

$$\begin{aligned} T^{ab} &= 8\pi Q^{ab}(x^c)Y^{lm}(\theta^C), \\ T^{aA} &= \frac{4\pi}{r^2}\left[Q^a(x^c)Z^A_{lm}(\theta^C) + P^a(x^c)X^A_{lm}(\theta^C)\right], \\ T^{AB} &= \frac{4\pi}{r^4}\left[r^2 Q^\flat(x^c)U^{AB}_{lm}(\theta^C) + Q^\sharp(x^c)V^{AB}_{lm}(\theta^C) + P(x^c)W^{AB}_{lm}(\theta^C)\right]. \end{aligned} \quad (2.39)$$

We stress that the indices on the tensorial spherical harmonics are raised with Ω^{AB} and not with the full-metric g^{AB}; this explains the factors of r^{-2} appearing in Eq. (2.39).

We recall that Q^{ab}, Q^a, P^a, and P possess indices l and m, and that summation over these is understood.

With the help of the Christoffel symbols given by Eq. (2.3), we get

$$\begin{aligned} T^{a\mu}{}_{;\mu} &= T^{ab}{}_{:b} + \frac{2}{r} r_{,b} T^{ab} + T^{aA}{}_{|A} - r r^{,a} \Omega_{AB} T^{AB}, \\ T^{A\mu}{}_{;\mu} &= T^{Aa}{}_{:a} + \frac{4}{r} r_{,a} T^{aA} + T^{AB}{}_{|B}. \end{aligned} \tag{2.40}$$

We can now use Eq. (A.11) and Eq. (A.12) to simplify $T^{aA}{}_{|A}$, and Eqs. (A.13)-(A.15) to simplify $T^{AB}{}_{|B}$.

There are three even parity and one odd parity Bianchi identities. Even identities are obtained by evaluating $\int d\Omega \; T^{a\mu}{}_{;\mu} \; Y^{lm*} = 0$ and $\int d\Omega \; T^{A\mu}{}_{;\mu} \; Z^{lm*}_A = 0$, while the odd parity identity comes from $\int d\Omega \; T^{A\mu}{}_{;\mu} \; X^{lm*}_A = 0$. Explicitly, we have

$$\begin{aligned} Q^{ab}{}_{:b} + \frac{2}{r} Q^{ab} r_{,b} - \frac{1}{r} r^{,a} Q^{\flat} - \frac{l(l+1)}{2r^2} Q^a &= 0, \\ Q^a{}_{:a} + \frac{2}{r} r_{,a} Q^a - \frac{(l-1)(l+2)}{2r^2} Q^{\sharp} + Q^{\flat} &= 0, \\ P^a{}_{:a} + \frac{2}{r} r_{,a} P^a + \frac{(l-1)(l+2)}{r^2} P &= 0. \end{aligned} \tag{2.41}$$

The remaining six perturbation equations are independent and determine uniquely the six gauge invariant quantities.

2.5 Decoupled master equations

We are interested in studying gravitational waves propagating in the spacetime of a Schwarzschild black hole. We therefore neglect the non-radiative $l = 0$ and $l = 1$ modes, which require a special treatment [20, 21, 41, 42], and concentrate on modes with $l \geq 2$. We shall provide decoupled equations for even and odd parity modes in terms of the Zerilli-Moncrief and Regge-Wheeler functions, respectively.

2.5.1 Zerilli-Moncrief function for even parity perturbations

The even parity metric perturbations of the Schwarzschild black hole can be decoupled by introducing the scalar field

$$\psi_{\rm ZM} = \frac{r}{\lambda+1}\left[\tilde{K} + \frac{1}{\Lambda}\left(r^{,a}r^{,b}\tilde{p}_{ab} - r r^{,a}\tilde{K}_{,a}\right)\right], \tag{2.42}$$

where $\lambda = (l+2)(l-1)/2$, $\Lambda = \lambda + 3M/r$, and the normalization is chosen to agree, in Schwarzschild coordinates, with the usual definition of the Zerilli-Moncrief function [22, 38].

The steps involved in decoupling the even parity equations are most transparent with the use of the traceless tensor

$$\tilde{k}_{ab} = \tilde{p}_{ab} - \frac{1}{2}g_{ab}\tilde{p}, \tag{2.43}$$

and the scalar field

$$v = r^{,a}r^{,b}\tilde{k}_{ab} - r r^{,a}\tilde{K}_{,a}, \tag{2.44}$$

where $\tilde{p} \equiv \tilde{p}^{a}{}_{a}$. From Eq. (2.34), $\tilde{p}$ is completely determined with the specification of $Q^{\sharp}$, and the transformation eliminates a degree of freedom that is already determined; the use of $\tilde{k}_{ab}$ is purely for convenience, as $\tilde{k}_{ab}$ and $\tilde{p}_{ab}$ are equal up to a source term. Replacing p_{ab} in favor of $\tilde{k}_{ab}$ in Eq. (2.31) yields

$$\begin{aligned} Q_{ab} &= \tilde{k}^{c}{}_{(a:b)c} - \frac{1}{2}g_{ab}\tilde{k}^{cd}{}_{:cd} - \frac{1}{2}\tilde{\Box}\tilde{k}_{ab} + \frac{2}{r}r^{,c}\left(\tilde{k}_{c(a:b)} - g_{ab}\tilde{k}^{d}{}_{c:d}\right) - \frac{r^{,c}}{r}\tilde{k}_{ab:c} + \frac{\lambda+1}{r^2}\tilde{k}_{ab} \\ &- \frac{1}{r^2}g_{ab}r^{,c}r^{,d}\tilde{k}_{cd} - \tilde{K}_{:ab} + g_{ab}\tilde{\Box}\tilde{K} - \frac{2}{r}r_{(,a}\tilde{K}_{,b)} + \frac{3}{r}g_{ab}r^{,c}\tilde{K}_{,c} - \frac{1}{r^2}g_{ab}\lambda\tilde{K} \\ &+ \frac{1}{r}r_{(,a}\tilde{p}_{,b)} - \frac{1}{2r}g_{ab}r^{,c}\tilde{p}_{,c} - \frac{1}{2r^2}g_{ab}(\lambda+2)\tilde{p}. \end{aligned} \tag{2.45}$$

The remaining two even parity perturbation equations can be used to express, in terms of $\tilde{K}$, those derivatives of $\tilde{k}_{ab}$ that cannot be expressed in terms of v. We have

$$r^{,a}\tilde{k}^{b}{}_{a:b} = r^{,a}\tilde{K}_{,a} + r^{,a}Q_{a} + \frac{1}{2}r^{,a}\tilde{p}_{,a} - \frac{f}{r}\tilde{p},$$

$$\tilde{k}^{ab}{}_{:ab} = \tilde{\Box}K - Q^b - \frac{2}{r}r^{,a}Q_a + \frac{1}{2}\tilde{\Box}\tilde{p} - \frac{1}{r}r^{,a}\tilde{p}_{,a} - \frac{1}{r^2}\left(\lambda - 1 + \frac{4M}{r}\right)\tilde{p}. \quad (2.46)$$

The first of these equality follows from rearranging Eq. (2.32), while the second relation is provided by Eq. (2.33).

Using the last three equations, it is possible to construct three differential equations involving only $\tilde{K}$ and v. The first equation is easily obtained by taking the trace of Eq. (2.45):

$$S_1 = \tilde{\Box}\tilde{K} - \frac{2\lambda}{r^2}\tilde{K} - \frac{2}{r^2}v, \quad (2.47)$$

where we used the first of Eq. (2.46) and defined

$$S_1 = Q^a{}_a + \frac{2r^{,a}}{r}Q_a + \frac{r^{,a}}{r}\tilde{p}_{,a} + \frac{1}{r^2}\left(\lambda + \frac{4M}{r}\right)\tilde{p}. \quad (2.48)$$

To obtain the second equation, we need

$$\tilde{k}^c{}_{(a:b)c} - \frac{1}{2}\tilde{\Box}\tilde{k}_{ab} - \frac{1}{2}g_{ab}\tilde{k}^{cd}{}_{:cd} = \frac{\mathcal{R}}{2}\tilde{k}_{ab} = \frac{2M}{r^3}\tilde{k}_{ab}, \quad (2.49)$$

which holds for an arbitrary symmetric and traceless tensor on a two-dimensional manifold [36, 37]. We also will make use of

$$\begin{aligned} r^{,a}r^{,b}r^{,c}\tilde{k}_{ab:c} &= r^{,c}\left(r^{,a}r^{,b}\tilde{k}_{ab}\right)_{,c} - \frac{2M}{r^2}r^{,a}r^{,b}\tilde{k}_{ab} \\ &= r^{,a}v_{,a} - \frac{2M}{r^2}v + rr^{,a}r^{,b}\tilde{K}_{:ab} + \left(1 - \frac{3M}{r}\right)r^{,a}\tilde{K}_{,a}, \end{aligned} \quad (2.50)$$

Substituting Eq. (2.49) in Eq. (2.45) eliminates all second-order derivatives of $\tilde{k}_{ab}$ from Q_{ab}. The term containing $\tilde{\Box}\tilde{K}$ is then eliminated by forming

$$\begin{aligned} fQ^a{}_a - Q_{ab}r^{,a}r^{,b} &= -\frac{r^{,a}r^{,b}}{r}\left(r^{,c}\tilde{k}_{ab:c} - r\tilde{K}_{:ab}\right) - \frac{1}{r^2}\left(\lambda + 2\right)r^{,a}r^{,b}\tilde{k}_{ab} \\ &+ \frac{3f}{r}r^{,a}\tilde{K}_{,a} - \frac{\lambda f}{r^2}\tilde{K} - \frac{f}{2r}r^{,a}\tilde{p}_{,a} - \frac{f}{2r^2}(\lambda + 2)\tilde{p}. \end{aligned} \quad (2.51)$$

The only term left involving a second derivative is the term proportional to $\tilde{K}_{:ab}$. From Eq. (2.50), we see that it is removed by eliminating $\tilde{k}_{ab}$ in favor of v. Eq. (2.51)

is then

$$S_2 = -\frac{1}{r}r^{,a}v_{,a} - \frac{1}{r^2}\left(\lambda + 2 - \frac{2M}{r}\right)v - \frac{\Lambda}{r}r^{,a}\tilde{K}_{,a} - \frac{\lambda f}{r^2}\tilde{K}, \tag{2.52}$$

where we have defined the source term

$$S_2 = fQ^a{}_a - Q_{ab}r^{,a}r^{,b} + \frac{f}{2r}r^{,a}\tilde{p}_{,a} + \frac{f}{2r^2}(\lambda+2)\tilde{p}. \tag{2.53}$$

Deriving the third and final equation requires more effort. It is obtained by forming the quantity

$$\begin{aligned}
\frac{2}{r}r^{,a}r^{,b}Q_{ab} + Q^a{}_{a,b}r^{,b} &= \frac{2}{r}r^{,a}r^{,b}\left(\tilde{k}^c{}_{a:bc} - \tilde{k}^c{}_{a:cb}\right) - \frac{f}{r}\tilde{k}^{ab}{}_{:ab} - \frac{1}{r}r^{,a}r^{,b}\tilde{\Box}\tilde{k}_{ab} \\
&- \frac{2}{r^2}\left(1 - \frac{M}{r}\right)r^{,a}\tilde{k}^b{}_{a:b} + \frac{2}{r^3}\left(\lambda + 2f\right)r^{,a}r^{,b}\tilde{k}_{ab} + \frac{2}{r}r^{,a}r^{,b}\tilde{K}_{:ab} \\
&+ \frac{2f}{r}\tilde{\Box}\tilde{K} + r^{,a}\left(\tilde{\Box}\tilde{K}\right)_{,a} - \frac{2}{r^2}\left(\lambda + 1 - \frac{4M}{r}\right)r^{,a}\tilde{K}_{,a} + \frac{2\lambda f}{r^3}\tilde{K} \\
&- \frac{1}{r^2}\left(\lambda + 1 + \frac{2M}{r}\right)r^{,a}\tilde{p}_{,a} + \frac{f}{r^3}(\lambda+2)\tilde{p}.
\end{aligned} \tag{2.54}$$

We simplify this expression by making use of the following relations:

$$\begin{aligned}
\left(\tilde{k}^c{}_{a:bc} - \tilde{k}^c{}_{a:cb}\right) &= -\mathcal{R}^c{}_{dbc}\tilde{k}^d{}_a + \mathcal{R}^d{}_{abc}\tilde{k}^c{}_d = \frac{4M}{r^3}\tilde{k}_{ab} \\
r^{,a}\left(\tilde{\Box}\tilde{K}\right)_{,a} &= g^{bc}r^{,a}\left(\tilde{K}_{:bac} + \mathcal{R}^d{}_{bca}\tilde{K}_{,d}\right) \\
&= g^{bc}\left(r^{,a}\tilde{K}_{:ab}\right)_{:c} - r^{:ab}\tilde{K}_{:ab} - \frac{2M}{r^3}r^{,a}\tilde{K}_{,a} \\
&= \tilde{\Box}\left(r^{,a}\tilde{K}_{,a}\right) - \frac{2M}{r^2}\tilde{\Box}\tilde{K}, \\
\tilde{\Box}\left(rr^{,a}\tilde{K}_{,a}\right) &= r\,\tilde{\Box}\left(r^{,a}\tilde{K}_{,a}\right) + 2r^{,a}r^{,b}\tilde{K}_{:ab} + \frac{4M}{r^2}r^{,a}\tilde{K}_{,a}, \\
r^{,a}r^{,b}\tilde{\Box}\tilde{k}_{ab} &= g^{cd}\left(r^{,a}r^{,b}\tilde{k}_{ab:c}\right)_{:d} - \left(r^{:ac}r^{,b} + r^{,a}r^{:bc}\right)\tilde{k}_{ab:c} \\
&= \tilde{\Box}\left(r^{,a}r^{,b}\tilde{k}_{ab}\right) - \left[\left(r^{:ac}r^{,b} + r^{,a}r^{:bc}\right)\tilde{k}_{ab}\right]_{:c} - \frac{2M}{r^2}r^{,a}\tilde{k}^b{}_{a:b} \\
&= \tilde{\Box}\left(r^{,a}r^{,b}\tilde{k}_{ab}\right) + \frac{4M}{r^3}r^{,a}r^{,b}\tilde{k}_{ab} - \frac{4M}{r^2}r^{,a}\tilde{k}^b{}_{a:b} \\
&= \tilde{\Box}v + \frac{4M}{r^3}v + r\,\tilde{\Box}\left(r^{,a}\tilde{K}_{,a}\right) + 2r^{,a}r^{,b}\tilde{K}_{:ab} + \frac{4M}{r^2}r^{,a}\tilde{K}_{,a} \\
&- \frac{4M}{r^2}\left(r^{,a}Q_a + \frac{1}{2}r^{,a}\tilde{p}_{,a} - \frac{f}{r}\tilde{p}\right),
\end{aligned} \tag{2.55}$$

where the first equality follows from commuting covariant derivatives, and using Eq. (2.11), with $\mathcal{R}$ given in Eq. (2.9); the second and third equalities are established by direct computation; the last relation can be obtained by substituting the definition of v, Eq. (2.44), into its third line, as well as using the first of Eq. (2.46) and the third identity of Eq. (2.55). Simplification of Eq. (2.54) is now straightforward and yields

$$\begin{aligned} S_3 &= -\frac{1}{r}\tilde{\Box}v + \frac{2}{r^3}\left[\lambda + 2\left(1-\frac{M}{r}\right)\right]v \\ &+ \frac{1}{r}\left(1-\frac{4M}{r}\right)\tilde{\Box}\tilde{K} + \frac{6M}{r^3}r^{,a}\tilde{K}_{,a} + \frac{2\lambda f}{r^3}\tilde{K}, \end{aligned} \tag{2.56}$$

where the source term is

$$\begin{aligned} S_3 &= \frac{2}{r}Q_{ab}r^{,a}r^{,b} + Q^a{}_{a,b}r^{,b} - \frac{f}{r}Q^b - \frac{2M}{r^3}r^{,a}Q_a + \frac{f}{2r}\tilde{\Box}\tilde{p} \\ &+ \frac{1}{r^2}\left(\lambda + 1 + \frac{M}{r}\right)r^{,a}\tilde{p}_{,a} - \frac{f}{r^3}\left(2\lambda + 3 - \frac{2M}{r}\right)\tilde{p}. \end{aligned} \tag{2.57}$$

To decouple the equations, we can eliminate $\tilde{K}$ or v in Eq. (2.47), Eq. (2.52), and Eq. (2.56) in favor of $\psi = r(\tilde{K} + \Lambda^{-1}v)$. We eliminate v:

$$\begin{aligned} S_1 &= \tilde{\Box}\tilde{K} + \frac{6M}{r^3}\tilde{K} - \frac{2\Lambda}{r^3}\psi \\ S_2 &= -\frac{\Lambda}{r^2}r^{,a}\psi_{,a} - \frac{1}{r^3}\left(\lambda(\lambda+1) + \frac{3M}{r}\lambda + \frac{6M^2}{r^2}\right)\psi + \frac{\lambda+1}{r^2}\Lambda\tilde{K} \\ S_3 &= -\frac{\Lambda}{r^2}\tilde{\Box}\psi + \frac{2}{r^3}\left(\lambda + \frac{6M}{r}\right)r^{,a}\psi_{,a} + \frac{2}{r^4}\left[\lambda(\lambda+1) + \frac{M}{r}(4\lambda-3) + 18\frac{M^2}{r^2}\right]\psi \\ &+ \frac{1}{r}\left(\lambda + 1 - \frac{M}{r}\right)\tilde{\Box}\tilde{K} - \frac{2}{r^3}\left(\lambda(\lambda+1) + \frac{3M}{r}(\lambda+1) + \frac{3M^2}{r^2}\right)\tilde{K} \end{aligned} \tag{2.58}$$

It is now easy to see that $\tilde{\Box}\tilde{K}$ is eliminated by combining S_3 and S_1, and that S_2 can then be used to eliminate the remaining term proportional to $\tilde{K}$. An equation for the Zerilli-Moncrief function, defined in Eq. (2.42), is obtained by substituting $\psi = (\lambda+1)\psi_{\rm ZM} - rf\tilde{p}/(2\Lambda)$. The covariant inhomogeneous Zerilli-Moncrief equation

is

$$\left[\tilde{\Box} - V_{\rm ZM}(r)\right]\psi_{\rm ZM}(x^c) = S_{\rm ZM}(x^c), \tag{2.59}$$

where $\tilde{\Box}\psi_{\rm ZM} = g_{ab}\psi^{;ab}_{\rm ZM}$,

$$V_{\rm ZM} = \frac{1}{r^2\Lambda^2}\left[2\lambda^2\left(\lambda+1+\frac{3M}{r}\right)+\frac{18M^2}{r^2}\left(\lambda+\frac{M}{r}\right)\right], \tag{2.60}$$

and the source term is

$$\begin{aligned} S_{\rm ZM} &= -\frac{r^2}{(\lambda+1)\Lambda}\left[S_3 - \frac{1}{r}\left(\lambda+1-\frac{M}{r}\right)S_1 + \frac{2}{r\Lambda}\left(\lambda+\frac{6M}{r}\right)S_2\right] \\ &\quad + \frac{1}{\lambda+1}\left[\tilde{\Box} - V_{\rm ZM}\right]\left(\frac{rf}{2\Lambda}\tilde{p}\right) \\ &= \frac{2}{\Lambda}r^{,a}Q_a - \frac{1}{r}Q^\sharp + \frac{r^2}{(\lambda+1)\Lambda}\Big[-(Q^a{}_a)_{,b}r^{,b} + \frac{6M}{r^2\Lambda}Q_{ab}r^{,a}r^{,b} + \frac{f}{r}Q^\flat \\ &\quad + \frac{1}{r\Lambda}\left(\lambda(\lambda-1)+\frac{3M}{r}(2\lambda-3)+\frac{21M^2}{r^2}\right)Q^a{}_a\Big]. \end{aligned} \tag{2.61}$$

Setting $S_{\rm ZM} = 0$, we recover the covariant Zerilli-Moncrief equation found in [35].

Once the Zerilli-Moncrief function is found (by solving Eq. (2.59)), the metric perturbations can be recovered by inverting the second of Eq. (2.58) for $\tilde{K}$, $\tilde{p}$ is known from Eq. (2.34), and v is solved for by inverting the definition of the Zerilli-Moncrief function. The remaining component is obtained from, for example, one of the components of Eq. (2.31).

In Schwarzschild coordinates, Eq. (2.59) is the Zerilli-Moncrief equation found in the literature [22, 38]. Relations between the Zerilli-Moncrief function as defined here and the definition adopted by various authors can be found in the paper by C.O. Lousto and R.H. Price [38]. The new result presented here is a covariant derivation of the inhomogeneous decoupled Zerilli-Moncrief equation. In doing so, we covariantly defined the Zerilli-Moncrief function, as well as calculated the complete covariant source term for arbitrary even perturbations.

2.5.2 Regge-Wheeler function for odd parity perturbations

Odd parity perturbations are decoupled by introducing the scalar field

$$\psi_{\rm RW} \equiv -r^{-1} r^{,a} \tilde{h}_a. \tag{2.62}$$

The negative sign is purely conventional and inserted so that, in Schwarzschild coordinates, our definition agrees with that of T. Regge and J.A. Wheeler [19].

To decouple the equations, we first note that $\tilde{h}^a{}_{:a}$, from Eq. (2.37), is proportional to a source term. Contracting Eq. (2.36) with $r^{-1} r^{,a}$, and using Eq. (2.7) to eliminate $r^{,a} r_{,a}$ leads to

$$\begin{aligned} \frac{r^{,a} P_a}{r} + \frac{2f}{r^2} P &= \frac{r^{,a}}{r} \left(-\tilde{\Box} \tilde{h}_a + \frac{2}{r} r^{,b} \tilde{h}_{b:a} + \tilde{h}^b{}_{:ab} \right) \\ &- \frac{1}{r^3} \left(2 - \frac{2M}{r} - l(l+1) \right) r^{,a} \tilde{h}_a. \end{aligned} \tag{2.63}$$

The task is completed once we have expressions for $r^{-1} r^{,a} \tilde{\Box} \tilde{h}_a$, $r^{,a} \tilde{h}^b{}_{:ab}$, and $r^{-1} r^{,a} r^{,b} h_{a:b}$ in terms of $\psi_{\rm RW}$.

First, we calculate $\tilde{h}^b{}_{:ab}$:

$$\begin{aligned} r^{,a} \tilde{h}^b{}_{:ab} &= r^{,a} \left(h^b{}_{:ba} - \mathcal{R}^b{}_{cab} \tilde{h}^c \right) \\ &= r^{,a} \tilde{h}^b{}_{:ba} + \frac{2M}{r^3} r^{,a} \tilde{h}_a \\ &= r^{,a} P_{,a} - \frac{2M}{r^2} \psi_{\rm RW}, \end{aligned} \tag{2.64}$$

where $\mathcal{R}^d{}_{acb}$ is defined in Eq. (2.11) and Eq. (2.9). Secondly, for $r^{-1} r^{,a} r^{,b} \tilde{h}_{a:b}$ we get

$$\begin{aligned} r^{-1} r^{,a} r^{,b} \tilde{h}_{a:b} &= r^{,b} \left(r^{-1} r^{,a} \tilde{h}_a \right)_{:b} - \frac{r^{,b}}{r} r_{:ab} \tilde{h}^b + \frac{r^{,b} r_{,b}}{r^2} r^{,a} \tilde{h}_a \\ &= -r^{,a} \psi_{RW,a} - \frac{1}{r} \left(1 - \frac{3M}{r} \right) \psi_{\rm RW}, \end{aligned} \tag{2.65}$$

where we used Eq. (2.7) and Eq. (2.10) to go from the first to the second line. Finally, for $r^{-1} r^{,a} \tilde{\Box} \tilde{h}_a$ we obtain

$$r^{-1} r^{,a} \tilde{\Box} \tilde{h}_a = g^{bc} \left(r^{-1} r^{,a} \tilde{h}_{a:b} \right)_{:c} - \frac{r^{:ab}}{r} \tilde{h}_{a:b} + \frac{r^{,a} r^{,b}}{r^2} h_{a:b}$$

$$
\begin{aligned}
&= g^{bc}\left(r^{-1}r^{,a}\tilde{h}_a\right)_{:bc} - \left(r^{-1}r^{:ab}\tilde{h}_a - r^{-2}r^{,b}r^{,a}\tilde{h}_a\right)_{:b} - \frac{r^{:ab}}{r}\tilde{h}_{a:b} + \frac{r^{,a}r^{,b}}{r^2}h_{a:b} \\
&= g^{bc}\left(r^{-1}r^{,a}\tilde{h}_a\right)_{:bc} + \frac{1}{r^2}\left(r\tilde{\Box}r - r^{,a}r_{,a}\right)\left(r^{-1}r^{,a}\tilde{h}_a\right) + \frac{r^{,b}}{r}\left(r^{-1}r^{,a}\tilde{h}_a\right)_{:b} \\
&+ \frac{r^{:ab}}{r^2}r_{,a}\tilde{h}_b - \frac{\tilde{\Box}r^{:a}}{r}\tilde{h}_a - \frac{r^{:ab}}{r}\tilde{h}_{a:b} \\
&= -\tilde{\Box}\psi_{\rm RW} - \frac{2}{r}r^a\psi_{RW,a} - \frac{4M}{r^3}\psi_{\rm RW} - \frac{2M}{r^3}P. \qquad (2.66)
\end{aligned}
$$

Inserting these three results back into Eq. (2.63) yields

$$\left[\tilde{\Box} - V_{\rm RW}(r)\right]\psi_{\rm RW}(x^c) = S_{\rm RW}(x^c), \qquad (2.67)$$

where $\tilde{\Box}\psi_{\rm RW} = g_{ab}\psi^{:ab}_{\rm RW}$,

$$V_{\rm RW} = \frac{1}{r^2}\left[l(l+1) - \frac{6M}{r}\right], \qquad (2.68)$$

and

$$S_{\rm RW} = \frac{2}{r^2}\left(1 - \frac{3M}{r}\right)P + \frac{r^{,a}}{r}\left(P_a - P_{,a}\right). \qquad (2.69)$$

Setting $S_{\rm RW} = 0$, we recover the expression for the covariant Regge-Wheeler equation found in [35].

Once the solution to the Regge-Wheeler function is known, the vector field $\tilde{h}_a$ can be reconstructed by solving $-r^{-1}r^{,a}\tilde{h}_a = \psi_{\rm RW}$ and Eq. (2.37), a first-order differential equation.

In Schwarzschild coordinates, Eq. (2.67) governing the evolution of $\psi_{\rm RW}$ reduces to the famous Regge-Wheeler equation [19]. Here, we provided a covariant definition for the Regge-Wheeler function as well as a covariant derivation of the equation it satisfies, including a complete covariant expression for the source term.

Chapter 3

Perturbations of a Schwarzschild black hole in Schwarzschild coordinates

In the previous chapter, we have developed a completely covariant and gauge invariant description of the perturbations of a Schwarzschild black hole. The perturbations are completely specified by two scalar functions from which the metric perturbations can be reconstructed. In this dissertation, we shall study the perturbations of the Schwarzschild black hole in Schwarzschild coordinates, and, for convenience, we list the equations in those coordinates in Sec. 3.1, while the Zerilli-Moncrief and Regge-Wheeler equations, including the source terms, are given in Sec. 3.2.

The remaining step is to extract physical information from the perturbations. The master wave equations obeyed by the scalar functions are wave equations that describe the propagation of gravitational waves in the Schwarzschild background. We are interested in extracting the waveforms, as well as the energy and angular

momentum carried by the radiation.

The Regge-Wheeler gauge is not an asymptotically flat gauge, and is therefore not well suited to describe the radiation and calculate the fluxes. Because the radiative part of the perturbation tensor is the one that carries energy and angular momentum, a natural choice of gauge for the purpose of calculating fluxes is a radiation gauge. Physically, the fields are required to be outgoing at null-infinity and ingoing at the event horizon, and we need to express the perturbation tensor in an outgoing (ingoing) radiation gauge to describe the radiation and calculate the fluxes at null-infinity (the event horizon).

Starting from the perturbation tensor in the Regge-Wheeler gauge, we provide an explicit prescription to reconstruct the components of p_{ab} and h_a as well as K from the Zerilli-Moncrief and Regge-Wheeler functions. This is done in Sec. 3.3.1. This is a necessary step: the gauge transformation equations can be solved only when all components of the metric perturbation are known in the initial gauge (the Regge-Wheeler gauge in this case). In Sec. 3.3.2, we provide approximate solutions to the gauge transformation equations and obtain the perturbation tensor in both outgoing and ingoing radiation gauges. In that section, we also make a connection between the Zerilli-Moncrief and Regge-Wheeler functions and the two gravitational-wave polarizations. Finally, in Sec. 3.3.3, we present a derivation of the fluxes of energy and angular momentum, in terms of the Zerilli-Moncrief and Regge-Wheeler functions.

3.1 Metric Perturbations in Schwarzschild coordinates

With the use of the metric of Eq. (2.6), it is quite easy to give the metric perturbation equations in Schwarzschild coordinates. Below, we express the perturbation equations in terms of components of the perturbation tensor. These equations are used throughout the dissertation and we find it convenient to group them here. We let $\tilde{p}_{tt} = f\tilde{H}_0$, $\tilde{p}_{tr} = \tilde{H}_1$, and $\tilde{p}_{rr} = f^{-1}\tilde{H}_2$, where $f = 1 - 2M/r$, in terms of which the even parity perturbation equations read

$$\begin{aligned}
Q^{tt} &= -\frac{\partial^2}{\partial r^2}\tilde{K} - \frac{3r-5M}{r^2 f}\frac{\partial}{\partial r}\tilde{K} + \frac{1}{r}\frac{\partial}{\partial r}\tilde{H}_2 + \frac{1}{r^2 f}\Big(\tilde{H}_2 - \tilde{K}\Big) \\
&+ \frac{l(l+1)}{2r^2 f}\Big(\tilde{H}_2 + \tilde{K}\Big), && (3.1)\\
Q^{tr} &= \frac{\partial}{\partial t}\left(\frac{\partial}{\partial r}\tilde{K} - \frac{1}{r}\tilde{H}_2 + \frac{r-3M}{r^2 f}\tilde{K}\right) - \frac{l(l+1)}{2r^2}\tilde{H}_1, && (3.2)\\
Q^{rr} &= -\frac{\partial^2}{\partial t^2}\tilde{K} + \frac{r-M}{r^2} f\frac{\partial}{\partial r}\tilde{K} - \frac{f^2}{r}\frac{\partial}{\partial r}\tilde{H}_0 + \frac{2f}{r}\frac{\partial}{\partial t}\tilde{H}_1 + \frac{f}{r^2}\Big(\tilde{K} - \tilde{H}_2\Big) \\
&+ \frac{l(l+1)}{2r^2} f\Big(\tilde{H}_0 - \tilde{K}\Big), && (3.3)\\
Q^{t} &= \frac{1}{f}\frac{\partial}{\partial t}\Big(\tilde{K} + \tilde{H}_2\Big) - \frac{\partial}{\partial r}\tilde{H}_1 - \frac{2M}{r^2 f}\tilde{H}_1, && (3.4)\\
Q^{r} &= f\frac{\partial}{\partial r}\Big(\tilde{H}_0 - \tilde{K}\Big) - \frac{\partial}{\partial t}\tilde{H}_1 - \frac{r-3M}{r^2}\tilde{H}_0 + \frac{r-M}{r^2}\tilde{H}_2, && (3.5)\\
Q^{\flat} &= -\frac{1}{f}\frac{\partial^2}{\partial t^2}\Big(\tilde{K} + \tilde{H}_2\Big) + f\frac{\partial^2}{\partial r^2}\Big(\tilde{K} - \tilde{H}_0\Big) + 2\frac{\partial^2}{\partial t \partial r}\tilde{H}_1 + 2\frac{r-M}{r^2 f}\frac{\partial}{\partial t}\tilde{H}_1 \\
&- \frac{r+M}{r^2}\frac{\partial}{\partial r}\tilde{H}_0 + \frac{r-M}{r^2}\frac{\partial}{\partial r}\Big(2\tilde{K} - \tilde{H}_2\Big) + \frac{l(l+1)}{2r^2}\Big(\tilde{H}_0 - \tilde{H}_2\Big), && (3.6)\\
Q^{\sharp} &= \tilde{H}_0 - \tilde{H}_2. && (3.7)
\end{aligned}$$

For odd parity modes, we express the vector field $\tilde{h}_a$ in terms of its components $(\tilde{h}_0, \tilde{h}_1)$, and the odd parity perturbation equations read

$$P^t = \frac{\partial^2}{\partial r^2}\tilde{h}_0 - \frac{\partial^2}{\partial t \partial r}\tilde{h}_1 - \frac{2}{r}\frac{\partial}{\partial t}\tilde{h}_1 - \frac{1}{f}\left[\frac{l(l+1)}{r^2} - \frac{4M}{r^3}\right]\tilde{h}_0, \qquad (3.8)$$

$$P^r = \frac{\partial^2}{\partial t^2}\tilde{h}_1 - \frac{\partial^2}{\partial t \partial r}\tilde{h}_0 + \frac{2}{r}\frac{\partial}{\partial t}\tilde{h}_0 + \frac{(l-1)(l+2)}{r^2} f\tilde{h}_1, \tag{3.9}$$

$$P = -\frac{1}{f}\frac{\partial}{\partial t}\tilde{h}_0 + f\frac{\partial}{\partial r}\tilde{h}_1 + \frac{2M}{r^2}\tilde{h}_1. \tag{3.10}$$

The source terms for these equations are given in Chapter 2 by Eq. (2.35) and Eq. (2.38).

3.2 Master equations in Schwarzschild coordinates

In terms of the components introduced in the previous section ($\tilde{h}_t = \tilde{h}_0$, $\tilde{h}_r = \tilde{h}_1$, $\tilde{p}_{tt} = f\tilde{H}_0$, $\tilde{p}_{tr} = \tilde{H}_1$, and $\tilde{p}_{rr} = f^{-1}\tilde{H}_2$), and the metric of Eq. (2.6), we find that the Zerilli-Moncrief and the Regge-Wheeler functions are expressed as

$$\begin{aligned} \psi_{\rm ZM} &= \frac{r}{\lambda+1}\left[\tilde{K} + \frac{f}{\Lambda}\left(\tilde{H}_2 - r\frac{\partial}{\partial r}\tilde{K}\right)\right], \\ \psi_{\rm RW} &= -\frac{f}{r}\tilde{h}_1, \end{aligned} \tag{3.11}$$

where $\lambda = (l+2)(l-1)/2$, and $\Lambda = \lambda + 3M/r$.

In Schwarzschild coordinates, the action of the operator $\tilde{\Box}$ on a scalar field χ is given by

$$\tilde{\Box}\chi = -f^{-1}\left[\frac{\partial^2}{\partial t^2} - \frac{\partial^2}{\partial r^{*2}}\right]\chi.$$

The Zerilli-Moncrief and Regge-Wheeler master equations, given by Eq. (2.59) and Eq. (2.67), respectively, become

$$\left[-\frac{\partial^2}{\partial t^2} + \frac{\partial^2}{\partial r^{*2}} - fV_{\rm ZM}(r)\right]\psi_{\rm ZM}(r,t) = S_{\rm ZM}(r,t), \tag{3.12}$$

$$\left[-\frac{\partial^2}{\partial t^2} + \frac{\partial^2}{\partial r^{*2}} - fV_{\rm RW}(r)\right]\psi_{\rm RW}(r,t) = S_{\rm RW}(r,t), \tag{3.13}$$

where $V_{\rm ZM}$ and $V_{\rm RW}$ are given by Eq. (2.60) and Eq. (2.68), respectively, and

$$S_{\rm ZM} = \frac{1}{(\lambda+1)\Lambda}\left\{r^2 f\left(f^2\frac{\partial}{\partial r}Q^{tt} - \frac{\partial}{\partial r}Q^{rr}\right) + r(\Lambda - f)Q^{rr} + rf^2Q^{\flat}\right.$$

$$-\frac{f^2}{r\Lambda}\Big[\lambda(\lambda-1)r^2+(4\lambda-9)Mr+15M^2\Big]Q^{tt}\Big\}+\frac{2f}{\Lambda}Q^r-\frac{f}{r}Q^\sharp, \quad (3.14)$$

$$S_{\rm RW} = \frac{f}{r}\left[\frac{2}{r}\Big(1-\frac{3M}{r}\Big)P-f\frac{\partial}{\partial r}P+P^r\right], \quad (3.15)$$

are the source terms calculated from Eq. (2.61) and Eq. (2.69), respectively.

These are used explicitly in Chapter 4 and in Chapter 5 to obtain gravitational waveforms as well as the energy and angular momentum fluxes for arbitrary motion of a point-particle around a Schwarzschild black hole.

3.3 Fluxes of energy and angular momentum

We have derived the inhomogeneous decoupled equations governing the evolution of even and odd parity perturbations of a Schwarzschild black hole and expressed them in Schwarzschild coordinates. We showed that once the source term is specified, the Zerilli-Moncrief and Regge-Wheeler functions can be found by solving Eq. (3.12) and Eq. (3.13). In this section, it is assumed that the Zerilli-Moncrief and Regge-Wheeler functions are known everywhere in the spacetime.

We are then interested in obtaining expressions for the fluxes of energy and angular momentum in terms of these two scalar functions. More precisely, we want to relate the fluxes of energy and angular momentum escaping to infinity and flowing through the event horizon to the Zerilli-Moncrief and Regge-Wheeler functions. This requires the introduction of a stress-energy tensor for gravitational-waves; we use the definition given by Isaacson, which can be defined in any region of spacetime where the gravitational wavelength is small compared with the radius of curvature [43].

The relations are easier to establish by first isolating the radiative part of $h_{\mu\nu}$. We now turn to this problem.

3.3.1 Reconstructing the metric perturbations in Schwarzschild coordinates

The radiative part of the perturbation tensor can be isolated by calculating its components in a radiation gauge. We start from the perturbation tensor in the Regge-Wheeler gauge, and solve the gauge transformation equations given in Eq. (2.23) and Eq. (2.27) to obtain $h_{\mu\nu}$ in a radiation gauge.

In Sec. 2.5.1 and Sec. 2.5.2, we provided some information about reconstructing the metric perturbations from the Zerilli-Moncrief and Regge-Wheeler functions. The information missing from these two sections is found from Eq. (3.2) and from Eq. (3.10). The Q^{tr} equation provides an equation for $\tilde{H}_1$, while P is a differential equation for $\tilde{h}_0$. In Schwarzschild coordinates, we are able to give explicit formulae for reconstructing the metric perturbations in the Regge-Wheeler gauge.

For even perturbations, once $\psi_{\rm ZM}$ is found, $\tilde{K}$ can be obtained from Eq. (2.58), $\tilde{H}_2$ is obtained by inverting the definition of the Zerilli-Moncrief function given by Eq. (3.11), $\tilde{H}_1$ from Q^{tr}, and, finally, $\tilde{H}_0$ is obtained from the trace condition, Eq. (3.7). The inversion is straightforward and yields

$$\begin{aligned}
\tilde{K} &= f\frac{\partial}{\partial r}\psi_{\rm ZM} + A(r)\psi_{\rm ZM} - \frac{r^2 f^2}{(\lambda+1)\Lambda}Q^{tt}, \\
\tilde{H}_2 &= \frac{\Lambda}{f}\left[\frac{\lambda+1}{r}\psi_{\rm ZM} - \tilde{K}\right] + r\frac{\partial}{\partial r}\tilde{K}, \\
\tilde{H}_1 &= r\frac{\partial}{\partial t}\left[\frac{\partial}{\partial r}\psi_{\rm ZM} + B(r)\psi_{\rm ZM}\right] - \frac{r^2}{\lambda+1}\left[Q^{tr} + \frac{rf}{\Lambda}\frac{\partial}{\partial t}Q^{tt}\right], \\
\tilde{H}_0 &= \tilde{H}_2 + Q^{\sharp}, \qquad (3.16)
\end{aligned}$$

where $A(r) = [\lambda(\lambda+1) + 3M/r\,(\lambda + 2M/r)]/(r\Lambda)$ and $B(r) = [\lambda(1 - 3M/r) - 3M^2/r^2]/(rf\Lambda)$.

For odd parity perturbations, $\tilde{h}_1$ is directly proportional to $\psi_{\rm RW}$ and can easily

be obtained. Reconstructing the second component entails solving Eq. (2.37). The result for both components is

$$\begin{aligned}\tilde{h}_0 &= -f\int_{-\infty}^{t} dt'\left[\frac{\partial}{\partial r}\Big(r\psi_{\rm RW}(t',r)\Big)+P\right]+C(r),\\ \tilde{h}_1 &= -rf^{-1}\psi_{\rm RW},\end{aligned} \tag{3.17}$$

where $C(r)$ is an integration constant: it represents a static perturbation that can be freely specified; we take $C(r)=0$.

The equations above can be used to construct the gauge invariant metric perturbations. Unfortunately, this is not sufficient to solve the gauge transformation equations; we need explicit expressions for all the metric components. This is the justification behind the choice for the Regge-Wheeler gauge. In this gauge, the *only* non-vanishing components of the perturbation tensor are the ones listed above. ($G^{\rm RW}=0$, $q_a^{\rm RW}=0$ and $h_2^{\rm RW}=0$.) Eq. (3.16) and Eq. (3.17) then contain all the information needed.

In the next section, we start from the Regge-Wheeler gauge (and drop the tilde on $\tilde{K}$, $\tilde{p}_{ab}$ and $\tilde{h}_a$), and obtain the perturbation tensor in outgoing and ingoing radiation gauges. These gauges are a natural choice, since the appropriate ingoing-wave and outgoing-wave boundary conditions for the radiation field are built into them.

3.3.2 From gauge to gauge to gauge

We need to solve Eqs. (2.23)-(2.28) to obtain the metric perturbations in radiation gauges (RG). In Schwarzschild coordinates, the even parity transformation equations are

$$\begin{aligned}p_{tt}^{RG} &= fH_0^{\rm RW}-2\Big(\dot{\alpha}_t-\frac{M}{r^2}f\alpha_r\Big),\\ p_{tr}^{RG} &= H_1^{\rm RW}-\Big(\alpha_t'+\dot{\alpha}_r-\frac{2M}{r^2}f^{-1}\alpha_t\Big),\end{aligned}$$

$$
\begin{aligned}
p^{RG}_{rr} &= f^{-1}H_2^{\rm RW} - 2\left(\alpha'_r + \frac{M}{r^2}f^{-1}\alpha_r\right), \\
q^{RG}_{t} &= -\left(\alpha_t + r^2\dot{\beta}\right), \\
q^{RG}_{r} &= -\left(\alpha_r + r^2\beta'\right), \\
K^{RG} &= K^{\rm RW} - \left(\frac{2f}{r}\alpha_r - l(l+1)\beta\right), \\
G^{RG} &= -2\beta. \qquad (3.18)
\end{aligned}
$$

An overdot indicates time differentiation, while a prime indicates differentiation with respect to r. The odd transformation equations are

$$
\begin{aligned}
h^{RG}_{t} &= h_0^{\rm RW} - r^2\dot{\gamma}, \\
h^{RG}_{r} &= h_1^{\rm RW} - r^2\gamma', \\
h^{RG}_{2} &= -2r^2\gamma. \qquad (3.19)
\end{aligned}
$$

We use $\alpha_a = (\alpha_t, \alpha_r)$ in Eq. (2.23), the superscript RG refers to components in a radiation gauge, and RW refers to the Regge-Wheeler gauge.

The radiation gauges are easily defined by first introducing a complex null-tetrad l^ν, n^ν, and m^μ. The vectors l^μ and n^ν are null-vectors, and are tangent to outgoing and ingoing radial light rays, respectively; the vector m^μ is a complex null-vector (with complex conjugate $\bar{m}^\mu$) on the two-sphere. They satisfy the relations:

$$
l^\mu l_\mu = 0 = n^\mu n_\mu, \qquad m^\mu m_\mu = 0 = \bar{m}^\mu \bar{m}_\mu, \qquad l^\mu n_\mu = -1 = -m^\mu \bar{m}_\mu. \qquad (3.20)
$$

From these, we can write the completeness relation

$$
g_{\mu\nu} = 2[-l_{(\mu}n_{\nu)} + m_{(\mu}\bar{m}_{\nu)}]
$$

for the spacetime metric tensor, and

$$
\Omega_{AB} = 2m_{(A}\bar{m}_{B)}
$$

and for the metric of the unit-two sphere, where $m^A = r\,(\partial\theta^A/\partial x^\mu)\,m^\mu$. In Schwarzschild coordinates, these vectors are

$$l_\mu = (-1, f^{-1}, 0, 0), \qquad n_\mu = -\frac{1}{2}(f, 1, 0, 0), \qquad m_\mu = \frac{\sqrt{2}}{2} r(0, 0, 1, \imath \sin\theta). \quad (3.21)$$

Outgoing radiation gauge

In an outgoing radiation gauge $h^{ORG}_{\mu\nu}$, the perturbation tensor satisfies [44]

$$\begin{aligned} h^{ORG}_{\mu\nu} n^\mu n^\nu &= 0, \\ h^{ORG}_{\mu\nu} n^\mu m^\nu &= 0 = h^{ORG}_{\mu\nu} n^\mu \bar{m}^\nu, \\ h^{ORG}_{\mu\nu} n^\mu l^\nu &= 0 = h^{ORG}_{\mu\nu} m^\mu \bar{m}^\nu. \end{aligned} \quad (3.22)$$

The first two conditions indicate the $h^{ORG}_{\mu\nu}$ is transverse to outgoing null rays, while the last condition indicates that it is traceless. Eqs. (3.22) involve five conditions, one too many for the specification of a gauge. But this system is not overdetermined: once four of these equations are enforced, the fifth is found to be satisfied automatically in the radiation zone.

Substitution of Eq. (3.18) and Eq. (3.19) into Eq. (3.22) leads to a set of differential equations for the gauge functions. To leading-order in r^{-1}, they are

$$\begin{aligned} 2\,(\dot{\alpha}_t - \alpha'_t - \dot{\alpha}_r + \alpha'_r) &= H_0^{\mathrm{RW}} + H_2^{\mathrm{RW}} - 2H_1^{\mathrm{RW}}, \\ \alpha_t - \alpha_r + r^2(\dot{\beta} - \beta') &= 0, \\ 2\,(\dot{\alpha}_t - \alpha'_r) &= 0, \\ \frac{2}{r}\alpha_r &= -K^{\mathrm{RW}}, \end{aligned} \quad (3.23)$$

for even parity modes, and

$$r^2\,(\dot{\gamma} - \gamma') = h_1^{\mathrm{RW}} - h_0^{\mathrm{RW}}, \quad (3.24)$$

for odd parity modes; an overdot and a prime denote a derivative with respect to t and r, respectively. Because we are assuming that the metric perturbations in the Regge-Wheeler gauges are known functions, they act as source terms for the gauge transformation. From Eq. (3.16), we find that in the radiation zone

$$K^{\rm RW} \approx -\dot{\psi}_{\rm ZM}, \quad H_2^{\rm RW} \approx H_0^{\rm RW} \approx -H_1^{\rm RW} \approx r\ddot{\psi}_{\rm ZM},$$

while Eq. (3.17) yields

$$h_0 \approx -h_1 \approx r\psi_{\rm RW}.$$

The gauge transformation equations can be simplified further, since, in the radiation zone, $\dot{\xi} \approx -\xi' + \mathcal{O}(r^{-1})$ for any field ξ that behaves as an outgoing wave. This follows from the outgoing character of the radiation field in this region of spacetime.

Solving Eq. (3.23) and Eq. (3.24) for α_t, α_r β and γ is then quite easy. For even modes, the last of Eq. (3.23) provides a solution for α_r:

$$\alpha_r = \frac{r}{2}K^{\rm RW} = -\frac{r}{2}\dot{\psi}_{\rm ZM}.$$

The remaining two even parity gauge functions are found from the second and the third of Eq. (3.23). The later yields $\alpha_t = -\alpha_r$, while the former becomes

$$r^2\dot{\beta} = \alpha_r \;\Rightarrow\; \beta = -\psi_{\rm ZM}/(2r).$$

We did not use the first of Eq. (3.23), but it is straightforward to verify that, in the radiation zone, it is consistent with the solution above. For odd modes, the solution is even shorter. We use the approximate form of $h_0^{\rm RW}$ and $h_1^{\rm RW}$ in Eq. (3.24) and obtain

$$\gamma = \frac{1}{r}\int_{-\infty}^{t} dt'\psi_{\rm RW}(t').$$

These functions now completely specify the transformation from the Regge-Wheeler gauge to the outgoing radiation gauge. Going back to Eq. (3.18) and Eq. (3.19), we

construct the perturbation tensor in the outgoing radiation gauge:

$$\begin{aligned} p_{ab}^{ORG} &\sim \mathcal{O}(r^{-2}), \\ q_a^{ORG} &\sim \mathcal{O}(r^{-1}), \\ K^{ORG} &\sim \mathcal{O}(r^{-2}), \\ G^{ORG} &= \frac{1}{r}\psi_{\mathrm{ZM}}, \end{aligned} \tag{3.25}$$

for even modes, and

$$\begin{aligned} h_a^{ORG} &\sim \mathcal{O}(r^{-1}), \\ h_2^{ORG} &= -2r\int_{-\infty}^{t} dt'\psi_{\mathrm{RW}}(t'), \end{aligned} \tag{3.26}$$

for odd modes.

The radiative part of the perturbation tensor is entirely contained in h_{AB}^{ORG}:

$$h_{AB}^{ORG} = r\sum_{lm}\left(\psi_{\mathrm{ZM}}^{lm}(t)V_{AB}^{lm} - 2\int_{-\infty}^{t} dt'\psi_{\mathrm{RW}}^{lm}(t')W_{AB}^{lm}\right) \tag{3.27}$$

In terms of the two gravitational-wave polarizations

$$h_+ = h_{\theta\theta}^{ORG}/r^2 \qquad \text{and} \qquad h_\times = h_{\theta\phi}^{ORG}/(r^2\sin\theta),$$

we have

$$h_+ - \imath h_\times = \frac{1}{2r}\sum_{lm}\sqrt{\frac{(l+2)!}{(l-2)!}}\left(\psi_{\mathrm{ZM}}^{lm}(t) - 2\imath\int_{-\infty}^{t} dt'\psi_{\mathrm{RW}}^{lm}(t')\right)\ {}_{-2}Y^{lm}(\theta,\phi), \tag{3.28}$$

where we introduce the spherical harmonic of spin-weight $s = -2$ [45]:

$$V_{AB}^{lm}\ \bar{m}^A\ \bar{m}^B = \frac{1}{2}\sqrt{\frac{(l+2)!}{(l-2)!}}\ {}_{-2}Y^{lm}(\theta,\phi) = -\imath W_{AB}^{lm}\ \bar{m}^A\ \bar{m}^B,$$

and m^A is given at the end of the previous section.

This completely specifies the relation between the Zerilli-Moncrief and the Regge-Wheeler functions, and the radiative part of the gravitational field in the far zone.

The Zerilli-Moncrief and the Regge-Wheeler functions can be calculated for any type of perturbing stress-energy tensor and in any coordinate system through Eq. (2.59) and Eq. (2.67). Once these functions are known, the gravitational waveforms are given by Eq. (3.28) above.

Ingoing radiation gauge

The ingoing radiation gauge can be constructed by interchanging l^μ and n^μ in Eq. (3.22). In this gauge, the perturbation tensor $h^{IRG}_{\mu\nu}$ satisfies [44]

$$\begin{aligned} h^{IRG}_{\mu\nu} l^\mu l^\nu &= 0, \\ h^{IRG}_{\mu\nu} l^\mu m^\nu &= 0 = h^{IRG}_{\mu\nu} l^\mu \bar{m}^\nu, \\ h^{IRG}_{\mu\nu} n^\mu l^\nu &= 0 = h^{IRG}_{\mu\nu} m^\mu \bar{m}^\nu. \end{aligned} \tag{3.29}$$

The first two conditions indicate the $h^{IRG}_{\mu\nu}$ is transverse to ingoing null-rays, while the last condition indicates that it is traceless. We seek to impose this condition near the event horizon, where $f \to 0$. The same comment about the number of gauge conditions that was made about the outgoing radiation gauge can be made here: only four gauge conditions need to be imposed, and the fifth condition is satisfied automatically near the event horizon.

The calculation shadows the steps of the previous section with two minor changes: First, the component α_r is divergent at the event horizon, we remove this divergence by making the substitution $\alpha_r \to f^{-1}\alpha_r$ in Eq. (3.18). Second, the field at the event horizon is ingoing and the appropriate relation between time and radial derivatives is $\dot{\xi} = \partial\xi/\partial r^* + \mathcal{O}(f)$, where $r^* = r + 2M\log(r/2M - 1)$ is the usual tortoise coordinate. With these changes, substitution of Eq. (3.18) and Eq. (3.19) into the ingoing

radiation gauge conditions yields

$$\begin{aligned} 4(\dot{\alpha}_t + \dot{\alpha}_r) - \frac{1}{M}(\alpha_t + \alpha_r) &= 2f\left(H_2^{\rm RW} + H_1^{\rm RW}\right), \\ \dot{\alpha}_t - \dot{\alpha}_r &= 0, \\ 8M^2\dot{\beta} + \alpha_t + \alpha_r &= 0, \\ \frac{1}{M}\alpha_r - \beta &= K^{\rm RW}, \end{aligned} \tag{3.30}$$

for the gauge transformations of even parity modes, and

$$r^2\dot{\gamma} = r(h_0^{\rm RW} + f h_1^{\rm RW}), \tag{3.31}$$

for those of odd parity modes. The metric perturbations in the Regge-Wheeler gauge act as a source for the gauge transformation equations. From Eq. (3.16), and Eq. (3.17), we get the asymptotic form of the metric perturbations near the event horizon:

$$K^{\rm RW} \approx \dot{\psi}_{\rm ZM} + \frac{\lambda+1}{2M}\psi_{\rm ZM}, \quad H_2^{\rm RW} = H_0^{\rm RW} = H_1^{\rm RW} = f^{-1}\left(2M\ddot{\psi}_{\rm ZM} - \frac{1}{2}\dot{\psi}_{\rm ZM}\right),$$

for even parity modes, and

$$h_0^{\rm RW} = f h_1^{\rm RW} = -2M\psi_{\rm RW},$$

for odd parity ones.

The solution to the gauge transformation proceeds as follow. For even parity modes, the second and third equations yield $\alpha_r = \alpha_t$ and $4M^2\dot{\beta} = -\alpha_t$. These can be substituted into the first and the time derivative of the fourth of Eq. (3.30). Combining this with the asymptotic form of the even metric perturbations provides a system of two equations for α_t:

$$\dot{\alpha}_t - \frac{1}{4M}\alpha_t = M\ddot{\psi}_{\rm ZM} - \frac{1}{4}\dot{\psi}_{\rm ZM}, \tag{3.32}$$

$$\dot{\alpha}_t + \frac{\lambda+1}{2M}\alpha_t = M\ddot{\psi}_{\rm ZM} + \frac{\lambda+1}{2}\dot{\psi}_{\rm ZM}. \tag{3.33}$$

Eliminating the time derivative by subtraction, we find $\alpha_t = M\dot{\psi}_{\rm ZM}$. For odd parity modes, integration of Eq. (3.31), combined with the asymptotic form of $h_0^{\rm RW}$ and $h_1^{\rm RW}$, yields $\gamma = -1/(2M)\int dt'\ \psi_{\rm RW}(t')$.

These functions now completely specify the transformation from the Regge-Wheeler gauge to the ingoing radiation gauge. Going back to Eq. (3.18) and Eq. (3.19), we construct the perturbation tensor in this gauge:

$$\begin{aligned} H_2^{IRG} &\sim H_0^{IRG} \sim H_1^{IRG} \sim \mathcal{O}(1), \\ q_t^{IRG} &\sim \mathcal{O}(f), \qquad \text{and} \qquad q_r^{IRG} \sim \mathcal{O}(1), \\ G^{IRG} &= -\frac{1}{2M}\psi_{\rm ZM}. \end{aligned} \tag{3.34}$$

for even parity modes, and

$$\begin{aligned} h_t^{IRG} &\sim \mathcal{O}(f), \qquad \text{and } h_r^{IRG} \sim \mathcal{O}(1), \\ h_2^{IRG} &= 4M\int dt'\ \psi_{\rm RW}(t'), \end{aligned} \tag{3.35}$$

for odd parity modes.

It appears as though most of the metric components are of the same order as G^{IRG} and h_2^{IRG}, but we show in the next section that only G^{IRG} and h_2^{IRG} contribute to the fluxes of energy and angular momentum through the event horizon. We shall therefore refer to

$$h_{AB}^{IRG} = 2M\sum_{lm}\left[\psi_{\rm ZM}^{lm}V_{AB}^{lm} + 2\int dt'\psi_{\rm RW}^{lm}(t')W_{AB}^{lm}\right]. \tag{3.36}$$

as the radiative part of the metric perturbation. In analogy with the far zone definitions, the two gravitational-wave polarizations are $h_+ = h_{\theta\theta}^{IRG}/4M^2$ and $h_\times = h_{\theta\phi}^{IRG}/(4M^2\sin\theta)$. They are given by

$$h_+ + \imath h_\times = \frac{1}{4M}\sum_{lm}\sqrt{\frac{(l+2)!}{(l-2)!}}\left(\psi_{\rm ZM}^{lm}(t) - 2\imath\int^t dt'\psi_{\rm RW}^{lm}(t')\right){}_2Y^{lm}(\theta,\phi), \tag{3.37}$$

in terms of the spherical harmonic of spin-weight $s = 2$ [45]:

$$V^{lm}_{AB}\, m^A\, m^B = \frac{1}{2}\sqrt{\frac{(l+2)!}{(l-2)!}}\, {}_2Y^{lm}(\theta,\phi) = \imath W^{lm}_{AB}\, m^A\, m^B.$$

3.3.3 Fluxes of energy and angular momentum

There is an ambiguity in defining a stress-energy tensor for gravitational waves. The problem is of course rooted in the equivalence principle, which forbids the formulation of a local energy density for the gravitational field.

The stress-energy tensor of the gravitational waves, $T^{GW}_{\mu\nu}$, can be constructed by examining the second-order terms in $h_{\mu\nu}$ that were neglected in developing the perturbation equations, starting from Eq. (2.15). Starting from these, Isaacson was able to find a gauge invariant stress-energy tensor for gravitational waves [43]:

$$T^{GW}_{\mu\nu} = \frac{1}{64\pi}\left\langle h^{\alpha\beta}{}_{;\mu} h_{\alpha\beta;\nu}\right\rangle, \tag{3.38}$$

where $\langle \ldots \rangle$ denotes an average over a region of spacetime large compared with the wavelength of the radiation. Typically, $T^{GW}_{\mu\nu}$ can be defined when the wavelength of the radiation, λ, is small compared to a typical radius of curvature $\mathcal{R}$. By definition, $\lambda \ll \mathcal{R}$ in the radiation zone and the stress-energy tensor for gravitational waves can be defined there. There is a second region where the condition $\lambda \ll \mathcal{R}$ is satisfied: A stationary observer near $r = 2M$ sees $\mathcal{R} \sim 2M$, but the radiation is strongly blueshifted and $\lambda \to 0$; that this is the case is clear from the divergence in Eq. (3.63) below.

Our calculation of the fluxes uses the Killing vectors of the Schwarzschild metric ${}_{(t)}\xi^\alpha = \delta^\alpha_t$ and ${}_{(\phi)}\xi^\alpha = \delta^\alpha_\phi$. They satisfy ${}_{(t)}\xi_{(\alpha;\beta)} = 0 = {}_{(\phi)}\xi_{(\alpha;\beta)}$. The existence of these vectors is associated with conserved quantities in the spacetime, which we

exploit by constructing the vectors

$$t^\mu = -T^\mu_{\ \nu\,(t)}\xi^\nu \qquad \text{and} \qquad j^\mu = T^\mu_{\ \nu\,(\phi)}\xi^\nu,$$

which encode the information about the flow of energy (t^μ) and angular momentum (j^μ) associated with $T^{\mu\nu}$. By construction, both vectors are divergence-free: $t^\mu_{\ ;\mu} = 0 = j^\mu_{\ ;\mu}$. (This is easily established from Killing's equation and energy conservation $T^{\mu\nu}_{\ \ ;\nu} = 0$.)

We consider a four-dimensional volume V with boundary ∂V. Integrating the divergence of t_μ and j_μ over V and using Gauss theorem provides us with

$$\begin{aligned} \int_V dV t^\mu_{\ ;\mu} &= \oint_{\partial V} t^\mu d\Sigma_\mu = 0, \\ \int_V dV j^\mu_{\ ;\mu} &= \oint_{\partial V} j^\mu d\Sigma_\mu = 0, \end{aligned} \tag{3.39}$$

where $d\Sigma_\mu$ is an oriented surface element on ∂V. The first equality states that the flow of energy through a closed three-surface vanishes, while the second is the equivalent statement for the flow of angular momentum. The fluxes of energy and angular momentum across a surface $r = const.$ denoted Σ are then inferred to be

$$\Delta E = \int_\Sigma t^\mu d\Sigma_\mu, \tag{3.40}$$

$$\Delta L = \int_\Sigma j^\mu d\Sigma_\mu, \tag{3.41}$$

where

$$d\Sigma_\mu = \eta_\mu |\sigma|^{\frac{1}{2}}\, dt\, d\theta\, d\phi, \tag{3.42}$$

σ is the determinant of the induced metric on Σ, and η_μ is normal to surfaces $r = const.$ We have

$$\eta_\mu = \epsilon \frac{r_{,\mu}}{(r^{,\nu} r_{,\nu})^{1/2}} = \epsilon f^{-1/2} \delta^r_{\ \mu}, \tag{3.43}$$

$$\sigma_{\mu\nu} = g_{\mu\nu} - \eta_\mu \eta_\nu, \tag{3.44}$$

where $\epsilon = \pm 1$ is chosen so that $d\Sigma_\mu$ is outward directed with respect to V: for $\epsilon = 1$, $d\Sigma_\mu$ points toward increasing r, while for $\epsilon = -1$, it points toward decreasing r. In usual Schwarzschild coordinates, the determinant is $|\sigma|^{1/2} = \sqrt{f} r^2 \sin\theta$.

The expressions for the energy and angular momentum flow through *any* surface $r = const.$ are therefore

$$\begin{aligned} \Delta E &= -\epsilon r^2 f \int d\Omega\, dt\, T_{rt}, \qquad \text{or} \qquad \frac{dE}{dt} = -\epsilon r^2 f \int d\Omega\, T_{tr}, \\ \Delta L &= \epsilon r^2 f \int d\Omega\, dt\, T_{r\phi}, \qquad \text{or} \qquad \frac{dL}{dt} = \epsilon r^2 f \int d\Omega\, T_{r\phi}. \end{aligned} \tag{3.45}$$

Below, we evaluate these expressions for the energy and angular momentum radiated per unit time by using Eq. (3.27) and Eq. (3.36) for the perturbation tensor expressed in the outgoing and ingoing gauges.

Radiation zone fluxes

We start by obtaining the components of $T^{GW}_{\mu\nu}$ that are needed for the purpose of calculating the fluxes, i.e. T^{GW}_{tr}, and $T^{GW}_{r\phi}$.

The calculations are simplified if we first express the metric perturbation tensor in terms of its tetrad components. Using the tetrad of Eq. (3.21) with Eq. (3.22) for the outgoing radiation gauge conditions, we express $h^{ORG}_{\mu\nu}$ as

$$\begin{aligned} h^{ORG}_{\mu\nu} &= h_{ll}\, n_\mu n_\nu + 2\left(h_{l\bar{m}} n_{(\mu} m_{\nu)} + h_{lm} n_{(\mu} \bar{m}_{\nu)}\right) \\ &+ h_{\bar{m}\bar{m}} m_\mu m_\nu + h_{mm} \bar{m}_\mu \bar{m}_\nu, \end{aligned} \tag{3.46}$$

where, for example, $h_{vv} = h_{\mu\nu} v^\mu v^\nu$ for any vector v^μ belonging to the tetrad. With the help of the asymptotic form of the perturbation tensor, Eq. (3.25) and Eq. (3.26), the tetrad components are easily evaluated. They are

$$h_{ll} \approx h^{ORG}_{tt} + 2h^{ORG}_{tr} + h^{ORG}_{rr} \sim \mathcal{O}(r^{-2}),$$

$$
\begin{aligned}
h_{lm} &\approx \frac{\sqrt{2}}{2r}\left[h^{ORG}_{t\theta} + h^{ORG}_{r\theta} + \frac{i}{\sin\theta}(h^{ORG}_{t\phi} + h^{ORG}_{r\phi})\right] \sim \mathcal{O}(r^{-2}), \\
h_{\bar{m}\bar{m}} &= \frac{1}{r^2} h^{ORG}_{AB}\ \bar{m}^A \bar{m}^B, \\
h_{mm} &= \frac{1}{r^2} h^{ORG}_{AB}\ m^A m^B,
\end{aligned} \tag{3.47}
$$

where the vector m^A was introduced previously, and h^{ORG}_{AB} is given by Eq. (3.27).

The covariant derivative of $h^{ORG}_{\mu\nu}$ is of the form

$$
h^{ORG}_{\alpha\beta;\mu} = \eta_{\alpha\beta\mu} + \rho_{\alpha\beta\mu}, \tag{3.48}
$$

where

$$
\begin{aligned}
\eta_{\alpha\beta\mu} &= h_{ll,\mu} n_\alpha n_\beta + 2h_{lm,\mu} n_{(\alpha}\bar{m}_{\beta)} + 2h_{l\bar{m},\mu} n_{(\alpha} m_{\beta)} \\
&+ h_{mm,\mu}\bar{m}_\alpha \bar{m}_\beta + h_{\bar{m}\bar{m},\mu} m_\alpha m_\beta, \\
\rho_{\alpha\beta\mu} &= h_{ll}[n_\alpha n_\beta]_{;\mu} + 2h_{lm}[n_{(\alpha}\bar{m}_{\beta)}]_{;\mu} + 2h_{l\bar{m}}[n_{(\alpha} m_{\beta)}]_{;\mu} \\
&+ h_{mm}[\bar{m}_\alpha \bar{m}_\beta]_{;\mu} + h_{\bar{m}\bar{m}}[m_\alpha m_\beta]_{;\mu}.
\end{aligned} \tag{3.49}
$$

From Eq. (3.38), the stress-energy tensor then becomes

$$
T^{GW}_{\mu\nu} = \frac{1}{64\pi}\left[\eta^{\alpha\beta}{}_{\mu}\eta^*_{\alpha\beta\nu} + \eta^{\alpha\beta}{}_{\mu}\rho^*_{\alpha\beta\nu} + \rho^{\alpha\beta}{}_{\mu}\eta^*_{\alpha\beta\nu} + \rho^{\alpha\beta}{}_{\mu}\rho^*_{\alpha\beta\nu}\right] + c.c.\ , \tag{3.50}
$$

where an asterisk stands for complex conjugation. This seems like a rather complicated expression, but its evaluation is easy.

The term involving the square of $\eta_{\alpha\beta\mu}$ can be simplified, without approximation, by using the orthogonality of the tetrad vectors. From Eq. (3.20), we have

$$
\eta^{\alpha\beta}{}_{\mu}\eta^*_{\alpha\beta\nu} = h_{mm,\mu} h^*_{\bar{m}\bar{m},\nu} + h_{\bar{m}\bar{m},\mu} h^*_{mm,\nu}. \tag{3.51}
$$

The remaining terms in the stress-energy tensor involve covariant derivatives of the tetrad vectors: terms of the form $\eta\rho$ are proportional to a tetrad vector contracted with the covariant derivative of a second derivative; terms of the form $\rho\rho$ are

proportional to the contraction of the covariant derivatives of two tetrad vectors. A short calculation reveals that

$$\begin{aligned} m^{\alpha} n_{\alpha;\phi} &= -\frac{\sqrt{2}}{4} \imath f \sin\theta, \qquad (3.52) \\ \bar{m}^{\alpha} m_{\alpha;\phi} &= -\imath \cos\theta, \\ m^{\alpha}_{\ ;\phi} n_{\alpha;r} &= \frac{\sqrt{2}M}{4r^2} \imath \sin\theta, \qquad (3.53) \end{aligned}$$

and their complex conjugates are the only non-vanishing components of interest: for the t, r and ϕ components of interest, every other contraction of covariant derivatives of tetrad vectors vanish identically. (Note that $n^{\alpha} m_{\alpha;\phi} = -m^{\alpha} n_{\alpha;\phi}$ and $m^{\alpha} \bar{m}_{\alpha;\mu} = -\bar{m}^{\alpha} m_{\alpha;\mu}$.) Keeping only terms proportional to these combinations, we find that

$$\eta^{\alpha\beta}{}_{\mu} \rho^{*}_{\alpha\beta\nu} = \begin{cases} 2(h_{mm,r} h^{*}_{l\bar{m}} \bar{m}^{\alpha} n_{\alpha;\phi} + h_{\bar{m}\bar{m},r} h^{*}_{lm} m^{\alpha} n_{\alpha;\phi} \\ +h_{mm,r} h^{*}_{\bar{m}\bar{m}} \bar{m}^{\alpha} m_{\alpha;\phi} + h_{\bar{m}\bar{m},r} h^{*}_{mm} m^{\alpha} \bar{m}_{\alpha;\phi}), & \text{for } \mu = r \text{ and } \nu = \phi, \\ 0, & \text{for } \mu = t \text{ and } \nu = r, \end{cases}$$

$$\rho^{\alpha\beta}{}_{\mu} \rho^{*}_{\alpha\beta\nu} = \begin{cases} 2h_{lm} h^{*}_{\bar{m}\bar{m}} n^{\alpha}_{\ ;r} m_{\alpha;\phi} + 2h_{l\bar{m}} h^{*}_{mm} n^{\alpha}_{\ ;r} \bar{m}_{\alpha;\phi}, & \text{for } \mu = r \text{ and } \nu = \phi, \\ 0, & \text{for } \mu = t \text{ and } \nu = r, \end{cases} \qquad (3.54)$$

while $\rho^{\alpha\beta}{}_{\mu} \eta^{*}_{\alpha\beta\nu}$ and $\rho^{\alpha\beta}{}_{\nu} \rho^{*}_{\alpha\beta\mu}$ are easily obtained by substituting h^{*}_{AB} in place of h_{AB}.

Taking a derivative of a tetrad component cannot reduce its order in r^{-1}. Close inspection of Eq. (3.54), with the aid of Eq. (3.52), then reveals that the $r\phi$ component of $\rho^{\alpha\beta}{}_{\mu} \rho^{*}_{\alpha\beta\nu}$ is $\mathcal{O}(r^{-5})$, while the $r\phi$ component of $\eta^{\alpha\beta}{}_{\mu} \rho^{*}_{\alpha\beta\nu}$ contains terms that are $\mathcal{O}(r^{-2})$ and cannot be neglected. Collecting the results and inserting them in Eq. (3.50), we get

$$\begin{aligned} T^{GW}_{tr} &= \frac{1}{64\pi} (h_{mm,t} h^{*}_{\bar{m}\bar{m},r} + h_{\bar{m}\bar{m},t} h^{*}_{mm,r}) + c.c. \\ &= -\frac{1}{32\pi} (\dot{h}_{mm} \dot{h}^{*}_{\bar{m}\bar{m}} + \dot{h}_{\bar{m}\bar{m}} \dot{h}^{*}_{mm}) \qquad (3.55) \end{aligned}$$

$$
\begin{aligned}
T^{GW}_{r\phi} &= \frac{1}{64\pi}(h_{mm,r}h^*_{\bar{m}\bar{m},\phi} + h_{\bar{m}\bar{m},r}h^*_{mm,\phi}) \\
&- \frac{\imath}{64\pi}(h_{mm,r}h^*_{\bar{m}\bar{m}} + h_{\bar{m}\bar{m},r}h^*_{mm})\cos\theta + c.c. \\
&= -\frac{1}{64\pi}(\dot{h}_{mm}h^*_{\bar{m}\bar{m},\phi} + \dot{h}_{\bar{m}\bar{m}}h^*_{mm,\phi}) \\
&+ \frac{\imath}{64\pi}(\dot{h}_{mm}h^*_{\bar{m}\bar{m}} + \dot{h}_{\bar{m}\bar{m}}h^*_{mm})\cos\theta + c.c. \qquad (3.56)
\end{aligned}
$$

These expressions for the stress-energy tensor can now be used to calculate the fluxes in the radiation zone. Setting $\epsilon = 1$ and $f \approx 1$, and inserting Eq. (3.55) into the first of Eq. (3.45) yields, for the energy flux,

$$
\begin{aligned}
\frac{dE}{dt} &= \frac{r^2}{32\pi}\int d\Omega\ (\dot{h}_{mm}\dot{h}^*_{\bar{m}\bar{m}} + \dot{h}_{\bar{m}\bar{m}}\dot{h}^*_{mm}) \ = \ \frac{1}{32\pi}\int d\Omega\ \dot{h}_{AB}\dot{h}^{*AB} \\
&= \frac{1}{32\pi}\sum_{lm}\sum_{l'm'}\int d\Omega\ \left[|\dot{\psi}_{\rm ZM}|^2\ V^{lm}_{AB}V^{*AB}_{l'm'} + 4|\psi_{\rm RW}|^2 W^{lm}_{AB}W^{*AB}_{l'm'}\right] \\
&= \frac{1}{64\pi}\sum_{lm}\frac{(l+2)!}{(l-2)!}\left[|\dot{\psi}_{\rm ZM}|^2 + 4|\psi_{\rm RW}|^2\right], \qquad (3.57)
\end{aligned}
$$

where in the first line we used $\Omega^{AC}\Omega^{BD}h_{AB}h^*_{CD} = r^2(h_{mm}h^*_{\bar{m}\bar{m}} + h_{\bar{m}\bar{m}}h^*_{mm})$, which follows from the completeness relation for Ω_{AB}; the second line follows from Eq. (3.27), and the third line follows from evaluating the remaining angular integral with the aid of Eq. (A.9).

The angular momentum flux calculation follows similar steps as the calculation of the energy flux. Inserting Eq. (3.56) into the second of Eq. (3.45), we get

$$
\begin{aligned}
\frac{dL}{dt} &= -\frac{r^2}{64\pi}\int d\Omega\ \Big[(\dot{h}_{mm}h^*_{\bar{m}\bar{m},\phi} + \dot{h}_{\bar{m}\bar{m}}h^*_{mm,\phi}) \\
&\qquad -\imath(\dot{h}_{mm}h^*_{\bar{m}\bar{m}} + \dot{h}_{\bar{m}\bar{m}}h^*_{mm})\cos\theta\Big] + c.c. \qquad (3.58)
\end{aligned}
$$

Since $h_{mm} \propto {}_2Y^{lm}$, the term contained in the second line is proportional to $|\,{}_2Y^{lm}|^2\cos\theta$. This term is odd in θ with respect to $\pi/2$ and yields zero contribution to the angular momentum flux upon integration between $0 \le \theta \le \pi$. The remaining component is

simplified by noting that $h_{mm,\phi} = imh_{mm}$. The angular momentum flux is then

$$\begin{aligned}
\frac{dL}{dt} &= -\frac{r^2}{64\pi}\int d\Omega\ (\dot{h}_{mm}h^*_{\bar{m}\bar{m},\phi} + \dot{h}_{\bar{m}\bar{m}}h^*_{mm,\phi} + c.c.) \\
&= \frac{imr^2}{64\pi}\int d\Omega\ (\dot{h}_{mm}h^*_{\bar{m}\bar{m}} + \dot{h}_{\bar{m}\bar{m}}h^*_{mm}) + c.c.) \\
&= \frac{im}{64\pi}\int d\Omega\ (\dot{h}^{AB}h^*_{AB} + c.c.) \\
&= \frac{im}{64\pi}\sum_{lm}\sum_{l'm'}\int d\Omega\ \Big[\dot{\psi}_{\rm ZM}\psi^*_{\rm ZM}\ V^{lm}_{AB}V^{*AB}_{l'm'} \\
&\qquad\qquad +4\psi_{\rm RW}\int_{-\infty}^{t} dt'\psi^*_{\rm RW}(t')W^{AB}_{lm}W^{*AB}_{l'm'}\Big] + c.c. \\
&= \frac{im}{128\pi}\sum_{lm}\frac{(l+2)!}{(l-2)!}\Big[\dot{\psi}_{\rm ZM}\ \psi^*_{\rm ZM} + 4\psi_{\rm RW}\ \int_{-\infty}^{t} dt'\psi^*_{\rm RW}(t')\Big] + c.c.\ , \quad (3.59)
\end{aligned}$$

where, again, we used $\Omega^{AC}\Omega^{BD}h_{AB}h^*_{CD} = r^2(h_{mm}h^*_{\bar{m}\bar{m}} + c.c.)$ to go from the second to the third line, the fourth line follows from Eq. (3.45), and the last equality is obtained by evaluating the angular integral with the help of Eq. (A.9).

Black hole absorption

The calculation of the black hole absorption is similar to the calculation of the far-zone fluxes. The expansion parameter in this case is f, and from Eq. (3.45), we see that the tr and $r\phi$ components of $T^{GW}_{\mu\nu}$ need to be calculated to $\mathcal{O}(f^{-1})$, i.e. we need to isolate the divergent part of $T^{GW}_{\mu\nu}$ at the event horizon. We therefore neglect terms of order $\mathcal{O}(1)$.

The material developed in the previous sections can be used here simply by replacing $l^\mu \leftrightarrow n^\mu$. In an ingoing radiation gauge, the non-trivial tetrad components of the perturbation tensor are

$$\begin{aligned}
h_{nn} &= \frac{1}{4}(h^{IRG}_{tt} - 2fh^{IRG}_{tr} + f^2h^{IRG}_{rr}) \sim \mathcal{O}(f), \\
h_{nm} &\approx \frac{\sqrt{2}}{8M}\Big[h^{IRG}_{t\theta} - fh^{IRG}_{r\theta} + \frac{i}{\sin\theta}(h^{IRG}_{t\phi} - fh^{IRG}_{r\phi})\Big] \sim \mathcal{O}(f),
\end{aligned}$$

$$
\begin{aligned}
h_{\bar{m}\bar{m}} &= \frac{1}{4M^2} h^{IRG}_{AB}\ \bar{m}^A \bar{m}^B, \\
h_{mm} &= \frac{1}{4M^2} h^{IRG}_{AB}\ m^A m^B.
\end{aligned} \tag{3.60}
$$

With the replacement $n^\nu \leftrightarrow l^\nu$, the steps we follow are almost exactly the same as for the far-zone calculations. The stress-energy tensor is written as in Eq. (3.50), with $\eta_{\alpha\beta\mu}$ and $\rho_{\alpha\beta\nu}$ changed to reflect the exchange of tetrad vectors. It is not difficult to show that the non-vanishing components of the contracted derivatives of the tetrad vectors are now

$$
\begin{aligned}
m^\alpha l_{\alpha;\phi} &= \frac{\sqrt{2}}{2} \imath \sin\theta, \\
\bar{m}^\alpha m_{\alpha;\phi} &= -\imath \cos\theta, \\
m^\alpha{}_{;\phi} l_{\alpha;r} &= \frac{\sqrt{2}M}{2r^2} \imath f^{-1} \sin\theta,
\end{aligned} \tag{3.61}
$$

and keeping only terms proportional to these contracted derivatives in $\eta_{\alpha\beta\mu}$ and $\rho_{\alpha\beta\nu}$, we get

$$
\eta^{\alpha\beta}{}_{\mu}\rho^{*}_{\alpha\beta\nu} = \begin{cases} 2(h_{mm,r} h^{*}_{n\bar{m}} \bar{m}^\alpha l_{\alpha;\phi} + h_{\bar{m}\bar{m},r} h^{*}_{nm} m^\alpha l_{\alpha;\phi} \\ \quad + h_{mm,r} h^{*}_{\bar{m}\bar{m}} \bar{m}^\alpha m_{\alpha;\phi} + h_{\bar{m}\bar{m},r} h^{*}_{mm} m^\alpha \bar{m}_{\alpha;\phi}), & \text{for } \mu = r \text{ and } \nu = \phi, \\ 0, & \text{for } \mu = t \text{ and } \nu = r, \end{cases}
$$

$$
\rho^{\alpha\beta}{}_{\mu}\rho^{*}_{\alpha\beta\nu} = \begin{cases} 2h_{nm} h^{*}_{\bar{m}\bar{m}} l^\alpha{}_{;r} m_{\alpha;\phi} + 2h_{n\bar{m}} h^{*}_{mm} l^\alpha{}_{;r} \bar{m}_{\alpha;\phi}, & \text{for } \mu = r \text{ and } \nu = \phi, \\ 0, & \text{for } \mu = t \text{ and } \nu = r, \end{cases} \tag{3.62}
$$

and $\rho^{\alpha\beta}{}_{\mu}\eta^{*}_{\alpha\beta\nu}$ and $\rho^{\alpha\beta}{}_{\nu}\rho^{*}_{\alpha\beta\mu}$ are easily obtained by substituting h^{*}_{AB} in place of h_{AB}.

In the vicinity of the event horizon, we use $\partial/\partial r \approx f^{-1}\partial/\partial t$, so that terms containing an r derivative of a tetrad component gain a power of f^{-1}. Inspection of the $r\phi$ component of $\rho^{\alpha\beta}{}_{\mu}\rho^{*}_{\alpha\beta\nu}$ reveals that it is $\mathcal{O}(1)$ and can be neglected, while the $r\phi$ component of $\eta^{\alpha\beta}{}_{\mu}\rho^{*}_{\alpha\beta\nu}$ contains terms that are $\mathcal{O}(f^{-1})$ and cannot be neglected.

Collecting the results, we find that the divergent part of T^{GW}_{tr} and $T^{GW}_{r\phi}$ is

$$\begin{aligned} T^{GW}_{tr} &= \frac{1}{64\pi}(h_{mm,t}h^*_{\bar{m}\bar{m},r} + h_{\bar{m}\bar{m},t}h^*_{mm,r}) + c.c. \\ &= \frac{f^{-1}}{32\pi}(\dot{h}_{mm}\dot{h}^*_{\bar{m}\bar{m}} + \dot{h}_{\bar{m}\bar{m}}\dot{h}^*_{mm}) \end{aligned} \tag{3.63}$$

$$\begin{aligned} T^{GW}_{r\phi} &= \frac{1}{64\pi}(h_{mm,r}h^*_{\bar{m}\bar{m},\phi} + h_{\bar{m}\bar{m},r}h^*_{mm,\phi}) \\ &- \frac{\imath}{64\pi}(h_{mm,r}h^*_{\bar{m}\bar{m}} + h_{\bar{m}\bar{m},r}h^*_{mm})\cos\theta + c.c. \\ &= \frac{f^{-1}}{64\pi}(\dot{h}_{mm}h^*_{\bar{m}\bar{m},\phi} + \dot{h}_{\bar{m}\bar{m}}h^*_{mm,\phi}) \\ &\quad -\frac{\imath f^{-1}}{64\pi}(\dot{h}_{mm}h^*_{\bar{m}\bar{m}} + \dot{h}_{\bar{m}\bar{m}}h^*_{mm})\cos\theta + c.c. \end{aligned} \tag{3.64}$$

Note that this is exactly of the same form (apart from a factor of f^{-1}) as that obtained for T^{GW}_{tr} and $T^{GW}_{r\phi}$ in the far zone.

To calculate the fluxes, we insert these expressions for the stress-energy tensor into Eq. (3.45), where we set $\epsilon = -1$. The divergence in the stress-energy tensor is canceled by the factor of f appearing in the expressions for the fluxes. The remaining calculations are identical with those of the far-zone, with h^{IRG}_{AB} given by Eq. (3.36). The energy flux is

$$\frac{dE}{dt} = \frac{1}{64\pi}\sum_{lm}\frac{(l+2)!}{(l-2)!}\left[|\dot{\psi}_{\rm ZM}|^2 + 4|\psi_{\rm RW}|^2\right], \tag{3.65}$$

while the angular momentum flux is

$$\frac{dL}{dt} = \frac{\imath m}{128\pi}\sum_{lm}\frac{(l+2)!}{(l-2)!}\left[\dot{\psi}_{\rm ZM}\ \psi^*_{\rm ZM} + 4\psi_{\rm RW}\int_{-\infty}^{t}dt'\psi^*_{\rm RW}(t')\right] + c.c.\ . \tag{3.66}$$

In summary, we have provided a description of the metric perturbation tensor, $h_{\mu\nu}$, in terms of its radiative components at infinity and near the event horizon. The radiative part of the stress-energy tensor can be written in terms of the Zerilli-Moncrief and Regge-Wheeler functions. We have also developed expressions for the fluxes of energy and angular momentum at infinity and at the event horizon, in terms

of these two functions. We have shown that when written in terms of the Zerilli-Moncrief and Regge-Wheeler functions, the expressions for the fluxes through the event horizon are identical with the expressions found in the far-zone. The only difference is in the location at which the scalar functions are evaluated.

Chapter 4

Initial-value problem in General Relativity: A study using perturbation theory

4.1 Introduction

Detection of black hole collisions and successful extraction of the black-hole parameters require a detailed theoretical understanding of the gravitational waves emitted during the collision. The lack of solutions to the dynamical two-body problem in four-dimensional general relativity renewed interest in simulating black-hole collisions by numerically integrating the full non-linear Einstein field equations [24, 25, 26, 27, 28, 29, 30, 31, 32, 33]. The challenge is enormous. Recent progresses in the field of numerical relativity are reviewed in [46].

From a numerical point of view, long-term simulations of black-hole collisions are limited by the available memory [29] and instabilities associated with the numerical

implementation of the full non-linear equations [25, 31, 34]. Because of these difficulties, numerical relativity is not yet at the stage where it can simulate black-hole collisions for a very long time [32]. Most simulations are started at a late stage of the collision, when the two black holes are separated by a distance of just a few black-hole masses. As a result of these small initial separations, the gravitational waves contained on the initial hypersurface cannot escape from the system before the two black holes become strongly interacting. This situation implies that non-trivial initial values must be provided for the gravitational field in order to start the numerical evolution. In this chapter, we will see that the initial gravitational-wave content plays an important role in the modeling of the gravitational waveforms.

The initial-value problem consists of finding an initial three-metric γ_{ij}, and an initial extrinsic curvature K_{ij}, that encode all of the physical information about the system. The solution should contain information about the state of motion of the black holes, and information about the gravitational-wave content of the initial three-surface. The initial gravitational-wave content is important because it contains information about the motion of the black holes prior to the beginning of the numerical evolution: in the past of the initial hypersurface, the two black holes emitted gravitational waves that must be accounted for in the initial data.

For the case of colliding black holes, various methods have been developed to find initial data that satisfy the Hamiltonian and momentum constraints of general relativity, e.g. the apparent-horizon method [47], conformal-imaging method [48], and puncture method [49]. The starting point of these methods is a maximally embedded initial spacelike slice ($K^i{}_i = 0$). On this slice, the geometry is described by a conformally-flat initial metric, $\gamma_{ij} = \Psi^4 \bar{\gamma}_{ij}$, and a rescaled traceless extrinsic curvature $K_{ij} = \Psi^{-2} \bar{K}_{ij}$, where $\bar{\gamma}_{ij}$ is the metric of three-dimensional flat space, Ψ

the conformal factor, and $\bar{K}_{ij}$ the traceless conformal extrinsic curvature. With these choices, the momentum constraints in vacuum can be recast in terms of quantities defined in the conformal space: $\bar{\nabla}^j \bar{K}_{ij} = 0$, where $\bar{\nabla}^i$ is the flat-space covariant derivative. Bowen and York obtained solutions to this equation in terms of a vector field $\bar{V}^i$ that contains information about the spins and linear momenta of the holes [50, 51]. The solution is expressed as $\bar{K}^{ij} = \bar{\nabla}^i \bar{V}^j + \bar{\nabla}^j \bar{V}^i - 2/3 \bar{\gamma}^{ij} \bar{\nabla}^k \bar{V}_k$, and explicit forms for $\bar{V}^i$ can be found in [52]. The three techniques mentioned above rely on the Bowen-York solutions to construct $\bar{K}_{ij}$, but because of the different choices of topology for the initial hypersurface, the $\bar{K}_{ij}$'s they obtain are different. Since these differences in initial topology are mostly hidden behind the event horizons of the black holes, they cannot significantly influence the resulting dynamics. To reflect this, we will generically refer to a K_{ij} based on the Bowen-York solutions as a "longitudinal extrinsic curvature".

Thus, solutions to the initial-value problem can be generated, but the real problem is to construct physically suitable solutions. This is a difficult problem because of the non-linearities inherent to the theory. It is very hard in practice to identify which components of γ_{ij} and K_{ij} are to be constrained, and which are to be associated with dynamical and gauge degrees of freedom. It is now widely accepted that choosing a conformally-flat γ_{ij} and a longitudinal K_{ij} are unlikely to yield physically relevant initial data sets.

For example, the metric of a binary system is known not to be conformally-flat at the second post-Newtonian order, making the conformally-flat decomposition inadequate [52]. As well, any astrophysical black hole is likely to be rotating and, in this case, the assumption of conformal flatness yields poor initial data. The reason for this is well known: Garat and Price [53] have shown that there is no spatial slicing

of the Kerr solution that is both axisymmetric and conformally flat, and reduces smoothly to the Schwarzschild solution in the no-rotation limit. Nevertheless, the techniques mentioned above can provide solutions to the initial-value problem that represent a rotating black hole, but they cannot correspond to a stationary Kerr black hole; there must be some gravitational radiation on the initial slice.

Even in the case of a perturbed Schwarzschild black hole, where conformally-flat slices can be constructed, the solutions obtained with a longitudinal extrinsic curvature are not necessarily adequate. C.O. Lousto and R.H. Price [54] have shown that for the head-on collision of two nonrotating black holes in which one of the holes is much less massive than the other, conformally-flat γ_{ij} and longitudinal K_{ij} data (CFL data) do not reproduce the numerical results [54]. In their analysis, they imposed the CFL data at a time t_o and evolved it forward in time. They then looked at the conditions at a later time t_1, and found that the extrinsic curvature extracted from the numerical data agreed poorly with the extrinsic curvature obtained at $t = t_1$ from CFL data. Instead, they found that the extrinsic curvature was better represented by postulating a convective time derivative [55], which essentially means that the time derivative of the metric is proportional to the four-velocity of the small black hole.

The various problematic issues associated with the initial-value problem can be better understood by having recourse to approximate methods [56, 57]. For large initial separations and slow-motion processes, post-Newtonian theory is useful, especially when the post-Newtonian metric of two point masses is matched, in a buffer region, with the metric of two distorted Schwarzschild black holes [58]. For small mass ratios, black-hole perturbation theory can be very useful [59, 60, 61, 62], since in this case there is no restriction on the velocity of the small body.

In this chapter, we use the formalism of perturbation theory, developed in Chapter 2 and specialized to Schwarzschild coordinates in Chapter 3, to study the initial-value problem for binary systems consisting of a small compact object of mass μ orbiting a Schwarzschild black hole of much larger mass M. With these assumptions, the perturbing stress-energy tensor can be taken to be that of a point particle and is then given by Eq. (2.13). With this specific stress-energy tensor, the integrals appearing in the source terms of Eq. (2.31) to Eq. (2.37) can be evaluated explicitly by integrating over the four-dimensional δ-function. Working in Schwarzschild coordinates we obtain

$$\begin{aligned}
Q^{ab} &= \frac{8\pi}{r^2}\,\mu\,\frac{u^a u^b}{u^t} Y^{lm*}(t)\;\delta(r-r_p(t)),\\
Q^{a} &= \frac{16\pi}{l(l+1)}\,\mu\,\frac{u^a u^A}{u^t} Z^{lm*}_A(t)\;\delta(r-r_p(t)),\\
Q^{\flat} &= 8\pi\,\mu\,\frac{u^A u^B}{u^t} U^{lm*}_{AB}(t)\;\delta(r-r_p(t)),\\
Q^{\sharp} &= 32\pi\frac{(l-2)!}{(l+2)!}\,\mu\,r^2\frac{u^A u^B}{u^t} V^{lm*}_{AB}(t)\;\delta(r-r_p(t)),\\
P^{a} &= \frac{16\pi}{l(l+1)}\,\mu\,\frac{u^a u^A}{u^t} X^{lm*}_A(t)\;\delta(r-r_p(t)),\\
P &= 16\pi\frac{(l-2)!}{(l+2)!}\,\mu\,r^2\frac{u^A u^B}{u^t} W^{lm*}_{AB}(t)\;\delta(r-r_p(t)),
\end{aligned} \tag{4.1}$$

where $Y^{lm*}(t) \equiv Y^{lm*}(\theta_p(t),\phi_p(t))$ (equivalent definitions holding for the other spherical harmonics), $\theta_p(t)$, $\phi_p(t)$ and $r_p(t)$ are the time dependent coordinates of the point particle, u^α is the four-velocity of the particle with $u^t = \tilde{E}/f$, and $\tilde{E}$ is the conserved energy of the point particle divided by μ. On the initial hypersurface, we set $t = 0$ and define $r_p(0) \equiv r_o$ to be the initial position of the point particle.

Only four of the equations associated with the source terms above are constraint equations. Of these four equations, three are constraint equations for even parity modes, and the remaining equation constrains odd parity modes. In Sec. 4.2.1 and

Sec. 4.2.2, we will see that the constraint equations are given by the P^t equation for odd parity modes, and by the Q^{tt}, Q^{tr} and Q^t for even parity modes.

This chapter is organized as follow. In Sec. 4.2.1 and Sec. 4.2.2, we construct solutions to the constraint equations of both parities by postulating relations between certain components of the metric perturbations. These relations are not preserved by evolution, but are sufficient to provide an adequate initial-value formulation of the perturbed constraint equations. In Sec. 4.3, we specialize our initial-value formulation to the case of a radial infall of the point particle into the central black hole. In Sec. 4.3.2 and Sec. 4.3.3, we discuss the effects of the choice of initial data on the gravitational waveforms and on their frequency content. In Sec. 4.3.4, we discuss the influence of the initial data on the energy radiated to infinity. In Sec. 4.3.5, we summarize our findings in the case of radial infall of the point particle.

4.2 Initial-value problem in perturbation theory

4.2.1 Solutions to the odd parity constraint equation

There is a single odd parity constraint equation, which in Schwarzschild coordinates is given by Eq. (3.8). This equation involves $\tilde{h}_0$ and $\dot{\tilde{h}}_1$ only, but a second relation, involving $\dot{\tilde{h}}_0$ and $\tilde{h}_1$, can be obtained from one of the two evolution equations, namely Eq. (3.10) for P.

The difficulty associated with choosing physical initial data for odd parity perturbations then resides in the fact that both gauge invariant functions must satisfy the constraint equation, but there is still freedom left in specifying the gravitational-wave content of the initial hypersurface. We solve Eq. (3.10) and Eq. (3.8) for $\tilde{h}_1$ and $\dot{\tilde{h}}_1$

in terms of $\tilde{h}_0$ and $\dot{\tilde{h}}_0$. The solutions to the P and P^t equations are then

$$\begin{aligned}
\tilde{h}_1 &= \frac{1}{f}\int_{2M}^{r} dr' \left[\frac{\dot{\tilde{h}}_0}{f} - P(r')\right], \\
\dot{\tilde{h}}_1 &= \frac{1}{r^2}\int_{2M}^{r} dr'\, r'^2 \left[\frac{\partial^2}{\partial r'^2}\tilde{h}_0 - \frac{1}{r^2 f}\left(l(l+1) - \frac{4M}{r}\right)\tilde{h}_0 - P^t(r')\right].
\end{aligned} \tag{4.2}$$

Once a choice is made for $\tilde{h}_0$ and its time derivative, the initial gravitational-wave content is fixed and $\tilde{h}_1$ and its time derivative can be obtained from Eq. (4.2). For example, they are easily constructed with $\tilde{h}_0 = 0$ and $\dot{\tilde{h}}_0 = 0$ in Eq. (4.2). In Sec. 4.3 we will study in detail the effects of the choice of initial data on the gravitational waveforms for the case of radial infall. In this situation, odd modes are not excited by the particle, and we shall not need to develop the solutions to the odd parity constraint equation any further.

4.2.2 Solutions for even parity constraint equations

The even parity perturbations modes must satisfy three constraint equations: they are given by Eq. (3.1), Eq. (3.2), and Eq. (3.4). The Q^{tt} equation does not involve any time derivative of the metric perturbations; it is the perturbed Hamiltonian constraint. The remaining constraint equations involve at most a single time derivative; they are the momentum constraints.

We have seen in Sec. 3.3.3 that the Zerilli-Moncrief function contains all the (even parity) information about gravitational waves at infinity and in the vicinity of the event horizon. In particular, this function can be used to determine the rate at which gravitational waves carry energy and angular momentum to infinity and through the event horizon. It was shown in Sec. 3.2 that in Schwarzschild coordinates the Zerilli-Moncrief function can be constructed from $\tilde{H}_2$ and $\tilde{K}$ only. For these reasons, we now concentrate on constructing initial data for $\tilde{H}_2$ and $\tilde{K}$, and their time derivatives. (It

is clear from Eq. (3.2) for Q^{tr} that $\tilde{H}_1(0,r)$ is completely determined once $\dot{\tilde{K}}(0,r)$ and $\dot{\tilde{H}}_2(0,r)$ are known.)

Eq. (3.1) for Q^{tt} involves only $\tilde{K}$ and $\tilde{H}_2$. Defining $J \equiv -(\partial/\partial r)(r^2 f Q^{tr}) + l(l+1) f Q^t/2$, we obtain a second equation involving only $\dot{\tilde{K}}$ and $\dot{\tilde{H}}_2$:

$$\begin{aligned} J &= r^2 f\Big[-\frac{\partial^2}{\partial r^2}\dot{\tilde{K}} - \frac{3r-5M}{r^2 f}\frac{\partial}{\partial r}\dot{\tilde{K}} + \frac{1}{r}\frac{\partial}{\partial r}\dot{\tilde{H}}_2 \\ &+ \frac{l(l+1)}{2r^2 f}\left(\dot{\tilde{H}}_2 + \dot{\tilde{K}}\right) + \frac{1}{r^2 f}\left(\dot{\tilde{H}}_2 - \dot{\tilde{K}}\right)\Big]. \end{aligned} \tag{4.3}$$

The structure of this equation is the same as that of Eq. (3.1) with $\tilde{K}$ and $\tilde{H}_2$ replaced by their time derivatives. However, it cannot be obtained by taking a simple time derivative of the first of Eq. (3.1), as can easily be seen from the Bianchi identities developed in Chap. 2, Eq. (2.41).

From Eq. (4.1) above, we see that on the initial hypersurface every source term is proportional to $\delta(r-r_o)$. Solutions to the constraint equations are then constructed from homogeneous solutions to Eq. (3.1) and Eq. (4.3) matched at r_o, where the source term is singular. For later purposes, the singular source terms are written as

$$\begin{aligned} r^2 f\ Q^{tt}(r, t=0) &= \rho(r_o)\delta(r-r_o), \\ J(r, t=0) &= j(r_o)\delta(r-r_o) + j'(r_o)\delta'(r-r_o), \end{aligned} \tag{4.4}$$

where $\delta'(r-r_o) = (d/dr)\delta(r-r_o)$ and

$$\begin{aligned} \rho(r_o) &= 8\pi\mu\tilde{E}Y^{lm*}(0), \\ j(r_o) &= 8\pi\mu f_o\Big[-\frac{2u^r}{r_o f_o}\left(1-\frac{M}{r_o}\right)Y^{lm*}(0) + u^A Z_A^{lm*}(0)\Big], \\ j'(r_o) &= 8\pi\mu f_o u^r Y^{lm*}(0), \end{aligned} \tag{4.5}$$

where $f_o = 1 - 2M/r_o$ and the harmonic functions are evaluated at $\theta_p(0)$ and $\phi_p(0)$. The source term for J easily follows from Eq. (4.3). We note that J is proportional

to the four-velocity of the particle, but this is not quite equivalent to the convective initial data used in [55]. This would require Eq. (4.3) to follow from Eq. (3.1) by simple time differentiation.

As was the case for odd modes, there is freedom in choosing appropriate initial conditions for the even modes, i.e. the initial gravitational-wave content of the initial hypersurface can be freely specified. In principle, we could let H_2 and $\dot{\tilde{H}}_2$ be freely specifiable functions and obtain $\tilde{K}$ and its time derivative from Eq. (3.1) and Eq. (4.3). Instead, we postulate a relationship between $\tilde{K}$ and $\tilde{H}_2$ and between their time derivatives:

$$\begin{aligned} \tilde{H}_2 &= \alpha \tilde{K}, \\ \dot{\tilde{H}}_2 &= \dot{\alpha} \dot{\tilde{K}}, \end{aligned} \tag{4.6}$$

where α and $\dot{\alpha}$ are constants. The notation $\dot{\alpha}$ is not meant to represent the time derivative of α. Instead it is used to remind us that $\dot{\alpha}$ defines the relationship between $\dot{\tilde{H}}_2$ and $\dot{\tilde{K}}$.

The motivation for postulating these relations is based on two much-studied conformally-flat solutions to the initial-value problem: the Misner solution [63, 64] (which is generalized by the conformal-imaging method to situations where the initial hypersurface is not a moment of time-symmetry) and the Brill-Lindquist solution [65, 66] (which is generalized by the puncture method). They represent the spatial metric of two black holes momentarily at rest, and about to undergo a head-on collision. Because the initial hypersurface is a moment of time symmetry, $K_{ij} = 0$ and the initial-value problem reduces to finding γ_{ij} (or the conformal factor). These solutions and their generalizations were used as initial data for the study of the head-on collision of two equal-mass black holes in full numerical relativity [26, 27, 30, 61].

Demanding that the initial three-metric be conformally flat is equivalent to the requirement that, in the Regge-Wheeler gauge, $H_2 = K$, and $H_1 = 0$. In this gauge and with these relations, the line-element is

$$\begin{aligned} \mathrm{d}s^2|_{t=0} &= \left(1 + K_{lm}(r)Y_{lm}(\theta,\phi)\right)\left(f^{-1}\mathrm{d}r^2 + r^2\mathrm{d}\Omega^2\right) \\ &= \left(1 + K_{lm}(r)Y_{lm}(\theta,\phi)\right)\left(1 + \frac{M}{2\bar{r}}\right)^4\left(\mathrm{d}\bar{r}^2 + \bar{r}^2\mathrm{d}\Omega^2\right), \end{aligned} \tag{4.7}$$

where $\bar{r} = r(1+\sqrt{f})^2/4$ is the isotropic radius. On the other hand, at a moment of time symmetry $\dot{H}_2 = \dot{K} = 0$ and $\dot{H}_1 = 0$.

The ansatz of Eq. (4.6) generalizes the time-symmetric and conformally-flat solutions in three ways. First, we promote the relation $\tilde{H}_2 = \tilde{K}$ to a gauge invariant statement[1]. Secondly, we generalize the conformally-flat statement to $\tilde{H}_2 = \alpha\tilde{K}$. Finally, we postulate $\dot{\tilde{H}}_2 = \dot{\alpha}\dot{\tilde{K}}$, which is trivially satisfied at a moment of time-symmetry.

Making the choice $\tilde{H}_2 = \tilde{K}$ turns Eq. (3.1) into a hypergeometric equation for $\tilde{K}$. The more general relation $\tilde{H}_2 = \alpha\tilde{K}$ also turns this equation into a hypergeometric equation, for which we are able to find solutions that generalize the conformally-flat solutions. As well, postulating the second of Eq. (4.6) turns Eq. (4.3) into another hypergeometric equation and we can also generate solutions. Our solutions are parameterized by α and $\dot{\alpha}$, and the procedure outlined above produces a two-parameter family of initial-data sets.

Because both Eq. (3.1) and Eq. (4.3) are of the same form, we develop the solution for $\dot{\tilde{K}}$. Solutions for $\tilde{K}$ can be obtained from the solution for $\dot{\tilde{K}}$ by substituting $\rho(r_o)$ for $j(r_o)$, α for $\dot{\alpha}$, as well as $j'(r_o) = 0$. Postulating the ansatz of Eq. (4.6) at the

[1]Because $\tilde{H}_2$ and $\tilde{K}$ are used to construct the gauge-invariant Zerilli-Moncrief function, the difference between the two statements is inconsequential for the purpose of extracting information about gravitational waves in the far-zone. It does however affect Eq. (4.7) which holds only in the Regge-Wheeler gauge. By extension, we will refer to initial-data obtained with $\tilde{H}_2 = \tilde{K}$ as conformally-flat.

initial moment $t = 0$, Eq. (4.3) becomes ($z \equiv r/2M$)

$$z(1-z)\frac{\mathrm{d}^2}{\mathrm{d}z^2}\dot{\tilde{K}} + \left(\frac{5}{2} - \dot{\alpha} - (3-\dot{\alpha})z\right)\frac{\mathrm{d}}{\mathrm{d}z}\dot{\tilde{K}} - \left((1-\dot{\alpha}) - \frac{l(l+1)}{2}(1+\dot{\alpha})\right)\dot{\tilde{K}} = J. \quad (4.8)$$

On either side of the particle's initial position, $r \neq r_o$ and $J = 0$, and this is the homogeneous hypergeometric equation. For $r < r_o$ we must choose a solution that is regular at $r = 2M$, but that is allowed to diverge at $r \to \infty$. We denote this solution by $\dot{\tilde{K}}_<(r)$. For $r > r_o$ we must choose a solution that is regular at $r \to \infty$, but that may diverge at $r = 2M$. This solution is denoted by $\dot{\tilde{K}}_>(r)$. In terms of these, the solution for $\dot{\tilde{K}}(r,0)$ takes the form[2]

$$\dot{\tilde{K}}(r,0) = C_<(r_o)\dot{\tilde{K}}_<(r)\Theta(r_o - r) + C_>(r_o)\dot{\tilde{K}}_>(r)\Theta(r - r_o), \quad (4.9)$$

where

$$\begin{aligned}
\dot{\tilde{K}}_<(r) &= \left(\frac{r}{2M}\right)^{-b} F\left(b, b-c+1; 1-a+b; \frac{2M}{r}\right), \\
\dot{\tilde{K}}_>(r) &= \left(\frac{r}{2M}\right)^{-a} F\left(a, a-c+1; 1-b+a; \frac{2M}{r}\right),
\end{aligned} \quad (4.10)$$

$F(,;,)$ is the hypergeometric function,

$$\begin{aligned}
a &= 1 - \frac{\dot{\alpha}}{2} + \frac{1}{2}\left[\dot{\alpha}^2 + 2(1+\dot{\alpha})l(l+1)\right]^{1/2}, \\
b &= 1 - \frac{\dot{\alpha}}{2} - \frac{1}{2}\left[\dot{\alpha}^2 + 2(1+\dot{\alpha})l(l+1)\right]^{1/2}, \\
c &= \frac{5}{2} - \dot{\alpha},
\end{aligned} \quad (4.11)$$

and $C_<(r_o)$ and $C_>(r_o)$ are constants ensuring that $\dot{\tilde{K}}$ and $(\partial/\partial r)\dot{\tilde{K}}$ have the correct discontinuity at $r = r_o$.

Evaluating the first and second r-derivative of Eq. (4.9) and inserting the result into Eq. (4.8), it is easy to show that the two constants $C_<(r_o)$ and $C_>(r_o)$ are given

[2]In principle, we are free to add any multiple of $\tilde{K}_>(r)$ and $\dot{\tilde{K}}_>(r)$ to our particular solutions. This represents a different choice of initial three-geometry [54] and embedding (if the solutions are regular at $r = 2M$), and we do not consider this possibility here.

by

$$
\begin{aligned}
C_<(r_o) &= r_o\left(\frac{r_o}{2M}\right)^{2-\dot{\alpha}}\Gamma(r_o)\left(q\dot{\tilde{K}}_>(r_o)+q'\frac{\partial}{\partial r}\dot{\tilde{K}}_>\right), \\
C_>(r_o) &= r_o\left(\frac{r_o}{2M}\right)^{2-\dot{\alpha}}\Gamma(r_o)\left(q\dot{\tilde{K}}_<(r_o)+q'\frac{\partial}{\partial r}\dot{\tilde{K}}_<\right),
\end{aligned}
\tag{4.12}
$$

where we have defined

$$
\begin{aligned}
q &= \frac{1}{2r_o(r_o-2M)}\left[j(r_o)+(2Mc-(a+b+1)r_o)\frac{j'(r_o)}{r_o(r_o-2M)}\right], \\
q' &= \frac{j'(r_o)}{r_o(r_o-2M)},
\end{aligned}
\tag{4.13}
$$

and also

$$
\begin{aligned}
\Gamma(r_o) &= r_o^{-1}\left(\frac{2M}{r_o}\right)^{2-\dot{\alpha}}\left[\dot{\tilde{K}}_>\frac{\partial}{\partial r}\dot{\tilde{K}}_< - \dot{\tilde{K}}_<\frac{\partial}{\partial r}\dot{\tilde{K}}_>\right]^{-1}\Bigg|_{r=r_o} \\
&= \left[aF\left(a+1,a-c+1;1-b+a;\frac{2M}{r_o}\right)F\left(b,b-c+1;1-a+b;\frac{2M}{r_o}\right)\right. \\
&- \left. bF\left(a,a-c+1;1-b+a;\frac{2M}{r_o}\right)F\left(b+1,b-c+1;1-a+b;\frac{2M}{r_o}\right)\right]^{-1}.
\end{aligned}
\tag{4.14}
$$

The second equality in Eq. (4.14) follows from Eq. (15.2.3) of [67] together with Eq. (4.10) to evaluate $(\partial/\partial r)\dot{\tilde{K}}_<(r_o)$ and $(\partial/\partial r)\dot{\tilde{K}}_>(r_o)$. We re-emphasize that the solution for $\tilde{K}$ can then be obtained by substituting $\rho(r_o)$ and α in place of $j(r_o)$ and $\dot{\alpha}$ and setting $j'(r_o)=0$ in Eq. (4.13).

In order for the perturbed metric to be real (as opposed to complex), the solutions to Eq. (4.8) must be real functions. Thus, $\dot{\alpha}$ must be such that the parameters a and b, as listed in Eqs. (4.11), are real. It is easy to verify that the quantity appearing under the square root will be positive if $\dot{\alpha}\geq\dot{\alpha}_+$, or $\dot{\alpha}\leq\dot{\alpha}_-$, where

$$
\dot{\alpha}_\pm = -l(l+1)\pm\sqrt{(l+2)(l+1)l(l-1)}. \tag{4.15}
$$

It can be verified that $\dot{\alpha}_+$ varies between -1.10102 (when $l=2$) and -1 (for $l\to\infty$). On the other hand, $\dot{\alpha}_-$ monotonically decreases from -10.8990 (when $l=2$) as l

increases. Hence, the metric functions will be real for all values of l if $\dot{\alpha}$ is restricted by $\dot{\alpha} \geq -1$. The same relation must also be satisfied by α.

The initial value of the Zerilli-Moncrief function can now be obtained by inserting $\tilde{K}(r)$ and $\tilde{H}_2(r) = \alpha\tilde{K}(r)$ in Eq. (3.11). Similarly, initial data for $\dot{\psi}_{\rm ZM}$ can be obtained by substituting $\dot{\tilde{K}}(r)$ and $\dot{\tilde{H}}_2(r) = \dot{\alpha}\tilde{K}(r)$ into the time derivative of Eq. (3.11).

4.3 A worked example: Radial infall of a point-particle into a Schwarzschild black hole

We now consider the radial infall along the z-axis of a particle of mass μ, starting from rest at a radius r_o, into a Schwarzschild black hole. The perturbations and the initial data associated with this type of motion can be analyzed using the formalism developed in the previous sections. Because of the azimuthal symmetry of the problem, only even-parity perturbations with $m = 0$ are excited and we can ignore odd-parity perturbations.

The evolution of the Zerilli-Moncrief function is given by Eq. (3.12), and, for radial infall, the source term given by Eq. (3.14) reduces to

$$\begin{aligned} S_{\rm ZM}(r,t) &= \frac{2}{l(l+1)\Lambda}\Big\{r^2 f\Big[f^2\frac{\partial}{\partial r}Q^{tt} - \frac{\partial}{\partial r}Q^{rr}\Big] + r\Big(\Lambda - f\Big)Q^{rr} \\ &- \frac{f^2}{\Lambda r}\Big[\lambda(\lambda-1)r^2 + (4\lambda-9)Mr + 15M^2\Big]Q^{tt}\Big\}, \end{aligned} \tag{4.16}$$

and we use the fact that, for radial infall, the four-velocity is $u^\nu = [\tilde{E}/f, -(\tilde{E}^2 - f)^{1/2}, 0, 0]$. We assume, without loss of generality, that the motion proceeds along the negative z direction, so that $\theta_p = 0$ on the world line. Evaluating Eq. (4.16) with the

aid of Eqs. (4.1), we obtain[3]

$$S_{\rm ZM}(r,t) = G(r)\delta(r-r_p(t)) + F(r)\delta'(r-r_p(t)), \tag{4.17}$$

where

$$\begin{aligned} G(r) &= -16\pi\frac{\sqrt{(2l+1)/(4\pi)}}{l(l+1)}\frac{\mu}{\tilde{E}}\frac{f^3}{\Lambda}\left[\frac{(\lambda+1)r-3M}{r^2 f} - \frac{6M\tilde{E}^2}{\Lambda r^2 f}\right], \\ F(r) &= 16\pi\frac{\sqrt{(2l+1)/(4\pi)}}{l(l+1)}\frac{\mu}{\tilde{E}}\frac{f^3}{\Lambda}, \end{aligned} \tag{4.18}$$

and we have used $Y^{l0}(0) = \sqrt{(2l+1)/(4\pi)}$, appropriate for motion along the z-axis. The functions $G(r)$ and $F(r)$ are needed for the numerical algorithm presented in Appendix C. (There we consider the more general case where they depend on time. For radial infall, the source term depends on time only through $\delta(r-r_p(t))$ and $\delta'(r-r_p(t))$.) For the radial infall of a particle starting from rest, $r_p(t)$ is given implicitly by

$$\begin{aligned} t &= -4M\tilde{E}\left\{-\frac{1}{2}\frac{r_o}{2M}\sqrt{\frac{r_p}{2M}}\sqrt{1-\frac{r_p}{r_o}} + \sqrt{\frac{r_o}{2M}}\left(1+\frac{r_o}{4M}\right)\arcsin\sqrt{\frac{r_p}{r_o}}\right. \\ &+ \left.\frac{1}{4\tilde{E}^2}\ln\left[\frac{1+\frac{r_p}{2M}-2\frac{r_p}{r_o}-2\tilde{E}\sqrt{\frac{r_p}{2M}}\sqrt{1-\frac{r_p}{r_o}}}{1+\frac{r_p}{2M}-2\frac{r_p}{r_o}+2\tilde{E}\sqrt{\frac{r_p}{2M}}\sqrt{1-\frac{r_p}{r_o}}}\right] - \frac{\pi}{2}\sqrt{\frac{r_o}{2M}}\left(1+\frac{r_o}{4M}\right)\right\}, \end{aligned} \tag{4.19}$$

where, as before, $r_o \equiv r_p(0)$ is the initial position of the particle, and $\tilde{E} = \sqrt{1-2M/r_o}$. The integration of Eq. (3.12) requires the specification of initial data for the Zerilli-Moncrief function: both $\psi_{\rm ZM}(r,t=0)$ and $(\partial/\partial t)\psi_{\rm ZM}(r,t=0)$ must be known. In the next section, we specialize the solutions to the initial-value problem discussed previously to the case of radial infall.

In Sec. 4.3.2 we present the results of the numerical integration of Eq. (3.12) with the source term of Eq. (4.17). We recall that a numerical method was presented by

[3]The source term given here agrees with the source term given in [38, 54] if we substitute "$(1-2M/r_p(t))\delta'(r-r_p(t)) - 2M/r^2\delta(r-r_p(t))$" for "$(1-2M/r)\delta'(r-r_p(t))$" in our source term.

C.O. Lousto and R.H. Price [54] and we employ it here with a slight modification. The method and our modification are presented in Appendix C. The integration was performed over the region of spacetime bounded by the spacelike hypersurface $t = 0$ (the moment of time symmetry), a null hypersurface approximating the event horizon [located at $u = T - r_p^*(T)$, where T is given by Eq. (4.19) with $r_p(T)/2M = 1.0001$] [4], and a null hypersurface approximating future null-infinity [located at $v/2M = (t + r^*)/2M \approx 1500$]. The Zerilli-Moncrief function is extracted from the numerical data on this last hypersurface, i.e. $\psi_{\rm ZM}(r,t)$ is evaluated at $v/2M \approx 1500$ and expressed as a function of $u = t - r^*$. The results presented in Sec. 4.3.2 were obtained with a stepsize of $\Delta = 0.01$.

The relation between the Zerilli-Moncrief function and the gravitational-wave luminosity was given in Chap. 3, Eq. (3.28)[5]. Because in this section the gravitational waveforms are numerically extracted on a null surface approximating $\mathcal{J}^+$, the flux formula presented in Eq. (3.57) cannot be employed directly. Fortunately, in the far-zone the simple substitution $d/dt \to d/du$ is sufficient to produce the correct flux formula. For the reminder of this chapter, we calculate the energy flux using

$$\frac{\mathrm{d}}{\mathrm{d}u}E_l = \frac{1}{64\pi}\frac{(l+2)!}{(l-2)!}\left(\frac{\partial}{\partial u}\psi_{\rm ZM}\right)^2. \tag{4.20}$$

In Sec. 4.3.3 we calculate the power spectrum. It is obtained by first evaluating the Fourier transform of $\psi_{\rm ZM}(u)$,

$$\tilde{\psi}_{\rm ZM}(\omega) = \int_{-\infty}^{\infty} \mathrm{d}\omega e^{i\omega u}\psi_{\rm ZM}(u), \tag{4.21}$$

where ω is the frequency. We evaluate this with the help of a fast Fourier transform algorithm [68]. From Eq. (4.20) and Parseval's theorem, we find that the power

[4]This choice is made to ensure that the particle's contribution to the radiation is (almost) zero at the end of the numerical integration. This means that the value of u associated with the event horizon in our numerical grid changes every time we change r_o.

[5]Because of the symmetry of the problem, $h_+ = 1/2\sqrt{(l+2)(l+1)l(l-1)}\psi_{\rm ZM}(u)\,{}_{-2}Y^{l0}(\theta,\varphi)/r$, while $h_\times$, in this orientation, is zero.

spectrum is

$$\frac{\mathrm{d}}{\mathrm{d}\omega}E_l = \frac{1}{64\pi^2}\frac{(l+2)!}{(l-2)!}\omega^2\left|\tilde{\psi}_{\mathrm{ZM}}(\omega)\right|^2. \tag{4.22}$$

The total energy radiated in each multipole moment is calculated by performing a Romberg integration over all frequencies. The results are presented in Sec. 4.3.4.

4.3.1 Initial Data

In this section, we specialize the solutions to the initial-value problem, developed previously, to the case of the radial infall of a point-particle, starting from rest, into a Schwarzschild black hole. This is the equivalent, in perturbation theory, to the Brill-Lindquist and Misner solutions. We will concentrate on Brill-Lindquist type initial data. (Unlike the Misner solution, our initial data sets are not taken to be inversion symmetric with respect to the throat of the black hole.) The Brill-Lindquist solution can be expanded in powers of μ/M to yield an approximate solution to the initial-value problem appropriate for perturbation theory; in the Regge-Wheeler gauge, it is given by $\tilde{H}_1 = 0$ and

$$\tilde{H}_2 = \tilde{K} = 2\mu\frac{\sqrt{4\pi/(2l+1)}}{(1+M/2\bar{r}_o)(1+M/2\bar{r})}\frac{\bar{r}_<^l}{\bar{r}_>^{l+1}}, \tag{4.23}$$

where again $\bar{r}$ is the isotropic radius, and $\bar{r}_<$ ($\bar{r}_>$) is the smaller (greater) of $\bar{r}$ and $\bar{r}_o$. This solution was first examined by C.O. Lousto and R.H. Price [38]. We shall now generalize it by allowing α to be different from 1.

Since the initial hypersurface is a moment of time-symmetry, we have that $\dot{\tilde{H}}_2 = 0 = \dot{\tilde{K}}$. Substituting $Y^{l0*}(0) = \sqrt{(2l+1)/4\pi}$ and $\tilde{E} = \sqrt{1-2M/r_o}$ into Eq. (4.12) (where α must also be used in place of $\dot{\alpha}$), we find that the solution for $\tilde{K}$ can be written as

$$\tilde{K}(r,0) = C(r_o)\tilde{K}_<(r_<)\tilde{K}_>(r_>), \tag{4.24}$$

where $r_<$ ($r_>$) is the smaller (greater) of r and r_o, $\tilde{K}_<$ and $\tilde{K}_>$ are given by Eq. (4.8) (without the overdots), and

$$C(r_o) = 4\pi\sqrt{\frac{2l+1}{4\pi}}\frac{\mu}{M}\left(\frac{r_o}{2M}\right)^{1-\alpha}\frac{\Gamma(r_o)}{\tilde{E}}, \tag{4.25}$$

where $\Gamma(r_o)$ is given by Eq. (4.14).

The conformally-flat solution can now easily be recovered as a special case of the initial-data sets presented above. For a conformally-flat initial three-geometry ($\alpha = 1$), the parameters appearing in the hypergeometric functions given by Eq. (4.11) take the values $a = l+1$, $b = -l$, and $c = 3/2$, and Eq. (4.10) becomes

$$\begin{aligned}
\tilde{K}_<(r) &= \left(\frac{r}{2M}\right)^l F(-l,-l-1/2;-2l;2M/r) \\
&= 2^{-(2l+1)}\left(\frac{r}{2M}\right)^l\left(1+\sqrt{f}\right)^{2l+1} \\
&= \left(\frac{\bar{r}}{2M}\right)^l\frac{1}{1+M/2\bar{r}}, \qquad (4.26) \\
\tilde{K}_>(r) &= \left(\frac{r}{2M}\right)^{-(l+1)} F(l+1,l+1/2;2(l+1);2M/r) \\
&= 2^{2l+1}\left(\frac{r}{2M}\right)^{-(l+1)}\left(1+\sqrt{f}\right)^{-(2l+1)} \\
&= \left(\frac{2M}{\bar{r}}\right)^{l+1}\frac{1}{1+M/2\bar{r}}, \qquad (4.27)
\end{aligned}$$

where we have used Eq. (15.1.13) of [67]. With these results, it is a trivial matter to show that

$$\tilde{K}_<(r_<)\tilde{K}_>(r_>) = \frac{2M}{(1+M/2\bar{r}_o)(1+M/2\bar{r})}\frac{\bar{r}_<^l}{\bar{r}_>^{l+1}}. \tag{4.28}$$

With the conformally-flat values of a, b, and c, $\Gamma(r_o)$ given by Eq. (4.14) becomes

$$\begin{aligned}
\Gamma(r_o) &= \Big[(l+1)F\left(l+2,l+1/2;2(l+1);2M/r_o\right)F\left(-l,-l-1/2;-2l;2M/r_o\right) \\
&\quad +lF\left(-l+1,-l-1/2;-2l;2M/r_o\right)F\left(l+1,l+1/2;2(l+1);2M/r_o\right)\Big]^{-1} \\
&= \frac{\tilde{E}}{2l+1}\Big[F(-l,-l-1/2;-2l;2M/r_o)F(l+1,l+1/2;2(l+1);2M/r_o)\Big]^{-1} \\
&= \frac{\tilde{E}}{2l+1}, \qquad (4.29)
\end{aligned}$$

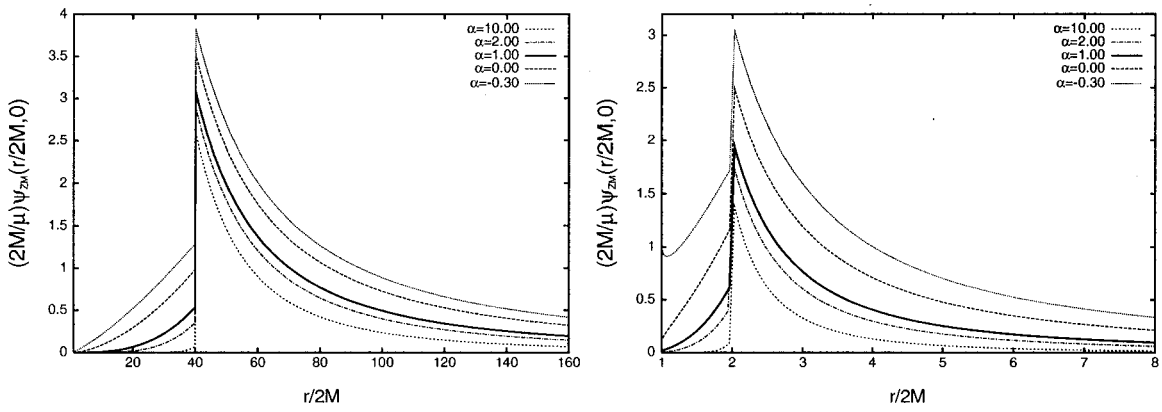

Figure 4.1: Initial values of $\psi_{\rm ZM}(r,0)$ for $l=2$; the particle is initially located at $r_o/2M=40$ (left) and $r_o/2M=2$ (right). In both cases $\psi_{\rm ZM}(r,0)$ is peaked and discontinuous at the particle's location, $r=r_o$. Decreasing (increasing) the value of α increases (decreases) the amplitude and width of the initial pulse. These properties can be associated with the amount of gravitational radiation present on the initial hypersurface. For fixed α, the amplitude of the peak decreases with decreasing r_o.

where the second equality follows from the second identity of Eq. (15.1.13) of [67] applied to $F(l+2,;;)$ and $F(l+1,;;)$, and the third equality from the first identity of Eq. (15.1.13) of [67] applied to both hypergeometric functions. Substituting this results into Eq. (4.25) yields

$$C(r_o) \;=\; \sqrt{\frac{4\pi}{2l+1}}\frac{\mu}{M}. \tag{4.30}$$

Finally, inserting Eq. (4.28) and Eq. (4.30) into Eq. (4.24) gives

$$\tilde{K}(r) = 2\mu\frac{\sqrt{4\pi/(2l+1)}}{(1+M/2\bar{r}_o)(1+M/2\bar{r})}\frac{\bar{r}_<^l}{\bar{r}_>^{l+1}} \tag{4.31}$$

which, in the Regge-Wheeler gauge, is indeed the conformally-flat solution of Eq. (4.23).

Figure 4.1 displays the Zerilli-Moncrief function $\psi_{\rm ZM}(r,0)$ for the cases $r_o/2M=40$ and $r_o/2M=2$, for selected values of α. The figure shows that $\psi_{\rm ZM}(r,0)$ is peaked at the particle's location, and its amplitude and width change with the value of α; the

function is discontinuous at $r = r_o$ because of the discontinuity in the term $\partial\tilde{K}/\partial r$ appearing in Eq. (3.11). We see that the amplitude of the peak increases with decreasing values of α, and this effect is more pronounced as r_o decreases. Intuitively, we associate a smaller (larger) amplitude with a smaller (larger) amount of gravitational radiation initially present in the spacetime. Thus, to initial data with a small (large) value of α we associate a large (small) amount of initial radiation.

4.3.2 Radial infall of the point particle: Gravitational waveforms

The radiation arriving at the null boundary of our domain of integration contains radiation from the initial data, radiation emitted by the particle as it falls toward the black hole, and radiation corresponding to the black hole's response to the perturbation. Because the particle is at rest at $t = 0$, it initially produces very little radiation. The early part of the waveform is therefore dominated by radiation contained in the initial data. As time proceeds, the radiation produced by the particle becomes noticeable, and the dynamics associated with the perturbation of the event horizon starts to play a role. The radiative process can therefore be separated into three stages. The first stage is associated with the initial data, the second with the infalling particle, and the third with the event-horizon dynamics. We now describe these stages in detail.

The initial data is time-symmetric, and it therefore consists of two radiation pulses: one pulse is outgoing, and the other is incoming. The outgoing pulse proceeds to infinity, with some backscattering [which is small, unless the pulse originates in the strong-field region of the spacetime ($r^* \leq 0$)]. On the other hand, the ingoing pulse moves toward the black hole and is backscattered by the potential barrier at $r^* \approx 0$.

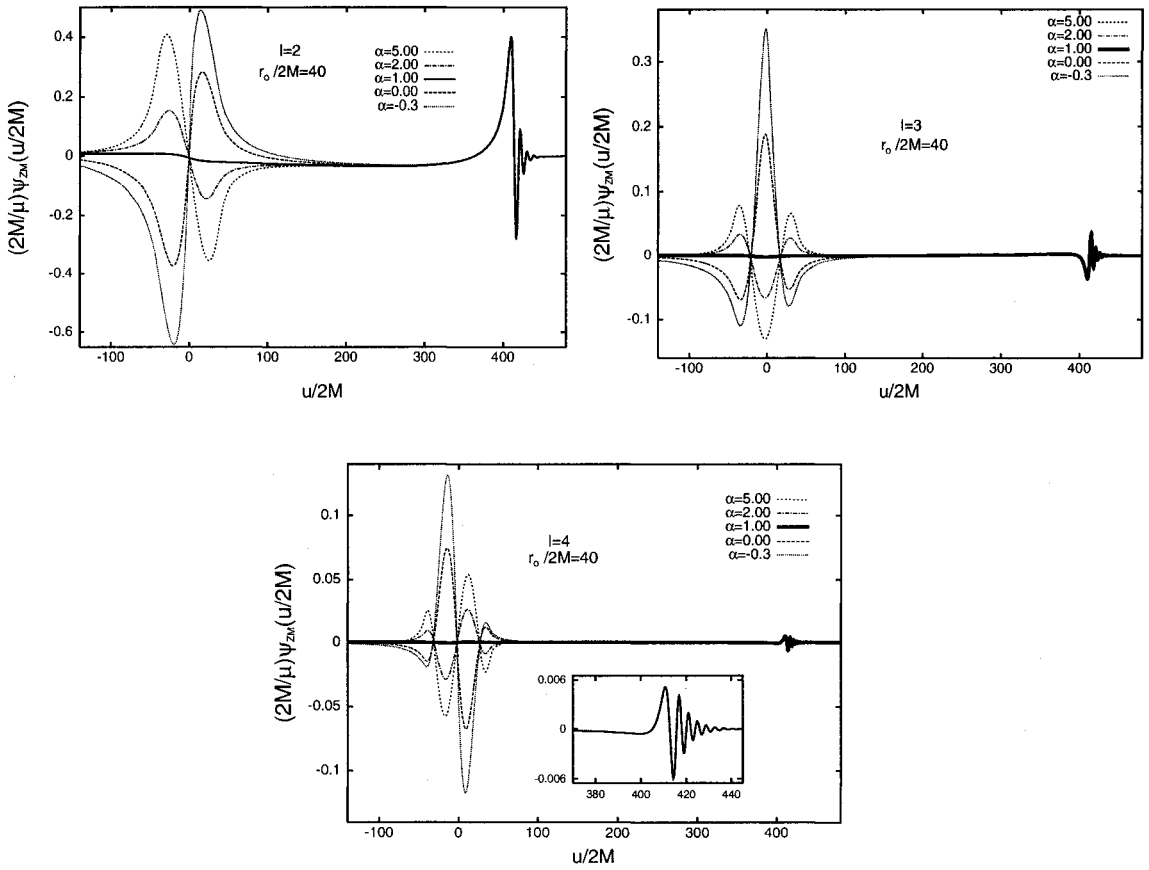

Figure 4.2: The $l = 2$, 3, and 4 modes of the Zerilli-Moncrief function for infall from $r_o/2M = 40$, for $\alpha = -0.3$, 0, 1, 2, and 5. For each multipole moment, the early-time behaviour is dominated by the initial data contribution ($u/2M < 350$), while the late-time behaviour is dominated by radiation emitted by the particle in the strong-field region ($350 < u/2M < 400$) and by quasi-normal ringing of the black hole ($u/2M > 400$). The early-time portion of the waveforms (first stage) depends strongly on the parameter α, which labels the choice of initial data. In contrast, the late-time portion (second and third stages) is completely insensitive to the choice of initial data.

The reflected pulse then proceeds to infinity, where it arrives delayed with respect to the original outgoing pulse. This is the first stage of the radiative process, and it is directly associated with the initial data. The second stage is associated with the motion of the particle. As the particle accelerates toward the black hole, it produces radiation which propagates to infinity. This happens either by direct propagation or by backscattering from the potential barrier. The third and final stage of the

radiative process is the response of the black hole to the perturbation. As the particle approaches the black hole, it tidally deforms the event horizon, which becomes dynamical. The radiation produced in this process interacts strongly with the potential barrier outside the black hole, and the result, after transmission to infinity, is a pattern of damped oscillations. This response of the black hole to the perturbation created by the particle is known as quasi-normal ringing [69].

As long as $r_o \gg 2M$, the different stages of the radiative process can be clearly distinguished (initial-data pulses, acceleration radiation, and quasi-normal ringing). But when r_o is comparable to $2M$, the three epochs become confused, and this gives rise to interfering waveforms. For this reason, varying the initial separation between the particle and the black hole can have an important effect on the gravitational waveforms.

Let us describe more fully the first stage of the radiative process. For infall from a large distance ($r_o \gg 2M$), the outgoing pulse travels directly to future null-infinity with very little backscattering, since the pulse originates in a region where the potential of Eq. (2.60) is weak. This is shown in the waveform as a single pulse of radiation at early times ($u \approx -r_o^*$). The ingoing pulse, on the other hand, proceeds toward the black hole, where it is almost entirely backscattered by the potential barrier. The reflected pulse then proceeds to infinity and this gives rise to a second pulse of radiation at $u \approx r_o^*$. Varying α changes the amount of gravitational radiation initially present at $t = 0$, and the amplitude of the two pulses depends on α. This can be seen in Fig. 4.2, where the $l = 2$, 3, and 4 modes of the Zerilli-Moncrief function are displayed for infall from $r_o/2M = 40$, for several values of α. For $l = 2$, the two pulses have a minimum amplitude when $\alpha = 1$, and the amplitudes vary smoothly with α.

At later times, once the pulses have made their way to infinity, the radiative process becomes dominated by the particle's contribution; this is the second stage. At this time, the particle has entered the strong-field region of the spacetime, its acceleration is large, and it radiates strongly. This stage lasts for a short time, because the particle quickly falls into the black hole. The burst of radiation from the particle is then quickly replaced by the third stage, quasi-normal ringing. When $r_o \gg 2M$, the acceleration radiation and the quasi-normal ringing stages are insensitive to the choice of initial data. This is illustrated in Fig. 4.2.

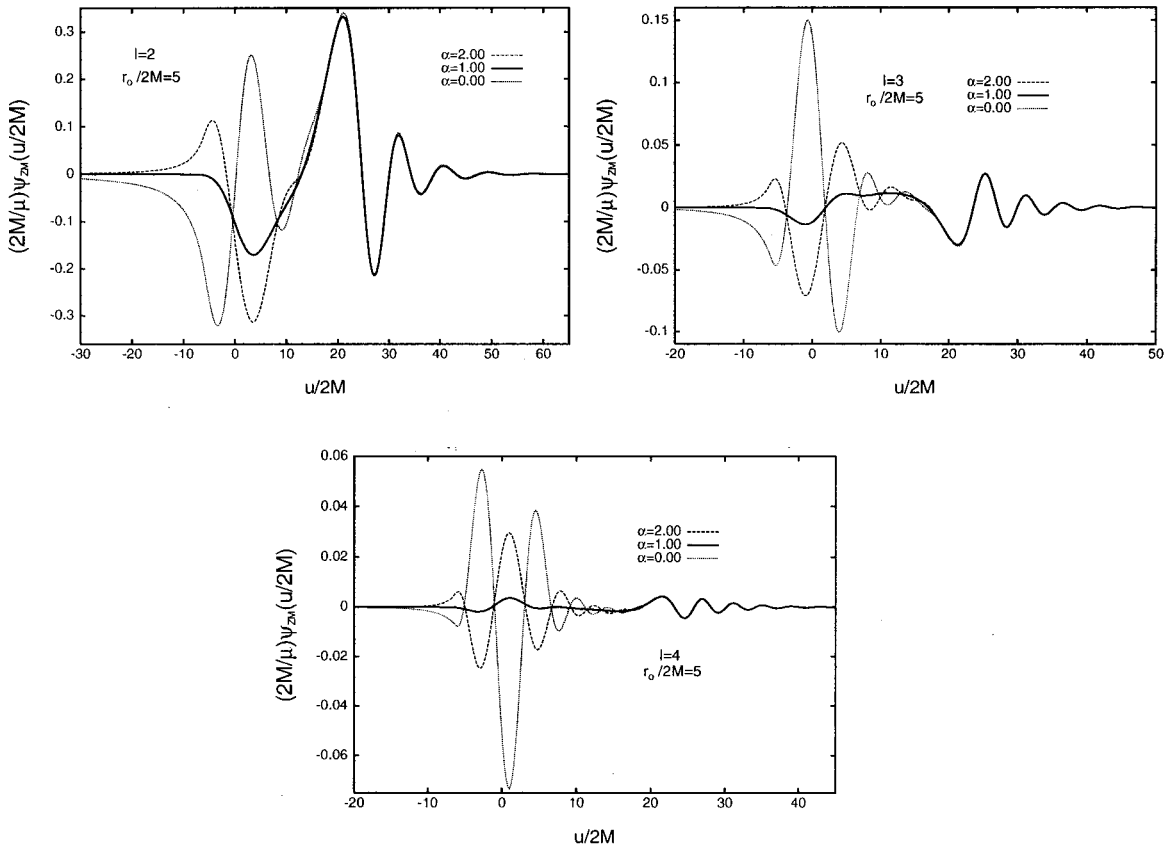

Figure 4.3: The $l = 2$, 3, and 4 modes of the Zerilli-Moncrief function for infall from $r_o/2M = 5$, for $\alpha = 0$, 1, and 2. The waveform changes smoothly as α is varied away from 1, but the change is more dramatic when α is decreased. The three stages of the radiative process now overlap and become confused. However, we still witness an early-time sensitivity, and a late-time insensitivity, to the choice of initial data.

The situation changes when r_o is chosen within the strong-field region of the

spacetime. The outgoing pulse from the initial data still proceeds directly to infinity with little backscattering, creating a pulse at $u \approx -r_o^*$ (see Fig. 4.3). However, the ingoing pulse is no longer entirely backscattered by the potential barrier; part of the pulse is now transmitted to the black hole. The backscattered portion of the ingoing pulse proceeds to infinity where it generates a second pulse at $u \approx r_o^*$, while the transmitted pulse reaches the event horizon. As a result, the event horizon becomes distorted, and starts radiating into quasi-normal modes; the second pulse is therefore immediately followed by an epoch of quasi-normal ringing excited by the transmitted pulse. The amplitude of the quasi-normal ringing depends on the strength of the excitation, and is therefore highly sensitive to the choice of initial data. This early epoch of quasi-normal ringing cannot be seen for infall from large r_o, because in that case the initial data contains mostly low-frequency gravitational radiation that is almost totally reflected by the potential barrier surrounding the black hole [70].

For intermediate values of r_o ($4 \lesssim r_o/2M < 10$), the particle starts in the strong-field region of the spacetime, and its large acceleration causes it to radiate strongly almost immediately. The second stage, which for infall from large r_o was dominated by acceleration radiation, is now the sum of acceleration radiation and quasi-normal ringing excited by the initial ingoing pulse, as was discussed above. This can be seen especially clearly for the $l = 3$ and 4 modes of the Zerilli-Moncrief function displayed in Fig. 4.3, for infall from $r_o/2M = 5$. The superposition can be seen in the interval $5 < u/2M < 20$; it is small for $\alpha = 1$, but large for $\alpha \neq 1$. The third stage of the radiative process is the quasi-normal ringing of the black hole, excited by the particle as it reaches the event horizon. This phase of quasi-normal ringing is to be distinguished from the earlier phase associated with the transmitted pulse; this new phase is insensitive to the choice of initial data.

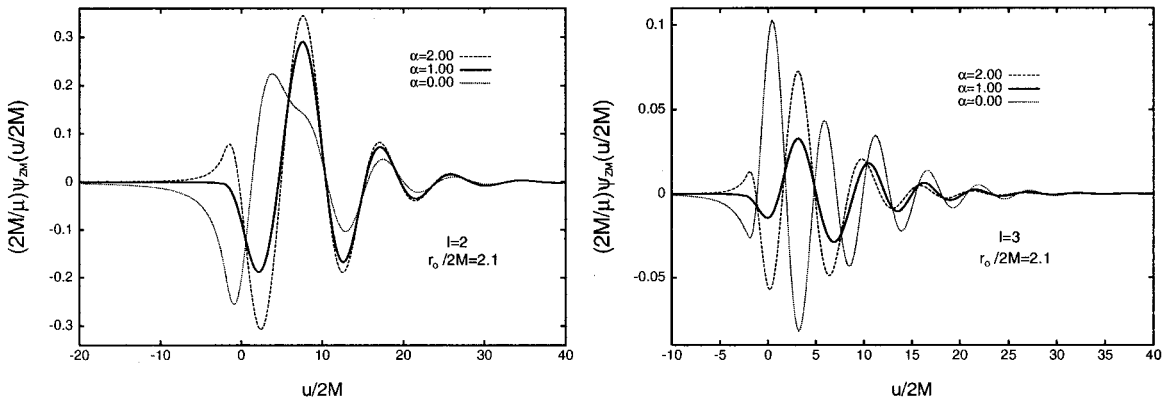

Figure 4.4: The $l = 2$ and 3 modes of the Zerilli-Moncrief function for a particle falling from $r_o/2M = 2.1$, for $\alpha = 0$, 1, and 2. At intermediate times, the waveform is a superposition of the backscattered ingoing pulse from the initial data, and acceleration radiation from the particle. The choice of initial data has an influence at late times; it affects the amplitude and the phase of the quasi-normal ringing.

As r_o is decreased further ($1.3 \lesssim r_o/2M \lesssim 4$), the waveforms become increasingly confused. In this range of initial separations, the particle radiates strongly immediately, and the reflected pulse of ingoing radiation does not reach infinity before the radiation from the particle becomes significant. The interference between these two contributions to the waveform is fairly small, because the particle radiates for a short time before passing through the event horizon. Figure 4.4 displays the $l = 2$ and 3 modes of the Zerilli-Moncrief function for infall from $r_o/2M = 2.1$ for $\alpha = 0$, 1, and 2. The interference between the backscattered ingoing pulse and the radiation emitted by the particle is apparent, especially for $l = 2$ and $\alpha = 0$. A new phenomenon is observed for these values of r_o: the stage of pure quasi-normal ringing is now affected by the choice of initial data. The event horizon is distorted both by the transmitted ingoing pulse and the particle, and these factors act at roughly the same time. Different choices of initial data will therefore affect differently the amplitude and the phase of the quasi-normal ringing. This is displayed in Fig. 4.4.

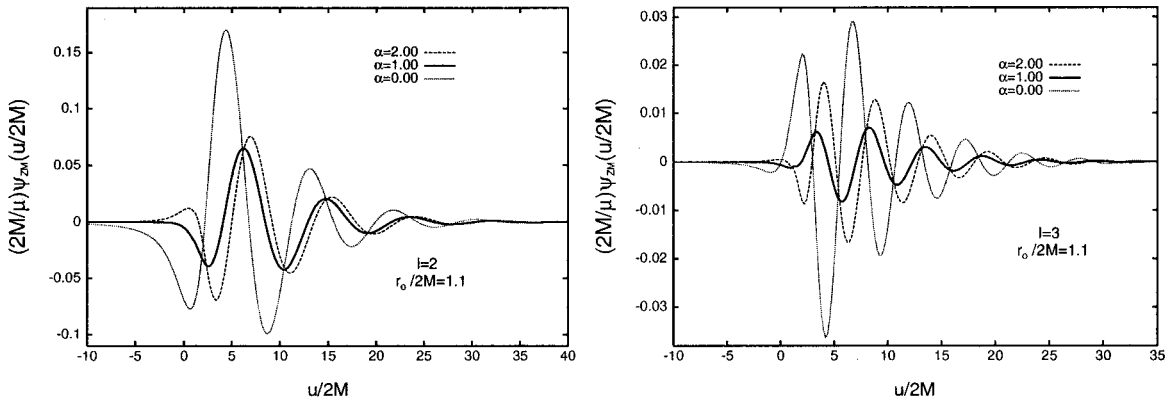

Figure 4.5: The $l = 2$ and 3 modes of the Zerilli-Moncrief function for a particle falling from $r_o/2M = 1.1$, for $\alpha = 0$, 1, and 2. For this very small initial separation, the particle is quickly absorbed by the black hole and cannot radiate much. The initial value of $\psi_{\rm ZM}(r,t)$ determines how strongly the event horizon is distorted, and it therefore has a major impact on the quasi-normal ringing phase of the radiation.

These effects disappear when r_o is moved past the potential barrier ($1 < r_o/2M \lesssim 1.3$). In such cases, most of the outgoing pulse in the initial data is reflected by the potential barrier, and does not register at infinity. Instead, the pulses in the initial data and the radiation from the particle work together to distort the event horizon. For these very small r_o, the quasi-normal ringing is the only feature that remains in the waveforms. The amplitude and the phase of the quasi-normal ringing are very sensitive to the choice of initial data, because the information about the initial distortion of the event horizon is entirely encoded in the initial data (see Fig. 4.5 for the case $r_o/2M = 1.1$). The contribution from the particle is minimal because it is almost immediately absorbed by the black hole.

4.3.3 Power Spectra

The power spectra, as calculated from Eq. (4.22) with a fast Fourier transform algorithm, tell a similar story. For a given choice of l, α, and r_o, the total power spectrum

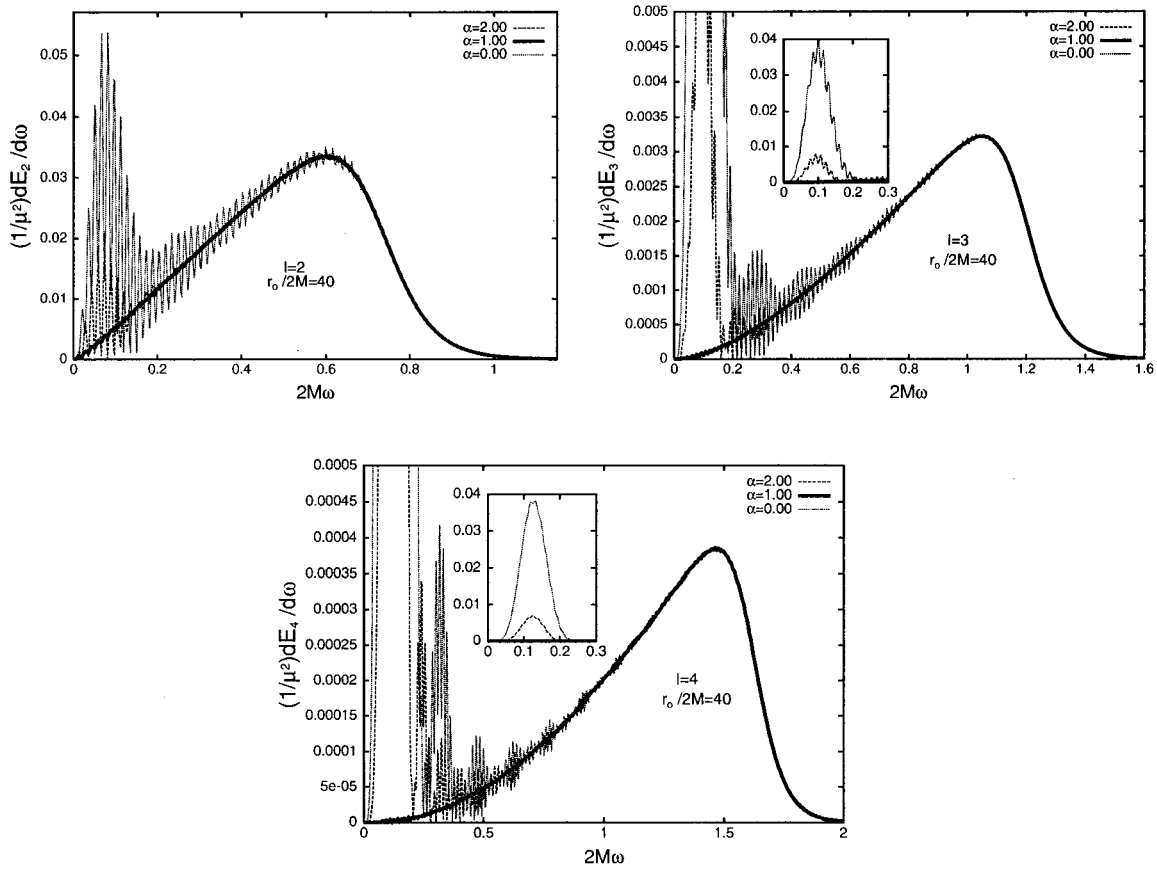

Figure 4.6: Power spectra for the $l = 2$, 3, and 4 modes of the Zerilli-Moncrief function for $r_o/2M = 40$, and $\alpha = 0$, 1, and 2. Varying α changes the shape of the spectra at low frequencies, but the effect disappears at high frequencies. The low-frequency oscillations are more important for $\alpha = 0$, compared with $\alpha = 1$ and 2, and $\alpha = 2$ produces more oscillations than $\alpha = 1$. The low-frequency part of the spectrum is due mostly to the low-frequency gravitational waves contained in the initial data.

is the sum of initial-data, particle, and quasi-normal ringing contributions, but it includes interference between these contributions.

The interference is important when the pulses associated with the initial data, the acceleration radiation, and the quasi-normal ringing contain overlapping frequencies. Typical frequencies are $\omega_o \sim r_o^{-1}$ for the initial-data radiation, $\omega_p \sim r_p^{-1}$ for the acceleration radiation, and $\omega_{QN} \sim M^{-1}$ for the quasi-normal ringing. As was mentioned in Sec. 4.3.2, the particle emits mostly in the strong-field region of the spacetime ($\omega_p \sim M^{-1}$) and consequently, the interference between acceleration radiation and

quasi-normal ringing is always present, while interference with the initial-data contribution is important only when r_o is not much larger than $2M$. In other words, interference effects involving the initial-data pulses are important when the particle is released in the strong-field region. This picture is somewhat simplistic, but it serves as a useful guide to determine when interference effects become important. Our numerical results are consistent with this picture.

For large initial separations ($r_o/2M \gg 1$), we expect the energy spectrum to be the direct sum of the powers in the initial-data and particle contributions, and in the quasi-normal ringing, without much interference. This is confirmed in Fig. 4.6, where the spectra for the $l = 2$, 3, and 4 modes of the Zerilli-Moncrief function for $r_o/2M = 40$, and $\alpha = 0$, 1, 2, are presented. At low frequencies, the initial data manifests itself as a strong pulse which dominates the spectrum. At higher frequencies, acceleration radiation and quasi-normal ringing dominate the spectrum; this part of the spectrum is easy to recognize, as it does not change when α is varied. As we move away from conformal flatness ($\alpha = 1$), the influence of the initial data spreads into higher frequencies. This can be seen as oscillations in the spectrum (cf. the cases $\alpha = 0$ and 2 in Fig. 4.6). These oscillations are also present for $\alpha = 1$, but increasing or decreasing the value of α increases their amplitude and the extent by which they spill into higher frequencies. In general, a choice of initial data with $\alpha < 1$, instead of $\alpha \geq 1$, produces larger oscillations, and the effect extends to higher frequencies. (The oscillations are the smallest when $\alpha = 1$.)

We have seen in the previous section that for intermediate values of r_o ($4 \lesssim r_o/2M < 10$), the choice of initial data affects the shape of the waveforms up to times where acceleration radiation starts to dominate the radiative process. For these initial separations, interference effects are important. This is confirmed by our numerical

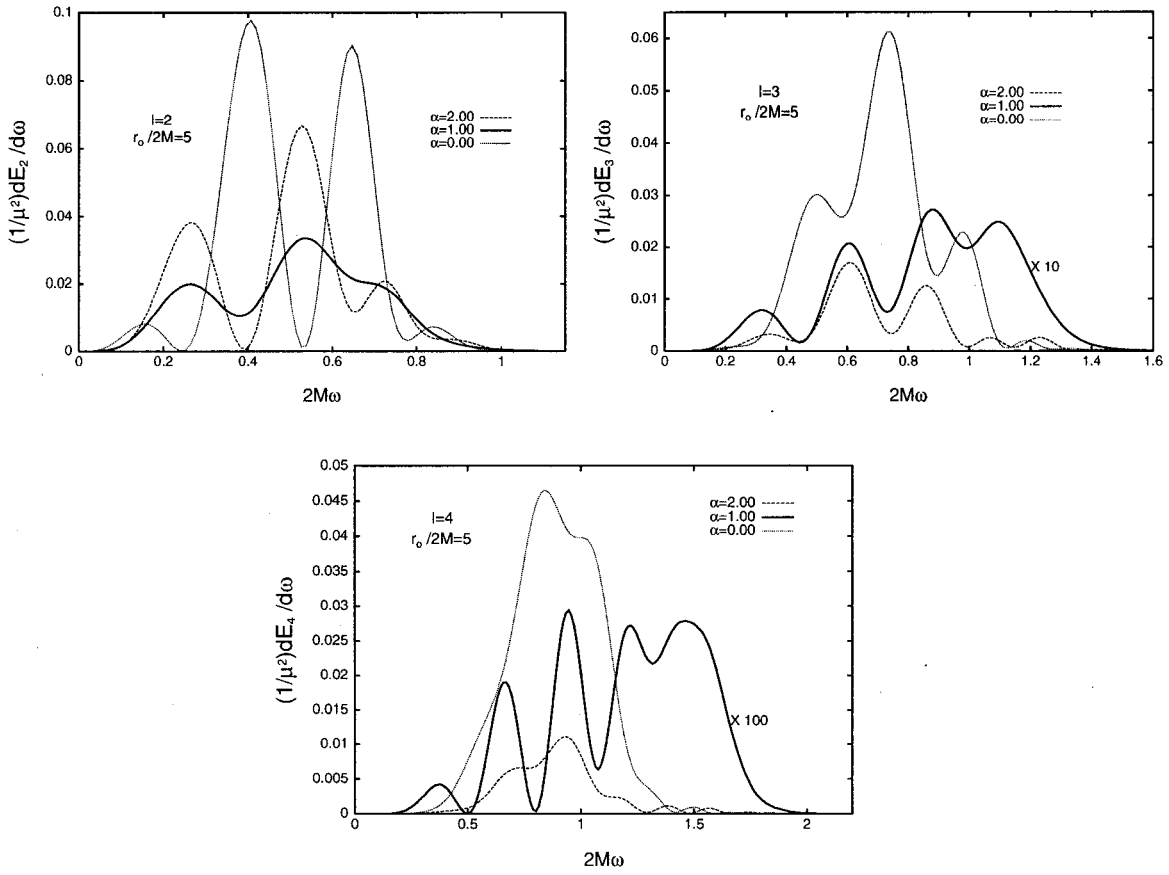

Figure 4.7: Power spectra for the $l = 2$, 3, and 4 modes of the Zerilli-Moncrief function for infall from $r_o/2M = 5$, and $\alpha = 0$, 1, and 2. Interference between the initial-data pulses, the acceleration radiation, and the quasi-normal ringing plays a crucial role in determining the shape of the spectra. For $\alpha = 0$ and $l = 2$, the spectrum has two maxima at $2M\omega = 0.4065$ and $2M\omega = 0.6455$, frequencies at which the spectra for $\alpha = 1$ and 2 have a local minimum. Similarly, the maximum at $2M\omega = 0.5364$ for $\alpha = 1$ and 2 is replaced by a minimum when $\alpha = 0$. This is indicative of strong interference effects. The labels "$\times 10$" and "$\times 100$" indicate the amount by which the amplitude of these two spectra were multiplied to be presented in the same figure.

simulations of infall from $r_o/2M = 5$. The spectra, for this value of r_o, are displayed in Fig. 4.7 for $l = 2$, 3, and 4, and $\alpha = 0$, 1, and 2. For $l = 2$, initial data with $\alpha > 1$ tend to amplify the features apparent for $\alpha = 1$ (see the case $\alpha = 2$ in Fig. 4.7), while decreasing the value of α changes the location of the maxima; local minima appear in the spectrum where maxima were seen for $\alpha = 1$ (see $\alpha = 0$ in Fig. 4.7). For $l = 3$ and 4 and $\alpha > 1$ ($\alpha < 1$), we observe a similar amplification (attenuation) of the features present for $\alpha = 1$, but the effect is much weaker than for $l = 2$.

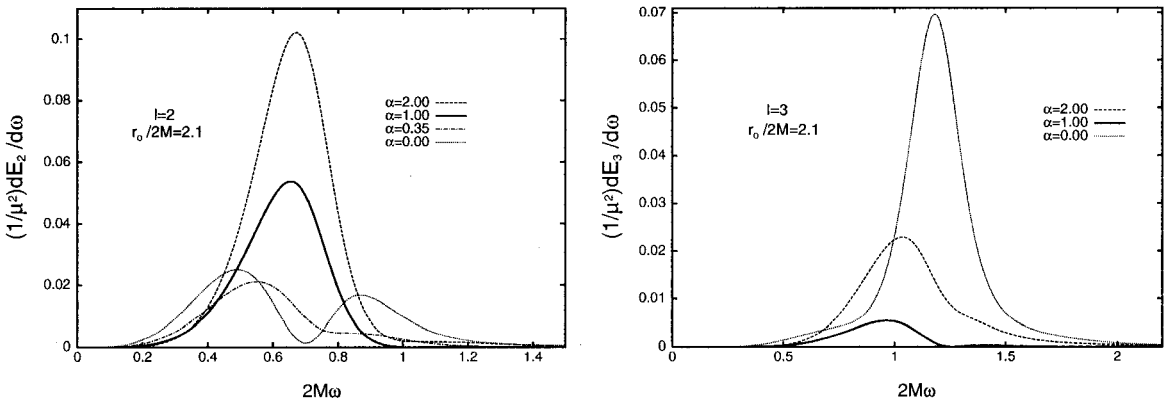

Figure 4.8: Power spectra for the $l = 2$ and 3 modes of the Zerilli-Moncrief function for infall from $r_o/2M = 2.1$, and $\alpha = 0$, 1, and 2. For $l = 2$, we also display $\alpha = 0.35$, to show the smooth transition between the single-maximum and two-maxima regimes described in the text. For such a small separation, acceleration radiation is small, and the interference effects are not very pronounced. They still, however, play an important role in determining the shape of the spectra. The spectrum for $l = 2$ and $\alpha = 0$ has a shape that indicates strong interference effects between initial-data, particle, and quasi-normal ringing contributions: the single maximum at $2M\omega = 0.6553$, seen for $\alpha = 1$ and 2, is replaced by two maxima at $2M\omega = 0.4915$ and $2M\omega = 0.8697$.

As r_o is taken closer to the potential barrier ($1.3 \lesssim r_o/2M \lesssim 4$), the interference becomes less important. In Sec. 4.3.2, we showed that for r_o close to the potential barrier, the particle does not radiate strongly before passing through the event horizon, and the interference is small because of the small amount of acceleration radiation. In Fig. 4.8 we present the spectra for infall from $r_o/2M = 2.1$, $\alpha = 0$, 1, and 2, and $l = 2$, and 3. Although interference effects are not as important as for infall from $r_o/2M = 5$, they still play a role in determining the shape of the spectrum, as can be seen for the case $\alpha = 0$. In this case, the spectrum has two maxima and a single minimum; this minimum occurs close to the fundamental quasi-normal frequency, which suggests a strong destructive interference between initial-data-excited and particle-excited quasi-normal ringing. This is different from the cases $\alpha = 1$ and 2, for which the spectra contain a single peak, indicating that most of the energy is

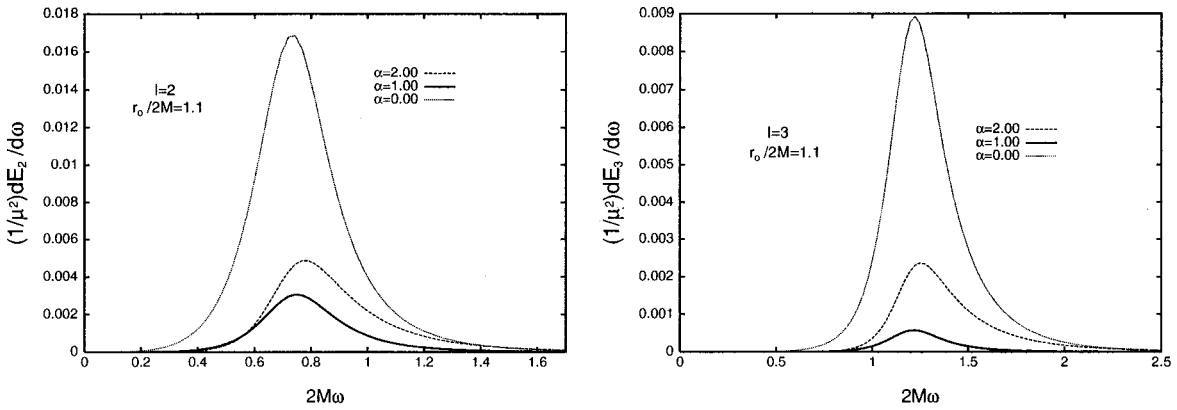

Figure 4.9: Power spectra for the $l = 2$ and 3 modes of the Zerilli-Moncrief function for infall from $r_o/2M = 1.1$, and $\alpha = 0$, 1, and 2. For r_o well inside the potential barrier, acceleration radiation is negligible since the particle is absorbed by the black hole immediately. The initial data distorts the event horizon, which becomes dynamical and starts radiating at its quasi-normal frequencies. The amplitude of the quasi-normal ringing is determined by the strength of the tidal distortion exerted on the event horizon by the initial data. For the cases displayed, the lowest amplitude is obtained for $\alpha = 1$, while the highest is obtained for $\alpha = 0$.

radiated into quasi-normal modes.

Interference effects, such as the ones shown in Fig. 4.8, have been observed previously by C.O. Lousto [71], but in a different context. Instead of evolving the perturbed Misner solution, appropriate for a head-on collision in perturbation theory, C.O. Lousto chose to use the full Misner solution [63, 64] as initial data for the Zerilli-Moncrief function. He then evolved these initial data using Eq. (3.12). In this case, the interference is due to the non-linear nature of the initial data he evolved.

Finally, when r_o is chosen well inside the potential barrier ($1 < r_o/2M \lesssim 1.3$), the interference effects mentioned previously disappear. For small r_o, the magnitude of the tidal distortion applied to the event horizon is affected only by the choice of initial data. Since the radiation is then dominated by quasi-normal ringing created by the initial tidal distortion of the black hole, the spectra contain a single peak, and its position is independent of α. The choice of initial data affects only the amplitude

of the quasi-normal ringing, and this is reflected in the amplitude of the spectra at the fundamental quasi-normal frequency. For infall from $r_o/2M = 1.1$, displayed in Fig. 4.9 for $l = 2$ and 3, and $\alpha = 0$, 1, and 2, the lowest amplitude occurs for $\alpha = 1$, while the highest occurs for $\alpha = 0$.

4.3.4 Total Energy Radiated

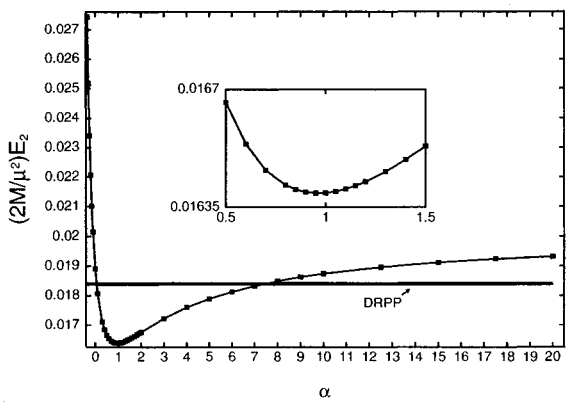

Figure 4.10: The total energy radiated in the $l = 2$ mode as a function of α for a particle falling in from $r_o/2M = 40$. Outside of the range $0 < \alpha < 7.5$, the total energy radiated exceeds the DRPP result. The energy is minimized for $\alpha \approx 1$.

In this subsection we calculate the total energy radiated as a function of α for infall from $r_o/2M = 40$, and as a function of r_o for six selected values of α. We also tabulate the total energy radiated (the sum of the $l = 2$, 3 and 4 modes) for selected values of r_o and α. The radiated energy was calculated using two different methods: direct numerical integration of Eq. (4.20), and numerical integration of Eq. (4.22). In this way, the accuracy of the algorithms used could be tested. The results were found to agree to better than 1%. For comparison, we include in our figures the energy radiated by a particle falling from infinity, as calculated by Davis, Ruffini, Press, and Price (DRPP) [72]. The DRPP result for the energy radiated in the $l = 2$ mode is

$(2M/\mu^2)E_2 = 1.84 \times 10^{-2}$.

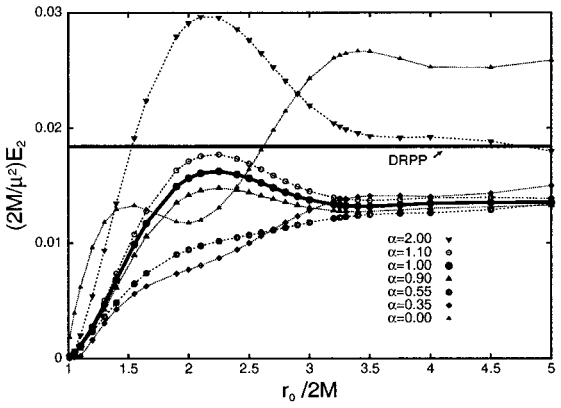

Figure 4.11: The total energy radiated by the $l = 2$ mode as a function of r_o. Displayed are six curves corresponding to the values $\alpha = 0$, 0.55, 0.9, 1, 1.1, and 2. For these small values of r_o, $\alpha = 1$ no longer minimizes the energy radiated. Instead, the value of α that minimizes the energy changes with r_o. This reflects the interference between the initial data, the particle, and the quasi-normal ringing contributions to the radiation. We were unable to find a single value of α that minimizes the energy for all values of r_o in the interval $1 < r_o/2M \leq 5$.

We have seen that for large initial separations, the different contributions to the gravitational radiation do not interfere. The energy emitted in each multipole is then the direct sum of the energy contained in the initial-data pulses, the energy emitted in the acceleration radiation, and the energy radiated in the quasi-normal modes. In Sec. 4.3.2 we showed that all choices of initial data result in two pulses at early times: the outgoing pulse and the backscattered ingoing pulse. These pulses have the smallest amplitude when $\alpha = 1$. Hence, for large initial separations, the waveforms obtained with $\alpha = 1$ are the ones that carry the least amount of energy to infinity.

The total energy radiated in the $l = 2$ mode is shown in Fig. 4.10 as a function of α, for $r_o/2M = 40$. We see that the energy is minimized for $\alpha \approx 1$, and that it exceeds the DRPP result if α is outside the interval $0 \lesssim \alpha \lesssim 7.5$. For such a large value of the initial radius, we confirm the general belief that the radiated energy is

Table 4.1: Total energy radiated (in units of $2M/\mu^2$) for the $l = 2$, 3, and 4 modes, and $\alpha = 0.75$, 0.8, 0.85, 0.9, and 1.0. The sum of the first three multipole moments is denoted by **E**. For infall from short and intermediate distances, the minimum in **E** is achieved for $\alpha < 1$.

$r_o/2M$	l	α=0.75	α =0.8	α=0.85	α=0.9	α=1.0
10.0	2	1.467e-2	1.464e-2	1.463e-2	1.464e-2	1.469e-2
	3	1.961e-3	1.876e-3	1.820e-3	1.789e-3	1.790e-3
	4	4.835e-4	3.778e-4	3.045e-4	2.595e-4	2.406e-4
	E	**1.711e-2**	**1.690e-2**	**1.675e-2**	**1.669e-2**	**1.672e-2**
5.0	2	1.305e-2	1.309e-2	1.316e-2	1.326e-2	1.353e-2
	3	1.725e-3	1.610e-3	1.546e-3	1.529e-3	1.606e-3
	4	5.600e-4	3.883e-4	2.761e-4	2.156e-4	2.249e-4
	E	**1.534e-2**	**1.509e-2**	**1.498e-2**	**1.500e-2**	**1.536e-2**
3.0	2	1.221e-2	1.246e-2	1.274e-2	1.305e-2	1.374e-2
	3	1.359e-3	1.307e-3	1.323e-3	1.398e-3	1.693e-3
	4	5.285e-4	3.298e-4	2.147e-4	1.721e-4	2.681e-4
	E	**1.410e-2**	**1.410e-2**	**1.428e-2**	**1.462e-2**	**1.570e-2**
2.1	2	1.238e-2	1.310e-2	1.383e-2	1.457e-2	1.608e-2
	3	1.270e-3	1.325e-3	1.446e-3	1.625e-3	2.120e-3
	4	4.134e-4	2.515e-4	1.757e-4	1.748e-4	3.598e-4
	E	**1.406e-2**	**1.468e-2**	**1.545e-2**	**1.637e-2**	**1.856e-2**
1.1	2	9.158e-4	9.068e-4	9.066e-4	9.144e-4	1.099e-3
	3	2.017e-4	1.892e-4	1.854e-4	1.894e-4	2.250e-4
	4	2.286e-4	5.415e-5	4.654e-5	4.529e-5	5.966e-5
	E	**1.346e-3**	**1.150e-3**	**1.139e-3**	**1.149e-3**	**1.384e-3**

minimized if the initial hypersurface is conformally flat [73, 74].

In Fig. 4.11 we plot the total energy radiated in the $l = 2$ mode as a function of r_o for selected values of α. In the range $1 < r_o/2M \leq 5$, the energy is no longer minimized by the choice $\alpha = 1$. Instead, we find that in the interval $2.7 < r_o/2M \leq 5$, the energy is minimized when $\alpha = 0.55$, while in the interval $1 \leq r_o/2M \leq 2.7$, the minimum is achieved when $\alpha = 0.35$. (These values are approximate, as we found it difficult in practice to locate the true minimum in the energy for a given r_o and l.) We also find that for a given r_o, no value of α minimizes the energy radiated for all

modes. For example, for infall from $r_o/2M = 5$ there is a minimum in the energy for the $l = 3$ and 4 modes when $\alpha = 0.9$, but this value of α does not minimize the energy in the $l = 2$ mode (see Table 4.1).

Although we are unable to find a single value of α that minimizes the energy radiated for all l and over the whole interval $1 < r_o/2M \leq 5$, we see that in the cases considered, the total energy radiated is never minimized by choosing initial data with $\alpha > 1$. Instead, for infall from a small r_o, it is minimized by a choice of $\alpha < 1$. This is due to strong interference effects for initial data with $\alpha < 1$ when r_o in the strong-field region of the spacetime; this interference was discussed in Secs. 4.3.2 and 4.3.3.

In Table 4.1 we display the total energy radiated in the $l = 2$, 3, and 4 modes of the Zerilli-Moncrief function, for selected values of α and r_o. In general, the features presented previously for the case $l = 2$ are also present for higher multipole moments: the total energy radiated in a given multipole is not minimized by the conformally-flat choice of initial data ($\alpha = 1$), but by some $\alpha < 1$. We find that in some cases, the interference effects become so important that the energy radiated increases with the multipole order l, e.g. $E_2 < E_3 < E_4$. This increase in energy with increasing l contradicts our slow-motion expectation, according to which the energy radiated should decrease with increasing multipole order. A typical example of this phenomenon is displayed in Table 4.1 for $r_o/2M = 1.1$ and $\alpha = 0.75$: here we find $E_4 > E_3$.

4.3.5 Summary

In this section, we studied the effects of the choice of initial data on the gravitational waveforms at infinity. This was done using a one-parameter family of time-symmetric

initial data, a special case of the two-parameter family of initial data sets developed in Sec. 4.2.2.

We showed that for large initial separations, three stages can be clearly identified in the radiative process: initial-data-produced pulses, particle-produced acceleration radiation, and black-hole-produced quasi-normal ringing. For smaller separations, the three stages become confused and interference takes place.

For large initial separations we confirmed the general belief that a conformally-flat initial three-geometry minimizes the radiated energy. But we showed that for $r_o/2M < 10$, the initial configuration that minimizes the energy is not the conformally-flat choice. Instead, the configuration that minimizes the gravitational-wave content has $\alpha < 1$.

Most importantly, our numerical simulations show to what extent the gravitational waveforms are influenced by the choice of initial data. As long as the particle falls toward the black hole from a distance $r_o/2M > 10$, the part of the waveform that is associated with acceleration radiation and quasi-normal ringing is insensitive to the choice of initial data. In these cases, waveforms obtained with conformally-flat initial data are an accurate representation of the true radiative process in the region of interest, because the unphysical radiation coming from the initial data propagates to null-infinity before the physical radiation becomes important. For $r_o/2M \lesssim 10$, however, the two contributions interfere, and uncertainties associated with the choice of initial data hopelessly contaminate the waveforms.

Chapter 5

Gravitational waveforms from a point particle orbiting a Schwarzschild black hole

5.1 Introduction

Tightly bound binary systems consisting of a compact object of a few solar masses and a supermassive black hole of $10^6 - 10^9\ M_\odot$ are very promising sources of gravitational waves for space-based detectors such as LISA [75, 76]. There is now strong evidence that most galaxies harbour a $10^6 - 10^9\ M_\odot$ supermassive black hole in their centre [77], and that they are likely surrounded by a large population of solar-mass compact objects that reside in the galactic cusp [11].

The motion of objects in the galactic cusp is governed by the gravity of the supermassive black hole, but they are also constantly scattered due to the presence of multiple compact objects. For a given compact object, this process occurs until it

settles on a highly eccentric orbit that is tightly bound to the central black hole. On such an orbit, the object, as it approaches the periastron, is very close to the black hole and it emits a significant amount of gravitational waves. Capture occurs for those orbits that are sufficiently eccentric and have a small periastron (on the order of M) [78]. In these cases, orbital evolution is driven by emission of gravitational waves, and the binary strongly radiates gravitational radiation, until the final plunge of the compact object into the central black hole.

The question is then to determine the rate at which solar-mass compact objects are captured by the central black hole and how quickly the orbits decay by emission of gravitational waves. Because capture occurs when the time to evolve due to emission of gravitational waves is much smaller than the time to evolve due to diffusion and scattering, determination of the type of orbits for which capture occurs and estimate of capture rates are sensitive to the strength of gravitational wave emission. Current estimates of orbital parameters for which capture occurs and associated capture rates are based on the quadrupole approximation for the emission of gravitational waves [79]. Although this is well justified for large periastron, it is not a good approximation for highly eccentric orbits with small periastron, those of interest for gravitational waves astronomy.

In this chapter, we consider a situation in which the compact object has already been captured by a spherically symmetric central black hole, and calculate the correct, general relativistic, rates at which the system loses energy and angular momentum to gravitational waves. We consider three types of orbits: circular, eccentric and parabolic orbits. These calculations will then be used to refine capture rates estimate, but this will be left for future work.

At this level of approximation, the internal dynamics of the small compact object

are irrelevant. We treat it as a point-particle and base our calculations on first-order perturbations of a Schwarzschild black hole, as presented in Chapter 2 and Chapter 3. The gravitational waveforms produced by the orbital motion are obtained by solving the even parity Zerilli-Moncrief [20, 22] and the odd parity Regge-Wheeler [19] equations; they are given, in Schwarzschild coordinates, by Eq. (3.12) and Eq. (3.13), respectively.

Instead of Fourier decomposing Eq. (3.12) and Eq. (3.13) and then solving in the frequency domain, we choose to integrate them in the time domain using the Lousto-Price algorithm presented in Appendix C. This method is advantageous compared to Fourier decomposition because of the need, in the case of highly eccentric orbits, to sum over a very large number of frequencies in order to obtain accurate results [80, 81]. As an added bonus, the time-domain method provides the Zerilli-Moncrief and Regge-Wheeler functions everywhere in the spacetime. For each multipole moment, information about the fluxes of energy and angular momentum at infinity and through the event horizon is obtained by a single numerical integration.

Astrophysical black holes are very likely to be rapidly rotating and the assumption of spherical symmetry for the central black hole is unrealistic. However, removing this assumption would require us to solve the inhomogeneous Teukolsky equation. The homogeneous case is presented in Chapter 6.

The chapter is organized as follows. In Sec. 5.2, we describe the orbital parametrization of bound and marginally-bound geodesics of the Schwarzschild spacetime. In Sec. 5.3.1, we provide the source terms of Eq. (3.12) and Eq. (3.13) for this type of motion. In Sec. 5.3.2, we explain our calculation of the total fluxes and provide a discussion of numerical issues that limit the accuracy with which they can be determined. In Sec. 5.3.3, Sec. 5.3.4, and Sec. 5.3.5, we present our results for the gravitational

waveforms and fluxes for circular, eccentric, and parabolic orbits, respectively. In Sec. 5.4 we summarize our findings.

5.2 Orbital parametrization

Following C. Cutler *et al.* [80], we introduce p, such that pM is the semi-latus rectum, and e, the eccentricity, as orbital parameters. They are defined so that the periastron and apastron are at $pM/(1+e)$ and $pM/(1-e)$, respectively. In terms of these parameters, the energy and angular momentum per unit mass of a point particle are

$$\begin{aligned} \tilde{E}^2 &= \frac{(p-2-2e)(p-2+2e)}{p(p-3-e^2)}, \\ \tilde{L}^2 &= \frac{M^2p^2}{p-3-e^2}. \end{aligned} \tag{5.1}$$

For $e=0$ the periastron and apastron coincide, and the orbit is circular. In the interval $0 \leq e < 1$, the motion occurs between two turning points, while for $e=1$, the apastron is pushed back to infinity and the motion is parabolic[1]. In all cases, stable orbits exist only if $p > 6+2e$.

The position of the particle at time t is given by the coordinates $(r_p(t), \varphi_p(t), \theta_p = \pi/2)$. Inspired by the solution to the two-body problem in Newtonian mechanics, the radial position of the particle is expressed as

$$r_p(\chi) = \frac{pM}{1+e\cos\chi}, \tag{5.2}$$

where χ is a parameter along the orbit. This is well behaved at the turning points ($\chi = 0,\ \pi$), which facilitates the numerical integration of the geodesic equations for the time and angular coordinates. In terms of χ, these are [80]

$$\frac{d}{d\chi}t = Mp^2 \frac{(p-2-2e)^{1/2}(p-2+2e)^{1/2}}{(p-2-2e\cos\chi)(1+e\cos\chi)^2(p-6-2e\cos\chi)^{1/2}}, \tag{5.3}$$

[1] In analogy with Newtonian mechanics, we use the term "parabolic" for marginally bound orbits: they have $e=1$ ($\tilde{E}=1$), but the trajectories traced out are *not* parabolae, except in the limit $p \gg 1$.

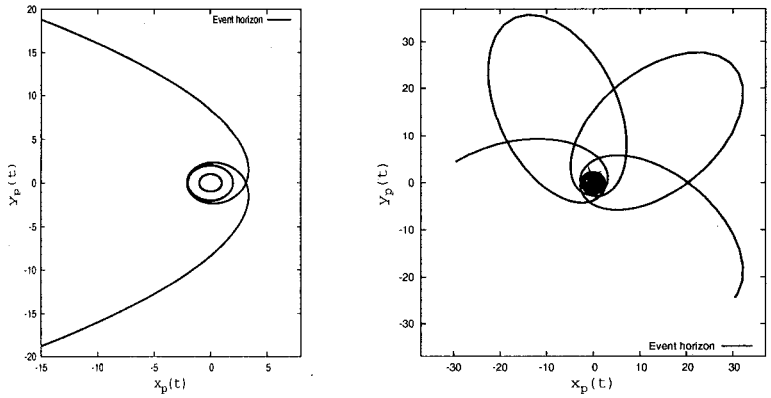

Figure 5.1: In the left panel, we display the trajectories in the x_p-y_p plane for a geodesic with $e = 1$, and $p = 8.001$. For this choice of parameters, the particle orbits the black hole approximately four times before leaving the central region. In the right panel, we display a $e = 0.9$ and $p = 7.8001$ geodesic. When the particle reaches the periastron, it orbits the black hole on a quasi-circular orbit for approximately six cycles. In both cases, the exact number of cycles is given by Eq. (5.5).

$$\frac{d}{d\chi}\varphi_p = \frac{p^{1/2}}{(p-6-2e\cos\chi)^{1/2}}. \tag{5.4}$$

The first of these equation can be numerically inverted to yield $\chi(t)$; knowledge of $r_p(\chi)$ and $\varphi_p(\chi)$ is then equivalent to $r_p(t)$ and $\varphi_p(t)$.

The geodesic equations, Eq. (5.3) and Eq. (5.4), are integrated using the Burlisch-Stoer method [68], and we choose the initial conditions as follows. The gravitational waveforms are extracted as a function of time at a location $r^*_{\rm obs}$. We take the initial moment $t = -t_o < 0$ to be one at which the particle is at periastron ($\chi = 0$, $r_p(-t_o) = Mp/(1+e)$, and $\varphi_p(-t_o) = 0$). We set t_o equal to the light travel time between the periastron and the observation point. Thus, radiation emitted at the initial moment will reach the observer at $t \approx 0$.

This parametrization of the geodesic is suitable for bound and unbound orbits of the Schwarzschild spacetime; for $e < 1$, the parameter χ can take any real value, whereas for $e \geq 1$, it is confined to $-\pi/e \leq \chi \leq \pi/e$. In this chapter, we consider

circular orbits, selected cases of eccentric orbits, and parabolic orbits ($e = 1$), but the code is capable of producing gravitational waveforms for any value of e. For any p and e, the particle orbits the central black hole a number $N = \Delta\varphi_p/(2\pi)$ of times before moving out of the central region. Integrating Eq. (5.4) over one radial period yields [80]

$$N = \frac{2}{\pi}\sqrt{\frac{p}{p-6+2e}}\,K\left(\frac{4e}{p-6+2e}\right), \tag{5.5}$$

where $K(m) = \int_0^{\pi/2} dx(1 - m\sin^2 x)^{-1/2}$ is the complete elliptic integral of the first kind. To visualize the trajectories, we introduce $x_p(t) = r_p(t)/(2M)\cos(\varphi_p(t))$ and $y_p(t) = r_p(t)/(2M)\sin(\varphi_p(t))$. In Fig. 5.1, we display trajectories in the x_p-y_p plane for $p = 7.8001$ and $e = 0.9$ (left), and $p = 8.001$ and $e = 1$ (right). In both cases, the number of times the particle orbits the central black hole is large. This is because p is close to the critical value $6 + 2e$ at which N diverges. In these cases, gravitational-wave emission is dominated by the quasi-circular portion of the orbit near periastron. The total energy emitted is then well approximated by $E = NE_{circular}$, where N is the (divergent) number of orbits, and $E_{circular}$ is the energy emitted by a particle at $r_p = Mp/(1 + e)$; a similar approximation holds for L.

5.3 Waveforms, energy and angular momentum radiated

To numerically evolve Eq. (3.12) and Eq. (3.13) initial conditions must be provided for the gravitational perturbations. The manner in which the initial configuration of the gravitational field influences the subsequent evolution has been studied in Chapter 4, where we gave a detailed discussion of the effects for radial geodesics.

For bound geodesics, the motion is quasi-periodic and waiting a sufficiently long time eliminates the contribution from the initial conditions, which simply propagates away. For marginally-bound geodesics, we choose the initial position of the particle to be very far from the periastron. Far away from the black hole, the velocity of the particle is small and it takes much longer for the particle to reach periastron than for the initial gravitational-wave content to escape from the system. At the point where the emission of radiation is strongest, there is no trace left of the initial configuration of the gravitational perturbations. This allows us to completely avoid problems related to the choice of initial data for both bound and marginally-bound geodesics. We choose zero initial conditions for the gravitational perturbations, acknowledging that this is inconsistent (creating the particle from nothing violates energy-momentum conservation), but recognizing that artifacts of this choice disappear in time. Fluxes may then be computed reliably after waiting a sufficiently long time.

5.3.1 Source term for bound and marginally-bound geodesic motion

The Zerilli-Moncrief and Regge-Wheeler functions are obtained by numerically integrating Eq. (3.12) and Eq. (3.13) with the source terms given by Eq. (3.14) and Eq. (3.15), respectively. These equations can be used and combined with the geodesic equations, given by Eq. (5.2), Eq. (5.4) and Eq. (5.3), to calculate explicit expressions for the functions $G(t,r)$ and $F(t,r)$ appearing in Eq. (C.2); they are needed in the Lousto-Price algorithm of Appendix C. For even parity modes, we get

$$\begin{aligned} G(r,t) &= a\, Y^*(t) + b\, Z^*_\varphi(t) + c\, U^*_{\varphi\varphi}(t) + d\, V^*_{\varphi\varphi}(t) \\ F(r,t) &= \frac{8\pi}{\lambda+1}\frac{f^2}{\Lambda}\frac{\tilde{V}^2}{\tilde{E}}\, Y^*(t), \end{aligned} \tag{5.6}$$

where $\tilde{V}^2 = f\left(1+\tilde{L}^2/r^2\right)$,

$$a = \frac{8\pi}{\lambda+1}\frac{f^2}{r\Lambda^2}\left\{\frac{6M}{r}\tilde{E} - \frac{\Lambda}{\tilde{E}}\left[\lambda+1-\frac{3M}{r}+\frac{\tilde{L}^2}{r^2}\left(\lambda+3-\frac{7M}{r}\right)\right]\right\},$$

and

$$b = \frac{16\pi}{\lambda+1}\frac{\tilde{L}}{\tilde{E}}\frac{f^2}{r^2\Lambda}\,u^r, \qquad c = \frac{8\pi}{\lambda+1}\frac{\tilde{L}^2}{\tilde{E}}\frac{f^3}{r^3\Lambda}, \qquad d = -32\pi\frac{(l-2)!}{(l+2)!}\frac{\tilde{L}^2}{\tilde{E}}\frac{f^2}{r^3}.$$

Finally, for odd parity modes the source terms are

$$\begin{aligned} G(r,t) &= \frac{f^2}{r^3}\left[\frac{4}{r}\left(1-\frac{3M}{r}\right)\alpha+\beta\right], \\ F(r,t) &= -\alpha\frac{f^3}{r^3}, \end{aligned} \tag{5.7}$$

where

$$\alpha = 16\pi\frac{(l-2)!}{(l+2)!}\frac{\tilde{L}^2}{\tilde{E}}\,W^{*lm}_{\varphi\varphi}(t), \quad \beta = \frac{8\pi}{\lambda+1}\frac{\tilde{L}}{\tilde{E}}\,u^r\,X^{*lm}_{\varphi}(t).$$

Note that $G(r,t)$ and $F(r,t)$ contain scalar, vectorial and tensorial harmonic functions evaluated at the angular position of the particle $\varphi_p(t)$. For example, for even modes, some terms in G and F are proportional to $Y^{lm}(\pi/2,\varphi_p(t))$. Because the orbital motion takes place in the equatorial plane, each spherical harmonic function is evaluated at $\theta_p = \pi/2$. A useful consequence of this is that the source term for the Zerilli-Moncrief function vanishes when $l+m$ is odd, while the source term for the Regge-Wheeler function vanishes when $l+m$ is even. This is used below to simplify the calculation of the fluxes.

These source terms are used to obtain the gravitational waveforms as well as the energy and angular momentum radiated by a particle in bound and marginally-bound geodesics of a Schwarzschild spacetime.

5.3.2 Accurate determination of the fluxes: numerical issues

The relations between the Zerilli-Moncrief and the Regge-Wheeler functions and the radiative portion of the metric perturbation at infinity and near the event horizon were presented in Chapter 3. These relations directly establish the connection between the Zerilli-Moncrief and Regge-Wheeler functions and the two gravitational-wave polarizations. The relations are given by Eq. (3.28) for the gravitational waves escaping to infinity, and by Eq. (3.37) for the gravitational waves near the event horizon.

The rates at which energy and angular momentum are carried to infinity by gravitational waves are given by Eq. (3.57) for $\dot{E}^{\infty}_{lm}$ and by Eq. (3.59) for $\dot{L}^{\infty}_{lm}$, while the rates at which they are carried through the event horizon are given by Eq. (3.65) for $\dot{E}^{\rm eh}_{lm}$ and Eq. (3.66) for $\dot{L}^{\rm eh}_{lm}$. As noted in Sec. 3.3.3, the difference in the expressions for the fluxes at infinity and near the event horizon is in the radial position at which the Zerilli-Moncrief and Regge-Wheeler functions are extracted. The fluxes at infinity are calculated using the Zerilli-Moncrief and Regge-Wheeler functions extracted at $r^* = r^*_{\rm obs}$, where $r^*_{\rm obs}$ is large and positive, while for the horizon fluxes, they are extracted at $r^* = r^*_{\rm eh}$, where $r^*_{\rm eh}$ is large and negative. Once $\dot{E}^{\infty,{\rm eh}}_{lm}$ and $\dot{L}^{\infty,{\rm eh}}_{lm}$ are known, the total fluxes are obtained by summing over all modes:

$$\dot{E}^{\infty,{\rm eh}} = \sum_{l=2}^{\infty} \dot{E}^{\infty,{\rm eh}}_{l}, \qquad \dot{E}^{\infty,{\rm eh}}_{l} = \dot{E}^{\infty,{\rm eh}}_{l0} + 2\sum_{m=1}^{l} \dot{E}^{\infty,{\rm eh}}_{lm}, \tag{5.8}$$

$$\dot{L}^{\infty,{\rm eh}} = \sum_{l=2}^{\infty} \dot{L}^{\infty,{\rm eh}}_{l}, \text{ and } \dot{L}^{\infty,{\rm eh}}_{l} = 2\sum_{m=1}^{l} \dot{L}^{\infty,{\rm eh}}_{lm}; \tag{5.9}$$

there is no $m = 0$ contribution to the angular momentum flux, and the factor of 2 in front of $\dot{E}^{\infty,{\rm eh}}_{lm}$ and $\dot{L}^{\infty,{\rm eh}}_{lm}$ comes from folding the $m < 0$ contributions over to $m > 0$. We justify folding these terms in the following way. By construction, the vectorial and tensorial spherical harmonics obey $S^{l,-m} = (-)^m S^{lm*}$, where S is any spherical harmonic function. (This relation holds for scalar spherical harmonics, and

since vectorial and tensorial spherical harmonics are obtained by the action of *real* operators on Y^{lm}, it also applies to these functions.) An important consequence of this relation is that for real metric perturbations, the multipole moments must satisfy $M^{l,-m} = (-)^m M^{lm*}$, where M^{lm} is any one of the metric components introduced in Sec. 3.1: H_0, H_1, H_2, q_0, q_1, K, G, h_0, h_1 and h_2. It is then easily established that $M^{lm}M^{*lm} = M^{l,-m}M^{*l,-m}$, and this is what appears in the expressions for the fluxes.

In a slow-motion, weak-field approximation the quadrupole moment dominates ($l = 2$ and $m = 2$) and the total energy and angular momentum radiated over one orbital period are [16]

$$E_Q(p,e) = \frac{64\pi}{5}\frac{\mu^2}{M}\left(1+\frac{73}{24}e^2+\frac{37}{96}e^4\right)p^{-7/2}, \tag{5.10}$$

$$L_Q(p,e) = \frac{64\pi}{5}\mu^2\left(1+\frac{7}{8}e^2\right)p^{-2}. \tag{5.11}$$

The average energy and angular momentum radiated per unit time, defined by performing an orbital average, are

$$\left\langle \dot{E}_Q \right\rangle = \frac{32}{5}\left(\frac{\mu}{M}\right)^2 \frac{(1-e^2)^{3/2}}{p^5}\left(1+\frac{73}{24}e^2+\frac{37}{96}e^4\right),$$

$$\left\langle \dot{L}_Q \right\rangle = \frac{32}{5}\frac{\mu^2}{M}\frac{(1-e^2)^{3/2}}{p^{7/2}}\left(1+\frac{7}{8}e^2\right). \tag{5.12}$$

For the binaries considered here, the slow-motion and weak-field approximations break down, and the fluxes must be computed using Eq. (5.8) and Eq. (5.9). Numerically we cannot perform the infinite sums, and we truncate them at a finite value $l_{\max}$. Below, we discuss the overall accuracy of the time-domain computation and explain the criteria used to choose $l_{\max}$.

In order to calculate the fluxes to a relative accuracy ε (we use $\varepsilon = 0.01$), we need to consider three sources of error: discretization of Eq. (3.12) and Eq. (3.13), effects of the finite size of our computational grid, as well as truncation of the sums in Eqs. (5.8) and (5.9).

Firstly, discretization of Eq. (3.12) and Eq. (3.13) introduces numerical truncation errors. This is discussed in Appendix C, where we show that the algorithm converges quadratically with the stepsize. Throughout this work we generated gravitational waveforms by setting $\Delta t = 0.1(2M)$ in the numerical algorithm; this proved sufficient to determine the fluxes at infinity to the desired 1% accuracy. However, for a given stepsize the fluxes through the event horizon are never determined as accurately as the fluxes at infinity. The gravitational waves flowing through the event horizon are weaker than the ones escaping to infinity, and, because of this difference in scales, horizon fluxes are determined with an accuracy $\lesssim 5\%$. But we will see below that horizon fluxes *never* amount to more than a few percents of the total fluxes. The lower accuracy with which black hole absorption is determined is then sufficient for our goal of 1% overall accuracy.

Secondly, the expressions for the fluxes given by Eq. (3.57), Eq. (3.59), Eq. (3.65) and Eq. (3.66) hold only asymptotically ($r^* \to \pm\infty$). Numerically we are forced to extract the waveforms at finite r^* values, and this introduces finite-size effects in our results. Numerical efficiency requires a small computational grid, but accuracy requires the waveforms to be extracted at a large and positive $r^*_{\rm obs}$ and at a large and negative $r^*_{\rm eh}$. The flux formulae developed in Sec. 3.3.3 are based on the stress-energy tensor for gravitational waves, as constructed by Isaacson [43]. The validity of the construction depends on $\lambda/\mathcal{R} \ll 1$ being satisfied, where λ is a wavelength of the radiation and $\mathcal{R}$ a typical radius of curvature. To calculate the fluxes far from the black hole, we extract the waveforms in an approximate radiation zone defined by $\lambda/r_{\rm obs} \ll 1$, where $\lambda^{-1} \sim (M/R_p^3)^{1/2}$ and R_p is a typical orbital radius. The radiation zone is then defined by $(R_p/r_{\rm obs})(R_p/M)^{1/2} \ll 1$. For relativistic motion $R_p \sim M$ and by imposing $R_p/r_{\rm obs} < \varepsilon$, we make an error of order ε in

approximating the radiation zone. This is somewhat different from the criterion for the validity of Isaacson's stress-energy tensor. Since $\mathcal{R}^{-1} \sim (M/r_{\rm obs}^3)^{1/2}$, we have that $\lambda/\mathcal{R} \sim (R_p/r_{\rm obs})^{3/2} \sim \varepsilon^{3/2}$, and the use of the stress-energy tensor is justified. In practice we also imposed $r^*_{\rm obs} > 750(2M)$. At the horizon, the situation is somewhat different. The typical radius of curvature is $\mathcal{R} \sim 2M$, but the radiation is blueshifted so that $\lambda \sim f_{\rm eh}(R_p^3/M)^{1/2} \to 0$, where $f_{\rm eh} = 1-2M/r_{\rm eh}$. The requirement $\lambda/\mathcal{R} \ll 1$ then translates to $f_{\rm eh}(R_p/(2M))^{3/2} < \varepsilon$. We used $R^*_p/|r^*_{\rm eh}| < \varepsilon$, as well as $r^*_{\rm eh} < -750(2M)$, which amply satisfies the above requirement. This yielded good results, but a better, more efficient choice would have been $r_{\rm eh} = 2M[1+(2M/R_p)^{3/2}\varepsilon]$. With these choices of $r^*_{\rm obs}$ and $r^*_{\rm eh}$, we are making an error of *at most* order ε in determining the fluxes at infinity and through the event horizon.

Finally, the last source of error limiting the accuracy of the determination of the fluxes arises from truncating the sums in Eqs. (5.8) and (5.9) at a finite value $l_{\rm max}$. The error is made small enough for our requirements by demanding that

$$\varepsilon \equiv \max\left(\frac{\dot{E}^\infty_{l_{max}}}{\dot{E}^\infty}, \frac{\dot{L}^\infty_{l_{max}}}{\dot{L}^\infty}\right) \leq 1\% \tag{5.13}$$

be satisfied. Typically, Eq. (5.13) is satisfied with l_{max} given by $(p/(1+e))^{-(l_{max}-2)} < \varepsilon$, which is known to hold for circular orbits [82]. Note that because $\dot{E}^\infty_{l_{\rm max}}$ and $\dot{L}^\infty_{l_{\rm max}}$ are included in the sum, the error comes from neglecting terms starting at $l = l_{\rm max}+1$. In effect, the relative error made from neglecting these terms is much smaller than 1%. In the sequel, we will return with empirical estimates of our numerical errors; these will confirm the preceding qualitative discussion.

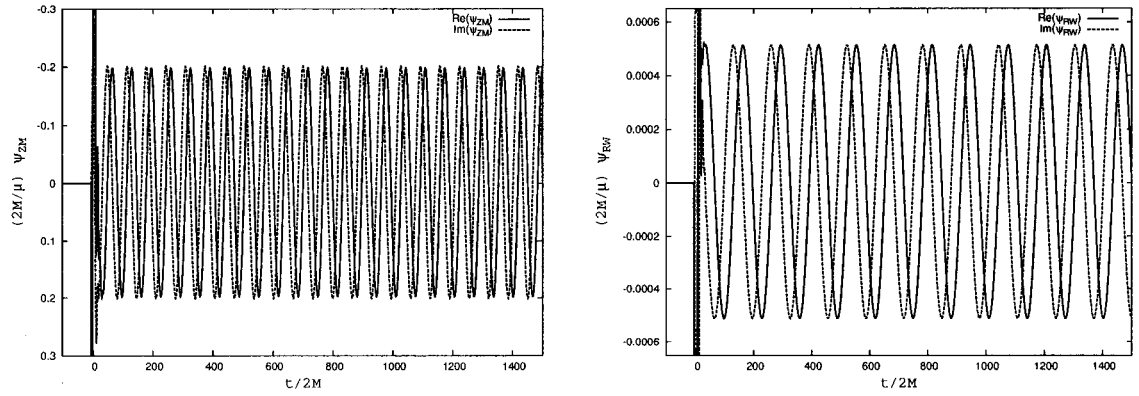

Figure 5.2: The dominant radiation modes for the Zerilli-Moncrief (left, $l = 2$ and $m = 2$) and Regge-Wheeler (right, $l = 2$ and $m = 1$) functions for a particle orbiting the black hole at $r_p = 12M$. At early times, the waveforms are dominated by the initial data content. We calculate the energy and angular momentum fluxes after a time $t/(2M) = 350.0$

5.3.3 Circular orbits

For circular orbits, $e = 0$ and the radius of the orbit is $r_p = pM$. In Fig. 5.2 we display typical gravitational waveforms emitted by a particle traveling on a circular orbit. Both waveforms have the same pattern: The field oscillates with an angular frequency given by $m\Omega$, where $\Omega = M^{-1}p^{-3/2}$ is the orbital angular velocity and m is the multipole index. The left panel contains the dominant quadrupolar mode ($l = 2$ and $m = 2$), while the right panel contains the dominant odd parity mode ($l = 2$ and $m = 1$).

The code outputs $\dot{E}_{GR}$ and $\dot{L}_{GR}$ directly, but it proves convenient to express the fluxes in terms of c_E and c_L: coefficients that remain close to 1 for all values of p. The total fluxes are calculated using Eqs. (5.8) and (5.9) and we express the numerically obtained results in the form

$$\begin{aligned} \dot{E}^{\infty}_{GR}(p) &= c_E\ \dot{E}_Q(p,0), \\ \dot{L}^{\infty}_{GR}(p) &= c_L\ \dot{L}_Q(p,0), \end{aligned} \tag{5.14}$$

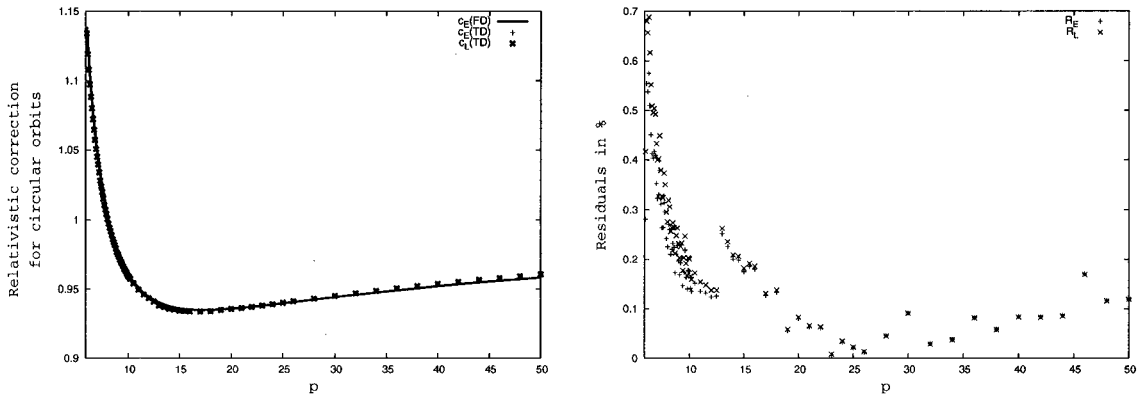

Figure 5.3: In the left panel, we display $c_E(FD)$, as well as $c_E(TD)$ and $c_L(TD)$, as functions of p. Both c_E and c_L slowly approach 1 from below for large p. For small values of p, the coefficients approach 1.15 as p approaches 6. In the right panel, we display the residuals R_E and R_L as defined in the text. Using the time-domain method, the fluxes are calculated accurately to 0.7% for $p = 6.0001$, and to 0.2% for large values of p.

where $\dot{E}_Q(p,0)$ and $\dot{L}_Q(p,0)$ are given by Eq. (5.12) above with $e = 0$. For circular orbits, we should find $\dot{E} = \Omega\dot{L}$ and therefore, $c_E = c_L$.

Circular orbits have been studied extensively and we use them to quantitatively test the accuracy of the time-domain method. We perform a comparison of our results with the time-domain code (TD) with results obtained in the frequency domain (FD) by E. Poisson [83, 84]. In the left panel of Fig. 5.3 we display $c_E(TD)$, $c_L(TD)$, and $c_E(FD)$. In the right panel, we display the residuals, $R_E = 100|c_E(TD) - c_E(FD)|/c_E(FD)$ and $R_L = 100|c_L(TD) - c_E(FD)|/c_E(FD)$. In the interval $6 < p \leq 50$, the time-domain code reproduces the frequency domain calculations to 0.7% or better, with the best agreement occurring for large values of p.

In Table 5.1 we perform a mode by mode comparison between the two methods for $p = 7.9456$ and $p = 46.062$. For $p = 7.9456$, the fluxes from each multipole moment calculated with the time-domain code agree to 1% or better with the fluxes calculated in the frequency domain. A similar agreement is found for $p = 46.062$,

Table 5.1: Energy and angular momentum fluxes for circular orbits, calculated using a time domain (TD) code, are compared with fluxes calculated by E. Poisson using a frequency domain (FD) approach [83, 84]. Here we choose $p = 7.9456$ and $p = 46.062$. The energy fluxes are in units of $(M/\mu)^2$, and the angular momentum fluxes are in units of M/μ^2. They are calculated at $r^*_{\rm obs} = 1500M$ and $r^*_{\rm obs} = 5200M$ for $p = 7.9456$ and $p = 46.062$, respectively.

l	m	$\dot{E}^\infty$ (FD)	$\dot{E}^\infty$ (TD)	rel. diff.	$\dot{L}^\infty$ (FD)	$\dot{L}^\infty$ (TD)	rel. diff.
	$p = 7.9456$						
2	1	8.1633e-07	8.1623e-07	$< 0.1\%$	1.8283e-05	1.8270e-05	0.1%
	2	1.7063e-04	1.7051e-04	$< 0.1\%$	3.8215e-03	3.8164e-03	0.1%
3	1	2.1731e-09	2.1741e-09	$< 0.1\%$	4.8670e-08	4.8684e-08	$< 0.1\%$
	2	2.5199e-07	2.5164e-07	0.1%	5.6439e-06	5.6262e-06	0.3%
	3	2.5471e-05	2.5432e-05	0.1%	5.7048e-04	5.6878e-04	0.3%
4	1	8.3956e-13	8.3507e-13	0.2%	1.8803e-11	1.8692e-11	0.6%
	2	2.5091e-09	2.4986e-09	0.4%	5.6195e-08	5.5926e-08	0.5%
	3	5.7751e-08	5.7464e-08	0.5%	1.2934e-06	1.2933e-06	$< 0.1\%$
	4	4.7256e-06	4.7080e-06	0.4%	1.0584e-04	1.0518e-04	0.6%
5	1	1.2594e-15	1.2544e-15	0.4%	2.8206e-14	2.8090e-14	0.4%
	2	2.7896e-12	2.7587e-12	1.1%	6.2479e-11	6.1679e-11	1.3%
	3	1.0933e-09	1.0830e-09	1.0%	2.4486e-08	2.4227e-08	1.1%
	4	1.2324e-08	1.2193e-08	1.1%	2.7603e-07	2.7114e-07	1.8%
	5	9.4563e-07	9.3835e-07	0.8%	2.1179e-05	2.0933e-05	1.2%
	Total	2.0317e-04	2.0273e-04	0.2%	4.5446e-03	4.5399e-03	0.1%
	$p = 46.062$						
2	1	1.8490e-11	1.8713e-11	1.2%	5.7804e-09	5.8497e-09	1.2%
	2	2.8650e-08	2.8728e-08	0.3%	8.9566e-06	8.9809e-06	0.3%
3	1	7.5485e-14	7.7275e-14	2.4%	2.3598e-11	2.4158e-11	2.4%
	2	1.0926e-12	1.0990e-12	0.6%	3.4157e-10	3.4359e-10	0.6%
	3	8.0640e-10	8.0835e-10	0.2%	2.5210e-07	2.5270e-07	0.2%
4	1	9.9792e-19	1.0390e-18	4.1%	3.1191e-16	3.2480e-16	4.1%
	2	1.6018e-14	1.6171e-14	1.0%	5.0075e-12	5.0555e-12	1.0%
	3	4.6603e-14	4.6799e-14	0.4%	1.4569e-11	1.4631e-11	0.4%
	4	2.7937e-11	2.7997e-11	0.2%	8.7339e-09	8.7525e-09	0.2%
	Total	2.9505e-04	2.9584e-08	0.3%	9.2239e-06	9.2486e-06	0.3%

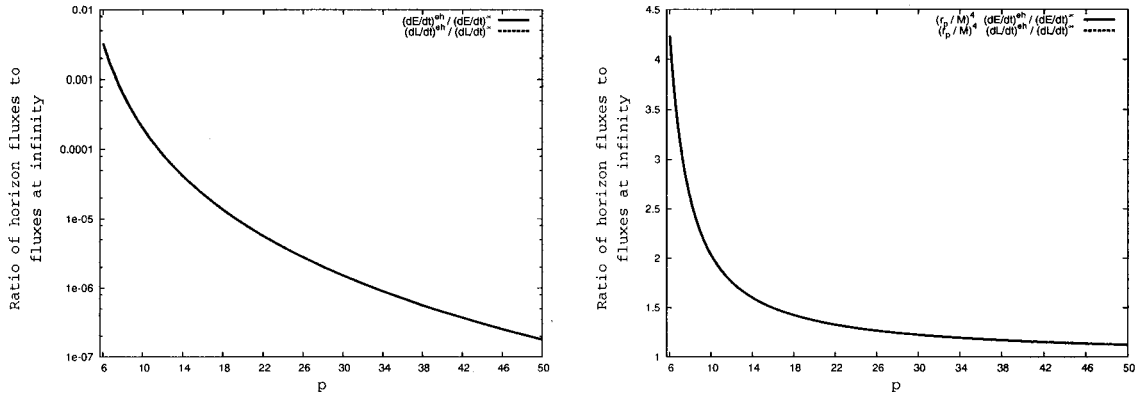

Figure 5.4: We display the energy and angular momentum fluxes through the event horizon normalized by the fluxes in the radiation zone. Even for highly relativistic motion, the horizon fluxes contribute less than 0.4% of the total fluxes. For circular orbits, the theoretical prediction is that $\dot{E}^{\rm eh}/\dot{E}^{\infty} = \dot{L}^{\rm eh}/\dot{L}^{\infty}$. Numerically, this relation is only approximate, but nevertheless the two curves are indistinguishable. The right panel displays these ratios normalized by $(r_p/M)^{-4}$, the weak-field and slow-motion approximation.

with the exception of the $l = 3$ and $m = 1$, and $l = 4$ and $m = 1$ modes, for which the relative difference is 2.4% and 4.1%, respectively. This results from the huge difference in amplitude between these modes and the dominant mode. Although the stepsize used throughout this work is sufficient to obtain an overall relative accuracy of 1%, it is not small enough to determine individual, small-amplitude modes to better than $2 \sim 5\%$. Although these modes could be resolved properly by using a smaller stepsize, it is not necessary for our goal of 1% overall accuracy; the contributions from these modes to the total fluxes are six and ten orders of magnitude smaller than the leading-order contributions, respectively. As such, they do not affect the overall accuracy of the computation, and for $p = 7.9456$ and $p = 46.062$ the total fluxes calculated with the time-domain method agree with the frequency domain results to within 0.2% and 0.3%, respectively.

Black hole absorption was calculated in a weak-field and slow-motion approximation for a particle in circular orbit by E. Poisson and M. Sasaki [85], and K. Alvi [58], who showed that it gives rise to a v^8 correction to the quadrupole formula: $\dot{E}^{\rm eh}/\dot{E}_Q = v^8 = \dot{L}^{\rm eh}/\dot{L}_Q$, where $v = p^{-1/2} = (M/r_p)^{1/2}$ is the orbital velocity. The time-domain method allows black hole absorption to be calculated for arbitrary geodesics. In particular, for circular orbits our results show that even when $v \sim 0.4$ and the particle travels in a region of strong gravitational field, the amount of energy and angular momentum absorbed by the black hole is always a small correction to the total fluxes. For highly relativistic motion, this never grows large enough to contribute more than 0.4% of the total fluxes (see left panel of Fig. 5.4). For the purpose of calculating total fluxes with an overall accuracy of 1%, black hole absorption can safely be ignored. The right panel displays the ratio of horizon fluxes to the fluxes at infinity, normalized by $(M/r_p)^4$, the weak-field and slow-motion approximation. As expected for circular motion, the normalized ratio for energy and angular momentum are equal to each other, and they approach 1 for large p.

We estimate the accuracy with which black hole absorption can be determined using the time-domain method to be 5%. This estimate is based on the following argument. For small amplitude modes, the accuracy with which their contribution to the total fluxes can be determined is limited by errors originating from the discretization of Eq. (3.12) and Eq. (3.13) and the finite stepsize used in the numerical evolution. Based on the accuracy of the $l = 4$ and $m = 1$ mode for $p = 46.062$ in Table 5.1, the error is seen to be $\lesssim 5\%$ for modes whose contribution is ten orders of magnitude smaller than the dominant mode. For the range of p values considered in this paper, black hole absorption is at most seven orders of magnitude smaller than the dominant contribution. (This is evaluated using the $(M/r_p)^4$ relation at

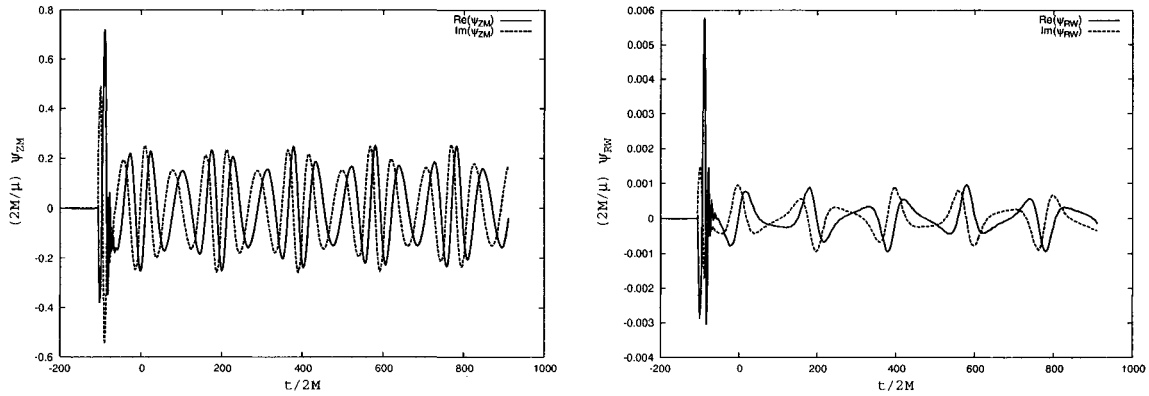

Figure 5.5: The Zerilli-Moncrief (left, $l = 2, m = 2$) and Regge-Wheeler (right, $l = 2, m = 1$) functions for $p = 12$ and $e = 0.2$. As in the case of circular orbits, early times are dominated by the initial data content.

$r_p = 50M$, the value at which black hole absorption is least significant.) It is then safe to assume that fluxes through the event horizon are determined with an accuracy $< 5\%$. (For values of p close to $6 + 2e$, black hole absorption is more important and therefore more accurately determined.)

5.3.4 Eccentric orbits

For eccentric orbits, $0 < e < 1$, and the radial motion is bounded by the periastron $r_p|_{\min} = pM/(1 + e)$ and the apastron $r_p|_{max} = pM/(1 - e)$. In Fig. 5.5 and Fig 5.6 we display waveforms for two cases: $p = 12$ and $e = 0.2$, as well as $p = 7.801$ and $e = 0.9$.

This type of orbital motion generates gravitational waveforms that are different in nature and in frequency content from circular orbits. Rather than being emitted uniformly along the orbit, the radiation is now emitted preferably at periastron. As the eccentricity increases the radiation is emitted in short bursts occurring near periastron. In these situations a time-domain approach is far more efficient than a

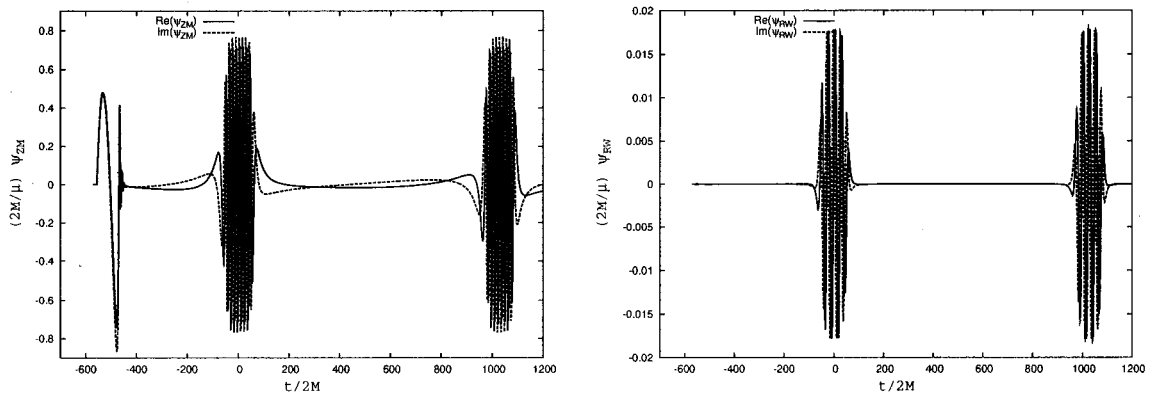

Figure 5.6: The Zerilli-Moncrief (left, $l = 2, m = 2$) and Regge-Wheeler (right, $l = 2, m = 1$) functions for $p = 7.801$ and $e = 0.9$. As in the case of circular orbits, early times are dominated by the initial data content. The radiation occurs in short bursts when the particle approaches the periastron. This is typical of the zoom-whirl behaviour studied in [81].

frequency-domain approach. The reason is that in order to correctly calculate the waveforms in the frequency domain, a large number of individual frequencies (harmonics of the radial and azimuthal frequencies) are required, and summing over them can be hugely expensive. By contrast, a time-domain method handles all frequencies simultaneously.

The fluxes are calculated over a number of wave cycles according to

$$< \dot{E} > \; = \; \frac{1}{T} \int_0^T \dot{E} \; dt, \tag{5.15}$$

where T is a few radial periods; a similar expression holds for $< \dot{L} >$. To obtain a quantitative idea of the relative accuracy of the time-domain method for eccentric orbits, we compute the fluxes for two points in the p-e plane and compare our calculations with Cutler *et al.* [80]: i) $p = 7.50478$ and $e = 0.188917$, and ii) $p = 8.75455$ and $e = 0.764124$. The results are displayed in Table 5.2. For small eccentricities, e.g. case (i), the agreement is similar to the agreement achieved for circular orbits. For large eccentricities, e.g. case (ii), the agreement is $\sim 2\%$. Because eccentric orbits

Table 5.2: Comparison of averaged fluxes for eccentric orbits with Cutler *et al.* for two points in the p-e plane [80]. The two cases presented are: i) $p = 7.50478$ and $e = 0.188917$, and ii) $p = 8.75455$ and $e = 0.764124$.

	case		Cutler *et al.*	time domain	rel. diff.
i)	$p = 7.50478$	$< \dot{E} >$	3.1680e-04	3.1770e-04	0.3%
	$e = 0.188917$	$< \dot{L} >$	5.9656e-03	5.9329e-03	0.5%
ii)	$p = 8.75455$	$< \dot{E} >$	2.1008e-04	2.1484e-04	2.3%
	$e = 0.764124$	$< \dot{L} >$	2.7503e-03	2.7932e-03	1.6%

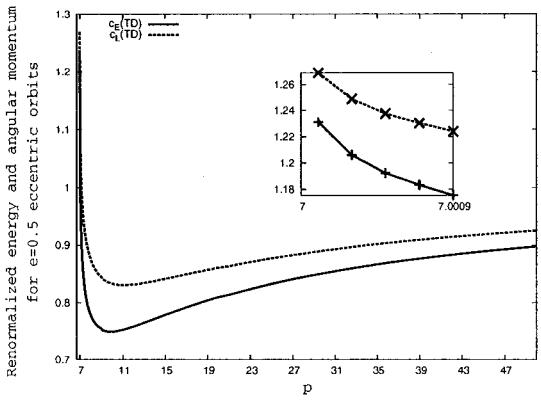

Figure 5.7: Coefficients c_E and c_L for the total energy and angular momentum radiated as functions of p for $e = 0.5$ eccentric orbits. Near the last stable orbit ($p = 7$), c_E approaches 1.24, while c_L approaches 1.26.

of the Schwarzschild spacetime are characterized by two incommensurate frequencies, the gravitational waveforms are quasi-periodic. By working in the frequency domain, Cutler *et al.* were able to formally average their fluxes over an infinite time. It is not, of course, possible to perform such an average in the time domain. Rather, for high eccentricities, the fluxes are averaged over a limited number of radial cycles (~ 3). This difference in averaging the fluxes is the most likely source of disagreement between time-domain and frequency-domain calculations for case (ii). For case (i), this is not as much of an issue, since the radial period is short enough to allow the time average to be performed over 10 cycles or more.

Finally, we calculate the total energy and angular momentum emitted during one radial period as functions of p for $e = 0.5$. We express the total energy and angular momentum radiated to infinity, as calculated from the time domain code, as

$$\begin{aligned} E_{GR}(p,e) &= c_E\left[E_Q(p,e) + (N-1)E_Q(p/(1+e),0)\right], \\ L_{GR}(p,e) &= c_L\left[L_Q(p,e) + (N-1)L_Q(p/(1+e),0)\right], \end{aligned} \tag{5.16}$$

where we use $E_{GR} = P(p,e) < \dot{E} >$, $P(p,e)$ is the radial period of the orbit obtained by integrating Eq. (5.3) over $0 \leq \chi \leq 2\pi$, $< \dot{E} >$ is given by Eq. (5.15), $N = N(p)$ is given by Eq. (5.5) with $e = 0.5$, $\dot{E}_Q(p,e)$ and $\dot{L}_Q(p,e)$ are given by Eq. (5.12), and c_E and c_L are parameters that stay close to 1 for all values of p. In Fig. 5.7 we display c_E and c_L as functions of p for $e = 0.5$. The coefficient c_E is close to 0.9 for large p and approaches 1.24 for p near 7. Similarly, the coefficient c_L stays close to 0.95 for large p and approaches 1.26 for p near 7. The formulae above for the total energy and angular momentum radiated by a particle in an eccentric orbit are justified by the fact that they have the correct limiting behaviour both for p large and for $p \to 6+2e$. For large p, the total energy and angular momentum radiated by a particle on an eccentric orbit are well approximated by the quadrupole formulae given by Eq. (5.10). In this limit, $N \to 1$ and Eq. (5.16) produces the correct approximate energy and angular momentum radiated. When $p \to 6 + 2e$, the particle orbits the black hole for a number $N - 1$ of quasi-circular orbits whose radius is equal to the periastron radius $r_p = Mp/(1+e)$. In this limit N is large and the second term of Eq. (5.16) dominates the energy and angular momentum radiated. This term corresponds to the energy and angular momentum radiated during $N - 1$ such quasi-circular orbits

The frequency of the radiation emitted by the orbiting particle increases as the

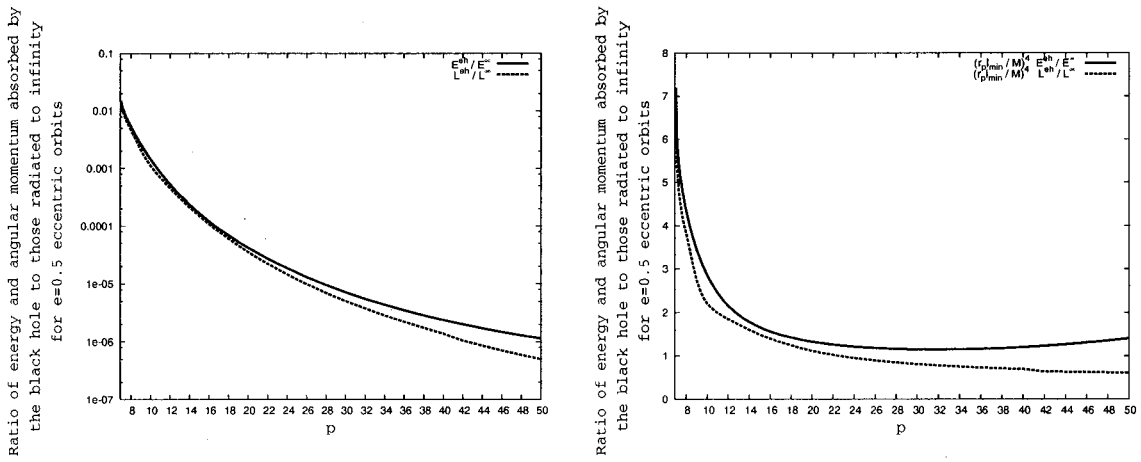

Figure 5.8: Black hole absorption for a particle in an $e = 0.5$ eccentric orbit. The absorption of both energy and angular momentum is negligible until the particle reaches $p \approx 7.3$, at which point it amounts to approximately $1 \sim 2\%$ of the total fluxes; these are eccentric orbits whose periastron is smaller than $4.9M$. The right panel displays the same ratio normalized by $(M/r_p|_{\rm min})^4$.

periastron of the orbit becomes smaller. Since for a given eccentricity e, the periastron is proportional to p, the frequency of the radiation increases with decreasing p. Because the potential barrier around the Schwarzschild black hole is less opaque to high-frequency gravitational waves [86], we expect an increase in black hole absorption with a decrease in p. This is confirmed numerically for $e = 0.5$ and displayed in Fig. 5.8. For $p \lesssim 7.3$ ($r_p \approx 4.9M$), the absorption of energy and angular momentum by the black hole amounts to more than 1% of the total fluxes, while for $p \gtrsim 7.3$ it contributes less than 1% and can be ignored when determining the total fluxes. In the right panel of the figure, we display black hole absorption for $e = 0.5$, normalized by $(M/r_p|_{\rm min})^4$, where $r_p|_{\rm min} = Mp/(1+e)$ is the periastron distance. This is the correction expected from black hole absorption for a particle on a *circular* orbit at $r_p|_{\rm min}$. We use this normalization here because black hole absorption for generic orbits has not been calculated analytically. For large p, black hole absorption for $e = 0.5$ does not seem to converge toward the slow-motion and weak-field approximation for

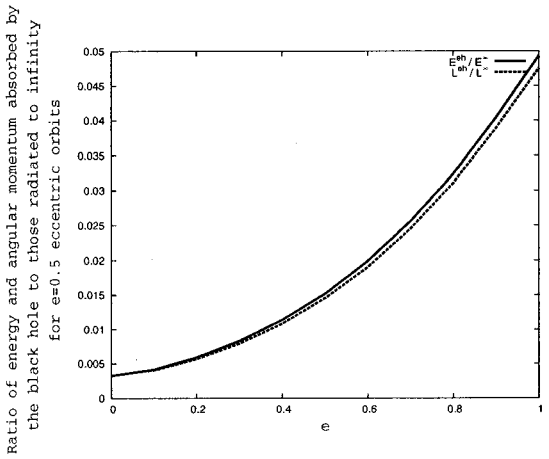

Figure 5.9: Displayed are $E^{\rm eh}/E^{\infty}$ and $L^{\rm eh}/L^{\infty}$ as functions of eccentricity along the curve $p = 6.001 + 2e$. Because of the decrease in periastron distance with increasing e, black hole absorption increases with e. A good approximation to these curves is given by $E^{\rm eh}/E^{\infty} = L^{\rm eh}/L^{\infty}(1 + 14e^2)\left(E^{\rm eh}/E^{\infty}\right)|_{e=0}$.

circular orbits. The normalized energy stays above 1, while the normalized angular momentum curve stays below 1. But because the relation $dE = \Omega dL$ used in deriving black hole absorption for circular orbits does not hold in general, there is no reason to believe that $(M/r_p|_{\rm min})^4$ should hold for generic orbits. Determining the differences in black hole absorption due to a finite eccentricity in a weak-field and slow-motion approximation would require a more detailed analysis than ours, since it is in this regime that our determination of black hole absorption is the least accurate.

For radiation emitted by a particle whose orbital parameters are $p = 6 + 2e$ and $0 \leq e \leq 1$, the argument relating black hole absorption to the orbital separation suggests that black hole absorption should be an increasing function of e along the line $p = 6+2e$ ($r_p|_{\rm min}$ is a decreasing function of e along this line). It then comes as no surprise that numerical results displayed in Fig. 5.9 support this assertion (we used $p = 6.001 + 2e$). Along this line, the radiation is emitted principally at periastron, where the orbit is quasi-circular. The relation $dE = \Omega dL$, where $\Omega = (M/r_p|_{\rm min})^{1/2}$ is the angular velocity of a particle on a circular orbit at $r_p|_{\rm min}$, holds approximately

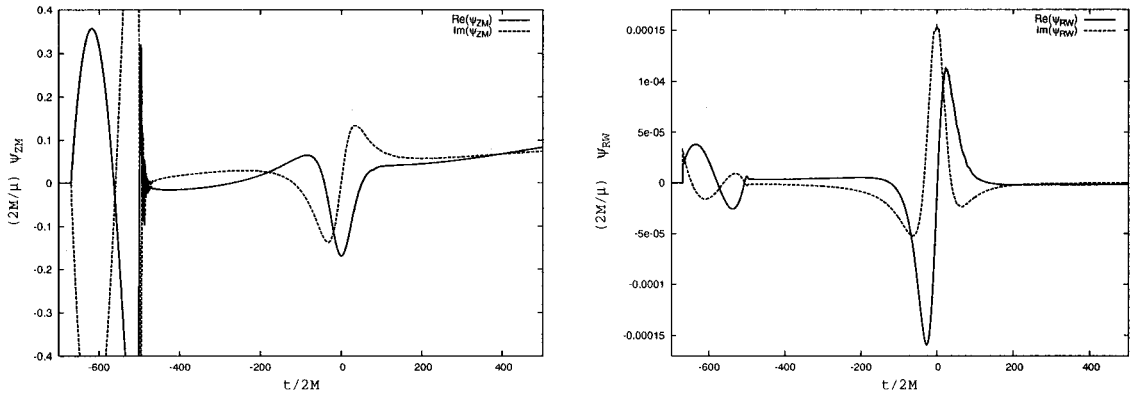

Figure 5.10: Displayed are $\psi_{\rm ZM}$ (left, $l = 2, m = 2$) and $\psi_{\rm RW}$ (right, $l = 2, m = 1$) as functions of time for $e = 1$ and $p = 40$. As in the case of circular orbits, early times are dominated by the initial data content. Total energy and angular momentum are calculated between $-300 \leq t/2M \leq 300$.

and we find $E^{\rm eh}/E^{\infty} \approx L^{\rm eh}/L^{\infty}$.

5.3.5 Parabolic orbits

Particles on a parabolic trajectory have $e = 1$ (equivalently $\tilde{E} = 1$), and p specifies the value of the periastron: $r_p|_{\rm min} = Mp/2$ with $p > 8$. For large values of p, the particle does not spend much time around $r_p|_{\rm min}$, the position where the radiation is maximum; the waveforms have a simple structure around $t = 0$, time at which the radiation emitted at $r_p|_{\rm min}$ reaches an observer at $r^*_{\rm obs}$. This is displayed for even and odd modes in Fig. 5.10. In contrast, when p approaches its minimum value ($p_{\rm min} \gtrsim 8$), the particle circles the black hole for a number N of cycles. Because N diverges at $p = 8$, we get the zoom-whirl behaviour displayed in Fig. 5.1 [81]. The quasi-circular nature of the motion when r_p approaches $r_p|_{\rm min}$ results in a number of oscillations in the waveforms; these occur near $t = 0$ for the observer at $r^*_{\rm obs}$, and are displayed in Fig. 5.11 for $p = 8.001$.

In similarity with eccentric orbits, we express the numerically calculated energy

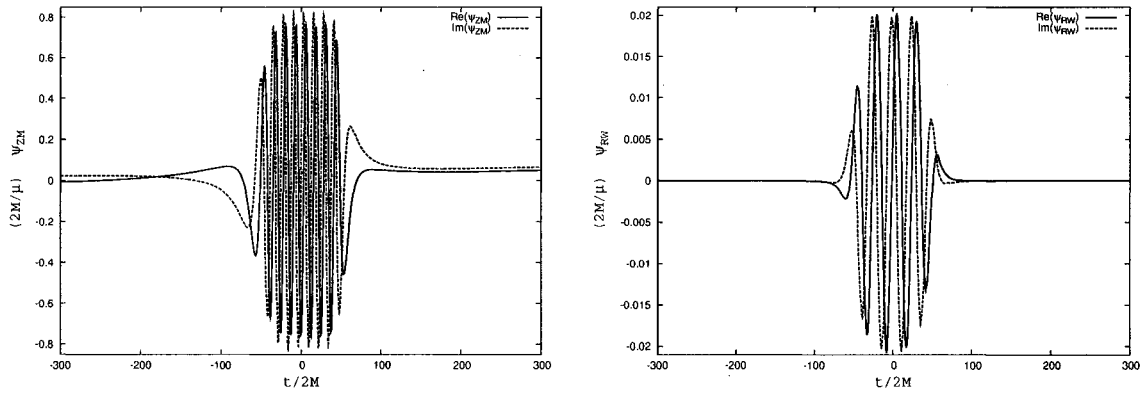

Figure 5.11: Displayed are $\psi_{\rm ZM}$ (left, $l = 2, m = 2$) and $\psi_{\rm RW}$ (right, $l = 2, m = 1$) as functions of time for $e = 1$ and $p = 8.001$. Early times, where the choice of initial data dominates, are not displayed in order to make the $t = 0$ region clearly visible. The energy and angular momentum fluxes are integrated between $-300 \leq t/2M \leq 300$ to obtain the total energy and angular momentum radiated.

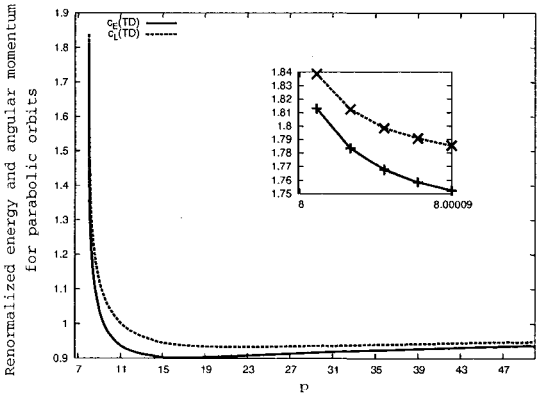

Figure 5.12: Coefficients c_E and c_L for the total energy and angular momentum radiated as functions of p for parabolic orbits. Near $p = 8$, c_E approaches 1.81 while c_L approaches 1.84.

and angular momentum radiated as

$$\begin{aligned} E_{GR}(p,1) &= c_E\left[E_Q(p,1)+(N-1)E_Q(p/2,0)\right], \\ L_{GR}(p,1) &= c_L\left[L_Q(p,1)+(N-1)L_Q(p/2,0)\right], \end{aligned} \tag{5.17}$$

where $N = N(p)$ is given by Eq. (5.5) with $e = 1$, $\dot{E}_Q(p,1)$ and $\dot{L}_Q(p,1)$ are given by Eq. (5.12), and c_E and c_L are again parameters that stay close to 1 for all p. For parabolic orbits, the total energy and angular momentum are computed using Eqs. (5.8) and (5.9) as

$$\begin{aligned} E^{\infty}_{GR} &= \int_{-T}^{T} \dot{E}^{\infty}\, dt, \\ L^{\infty}_{GR} &= \int_{-T}^{T} \dot{L}^{\infty}\, dt, \end{aligned} \tag{5.18}$$

for T large (we used $T = 300(2M)$). In Fig. 5.12, we display c_E and c_L for parabolic orbits. These quantities are close to 1 for large p, but increase above 1 as p approaches 8. Near this value of p, c_E reaches 1.81. We find a similar behaviour for c_L: near $p \gtrsim 8$ it reaches 1.84. As for eccentric orbits, we find that for large p the energy and angular momentum approach the values given by the quadrupole approximation, but for p close to $6+2e$ they are close to the values obtained for $N-1$ circular orbits of radius $r_p|_{\min} = Mp/(1+e)$.

The argument given previously for eccentric orbits holds true for parabolic orbits: when $p \gtrsim 8$ black hole absorption is more important than for circular or eccentric orbits (see Fig. 5.9). Our numerical results show that for $p > 10$, $E^{\rm eh}$ and $L^{\rm eh}$ account for less than 1% of the total energy and angular momentum radiated, while for $p \lesssim 10$ they can contribute as much as 5% of the total amounts (see Fig. 5.13). Hence, for $p \lesssim 10$, black hole absorption contributes a few percents of the total energy and angular momentum radiated and needs to be included in an accurate computation.

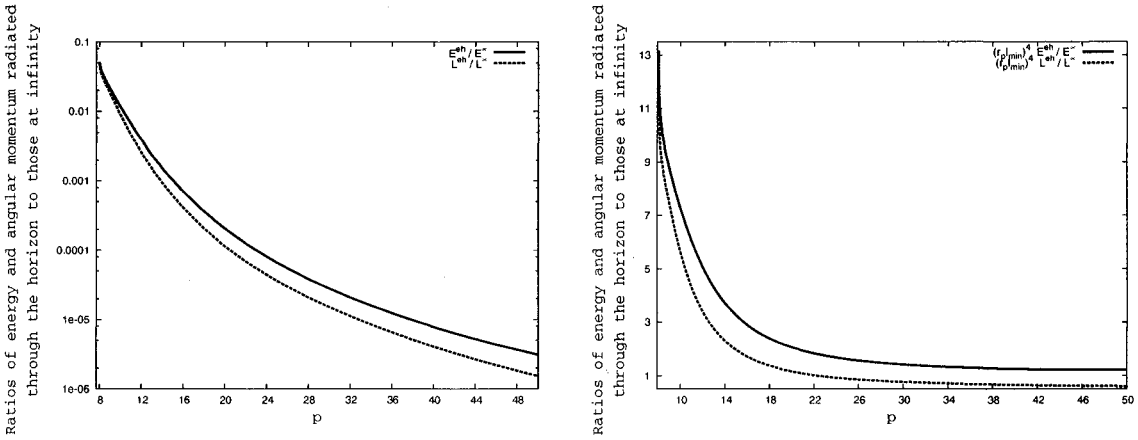

Figure 5.13: Black hole absorption for a particle following a parabolic geodesic. The absorption of both energy and angular momentum is negligible until the particle reaches $p \approx 10$ or $r_p|_{\rm min} \approx 5M$. The right panel displays the same ratio normalized by $(M/r_p|_{\rm min})^4$, where $r_p|_{\rm min}$ is the radius at periastron. Again, this factor is meaningful only for circular orbits, and is used only to illustrate the behaviour of black hole absorption as a function of p.

Black hole absorption is not determined as accurately as the energy and angular momentum radiated to infinity, but the error we make in evaluating it is never large enough to spoil our goal of $\sim 1\%$ overall accuracy.

For completeness, in Table 5.3 we display $E_{GR}^{\infty,\rm eh}$ and $L_{GR}^{\infty,\rm eh}$, the total energy and angular momentum radiated to infinity and through the event horizon, as returned by the time-domain code, for a wide range of p values. Based on the accuracy obtained for circular and eccentric orbits, we estimate that the total energy and angular momentum lost to gravitational waves are calculated to a relative accuracy of $1 \sim 2\%$. The actual accuracy is likely to be close to the accuracy achieved for circular orbits. The reason for this is quite simple. For parabolic orbits, there is no issue of performing a time-average, since the particle passes through periastron only once and we calculate the total energy for that motion.

Table 5.3: Total energy and angular momentum radiated by a particle orbiting a Schwarzschild black hole in a parabolic orbit. As usual, E^{∞}_{GR} and L^{∞}_{GR} denote the energy and angular momentum radiated to infinity, while $E^{\rm eh}_{GR}$ and $L^{\rm eh}_{GR}$ are the energy and angular momentum absorbed by the black hole. The black hole absorption contributes less than 1% when $p \gtrsim 10$: for parabolic orbits with periastron smaller than $5M$, black hole absorption contributes a significant amount to the total energy and angular momentum radiated.

p	E^{∞}_{GR}	$E^{\rm eh}_{GR}$	L^{∞}_{GR}	$L^{\rm eh}_{GR}$
8.00001	3.6703E+00	1.8876E-01	3.0133E+01	1.5208E+00
8.001	2.2809E+00	1.1260E-01	1.9088E+01	9.1166E-01
8.201	7.1130E-01	2.6586E-02	6.6010E+00	2.2142E-01
8.401	5.1740E-01	1.6534E-02	5.0433E+00	1.4244E-01
8.601	4.0970E-01	1.1376E-02	4.1665E+00	1.0148E-01
8.801	3.3767E-01	8.1988E-03	3.5706E+00	7.5175E-02
9.0	2.8419E-01	6.0880E-03	3.1196E+00	5.7026E-02
9.2	2.4409E-01	4.6044E-03	2.7756E+00	4.3891E-02
9.4	2.1228E-01	3.5352E-03	2.4973E+00	3.4211E-02
9.6	1.8644E-01	2.7473E-03	2.2665E+00	2.6951E-02
9.8	1.6506E-01	2.1565E-03	2.0718E+00	2.1428E-02
10.0	1.4712E-01	1.7072E-03	1.9048E+00	1.7176E-02
11.0	8.8979E-02	5.8626E-04	1.3320E+00	6.2819E-03
12.0	5.8467E-02	2.2778E-04	9.9827E-01	2.6152E-03
13.0	4.0567E-02	9.7321E-05	7.8158E-01	1.2036E-03
14.0	2.9303E-02	4.4999E-05	6.3136E-01	6.0123E-04
15.0	2.1774E-02	2.2273E-05	5.2088E-01	3.2171E-04
16.0	1.6636E-02	1.1675E-05	4.3867E-01	1.8241E-04
17.0	1.2978E-02	6.4484E-06	3.7499E-01	1.0869E-04
18.0	1.0303E-02	3.7241E-06	3.2454E-01	6.7569E-05
19.0	8.3029E-03	2.2354E-06	2.8383E-01	4.3565E-05
20.0	6.7794E-03	1.3882E-06	2.5047E-01	2.8990E-05
22.0	4.6735E-03	5.8355E-07	1.9949E-01	1.3895E-05
24.0	3.3426E-03	2.6965E-07	1.6280E-01	7.2550E-06
26.0	2.4638E-03	1.3447E-07	1.3549E-01	4.0539E-06
28.0	1.8620E-03	7.1373E-08	1.1459E-01	2.3931E-06
30.0	1.4374E-03	3.9949E-08	9.8213E-02	1.4781E-06
34.0	9.0223E-04	1.4201E-08	7.4534E-02	6.2832E-07
38.0	5.9799E-04	5.7886E-09	5.8484E-02	2.9873E-07
42.0	4.1455E-04	2.6163E-09	4.7168E-02	1.5469E-07
46.0	2.9763E-04	1.2887E-09	3.8849E-02	8.5683E-08
50.0	2.1993E-04	6.8343E-10	3.2550E-02	5.0118E-08

5.4 Summary

The time-domain method can produce waveforms and compute the associated fluxes of energy and angular momentum to a relative accuracy of a few percents. For circular orbits, the method is extremely reliable and produces fluxes with an overall accuracy of 1% or better over the whole range of p values explored. For eccentric orbits, the comparison with Cutler *et al.* [80] is spoiled by the difficulty of performing a time average of the fluxes over a sufficiently long time. Because the disagreement arises from the differences in time averaging, the time-domain method is still capable of producing accurate waveforms for highly eccentric motion. We stress here that the limitation is in the computation of the time-averaged fluxes, not in obtaining the waveforms. On the other hand, for geodesics with small eccentricities there is no such limitation and the time-domain results are in better agreement with those calculated by Cutler *et al.* [80]. In all cases, the time-domain method is capable of determining the fluxes accurately to $1 \sim 2\%$. Similar accuracy is obtained for the total energy and angular momentum radiated by a particle traveling on a parabolic orbit.

We also computed the absorption of energy and angular momentum by the black hole. For circular orbits with $p > 6$, this contribution can always be neglected, but not for orbits whose periastron is smaller than $5M$. For such orbits, black hole absorption contributes more than 1% of the total fluxes and cannot be ignored. We showed that for $e = 0.5$ it can constitute a correction as large as 2% to the total fluxes; for parabolic orbits the contribution increases to 5%.

Chapter 6

Integration of the Teukolsky equation in the time domain

6.1 Introduction

In previous chapters, we studied the perturbations of a Schwarzschild black hole and the gravitational waves produced by an orbiting particle. We now turn to the perturbations of a Kerr black hole.

Our study is limited to vacuum perturbations, but it constitutes a solid first step in constructing a numerical code that incorporates a source term contributed by a particle. This change is motivated by the fact that most astrophysical black holes are likely to be rotating [17], and that rotation affects the generation and the propagation of gravitational waves. Generation of gravitational radiation is affected because the motion of a particle around a Kerr black hole is different from its motion around a Schwarzschild black hole. Among other effects is the dragging of inertial frames that affects the particle: prograde and retrograde orbits differ in frequency. Propagation of gravitational radiation is affected mainly because of the difference in scattering

potentials between a Kerr and a Schwarzschild black hole. The most remarkable incarnation of these differences is the occurrence of super-radiant scattering [86, 87], which is for radiation the equivalent of the Penrose process for particles.

There is now a vast body of literature on the perturbations of a Kerr black hole, starting back with the work of S.A. Teukolsky. He first derived the master equation governing the curvature perturbations of a Kerr spacetime [18, 88, 89]. Since then, the Teukolsky equation has been integrated in a number of ways to study gravitational perturbations either in vacuum [87, 90, 91, 92, 93] or in the presence of a perturbing point particle. Most studies involving a point particle have been performed in the frequency domain [81, 94, 95, 96, 97, 98], but recently time domain methods have been suggested as a possible cost efficient alternative [99, 100].

There is currently a single numerical code available to integrate the inhomogeneous Teukolsky equation. It would be desirable to have access to *at least* another independent code. In cases where results from frequency domain methods are not available or inaccurate, this would provide a powerful way of cross-checking the numerical results. This chapter provides the first step in constructing a second numerical code capable of integrating the inhomogeneous equation: we develop a numerical method to accurately integrate the homogeneous Teukolsky equation. The method can be extended to include a source term contributed by an orbiting particle, but this is beyond the scope of this dissertation and will not be pursued here. We will restrict ourselves to comments on the possible ways the particle could be incorporated in the algorithm.

The chapter is divided as follows. We work in Boyer-Lindquist coordinates, and present the Teukolsky equation in Sec. 6.2. This section also lists some properties of the Teukolsky equation that are important in constructing our numerical method. In Sec. 6.3 we present all the details pertaining to the numerical algorithm. In Sec. 6.3.1

we present the time domain method for the integration of the Teukolsky equation. In many cases, direct discretization of the Teukolsky equation produced evolution algorithms that were unstable. Stability was achieved by the introduction of dissipative terms in the equation; this is explained in Sec. 6.3.1. In Sec. 6.3.2 we discuss the boundary conditions imposed on the Teukolsky function at the edges of the numerical grid, while Sec. 6.3.3 presents a convergence test of the numerical method. The remainder of the chapter contains two physical tests of the numerical code. First we show that in the absence of rotation the method reproduces the correct angular behaviour; this is done in Sec. 6.4.1. Then, in Sec. 6.4.2, we show that the method produces the correct quasi-normal modes of Schwarzschild and Kerr black holes. Finally, in Sec. 6.5 we discuss the extension of the method to include a point-particle as a source for the radiation field.

6.2 Perturbations of a Kerr black hole

The equation describing the gravitational perturbations of a Kerr black hole was first derived by S.A. Teukolsky [18] by studying the curvature perturbations of a Kerr black hole using the Newman-Penrose formalism. He also showed that the same equation governs the evolution of integer spin-fields, with the spin $|s| \leq 2$ of the field entering as a parameter. In the Newman-Penrose formalism, every tensorial quantity is expressed in terms of their projections along a null tetrad. The Teukolsky equation was derived with the use of the Kinnersley tetrad, which, in Boyer-Lindquist coordinates, is given by

$$\begin{aligned} l^\mu &= \frac{1}{\Delta}\left(r^2+a^2, \Delta, 0, a\right), \\ n^\mu &= \frac{1}{2\Sigma}\left(r^2+a^2, -\Delta, 0, a\right), \end{aligned}$$

$$m^{\mu} = \frac{\sqrt{2}}{2}\rho\left(\imath a\sin\theta, 0, 1, \imath\csc\theta\right), \tag{6.1}$$

where a is the angular momentum per unit mass of the black hole, $\Delta = r^2 - 2Mr + a^2$, $\Sigma = r^2 + a^2\cos^2\theta$, and $\rho = 1/(r - \imath a\cos\theta)$. The horizon of the black hole is located at $r = r_+ \equiv M + \sqrt{M^2 - a^2}$, the largest root of $\Delta = 0$. In the absence of rotation, $a = 0$, $\Delta = r^2 f$, $\Sigma = r^2$ and the tetrad vectors reduce to those introduced in Sec. 3.3.2.

For gravitational perturbations,

$$\begin{aligned} {}_2\psi &\equiv \Psi_0 = -C_{\mu\nu\alpha\beta} l^{\mu} m^{\nu} l^{\alpha} m^{\beta}, \\ {}_{-2}\psi &\equiv \rho^{-4}\Psi_4 = -C_{\mu\nu\alpha\beta} n^{\mu} \bar{m}^{\nu} n^{\alpha} \bar{m}^{\beta}, \end{aligned} \tag{6.2}$$

are the two complex tetrad components of the Weyl tensor $C_{\mu\nu\alpha\beta}$ encoding information about gravitational radiation at infinity (${}_{-2}\psi$) and at the horizon (${}_2\psi$). Both quantities vanish in the background Kerr spacetime and they are gauge invariant to first-order in the perturbation. They satisfy the Teukolsky equation, which, in Boyer-Lindquist coordinates, is

$$\begin{aligned} &\left[\frac{(r^2+a^2)^2}{\Delta} - a^2\sin^2\theta\right]\frac{\partial^2}{\partial t^2}\,{}_s\psi - \Delta^{-s}\frac{\partial}{\partial r}\left(\Delta^{s+1}\frac{\partial}{\partial r}\,{}_s\psi\right) + \frac{4Mar}{\Delta}\frac{\partial^2}{\partial t\partial\phi}\,{}_s\psi \\ &\quad -2s\left[\frac{a(r-M)}{\Delta} + \imath\frac{\cos\theta}{\sin^2\theta}\right]\frac{\partial}{\partial\phi}\,{}_s\psi - 2s\left[\frac{M(r^2-a^2)}{\Delta} - r - \imath a\cos\theta\right]\frac{\partial}{\partial t}\,{}_s\psi \\ &\quad -\csc\theta\frac{\partial}{\partial\theta}\left(\sin\theta\frac{\partial}{\partial\theta}\,{}_s\psi\right) + \left[\frac{a^2}{\Delta} - \csc^2\theta\right]\frac{\partial^2}{\partial\phi^2}\,{}_s\psi + \left(s^2\cot^2\theta - s\right){}_s\psi = S_T, \end{aligned} \tag{6.3}$$

where S_T is the source of the perturbation, and ${}_s\psi$ is the Teukolsky function. For $s = 0$ the Teukolsky equation governs the evolution of a scalar field, for $s = \pm 1$ it is associated with electromagnetic fields, and for $s = \pm 2$ it is the gravitational governs the evolution of gravitational perturbations.

A remarkable feature of the Teukolsky equation is that it is completely separable in the frequency domain. Solutions to the Teukolsky equation can then be found by

solving second-order ordinary differential equations. In the time domain, however, the equation is not separable. The dependence of ${}_s\psi$ on ϕ can be separated, but the θ and r variables stay coupled. We express the Teukolsky function as

$$ {}_s\psi \;=\; \frac{\Delta^{-s}}{r} \sum_{m=-\infty}^{\infty} e^{im\phi}\, {}_s\psi_m(t,r,\theta), \tag{6.4} $$

where the factor of Δ^{-s}/r is introduced to account for the behaviour of outgoing modes in the radiation zone and of ingoing modes near the horizon. Indeed a simple expansion in inverse powers of r shows that the solution of Eq. (6.3) for large r is [87]

$$ \lim_{r\to\infty} {}_s\psi \sim r^{-(2s+1)}. \tag{6.5} $$

Similarly, radiation at the horizon is physically required to be purely ingoing. Expanding Eq. (6.3) in powers of Δ, we get that

$$ \lim_{r\to r_+} {}_s\psi \sim \Delta^{-s}. \tag{6.6} $$

By removing Δ^{-s}/r, we get that ${}_s\psi_m$ is $\mathcal{O}(1)$ in both limits for any s. This property is convenient for the development of a numerical method to integrate the Teukolsky equation for arbitrary spin values. Also, we note here that the coordinate ϕ diverges as the horizon is approached along ingoing null rays:

$$ n^\mu \frac{\partial}{\partial x^\mu}\phi = \frac{a}{\Delta}, $$

which is singular at $\Delta = 0$. When solving the Teukolsky equation, we use the tortoise coordinate $r^* = \int (r^2+a^2)/\Delta \; dr$ and any coordinate singularity at the horizon is pushed back to $r^* \to -\infty$.

In a frequency domain approach, separation of variables goes one step further and we would decompose ${}_s\psi_m$ as

$$ {}_s\psi_m = \int_{-\infty}^{\infty} d\omega \; e^{-i\omega t}\, {}_sR(\omega,r) \;\; {}_s\Theta(a\omega,\theta), \tag{6.7} $$

where ${}_sR(\omega, r)$ and ${}_s\Theta(a\omega, \theta)$ are functions satisfying second-order ordinary differential equations. The disadvantage of this approach is that, contrary to what happens in spherical symmetry, both ${}_sR(\omega, r)$ and ${}_s\Theta(a\omega, \theta)$ depend on ω. To construct the Teukolsky function from Eq. (6.7), both the radial and angular functions need to be obtained by solving a second-order ordinary differential equation. Difficulties are encountered when the parameter $a\omega$ is large and when a large number of frequencies are required. For example, a particle in highly eccentric motion inclined with respect to the equatorial plane of the black hole generates radiation that contains three fundamental frequencies (radial, azimuthal and polar), as well as multiple harmonics of each individual frequency. An accurate reconstruction of ${}_s\psi_m$ is difficult in those cases. Instead of pursuing this approach, we stop at Eq. (6.4) and numerically solve the resulting two-dimensional partial differential equation.

Inserting Eq. (6.4) into Eq. (6.3), we find that ${}_s\psi_m$ satisfies

$$\left[\frac{\partial^2}{\partial t^2} - d_0\frac{\partial}{\partial t} - d_1\frac{\partial^2}{\partial r^{*2}} - d_2\frac{\partial}{\partial r^*} - \pi^2 d_3\frac{\partial^2}{\partial \theta^2} - \pi d_4\frac{\partial}{\partial \theta} - d_5\right]{}_s\psi_m \;=\; S_T^m, \quad (6.8)$$

where the factors of π in front of d_3 and d_4 are introduced for later convenience,

$$S_T^m \;=\; \frac{r\Delta^{s+1}}{(r^2+a^2)^2}\int_0^{2\pi} d\phi\; e^{-\imath m\phi}\; S_T, \quad (6.9)$$

and

$$\begin{aligned}
c &= \left(1 - \frac{\Delta}{(r^2+a^2)^2}a^2\sin^2(\theta)\right)^{-1},\\
d_0 &= -c\left\{\frac{2s}{(r^2+a^2)^2}[r^2(r-3M)+a^2(r+M)] + \frac{2\imath a}{(r^2+a^2)^2}(2Mmr + s\Delta\cos(\theta))\right\},\\
d_1 &= c,\\
d_2 &= \frac{c}{r^2+a^2}\left[-2\frac{a^2\Delta}{r(r^2+a^2)} - 2s(r-M)\right],\\
d_3 &= \frac{c}{\pi^2}\frac{\Delta}{(r^2+a^2)},
\end{aligned}$$

$$
\begin{aligned}
d_4 &= \frac{c}{\pi}\frac{\Delta}{(r^2+a^2)}\cot(\theta), \\
d_5 &= -\frac{c}{(r^2+a^2)^2}\Big\{ -m^2a^2 + \Delta\frac{(m+s\cos(\theta))^2}{\sin^2(\theta)} - \Delta\Big[s\left(1-\frac{2M}{r}\right) - \frac{2}{r^2}(Mr-a^2)\Big]\Big\} \\
&+ 2s\,\imath\,c\,ma\frac{(r-M)}{(r^2+a^2)^2}.
\end{aligned} \tag{6.10}
$$

In Sec. 6.3.2 we will need the behaviour of ${}_s\psi_m$ near the rotation axis. This can be determined by expanding Eq. (6.8) in powers of $\sin\theta$. It is then found that [101]

$$
{}_s\psi_m \approx \sin^{|m\pm s|}(\theta)\Big[q_0(t,r) + q_2(t,r)\sin^2(\theta) + \mathcal{O}\left(\sin^4(\theta)\right)\Big], \tag{6.11}
$$

where the upper (lower) sign applies to the field near $\theta = 0$ ($\theta = \pi$) and the exact dependence of the coefficients q_0 and q_2 on t and r is not needed. Note that unless $|m| = |s|$, ${}_s\psi_m$ vanishes on the axis.

Initial data for ${}_s\psi_m$ and its time derivative

In developing the numerical method, we will assume that $S_T^m \neq 0$, but that it is a slowly varying function of t, r and θ. This condition is obviously not satisfied by a singular source term such as produced by a point particle. And although we shall develop a general method, in all applications presented in this chapter we shall set $S_T^m = 0$. We shall thus be looking at the evolution of a pulse of gravitational waves starting from a prescribed initial profile.

The Teukolsky equation is second-order in time and a unique solution is selected by specifying initial data for ${}_s\psi_m$ and $\partial\,{}_s\psi_m/\partial t$ at $t = 0$. These initial conditions are completely arbitrary and we choose the initial configuration to be that of a Gaussian pulse that is outgoing when $a = 0$, i.e initially $(\partial/\partial v)\,{}_s\psi_m = 0$ ($v = t + r^*$). For all choices of black hole rotational parameter, we also choose the initial perturbation to be proportional to a spin-weighted spherical harmonic. For $a > 0$, there is nothing

special about this choice, but when $a = 0$ these harmonic functions are eigenfunctions of the Teukolsky equation and are a natural choice. Our initial data therefore consists of

$$\begin{aligned} {}_s\psi_m(r^*,\theta) &= e^{-\frac{(r^*-r_c^*)^2}{2\sigma^2}}\, {}_sY^{lm}(\theta,0), \\ \frac{\partial}{\partial t}\,{}_s\psi_m(r^*,\theta) &= -\frac{\partial}{\partial r^*}\,{}_s\psi_m(r^*,\theta), \end{aligned} \tag{6.12}$$

where r_c^* is the centre of the Gaussian pulse, σ its width, and ${}_sY^{lm}$ are the spin-weighted spherical harmonics. In our numerical simulations, we used $s = -2$ and $l = 2$ for which the ${}_sY^{lm}$ are

$$\begin{aligned} {}_{-2}Y^{20}(\theta,0) &= C_0 \sin^2\theta, \\ {}_{-2}Y^{21}(\theta,0) &= C_1 \sin\theta\,(1+\cos\theta)\,, \\ {}_{-2}Y^{22}(\theta,0) &= C_2\left(\frac{1}{4}+\frac{1}{2}\cos\theta+\frac{1}{4}\cos^2\theta\right), \end{aligned} \tag{6.13}$$

where the C_i's are normalization factors.

6.3 Numerical method

6.3.1 Modified Lax-Wendroff method

We now present the numerical method we developed to numerically integrate the Teukolsky equation for arbitrary values of the spin s.

The integration of a partial differential equation is simplified by introducing auxiliary fields whose purpose is to transform the original equation into a system of coupled first-order (in time) partial differential equations. To this end we introduce $A = {}_s\psi_m$ and $B = (\partial/\partial t)\,{}_s\psi_m$, in terms of which the Teukolsky equation reads

$$\frac{\partial}{\partial t}A = B,$$

$$\frac{\partial}{\partial t}B = d_0 B + d_1 \frac{\partial^2}{\partial x^2}A + d_2 \frac{\partial}{\partial x}A + d_3 \frac{\partial^2}{\partial y^2}A + d_4 \frac{\partial}{\partial y}A + d_5 A + S_T^m, \quad (6.14)$$

where t is scaled by $2M$ and is a dimensionless variable, $x \equiv r^*/2M$, $y = \theta/\pi$, and the dimensionless coefficients d_k are obtained by setting $M = 1/2$ in Eq. (6.10).

The numerical grid covers a finite region of two-dimensional space given by $0 \leq y \leq 1$ and $x_{\rm EH} \leq x \leq x_{\rm S}$, where $x_{\rm EH}$ approximates the event horizon, and $x_{\rm S}$ approximates spatial infinity. The three dimensions are discretized as

$$\begin{aligned} x_i &= x_{\rm EH} + (i-1)\Delta x, \qquad 1 \leq i \leq N_x, \\ y_j &= (j-1)\Delta y, \qquad 1 \leq j \leq N_y, \\ t_n &= n\Delta t \qquad 0 \leq n \leq N_t, \end{aligned} \quad (6.15)$$

where Δx, Δy, and Δt are the discretization stepsizes, N_x, N_y and N_t are the number of points in each dimension. We use the shorthand notation $A^n_{i,j} \equiv A(t_n, x_i, y_j)$ and $B^n_{i,j} \equiv B(t_n, x_i, y_j)$ for the fields at each grid point.

In the region of spacetime covered by the numerical grid, we solve Eq. (6.14) for $A^n_{i,j}$ and $B^n_{i,j}$ by approximating partial derivatives with centered differences. This type of approximation cannot provide evolution equations for field points located on the edges of the grid, i.e. $A^n_{1,j}$, $B^n_{1,j}$, $A^n_{N_x,j}$, $B^n_{N_x,j}$, $A^n_{i,1}$, $B^n_{i,1}$, A^n_{i,N_y}, and B^n_{i,N_y}. Instead, we use the information given in Sec. 6.2 to impose appropriate boundary conditions on the boundary fields. This is discussed in detail in Sec. 6.3.2, and for the moment we assume that A and B are known on the edges of the grid at all times. The numerical algorithm has to provide evolution equations for interior points only, and starting from $A^0_{i,j}$ and $B^0_{i,j}$, the algorithm provides both fields at all times t_n up to t_{N_t}, the final time.

The numerical method proceeds in two steps. First we obtain A and B at an intermediate time step $t_{n+1/2}$ from their values at time t_n. Second, the fields at time

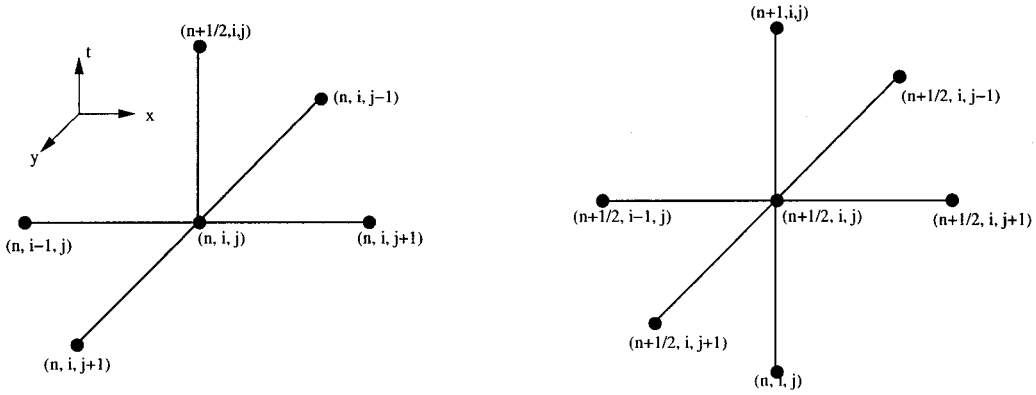

Figure 6.1: Depicted are the numerical cells used in solving Eq. (6.14). The first step is similar to a Lax step (left). The second step is a standard leapfrog step (right).

t_{n+1} are obtained from their values at times t_n *and* $t_{n+1/2}$. These are the two basic building blocks of our numerical method. The two grid cells associated with these steps are depicted in Fig. 6.1. The first step is similar to the first step of a standard Lax-Wendroff method (see for example [68]), but instead of evaluating $A^{n+1/2}_{i+1/2,j+1/2}$ and $B^{n+1/2}_{i+1/2,j+1/2}$, we determine $A^{n+1/2}_{i,j}$ and $B^{n+1/2}_{i,j}$. Nevertheless, because of the similarity, we refer to this step as a modified Lax step. The second step is a standard leapfrog step [68], just as in the original Lax-Wendroff method. We refer to our algorithm as a whole as a modified Lax-Wendroff method. To the knowledge of the author this modified version of the Lax-Wendroff method is presented here for the first time.

We now proceed with the discretization and introduce the finite-difference operators, δ_x, δ_x^2, δ_y, and δ_y^2. These operators are defined by their action on an arbitrary field C:

$$\begin{aligned} \delta_x C^n_{i,j} &= \frac{1}{2\Delta x}\Big[C^n_{i+1,j} - C^n_{i-1,j}\Big], \\ \delta_x^2 C^n_{i,j} &= \frac{1}{\Delta x^2}\Big[C^n_{i+1,j} - 2C^n_{i,j} + C^n_{i-1,j}\Big], \end{aligned} \tag{6.16}$$

and similar definitions hold for δ_y and δ_y^2. From these definitions and an elementary

application of Taylor expansion, it is easily established that substituting the discrete operators in place of the continuous partial derivatives produces an error proportional to the stepsize squared, i.e.

$$\begin{aligned}\frac{\partial}{\partial x}C(t_n, x_i, y_j) &= \delta_x C^n_{i,j} + \mathcal{O}(\Delta x^2), \\ \frac{\partial^2}{\partial x^2}C(t_n, x_i, y_j) &= \delta_x^2 C^n_{i,j} + \mathcal{O}(\Delta x^2),\end{aligned} \tag{6.17}$$

with similar expressions holding for δ_y and δ_y^2. This property is important because it determines the overall convergence rate of the numerical method.

To evolve the fields A and B forward in time, we need to approximate the time derivative appearing in Eq. (6.14). For the modified Lax step, we use

$$\frac{\partial}{\partial t}C^n_{i,j} = \frac{2}{\Delta t}\left[C^{n+1/2}_{i,j} - C^n_{i,j}\right] + \mathcal{O}(\Delta t^2). \tag{6.18}$$

and for the leapfrog step, we use

$$\frac{\partial}{\partial t}C^{n+1/2}_{i,j} = \frac{1}{\Delta t}\left[C^{n+1}_{i,j} - C^n_{i,j}\right] + \mathcal{O}(\Delta t^3). \tag{6.19}$$

Based on the leapfrog method for the wave equation in flat spacetime, we also use $B^{n+1/2}_{i,j} = 1/2(B^{n+1}_{i,j} + B^n_{i,j}) + \mathcal{O}(\Delta t^3)$ in the evolution equation for B while taking the leapfrog step [102].

Algebraically solving the discretized version of Eq. (6.14) for the field at $t_{n+1/2}$ yields, for the modified Lax step,

$$\begin{aligned}A^{n+1/2}_{i,j} &= A^n_{i,j} + \Delta t B^n_{i,j} + \mathcal{O}(\Delta t^2), \\ B^{n+1/2}_{i,j} &= \left(1 + \frac{\Delta t}{2}d_0\right)B^n_{i,j} + \frac{\Delta t}{2}\left[d_1\delta_x^2 + d_2\delta_x + d_3\delta_y^2 + d_4\delta_y + d_5\right]A^n_{i,j} \\ &+ \frac{\Delta t}{2}S^n_{i,j} + \mathcal{O}(\Delta t^2),\end{aligned} \tag{6.20}$$

and all the d_k's are evaluated at the central grid point (x_i, y_j). Once the fields A and B have been determined everywhere on the slice $t = t_{n+1/2}$, we can use the

approximations developed for the leapfrog step and obtain the field at time t_{n+1}. Using the discretization discussed, and solving for A^{n+1} and B^{n+1} yields, for the leapfrog step,

$$\begin{aligned} A_{i,j}^{n+1} &= A_{i,j}^{n-1} + \Delta t B_{i,j}^{n+1/2} + \mathcal{O}(\Delta t^3, \Delta t \Delta x^2, \Delta t \Delta y^2), \\ B_{i,j}^{n+1} &= \left(1 - \frac{\Delta t}{2} d_0\right)^{-1} \Bigg[\left(1 + \frac{\Delta t}{2} d_0\right) B_{i,j}^{n-1} \\ &+ \Delta t \Big(d_1 \delta_x^2 + d_2 \delta_x + d_3 \delta_y^2 + d_4 \delta_y + d_5 \Big) A_{i,j}^{n+1/2} \\ &+ \Delta t S_{i,j}^{n+1/2} \Bigg] + \mathcal{O}(\Delta t^3, \Delta t \Delta x^2, \Delta t \Delta y^2). \end{aligned} \tag{6.21}$$

Once the A^{n+1} and B^{n+1} have been computed, the fields at $t_{n+1/2}$ are discarded, and the procedure repeated to obtain the fields at t_{n+2}, and so on. Examining the modified Lax-Wendroff method, we see that after the leapfrog step the fields at t_{n+1} are inaccurate to order Δt^3. Because $A_{i,j}^{n+1}$ and $B_{i,j}^{n+1}$ are directly proportional to $A_{i,j}^{n}$ and $B_{i,j}^{n}$, respectively, field values at t_{n+1} inherit the error of their parent at t_n. The total error after the leapfrog step is then given by the sum of the errors from the parent field values and the truncation error. The total error then grows linearly with the number of steps taken. (We are assuming a fixed ratio between Δx and Δt, as well as between Δy and Δt.) After N_t steps, the error for the modified Lax-Wendroff method is $N_t \Delta t^3 \sim \Delta t^2$, and the method is second-order convergent. A similar argument shows that using only a modified Lax step would result in an algorithm with linear convergence.

Numerical viscosity and stability of the algorithm

From our discussion so far, it may seem as though solving partial differential equations is quite simple, but such is not the case. The discretized version of a partial

differential equation is only equivalent to the partial differential equation in the continuum limit. The discretized equation generally admits a larger class of solutions than the original equation. A consequence of this is the existence of exponentially growing solutions that are not solutions of the original equation, i.e. the discrete equation allows unstable modes to develop.

In the event where the coefficients of the partial differential equation are constant, a global stability analysis can provide conditions for the stability of the numerical method. Typically, this results in the stepsizes having to satisfy the Courant condition [68], i.e. information on the numerical grid should propagate faster than the physical speed of propagation. On the other hand, when the coefficients are not constant, a stability analysis is difficult to perform and does not provide information about global stability. It proves faster to numerically implement a candidate algorithm and look for growing modes.

The modified Lax-Wendroff method as it is presented in the last section, leads to the appearance of unstable modes. In general, reducing the time stepsize slowed the appearance of these modes, but this would not eliminate them completely[1]. The instabilities were eliminated by the addition of a small dissipative term in Eq. (6.14), i.e. we solved

$$\begin{aligned} \frac{\partial}{\partial t}A &= \{\ldots\} + D\Delta x^2 \frac{\partial^2}{\partial x^2}A, \\ \frac{\partial}{\partial t}B &= \{\ldots\} + D\Delta x^2 \frac{\partial^2}{\partial x^2}B, \end{aligned} \tag{6.22}$$

rather than the original equations, where $\{\ldots\}$ stands for the right-hand side of Eq. (6.14), and D is a diffusion coefficient. In principle, we could use two different diffusion coefficients for A and B, but, in practice, having a single diffusion coefficient

[1]Any method becomes stable if the ratios $\Delta x/\Delta t$ and $\Delta y/\Delta t$ are small enough. However, this is not a practical way to avoid exponentially growing modes.

yields good results. We chose the dissipative term to be proportional to Δx^2. This is of the same order as the truncation error made in approximating the partial derivatives, and it ensures that in the continuum limit, we recover the original Teukolsky equation.

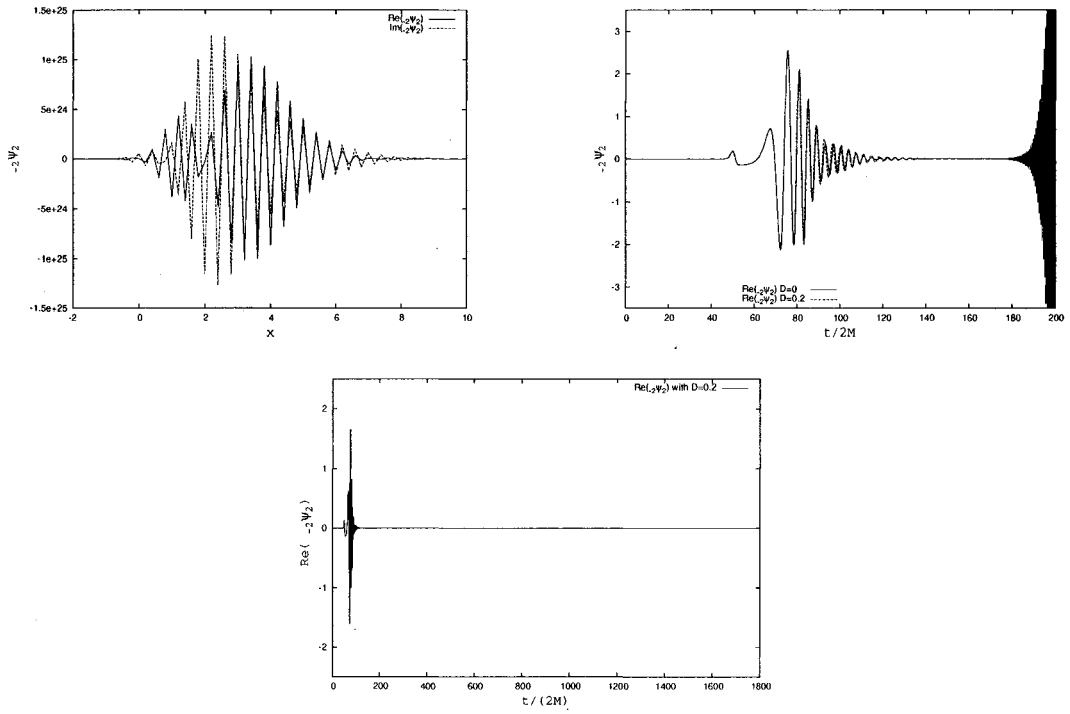

Figure 6.2: Teukolsky function obtained after evolving a pulse with $x_c = 10$, $\sigma = 1$, $s = -2$, and $m = 2$ for a time $t = 150(2M)$. The rotation parameter of the black hole is $a = 0.99M$, and we used $\Delta t = 0.025$, $\Delta x = 0.1$ and $\Delta y = 0.05$. The top left panel displays a spatial slice at $y = 0.5$ of the gravitational waveform at the final evolution time. In this case, the appearance of exponentially growing modes clearly points out the numerical instability of the algorithm. Addition of dissipation eliminates these instabilities. In the top right panel, we show waveforms as functions of time extracted at $x = 60$ and $y = 0.5$ for the same initial data. The solid line has $D = 0$, while the dashed curve has $D = 0.2$. Both waveforms are in good agreement, although the dissipative term has a small effect on the amplitude and the phase of the waveform. Around $t = 200(2M)$, unstable modes in the waveforms for $D = 0$ are clearly apparent. Bottom figure: with diffusion, the evolution proceeds for long times ($t < 1800(2M)$) without developing instabilities. (We used $\Delta t = 0.05$, $\Delta x = 0.2$ and $\Delta y = 0.1$ to reduce the computational time.)

In Fig. 6.2, we show the effect of adding a dissipative term to the discretized Teukolsky equation. We performed a simulation with $D = 0$ and $D = 0.2$, with

initial data given by $x_c = 10$, $\sigma = 1$, $s = -2$, and $m = 2$ in Eq. (6.12). The simulation was performed for a black hole with $a = 0.99M$. Without dissipation, unstable modes develop and dominate the numerical solution. The addition of a dissipative term stabilizes the algorithm, which can then be run for arbitrary long times. On the other hand, dissipation affects the amplitude and the phase of the waveforms and D must be chosen as small as possible. We found that $D = 0.2$ is large enough to eliminate unstable modes, while still producing waveforms accurate in amplitude and in phase compared with the waveforms obtained in the absence of diffusion. This is seen in the right panel of Fig. 6.2.

In practice, we find that the addition of dissipation stabilizes the numerical algorithm when $\Delta y \geq 2\Delta t$ and $\Delta x \geq 4\Delta t$. The most efficient choice of stepsizes is then given by $\Delta x = 2\Delta y = 4\Delta t$. With this choice of ratios for the stepsizes, the evolution can proceed for arbitrarily long times. In the bottom panel of Fig. 6.2, we show the real part of the $s = -2$ Teukolsky function for $a = 0.99M$ as a function of time extracted at $x = 60$ and $y = 0.5$. The evolution is stable for the entire simulation ($t < 1800(2M)$).

6.3.2 Boundary conditions

The modified Lax-Wendroff method does not provide evolution equations for the boundary points. In principle, the boundaries at $x = x_{\rm EH}$ and $x_{\rm S}$ can be pushed far enough that reflections from the boundaries cannot travel back into the region of interest (for example the region where the waveforms are extracted) by the time the simulation is stopped. This is a very costly way to reduce the impact of reflections. Instead, we use the information about the asymptotic behaviour of the Teukolsky function that was presented in Sec. (6.2). These approximate solutions can be used

to provide boundary conditions for A and B at the edges of the numerical grid, and this can be used to complete the method of integration.

In Eq. (6.4) we removed a factor of Δ^{-s}/r from ${}_s\psi$ to ensure that outgoing radiation modes at infinity and ingoing radiation modes at the horizon are both $\mathcal{O}(1)$. (To get this behaviour was the primary motivation for removing this factor.) For the boundary at $x_{\rm S}$, we have the approximate relation $A = A(u,\theta)$, which implies $\partial A/\partial v = 0$, or equivalently, $\partial A/\partial t = -\partial A/\partial x$. This is implemented as

$$A^{n+1}_{N_x,j} = A^{n+1}_{N_x-2,j} - 2\Delta x\ B^{n+1}_{N_x-1,j} + \mathcal{O}(\Delta x^3). \tag{6.23}$$

Similarly, near the horizon we have the approximate relation $A = A(v,\theta)$ and $\partial A/\partial u = 0$, which lead to

$$A^{n+1}_{1,j} = A^{n+1}_{3,j} - 2\Delta x\ B^{n+1}_{2,j} + \mathcal{O}(\Delta x^3). \tag{6.24}$$

Both boundary conditions can be imposed using information about A and B on a *single* time slice. Inspection of the modified Lax-Wendroff method reveals that values of B on the boundaries are never used in the evolution scheme of Eq. (6.20) and Eq. (6.21). We do not provide boundary values for B at $x_{\rm S}$ and $x_{\rm EH}$, because they do not propagate forward in time and are irrelevant.

Next, we obtain appropriate boundary conditions on the rotation axis. The behaviour of A is given in Eq. (6.11). Taking a time derivative of this equation yields a similar expansion for B (with q_0 and q_2 replaced by their time derivatives). The boundary conditions for both functions are then trivial if $|m| \neq |s|$, since $A^{n+1}_{i,1} = 0 = A^{n+1}_{i,N_y}$ and $B^{n+1}_{i,1} = 0 = B^{n+1}_{i,N_y}$ are exact boundary conditions. For $|m| = |s|$, A and B have non-zero values on the rotation axis. For $m = s$, the field and its time derivative vanish at $y_{N_y} = 1$, but not at $y_1 = 0$. In this case, the

boundary conditions are imposed as

$$A^{n+1}_{i,1} = \frac{-\sin^2(\pi y_3)\ A^{n+1}_{i,2} + \sin^2(\pi y_2)\ A^{n+1}_{i,3}}{\sin^2(\pi y_2) - \sin^2(\pi y_3)} + \mathcal{O}(\Delta y^4),$$
$$B^{n+1}_{i,1} = \frac{-\sin^2(\pi y_3)\ B^{n+1}_{i,2} + \sin^2(\pi y_2)\ B^{n+1}_{i,3}}{\sin^2(\pi y_2) - \sin^2(\pi y_3)} + \mathcal{O}(\Delta y^4), \qquad (6.25)$$

which represents a linear extrapolation from information at y_2 and y_3. For $m = -s$ the field vanishes at $y_1 = 0$, but not at $y_{N_y} = 1$. In this case, the boundary conditions are obtained from the formula above with the replacement $j = 1 \to N_y$, $j = 2 \to N_y - 2$, and $j = 3 \to N_y - 3$. Again the correct boundary conditions on the rotation axis are imposed using information on a single time slice.

In practice, we also need boundary conditions on A and B at $t_{n+1/2}$. Because the boundary conditions presented above rely on information on a single time slice, we can simply substitute $n + 1/2$ in place of $n + 1$ everywhere in Eq. (6.23), Eq. (6.24) and Eq. (6.25).

The boundary conditions are based on approximate asymptotic solutions of the Teukolsky equation. Because of the finite size of the grid, and because of the approximations involved, a certain amount of radiation is bound to be reflected from the edges of the numerical grid. The boundary conditions do not completely eliminate such reflections, but they strongly reduce their amplitude.

6.3.3 Convergence of the algorithm

We now discuss the convergence rate of our numerical method. Determining the convergence rate is done by fixing the ratios $\Delta x/\Delta t$ and $\Delta y/\Delta t$, and then comparing the results of simulations with different Δt. A more detailed discussion of this method is contained in Appendix C for the one-dimensional wave equation in a Schwarzschild spacetime.

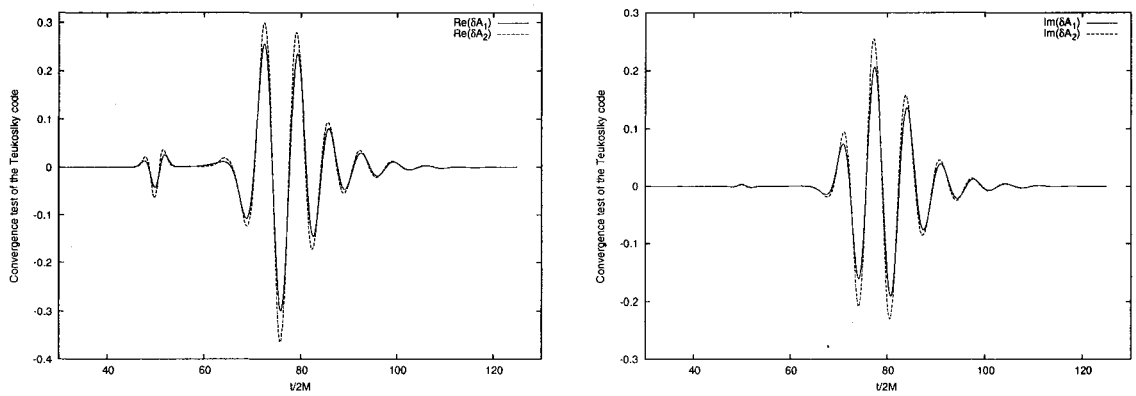

Figure 6.3: Convergence test of the numerical algorithm for the integration of the Teukolsky function with $a = 0.5M$. We show the difference between simulations with stepsizes $\Delta t = 0.05$ (A_1), $\Delta t = 0.025$ (A_2), and $\Delta t = 0.0125$ (A_4). The ratios of Δx and Δy to Δt are fixed for all three simulations. The two curves shown are $\delta A_1 \equiv A_1 - A_2$, and $\delta A_2 \equiv 4(A_2 - A_4)$. The fact that the two curves are close to each other in the interval displayed signals quadratic convergence. Left panel: Convergence test for the real part of the Teukolsky function. Right panel: convergence test for the imaginary part of the Teukolsky function.

In constructing the numerical algorithm, we neglected truncation errors of order Δt^3. As was previously discussed, the errors add up linearly so that after N_t steps, the error at each grid point is $\mathcal{O}(\Delta t^2)$. Examining the boundary conditions of Eq. (6.23) and Eq. (6.24), we see that both ingoing- and outgoing-wave boundary conditions generate an error term of order $\mathcal{O}(\Delta t^3)$, but these terms also accumulate linearly. The accumulated error from the boundary conditions, after N_t steps, is $\mathcal{O}(\Delta t^2)$, the same as the error from the evolution algorithm. Finally, the boundary conditions on the rotation axis are either exact or are given by Eq. (6.25). In the later case, the error is of order $\sin^4(\pi y) \approx \Delta y^4 \approx \Delta t^4$. This is much smaller than other contributions and can be ignored. After N_t steps, the largest error is $\mathcal{O}(\Delta t^2)$ and the method, including the boundary conditions, should converge quadratically.

According to the discussion of Appendix C, we can establish the convergence rate of the method by comparing three different simulations with stepsizes differing by

factors of 2. In Eq. (6.12), we set $x_c = 10$, $\sigma = 1$, $l = 2$, $m = 2$ and $s = -2$. We also choose the angular momentum of the black hole to be $a = 0.5M$ and the waveforms are extracted at $x = 60$ and $y = 0.5$.

For the first simulation, the stepsizes are $\Delta t = 0.05$, $\Delta x = 0.2$ and $\Delta y = 0.1$, the second simulation has $\Delta t = 0.025$, $\Delta x = 0.1$ and $\Delta y = 0.05$, and the third has $\Delta t = 0.0125$, $\Delta x = 0.05$ and $\Delta y = 0.025$. The first simulation is denoted by A_1, the second by A_2 and the third by A_4. In Fig. 6.3, we display $\delta A_1 \equiv A_1 - A_2$ and $\delta A_2 \equiv 4(A_2 - A_4)$, where the factor of 4 accounts for the factor of two between the stepsizes. The two curves directly measure the truncation error of the algorithm as a function of time. They are approximately equal to each other over the time interval ($t < 125(2M)$) and we conclude that the algorithm is converging quadratically. Note that although we started with real initial data, because $a \neq 0$ the imaginary part of the Teukolsky function grows during the evolution.

6.4 Physical tests of the numerical method

The results of the previous section show that the algorithm converges quadratically. The purpose of this section is to demonstrate that the method and its implementation reproduce well-known physical predictions of the Teukolsky equation. We show below that in the absence of rotation the numerical code reproduces the expected angular behaviour and that it outputs the correct quasi-normal modes of a Kerr black hole.

6.4.1 Angular profile of the solutions in the norotation limit

In the absence of rotation, the Teukolsky function describes the curvature perturbations of a Schwarzschild black hole. The equation can be completely separated in

the time domain and the angular profile of the radiation is given by spin-weighted spherical harmonics. Since these are eigenfunctions of the Teukolsky equation when $a = 0$, the initial angular profile should be preserved during the evolution. We shall verify this in this subsection.

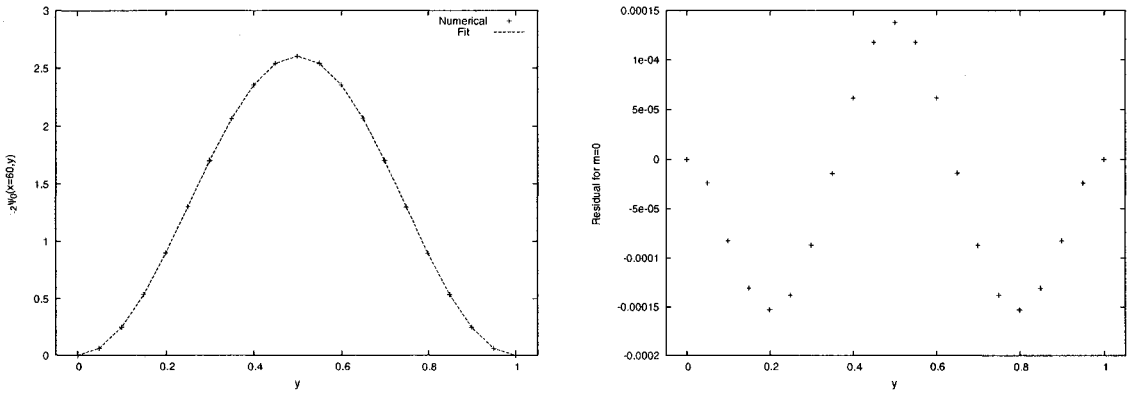

Figure 6.4: Left panel: angular profile obtained from numerical evolution of an $m = 0$, $s = -2$ Gaussian pulse centered at $x_c = 10$ with $\sigma = 1$. The field is extracted at $x = 60$ after a time $t = 75(2M)$. Also shown is the result of a least square fit for the amplitude of an $m = 0$ spin-weighted spherical harmonic. Right panel: residual of the amplitude fit. The curves differ by an amount 4 to 5 orders of magnitude smaller than the amplitude of the field at $x = 60$.

To perform this test, we chose initial data sets with $l = 2$ and $s = -2$. Our simulations are performed for $m = 0$, $m = 1$ and $m = 2$ and the waveforms are extracted at $x = 60$ after an evolution time of $t = 75(2M)$. Simulations are performed with $\Delta t = 0.025$, $\Delta x = 0.1$ and $\Delta y = 0.05$.

The angular profile of the numerically extracted A should be identical to the initial angular profile. We compare the numerical results with a profile of the form

$$A(x = 60, \theta) = A_f \ {}_{-2}Y^{2,m}(\theta),$$

where A_f is an amplitude determined by a least-square fit. We perform the fit and calculate the residual for $m = 0$, $m = 1$ and $m = 2$. Results are presented in

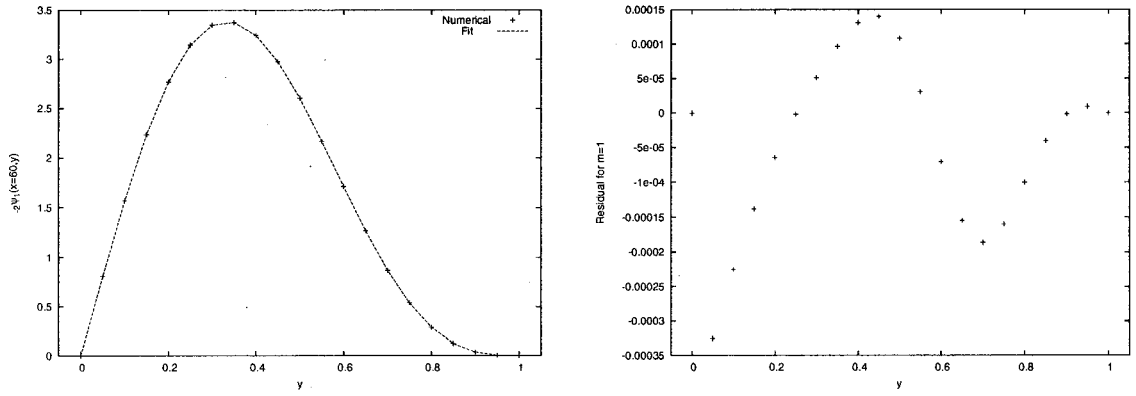

Figure 6.5: Left panel: angular profile obtained from numerical evolution of an $m = 1$, $s = -2$ Gaussian pulse centered at $x_c = 10$ with $\sigma = 1$. The field is extracted at $x = 60$ after a time $t = 75(2M)$. Also shown is the result of a least square fit for the amplitude of an $m = 1$ spin-weighted spherical harmonic. Right panel: residual of the amplitude fit. The curves differ by an amount 4 to 5 orders of magnitude smaller than the amplitude of the field at $x = 60$.

Fig. (6.4), Fig. (6.5) and Fig. (6.6), respectively. In all three cases, the residuals represent an error of $\sim 10^{-3}$, and angular profiles are therefore well preserved under evolution. This also shows that good angular resolution for $l = 2$ and $m = 0$, 1, and 2 is obtained with $N_y = 21$, a fairly small number of points. For higher multipole moments, a finer grid is needed.

6.4.2 Quasi-normal modes of the Schwarzschild and Kerr black holes

The second test focuses on black-hole quasi-normal ringing [69]. As a response to perturbations, black holes radiate at very specific frequencies and each mode is damped at a specific rate. The appearance of these modes in numerical simulations was seen and discussed in Chapter 4, Sec. 4.3.

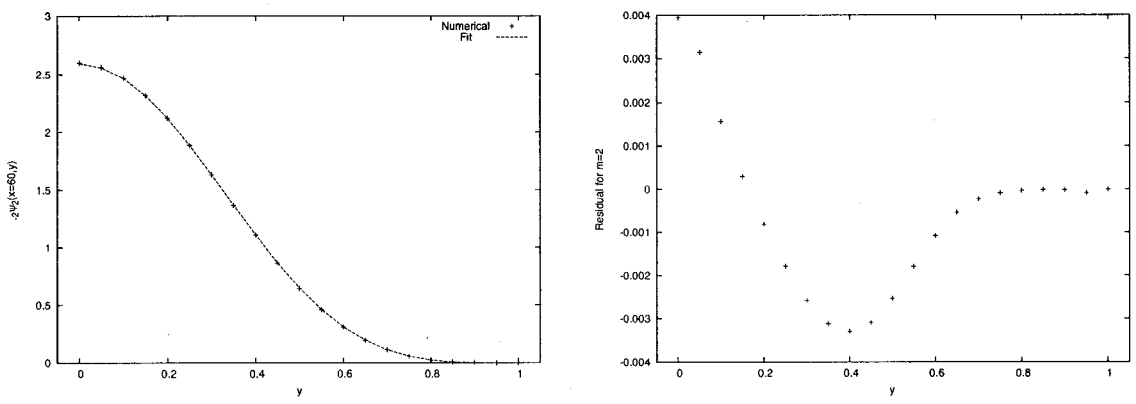

Figure 6.6: Left panel: angular profile obtained from numerical evolution of an $m = 2$, $s = -2$ Gaussian pulse centered at $x_c = 10$ with $\sigma = 1$. The field is extracted at $x = 60$ after a time $t = 75(2M)$. Also shown is the result of a least square fit for the amplitude of an $m = 2$ spin-weighted spherical harmonic. Right panel: residual of the amplitude fit. The curves differ by an amount 3 to 4 orders of magnitude smaller than the amplitude of the field at $x = 60$.

Methods to calculate the quasi-normal frequencies are based on a Fourier decomposition of the Teukolsky function: ${}_s\psi_m$ is decomposed as in Eq. (6.7). The radial function ${}_sR(\omega, r^*)$ is required to satisfy ingoing-wave boundary conditions at the horizon and outgoing-wave boundary conditions at infinity. Frequencies for which ${}_sR(\omega, r^*)$ satisfies both conditions simultaneously are the quasi-normal frequencies of the black hole. Black hole quasi-normal frequencies have been calculated by numerous authors [69, 103, 104, 105, 106], to cite just a few.

After complete separation of the variables, the potential for ${}_sR(\omega, r^*)$ depends on s, l, m and a, and as a result the quasi-normal frequencies also depend on these parameters. For a given set of parameters, there is an infinite discrete set of complex frequencies for which ${}_sR(\omega, r^*)$ satisfies both conditions. Each frequency is labeled with an index n. In the time domain we cannot excite just a single frequency, and the regime of quasi-normal ringing will involve a superposition of modes with different

Table 6.1: Dominant (least damped) quasi-normal frequencies for the gravitational perturbations of a Kerr black hole, as calculated by E. Leaver [69]. Since the potential in spherical symmetry does not depend on m the quasi-normal frequencies for $l = 2$, $m = 0$ and $l = 2$, $m = 1$ are identical.

	a/M	$2M\omega_Q$	$2M\gamma_Q$
$l = 2$	0.0	0.7474	0.178
$m = 0$	0.9	0.8240	0.157
$l = 2$	0.0	0.7474	0.178
$m = 1$	0.9	1.0326	0.140

index n. For this reason, time domain methods cannot be used to calculate all quasi-normal frequencies. On the other hand, the late stage of quasi-normal ringing is dominated by the fundamental frequency (the one that is the least damped) and the measured frequency of the time domain waveform should be very close to this fundamental frequency.

The comparison is done as follow. We perform a numerical evolution of the Teukolsky function and extract $A(t)$ at $y = 0.5$ and $x = 60$. We assume our waveforms are oscillating at the fundamental quasi-normal mode frequency, as calculated by E. Leaver [69]. We call this frequency ω_Q and its associated damping exponent γ_Q. These are displayed in Table 6.1 for $a = 0$ and $a = 0.9M$, $l = 2$ and $m = 0$, 1. The value for $m = 2$ is not given in a table by the author of [69]. Instead it is part of a figure which makes an exact comparison with our results difficult. We therefore exclude it from the discussion below. Next, we assume

$$A(t) = A_p e^{-i(\omega_Q - i\gamma_Q)(t-t_p)}, \tag{6.26}$$

where A_p and t_p are two fitting parameters.

In Fig. 6.7, we display the real part of the $s = -2$ Teukolsky function for $m = 0$ and $m = 1$ modes, for $a = 0$ and $0.9M$. Because of the logarithmic scale, the points

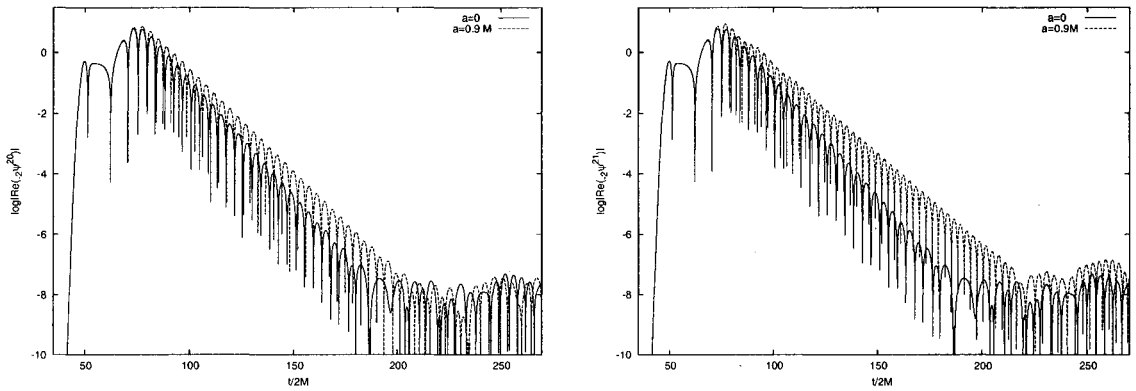

Figure 6.7: Displayed are the based 10 logarithms of the real part of the $s = -2$ Teukolsky function for $a = 0$ and $a = 0.9M$. The left panel contains the $m = 0$ modes, while the right panel contains the $m = 1$ modes. The frequency increases with increasing a, while the damping exponent decreases, as expected [69]. The last portion of the gravitational waveforms are dominated by boundary effects, and information about the physical signal is lost. For this reason, we restrict our fit to the region $100(2M) \leq t \leq 170(2M)$.

where the Teukolsky function goes to zero appear as sudden dips toward large negative values. These are typical results obtained after a run of the code for any value of m and $a < M$; we used $\Delta t = 0.0125$, $\Delta y = 0.025$ and $\Delta x = 0.125$. For the cases displayed, the initial data is given by Eq. (6.12) with $x_c = 10$ and $\sigma = 1$, and the waveform is extracted as a function of time at $x = 60$ and $y = 0.5$. The epoch of quasi-normal ringing occurs between $t/(2M) \approx 80$ and $t/(2M) \approx 200$. For the fits, we restrict this to $100 \leq t/(2M) \leq 170$.

In Fig. 6.8, we display typical examples of the agreement between our numerical results and the theoretical values for the quasi-normal modes. We display the cases $a = 0$, $m = 0$ and $a = 0.9M$, $m = 1$. In all cases, we found good agreement between the fitted waveforms and our numerical results. In the figure, the solid line is our numerical results, the long-dashed line is the fitted waveforms (for the most part it lays on top of the numerical results) and the dashed curve with a much lower

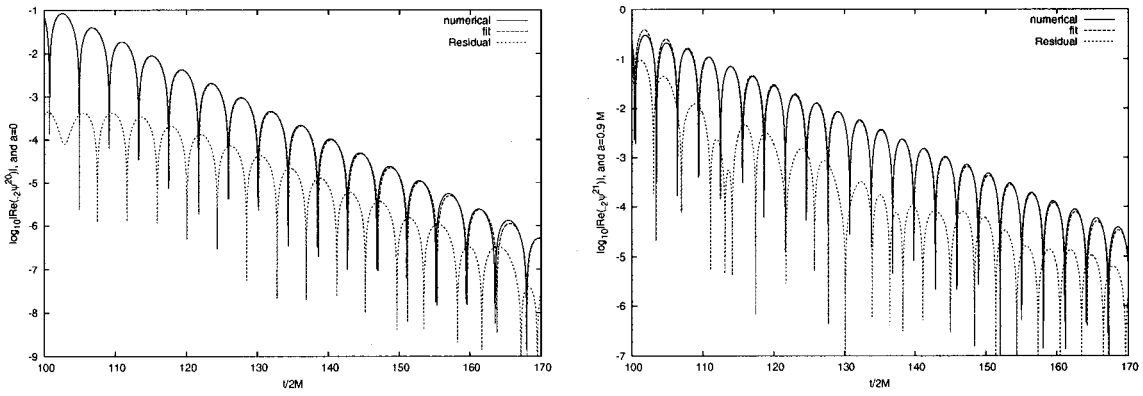

Figure 6.8: The solid line is the numerical result from the Teukolsky code, while the long-dashed line is a fit for the amplitude and the phase in Eq. (6.26). The numerical result and the fit are for the most part indistinguishable. The short-dashed curve is the residual of the fit. For $m = 0$ and $a = 0$ (left), as well as $m = 1$ and $a = 0.9M$ (right) the residual is at least 1 to 2 orders of magnitude smaller than the amplitude of the waveforms themselves. We recall that the field and the residual are plotted on a logarithmic scale.

amplitude is the absolute value of the residual plotted on a logarithmic scale. The residual is always at least 1 to 2 orders of magnitude smaller than the amplitude of the waveform.

We conclude that our method for integrating the Teukolsky equation in the time domain is stable, quadratically convergent, and that it correctly reproduces the angular profile and the quasi-normal frequencies of the radiation. Our method's reliability is therefore established.

6.5 Comments on the source term of a smeared particle

In developing our numerical method for the integration of the Teukolsky equation in the time domain, we allowed for the possibility of including a non-singular source

term to the equation. It is beyond the scope of this dissertation to proceed further in this direction, but we take the opportunity to comment on the possibility of modeling a point particle in terms of a non-singular source.

Finite-difference methods such as the one developed above for the integration of the vacuum Teukolsky equation are adequate to deal with fields that are at most discontinuous in some region of spacetime covered by the numerical grid. The structure of the Zerilli-Moncrief and Regge-Wheeler equations near the position of the particle is a crucial ingredient in constructing the Lousto-Price algorithm presented in Appendix C: here the field was discontinuous and the method was able to handle this type of singular behaviour. But in two spatial dimensions, the Teukolsky function is no longer simply discontinuous at the position of the particle. Instead, it is logarithmically divergent and finite-difference methods cannot be employed.

This behaviour of the field is unavoidable as long as we insist on working in the time domain with the source term of a point particle. Instead of abandoning time domain methods, we choose to smear the point particle and eliminate the singular behaviour of the source term in this way. The Teukolsky function will then be smooth and slowly varying everywhere in the region of spacetime covered by the numerical grid. The suggestion is then to use, for example, a narrow Gaussian function (and its derivative) to approximate a δ-function (and its derivative).

There are multiple reasons to be cautious about such a substitution. After all, the problem we are now solving is equivalent to the original problem only in the limit where the width of the Gaussian function goes to zero. Since we are no longer solving the original problem, it would be desirable to have a method to judge the quality of the approximation. For circular orbits in the equatorial plane of a Kerr black hole, results for energy fluxes can be compared with frequency domain fluxes calculated

in [94]. For general orbits, the comparison is more difficult because spectral methods are difficult to implement efficiently and accurately.

For the Schwarzschild spacetime, the Lousto-Price algorithm provides a mean of obtaining quantitative information about the accuracy of the smeared particle approach: fluxes obtained without approximating the δ-functions can be compared with fluxes calculated with a smeared particle. We therefore integrate the Zerilli-Moncrief and the Regge-Wheeler equations using a standard Lax-Wendroff method (see for example [68]) with a non-singular source term for a particle in circular orbit. The source term is given by Eq. (5.6) and Eq. (5.7) with $e = 0$, and the δ-function and its derivative are approximated as

$$\begin{aligned} \delta(r^* - r_p^*) &= \frac{1}{\sqrt{2\pi}\sigma} e^{-\frac{(r^*-r_p^*)^2}{2\sigma^2}}, \\ \delta'(r^* - r_p^*) &= \frac{-(r^* - r_p^*)}{\sqrt{2\pi}\sigma^3} e^{-\frac{(r^*-r_p^*)^2}{2\sigma^2}}, \end{aligned} \tag{6.27}$$

where a prime denotes a derivative with respect to r^*, and r_p^* is the radius of the circular orbit. In the limit $\sigma \to 0$, we recover the δ-function and its radial derivative.

The parameter controlling the smearing of the point particle is σ, its "width". The width of the particle is limited by the spatial stepsize $\Delta x \equiv \Delta r^*/(2M)$ of the numerical grid. We found that the best results are obtained when $\sigma = \Delta x$. For a smaller width, the particle "falls" between grid points, and the source term is not sufficiently sampled. The width can be made larger than Δx, but this produces a more diffuse particle and less accurate results.

In Table 6.2 we display the fluxes obtained from the Lousto-Price algorithm and the smeared-particle approach for selected values of m and two choices of orbital radius r_p. For these simulations, we used $\sigma = \Delta x = 0.8$ in the Lax-Wendroff algorithm. The results displayed here are typical of the accuracy achieved with other stepsizes (see

Table 6.2: Comparison of the fluxes for circular orbits in Schwarzschild from a smeared particle approach (SPA) with results obtained with the Lousto-Price algorithm (LP). In both cases, energy fluxes were calculated for an observer located at $r^*_{\rm obs} = 750(2M)$ and $\Delta x = 0.8$.

r_p/M	l	m	LP	SPA	% error
7.9456	2	1	$8.16e-07$	$1.22e-06$	50%
	2	2	$1.71e-04$	$1.55e-04$	4%
	3	3	$2.54e-05$	$2.31e-05$	10%
15.0	2	1	$1.61e-08$	$2.45e-08$	50%
	2	2	$7.21e-06$	$7.49e-06$	4%
	3	3	$5.89e-07$	$6.47e-07$	10%

Fig. 6.9).

The interesting observation here is that for even parity perturbations, we get good quantitative agreement between the smeared particle approach and the Lousto-Price algorithm, whereas for odd parity modes we get only an order of magnitude agreement. We note that the poor accuracy achieved for odd modes is similar to the accuracy of the calculations performed in [99, 100]. The authors of these papers also present results for the time domain integration of the inhomogeneous Teukolsky equation using a smeared particle approach. They find that for both circular and eccentric orbits, this type of approach yields an accuracy of the order of, at best, 20%. For example, for an $r_p = 12M$ circular orbit in the equatorial plane of a rotating Kerr black hole ($a/M = 0.9$), they find, for the $m = 2$ mode, an agreement of 40% with frequency domain calculation presented in [94].

In Fig. 6.9 we present the variation with the width σ, in the accuracy of the determination of the energy flux for an $l = 2$ and $m = 2$ even parity mode and an $l = 2$ and $m = 2$ odd parity mode for a circular orbit of radius $r_p = 15M$. In these cases, we extracted the energy flux at a location $r^*/(2M) = 50$ from the Lousto-Price algorithm as well as for the smeared particle approach. We present the variation

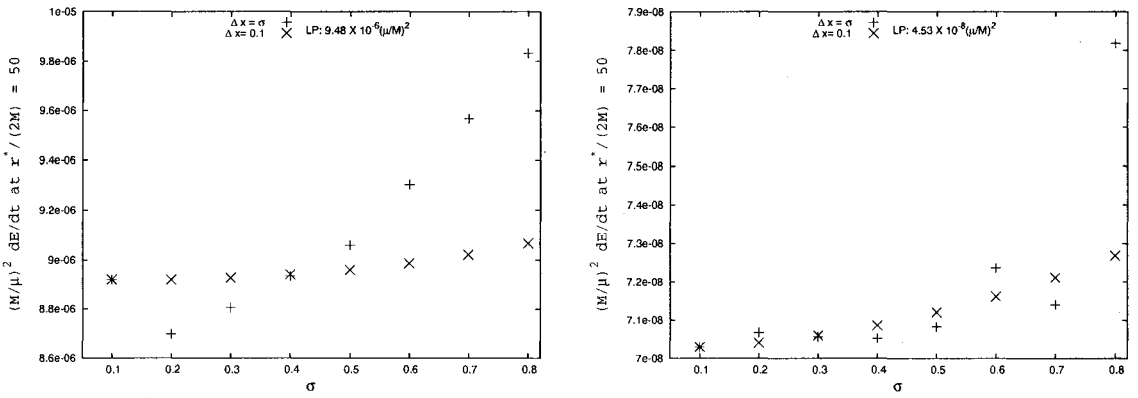

Figure 6.9: We display the variation in the energy flux from the $l = 2$, $m = 2$ (left) and $l = 2$, $m = 1$ (right) modes for a particle in a circular orbit at $r_p = 15M$ for various widths of the particle in a smeared particle approach. As the width of the particle is made smaller the $l = 2$ and $m = 1$ energy flux decreases, but it seems unlikely that the result from the Lousto-Price algorithm, $\dot{E} = 4.53 \times 10^{-8}(\mu/M)^2$, can be reproduced to better than 50% in this type of approximation. It is also clear from the left panel where the energy flux for even modes is displayed that the SPA for the $l = 2$ and $m =$ modes gives results that are closer to the flux from the Lousto-Price algorithm, but that do not converge for small Δx toward the correct value of $9.48 \times 10^{-6}(\mu/M)^2$.

obtained by reducing Δx from 0.8 to 0.1, while keeping $\sigma = \Delta x$, as well as the variation in the energy flux obtained with $\Delta x = 0.1$ and σ varying from 0.8 to 0.1. For the $l = 2$ and $m = 2$ mode, we find that the agreement between results from a smeared-particle approach and from the Lousto-Price algorithm is of the order of $4 \sim 6\%$, but that reducing the width of the particle does not improve the agreement between the two results. For the $l = 2$ and $m = 1$, we find that the energy flux decreases as the width is made smaller, but it seems unlikely that taking smaller stepsizes will yield the correct Lousto-Price result. It seems that a smeared particle approach can do no better than an accuracy of $4 \sim 6\%$ for even parity perturbations and 50% for odd parity perturbations of the Schwarzschild black hole.

Although the agreement between the two calculations improves when the width

of the Gaussian is made smaller, it seems that to get an agreement of a few percents we would need to use a prohibitively small stepsize Δx (if this approach converges at all). The fact that neither even nor odd parity modes results for a smeared-particle approach converge toward the Lousto-Price results is surprising and we do not yet understand the reason behind this result. But this simple demonstration suggests that direct substitution of Gaussian functions for δ-functions will not yield results sufficiently accurate for the purpose of producing gravitational waveforms. It might be necessary to use more elaborate prescriptions.

Chapter 7

Conclusion

7.1 Summary

In this dissertation, we studied the gravitational perturbations of Schwarzschild and Kerr black holes.

For the perturbations of a Schwarzschild black hole, we used a numerical method developed by C.O. Lousto and R.H. Price [54] to integrate the perturbation equations in the time domain. The method accounts for a point particle without approximating the singular source term. Using this method we were able to produce gravitational waveforms for arbitrary geodesic motion and to obtain the fluxes of energy and angular momentum carried to infinity and through the event horizon by the gravitational waves.

We also developed a method for the numerical integration, in the time domain, of the vacuum perturbations of a Kerr black hole. Singular source terms are more difficult to incorporate in such a scheme: this was not presented in this dissertation.

Let us briefly summarize the work contained in each chapter.

In Chapter 2, we presented a gauge invariant and covariant formalism for the

metric perturbations of a Schwarzschild black hole. In this formalism, information about the gravitational waves is encoded in two gauge-invariant scalar functions: the Zerilli-Moncrief and the Regge-Wheeler functions. The equations are derived allowing for the possibility that the perturbations are produced by an arbitrary stress-energy tensor. Such a formulation may be used to implement radiation reaction schemes or for the purpose of comparing with results obtained in numerical relativity in various coordinate systems, such as horizon penetrating coordinates.

In Chapter 3, we specialized the covariant black-hole perturbation equations to Schwarzschild coordinates. In this coordinate system, and in the Regge-Wheeler gauge, it is possible to completely reconstruct the metric perturbations from a knowledge of the Zerilli-Moncrief and Regge-Wheeler functions. We also provided a relation between the fluxes of energy and angular momentum at infinity and through the event horizon and the two gauge invariant scalar functions. The relations derived for the horizon fluxes are presented for the first time in this dissertation.

In Chapter 4 and Chapter 5, we used the formalism presented in previous chapters to obtain the gravitational waveforms associated with arbitrary geodesic motion of a particle around a Schwarzschild black hole. This was done in the time domain using a numerical method first developed by C.O. Lousto and R.H. Price, and corrected here to produce second-order convergence. The work presented in these chapters included a study of the effects of the choice of initial data on the evolution of the metric perturbations during the radial infall of the point particle. For close initial separations, contributions to the radiation field from the initial data content, the motion of the particle, and black hole ringing become strongly entangled. We also obtained the gravitational waveforms associated with circular, eccentric and parabolic orbital motion. Using the waveforms produced with the Lousto-Price algorithm, we

were able to evaluate the contribution of black hole absorption to the total fluxes of energy and angular momentum. For the cases considered, black hole absorption contributes more than 1% of the total fluxes when the periastron distance is smaller than $5M$. Work presented in Chapter 4 can be found in [107], while work presented in Chapter 5 has been accepted for publication in Physical Review D.

In Chapter 6, we developed an independent numerical method for the time domain integration of the homogeneous Teukolsky equation. The method is stable and quadratically convergent. It also reproduces well-known physical predictions of the Teukolsky equation, such as angular profiles for $a = 0$, and quasi-normal modes for various values of the angular momentum of the Kerr black hole.

7.2 Future Directions

For the purpose of developing accurate representations of gravitational waveforms emitted by a small object orbiting a supermassive black hole, time domain methods have a definite advantage over spectral methods: they can easily account for the sharp features that are present in the waveforms for highly eccentric motion. Another significant advantage is that the motion of the particle is affected by the emission of gravitational waves and this process is naturally described in the time domain. It should be straightforward to incorporate this effect in time domain methods, once a prescription is given to describe the motion.

The long term goal is to produce gravitational waveforms from a compact object in orbit around a rotating black hole, including radiation reaction effects on the motion of the small object. Although this effect is small, its accumulation over $\sim 10^5$ orbits will significantly affect the gravitational waves it emits. This leads to two extensions

of the work presented in this dissertation.

For the perturbations of the Schwarzschild black hole, we have a fast and accurate method to calculate the gravitational waveforms for geodesic motion. The method also permits the computation of the energy and angular momentum fluxes both at infinity and through the event horizon. This information is sufficient to determine the change in orbital energy and angular momentum of the particle. It will then be possible to map trajectories in the p and e plane, and subsequently use these maps to produce corrected waveforms [98, 95, 96, 97].

This type of method assumes that the orbit is slowly changing due to the emission of gravitational waves. For an adiabatic change, knowledge of the averaged fluxes of energy and angular momentum carried by the radiation may be sufficient to obtain the corrected motion. This should be the case for circular or mildly eccentric orbits. For highly eccentric orbits, where gravitational radiation is primarily emitted in bursts near periastron, using averaged fluxes to correct the motion may not be appropriate. We expect the motion to be rapidly affected by the emission of gravitational waves at periastron, and averaging the effect over a complete orbit may not be accurate. For these orbits, the motion needs to be corrected by a local self-force. In any event, once the corrected motion of the particle is known, it should be an easy task to adapt the code we used here to produce gravitational waveforms associated with this motion.

For the purpose of producing astrophysically relevant waveforms, we need to be able to numerically integrate the inhomogeneous Teukolsky equation in the time domain. Currently, the best time-domain methods produce gravitational waveforms from which fluxes of energy and angular momentum can be calculated with an accuracy of at best 20% [99, 100]. There is a long way to go to obtain acceptable accuracy.

Current methods are based on smearing the singular source term of the Teukolsky equation. Our limited experience with a smeared particle suggests that the simple replacement of δ-functions (and their derivatives) by narrow Gaussian pulses (and their derivatives) is not reliable. Smearing the source term for a particle in circular orbit around a Schwarzschild black hole shows that we get good agreement for even parity modes, but that for odd parity modes we get only an order-of-magnitude agreement. It may prove useful to try and understand the mechanism that gives rise to such different accuracies for different parity modes. This could prove useful in developing adequate approximations for the source term of the Teukolsky equation.

Another option is to completely abandon the idea of a point-particle and deal with an extended object right from the beginning. This is a much more complicated problem. The internal dynamics of the object would have to be described. This introduces many additional degrees of freedom that we would prefer to ignore.

At this stage, we are still far from having an accurate numerical method for the time domain integration of the inhomogeneous Teukolsky equation, even when the compact object is in geodesic motion around a Kerr black hole. It is a little premature to think about implementing radiation reaction schemes in Kerr, as was done in the frequency domain in [95, 96] for circular inclined orbits. To extend the time-domain methods to treat inclined eccentric orbits is the long term goal.

Bibliography

[1] J. Magorrian *et al. Astron. J.* **115**, 2285 (1998).

[2] D. Richstone *et al. Nature* **395**, A14 (1998).

[3] A. Eckart and R. Genzel. *Mont. Not. Roy. Astron. Soc.* **284**, 576 (1997).

[4] R. Genzel, A. Eckart, T. Ott, and F. Eisenhauer. *Mont. Not. Roy. Astron. Soc.* **291**, 219 (1997).

[5] A.M. Ghez *et al. Astrophys. J.* **586**, L127 (2003).

[6] R. Schödel *et al. Nature* **419**, 694 (2002).

[7] X. Fan *et al. Astron. J.* **122**, 2833 (2001).

[8] J.S.B. Whyithe and A. Loeb. *Astrophys. J.* **581**, 886 (2002).

[9] R.M. Wald. *General Relativity.* The University of Chicago Press, Chicago, (1984).

[10] K.S. Thorne. *Three hundred years of gravitation.* Cambridge University Press, New York, (1987). 330.

[11] J. Miralda-Escudé and A. Gould. *Submitted to Ap. J.*, `astro-ph/0003269`.

[12] B.F. Schutz. *Class. Quant. Grav.* **16**, A131 (1999).

[13] S.A. Hughes. *Annals Phys.* **303**, 142 (2003).

[14] The LIGO scientific collaboration: B. Abbot *et al.* gr-qc/0308069.

[15] S. Sidurdsson. *Class. Quant. Grav.* **14**, 1425 (1997).

[16] P.C. Peters. *Phys. Rev.* ***136***, vol. 4B, B1224 (1964).

[17] R. Genzel *et al. Nature* **425**, 934 (2003).

[18] S.A. Teukolsky. *Astrophys. J.* **185**, 635 (1973).

[19] T. Regge and J.A. Wheeler. *Phys. Rev.* **108**, 1063 (1957).

[20] F.J. Zerilli. *Phys. Rev. D* **2**, 2141 (1970).

[21] F.J. Zerilli. *Phys. Rev. Lett.* **24**, 737 (1970).

[22] V. Moncrief. *Annals of Physics* **88**, 323 (1974).

[23] C.W. Misner, K.S. Thorne, and J.A. Wheeler. *Gravitation.* Freemann, San Fransisco, (1973).

[24] G.B. Cook *et al. Phys. Rev. Lett.* **80**, 2512 (1998).

[25] R. Gómez *et al. Phys. Rev. Lett.* **80**, 3915 (1998).

[26] P. Anninos, D. Hobill, E. Seidel, L. Smarr, and W.-M. Suen. *Phys. Rev. Lett.* **71**, 2851 (1993).

[27] P. Anninos, D. Hobill, E. Seidel, L. Smarr, and W.-M. Suen. *Phys. Rev. D* **52**, 2044 (1995).

[28] M. Alcubierre, B. Brügmann, D. Pollney, E. Seidel, and R. Takahashi. *Phys. Rev. D* **64**, 061501 (2001).

[29] A.M. Abrahams *et al. Phys. Rev. Lett.* **80**, 1812 (1998).

[30] P. Anninos, S. Brandt, and P. Walker. *Phys. Rev. D* **57**, 6158 (1998).

[31] S. Brandt *et al. Phys. Rev. Lett.* **85**, 5496 (2000).

[32] K.C.B. New, D.-I. Choi, J.M. Centrella, P. MacNeice, M.F. Huq, and K. Olson. *Phys. Rev. D* **62**, 084039 (2000).

[33] J. Baker, M. Campanelli, and C.O. Lousto. *Phys. Rev. D* **65**, 044001 (2002).

[34] M. Miller. *submitted to Phys. Rev. D*, (2000).

[35] O. Sarbach and M.Tiglio. *Phys. Rev. D* **64**, 084016 (2001).

[36] U.H. Gerlach and U.K. Sengupta. *Phys. Rev. D* **19**, 2268 (1979).

[37] U.H. Gerlach and U.K. Sengupta. *Phys. Rev. D* **19**, 1300 (1980).

[38] C.O. Lousto and R.H. Price. *Phys. Rev. D* **55**, 2124 (1997).

[39] E. Poisson. *The internal structure of black holes.* Ph.D dissertation, University of Alberta, Department of Physics, Edmonton, Alberta, (1991).

[40] S. Weinberg. *Gravitation and Cosmology.* John Wiley and Sons, New York, (1972).

[41] R.H. Price. *Phys. Rev.* **5**, 2419 (1972).

[42] R.H. Price. *Phys. Rev.* **5**, 2439 (1972).

[43] R.A. Isaacson. *Phys. Rev.* **166**, 1272 (1968).

[44] P.L. Chrzanowski. *Phys. Rev. D* **11**, 2042 (1975).

[45] J.N. Goldberg, A.J. MacFarlane, E.T. Newman, F. Rohrlich, and E.C.G. Sudarshan. *J. Math. Phys.* **8**, 2155 (1967).

[46] L. Lehner. *Class. Quant. Grav.* **18**, R25 (2001).

[47] J. Thornburg. *Class. Quant. Grav.* **4**, 1119 (1987).

[48] G.B. Cook *et al. Phys. Rev. D* **47**, 1471 (1993).

[49] S. Brandt and B. Brügmann. *Phys. Rev. Lett.* **78**, 3606 (1997).

[50] J. Bowen. *Gen. Relativ. Gravit.* **11**, 227 (1979).

[51] J.M. Bowen and J.W. York. *Phys. Rev. D* **21**, 2047 (1980).

[52] G.B. Cook. *Living Rev. Rel.* **3**, 5 (2000).

[53] A. Garat and R.H. Price. *Phys. Rev. D* **61**, 124011 (2000).

[54] C.O. Lousto and R.H. Price. *Phys. Rev. D* **56**, 6439 (1997).

[55] C.O. Lousto and R.H. Price. *Phys. Rev. D* **57**, 1073 (1998).

[56] P. Anninos, R.H. Price, J. Pullin, E. Seidel, and W.-M. Suen. *Phys. Rev. D* **52**, 4462 (1995).

[57] G. Khanna *et al. Phys. Rev. Lett.* **83**, 3581 (1999).

[58] K. Alvi. *Phys. Rev. D* **61**, 124013 (2000).

[59] J. Pullin. *Prog. Theor. Phys. Suppl.* **136**, 107 (1999).

[60] J. Baker, B. Brügamnn, M. Campanelli, and C.O. Lousto. *Class. Quant. Grav.* **17**, L149 (2000).

[61] A.M. Abrahams and R.H. Price. *Phys. Rev. D* **53**, 1963 (1996).

[62] R.H. Price and J. Pullin. *Phys. Rev. Lett.* **72**, 3297 (1994).

[63] C.W. Misner. *Phys. Rev.* **118**, 1110 (1960).

[64] C.W. Misner. *Ann. Phys.* **24**, 102 (1963).

[65] D.R. Brill and R.W.Lindquist. *Phys. Rev.* **131**, 471 (1963).

[66] R.W. Lindquist. *J. Math. Phys.* **4**, 938 (1963).

[67] M. Abramowitz and I.A. Stegun. Handbook of Mathematical Functions with Formulas, Graphs, and Mathematical Tables. U.S. Govt. Print. Off., Washington, (1964).

[68] W.H. Press, S.A. Teukolsky, and W.T. Vetterling. *Numerical Recipes in C.* Cambridge University Press, New York, (1997).

[69] E.W. Leaver. *Proc. R. Soc. London* **A402**, 285 (1985).

[70] S. Chandrasekhar. *Proc. R. Soc. London* **A343**, 289 (1974).

[71] C.O. Lousto. *Phys. Rev. D* **63**, 047504 (2001).

[72] M. Davis, R. Ruffini, W.H. Press, and R.H. Price. *Phys. Rev. Lett.* **27**, 1466 (1971).

[73] Jr. J.W. York. *Phys. Rev. Lett.* **26**, 1656 (1971).

[74] M.D. Duez, T.W. Baumgarte, and S.L. Shapiro. *Phys. Rev. D* **63**, 084030 (2001).

[75] K. Danzmann et al. LISA-Proposal for a Laser-Interferometric Gravitational Wave Detector in Space. Max-Planck-Institut für Quantenoptic, Report MPQ 177, (1993).

[76] K. Danzmann et al. LISA- Laser Interferometer Space Antenna, Pre-Phase A Report. ax-Planck-Institut für Quantenoptic, Report MPQ 233, (1998).

[77] J. Kormendy and D. Richstone. *ARAA* **33**, 581 (1995).

[78] S. Sigurdsson and M.J. Rees. *Mont. Not. Roy. Astron. Soc.* **284**, 847 (2000).

[79] S. Sigurdsson. *Class. Qunat. Grav.* **14**, 1425 (1997).

[80] C. Cutler, D. Kennefick, and E. Poisson. *Phys. Rev. D* **50**, 3816 (1994).

[81] K. Glampedakis and D. Kennefick. *Phys. Rev. D* **66**, 044002 (2002).

[82] E. Poisson. *Phys. Rev. D* **47**, 1497 (1993).

[83] E. Poisson. *Phys. Rev. D* **52**, 5719 (1995).

[84] E. Poisson. *Phys. Rev. D* **55**, 7980 (1997).

[85] E. Poisson and M. Sasaki. *Phys. Rev. D* **51**, 5753 (1995).

[86] S. Chandrasekhar. *The Mathematical Theory of Black Holes.* Oxford University Press, New York, (1983).

[87] W. Krivan, P. Laguna, P.Papadopoulos, and N. Andersson. *Phys.Rev. D* **56**, 3395 (1997).

[88] S.A. Teukolsky and W.H. Press. *Astrophys. J.* **185**, 649 (1973).

[89] S.A. Teukolsky and W.H. Press. *Astrophys. J.* **193**, 443 (1974).

[90] W. Krivan, P. Laguna, and P.Papadopoulos. *Phys.Rev. D* **54**, 4728 (1996).

[91] K. Glampedakis and N.Andersson. *Phys. Rev. D* **64**, 104021 (2001).

[92] M. Campanelli, G. Khanna, P. Laguna, J. Pullin, and M.P. Ryan. *Class. Qunat. Grav.* **18**, 1543 (2001).

[93] L. Burko and G. Khanna. *Phys. Rev. D* **67**, 081502 (2003).

[94] L.S. Finn and K.S. Thorne. *Phys. Rev. D* **62**, 124021 (2000).

[95] S.A. Hughes. *Phys. Rev. D* **61**, 084004 (2000).

[96] S.A. Hughes. *Phys. Rev. D* **63**, 049902 (2001).

[97] S.A. Hughes. *Phys. Rev. D* **64**, 064004 (2001).

[98] K. Glampedakis, S.A. Hughes, and D. Kennefick. *Phys. Rev. D* **66**, 064005 (2002).

[99] R. Lopez-Aleman, G. Khanna, and J. Pullin. *Class. Quant. Grav.* **20**, 3259 (2003).

[100] G. Khanna. *Submitted to Phys. Rev. D*, `gr-qc/0309107`.

[101] J.A.H Futterman, F.A. Handler, and R.A. Matzner. Scattering from black holes. Cambridge University Press, Cambridge, 1988.

[102] A.B. Adib and C.A.S. de Almeida. `physics/0009068`.

[103] S. Detweiler. *Astrophys. J.* **239**, 292 (1980).

[104] K.D. Kokkotas and B.G. Schmidt. *Living Rev. Rel.* **2**, 2 (1999).

[105] S. Iyer and C.M. Will. *Phys. Rev. D* **35**, 3621+ (1987).

[106] E. Seidel and S. Iyer. *Phys. Rev. D* **41**, 374 (1990).

[107] K. Martel and E. Poisson. *Phys. Rev. D* **66**, 084001 (2002).

[108] J. Matthews. *J. Soc. Ind. Appl. Math.* **10**, 768 (1962).

[109] F.J. Zerilli. *J. Math. Phys.* **11**, 2203 (1970).

Appendix A

Tensorial spherical harmonics

We summarize some properties of the scalar, vectorial, and tensorial spherical harmonics used in this dissertation. The labels scalar, vectorial, and tensorial, here refer to the transformation properties of fields under a coordinate transformation of the spherical two-spaces $\theta^A \to \theta^{A'}$. Each type of spherical harmonic function, introduced below, forms a complete set and can be used to express any symmetric tensor field of rank 2 or less as a multipole expansion [19, 108, 109].

The harmonic functions come in two types: even and odd parity harmonics[1]. For a function χ, even parity modes are those which transform as $\chi^{lm}(\pi - \theta, \pi + \phi) = (-)^l \chi^{lm}(\theta, \phi)$, while odd parity modes are those that transform as $\chi(\pi - \theta, \pi + \phi) = (-)^{l+1} \chi^{lm}(\theta, \phi)$. The spherical symmetry of teh background spacetime prevents these modes from mixing.

In Sec. A.1, we introduce the usual spherical harmonics, in Sec. A.2 the vectorial spherical harmonics, and in Sec. A.3 the rank-2 tensorial spherical harmonics. Finally in Sec. A.4, we give some basic properties satisfied by tensorial spherical harmonics

[1]We follow here the terminology used by Regge-Wheeler [19]. The even (odd) parity modes are the electric (magnetic) parity modes of Zerilli [20].

and their derivatives.

We recall that indices are raised and lowered with Ω_{AB}, the metric of the unit two-sphere.

A.1 Scalar spherical harmonics

A scalar function $S(\theta^A)$ can be decomposed according to

$$S(\theta^A) \;=\; \sum_{lm} s_{lm} Y_{lm}(\theta^A), \quad \text{where} \quad s_{lm} = \int d\Omega \; S \; Y^*_{lm}, \tag{A.1}$$

and the Y^{lm}'s are the usual spherical harmonics. They satisfy the eigenvalue equation

$$\Omega^{AB} Y^{lm}_{|AB} + l(l+1) Y^{lm} = 0, \tag{A.2}$$

and are orthonormal

$$\int d\Omega \; Y_{lm} \; Y^*_{l'm'} = \delta_{ll'} \delta_{mm'}. \tag{A.3}$$

A.2 Vectorial spherical harmonics

Vectorial spherical harmonics of even and odd parity are defined as

$$Z_A = Y^{lm}_{|A} \quad \text{and} \quad X_A = \varepsilon_A{}^B Y^{lm}_{|B}, \tag{A.4}$$

where ε^{AB} is the Levi-Civita tensor ($\varepsilon_{\theta\phi} = \sin\theta$). They are orthogonal

$$\int d\Omega \; X^{lm}_A Z^{A*}_{l'm'} \;=\; 0, \tag{A.5}$$

but, by convention, not normalized

$$\begin{aligned} \int d\Omega \; Z^{lm}_A \; Z^{A*}_{l'm'} \;&=\; l(l+1)\delta_{ll'}\delta_{mm'} \\ \int d\Omega \; X^{lm}_A \; X^{A*}_{l'm'} \;&=\; l(l+1)\delta_{ll'}\delta_{mm'}. \end{aligned} \tag{A.6}$$

An arbitrary vector $V_A(\theta^B)$ can be decomposed according to

$$V_A(\theta^B) = \sum_{lm} \left[v_{lm} Z_A^{lm}(\theta^B) + \tilde{v}_{lm} X_A^{lm}(\theta^B) \right], \tag{A.7}$$

where

$$v_{lm} = \frac{1}{l(l+1)} \int d\Omega \; V_A \; Z_{lm}^{A*} \quad \text{and} \quad \tilde{v}_{lm} = \frac{1}{l(l+1)} \int d\Omega \; V_A \; X_{lm}^{A*}.$$

A.3 Rank-2 tensorial spherical harmonics

The perturbation tensor h_{AB} is a symmetric rank-2 tensor. Therefore, to obtain a multipole expansion of this tensor, it is sufficient to introduce three symmetric rank-2 tensorial spherical harmonics. In this thesis, we use

$$\begin{aligned} U_{AB} &= \Omega_{AB} Y^{lm} \\ V_{AB} &= Y^{lm}_{|AB} + \frac{l(l+1)}{2} \Omega_{AB} Y^{lm} \\ W_{AB} &= X^{lm}_{(A|B)}. \end{aligned} \tag{A.8}$$

The tensorial spherical harmonics are orthogonal

$$\int d\Omega \; V_{AB}^{lm} \; W_{l'm'}^{AB*} = 0, \quad V_{AB}^{lm} \; U_{l'm'}^{AB*} = 0, \quad W_{AB}^{lm} \; U_{l'm'}^{AB*} = 0,$$

but not normalized

$$\begin{aligned} \int d\Omega \; U_{AB}^{lm} \; U_{l'm'}^{AB*} &= 2\delta_{ll'}\delta_{mm'} \\ \int d\Omega \; V_{AB}^{lm} \; V_{l'm'}^{AB*} &= \frac{1}{2} \frac{(l+2)!}{(l-2)!} \delta_{ll'}\delta_{mm'} \\ \int d\Omega \; W_{AB}^{lm} \; W_{l'm'}^{AB*} &= \frac{1}{2} \frac{(l+2)!}{(l-2)!} \delta_{ll'}\delta_{mm'}. \end{aligned} \tag{A.9}$$

The orthogonality between U_{lm}^{AB}, and V_{lm}^{AB} or W_{lm}^{AB} holds point-wise, since by construction, V_{lm}^{AB} and W_{lm}^{AB} are traceless tensors.

A symmetric tensor $T_{AB}(\theta^C)$ is decomposed according to

$$T_{AB}(\theta^C) = \sum_{lm} \left[K_{lm} U^{lm}_{AB}(\theta^C) + G_{lm} V^{lm}_{AB}(\theta^C) + H_{lm} W^{lm}_{AB}(\theta^C) \right], \qquad \text{(A.10)}$$

where

$$K_{lm} = \frac{1}{2} \int d\Omega \; T_{AB} \; U^{AB*}_{lm}, \qquad G_{lm} = \frac{(l-2)!}{(l+2)!} \int d\Omega \; T_{AB} \; V^{AB*}_{lm},$$

and

$$H_{lm} = \frac{(l-2)!}{(l+2)!} \int d\Omega \; T_{AB} \; W^{AB*}_{lm}.$$

A.4 Basic identities

Since the tensorial harmonics are obtained from each other by differentiation, it is possible to derive some basic relations satisfied by the spherical harmonic functions. We list relations for derivatives of the harmonic functions up to second-order derivatives, the highest order appearing in the variation of the Einstein tensor. In deriving the relations below, we use the Riemann tensor of the unit two-sphere, introduced in Eq. (2.12). It appears every time we commute covariant derivatives [23].

A.4.1 Derivatives of Z^{lm}_A and X^{lm}_A

From the definitions of the vectorial spherical harmonics it is easy to show that $Z^{lm}_{A|B} = Z^{lm}_{B|A}$ and

$$\begin{aligned}
\Omega^{AB} Z^{lm}_{A|B} &= -l(l+1) Y^{lm}, \\
\Omega^{BC} Z^{lm}_{B|CA} &= -l(l+1) Z^{lm}_A, \\
\Omega^{BC} Z^{lm}_{A|BC} &= \Omega^{BC} Z^{lm}_{B|AC} \\
&= \Omega^{BC} \left(Z^{lm}_{B|CA} - R^D{}_{BCA} Z^{lm}_D \right) \\
&= \left[1 - l(l+1) \right] Z^{lm}_A. \qquad \text{(A.11)}
\end{aligned}$$

The first result follows from the eigenvalue equation, Eq. (A.2), the third follows from commuting covariant derivatives, and the last is obtained with the use of Eq. (2.12) and Eq. (A.2).

A similar exercise for X^{lm}_A reveals that

$$\begin{aligned}
\Omega^{AB} X^{lm}_{A|B} &= 0 = \Omega^{BC} X^{lm}_{B|CA}\,, \\
\Omega^{BC} X^{lm}_{A|BC} &= \Omega^{BC} \varepsilon_A{}^D Z^{lm}_{D|BC} \\
&= [1 - l(l+1)] X^{lm}_A, \\
\Omega^{BC} X^{lm}_{B|AC} &= \Omega^{BC} \varepsilon_B{}^D Y^{lm}_{|DAC} = \varepsilon^{BC} Y^{lm}_{|BAC} \\
&= \varepsilon^{BC} \left(Y^{lm}_{|BCA} - R^D{}_{BAC} Y^{lm}_{|D} \right) \\
&= X^{lm}_A. \qquad \text{(A.12)}
\end{aligned}$$

The first line follows from symmetry arguments and $\varepsilon_{AB|C} = 0$, the third line follows from Eq. (A.11), and the fifth line follows from $\varepsilon^{AB} Y^{lm}_{|AB} = 0$ and Eq. (2.12).

A.4.2 Derivatives of U^{lm}_{AB}, V^{lm}_{AB}, and W^{lm}_{AB}

From the eigenvalue equation, and the definition of Z^{lm}_A (Eq. (A.4)), it follows that

$$\begin{aligned}
\Omega^{BC} U^{lm}_{BC|A} &= 2\Omega^{BC} U^{lm}_{BA|C} = 2 Z^{lm}_A, \\
\Omega^{CD} U^{lm}_{AB|CD} &= -l(l+1) U_{AB}, \\
\Omega^{CD} U^{lm}_{CD|AB} &= 2\Omega^{CD} U^{lm}_{CA|BD} = 2\Omega^{CD} U^{lm}_{AC|DB} \\
&= 2V^{lm}_{AB} - l(l+1) U^{lm}_{AB}.
\end{aligned} \qquad \text{(A.13)}$$

The first line follows from the definition of Z^{lm}_A while the last line follows from the definition of V^{lm}_{AB}.

For V^{lm}_{AB} and W^{lm}_{AB}, the derivatives are only needed in evaluating the Bianchi identities in Sec. 2.4. This involves evaluating first-order derivatives. The relations needed are listed below. For V^{lm}_{AB}, we get

$$\begin{aligned}
\Omega^{BC}V^{lm}_{BC|A} &= 0, \\
\Omega^{BC}V^{lm}_{AB|C} &= \Omega^{BC}\left(Y^{lm}_{|BAC} + \frac{l(l+1)}{2}\Omega_{BA}Y^{lm}_{|C}\right) \\
&= \Omega^{BC}Z^{lm}_{B|AC} + \frac{l(l+1)}{2}Z^{lm}_{A} \\
&= \left[1 - \frac{l(l+1)}{2}\right]Z^{lm}_{A}, \qquad \text{(A.14)}
\end{aligned}$$

where in going from the third to the fourth line, Eq. (A.11) was used.

Finally, for W^{lm}_{AB} we get

$$\begin{aligned}
\Omega^{BC}W^{lm}_{BC|A} &= 0, \\
\Omega^{BC}W^{lm}_{AB|C} &= \Omega^{BC}X^{lm}_{(A|B)C} \\
&= \frac{1}{2}\Omega^{BC}\left(X^{lm}_{A|BC} + X^{lm}_{B|AC}\right) \\
&= \left[1 - \frac{l(l+1)}{2}\right]X^{lm}_{A}, \qquad \text{(A.15)}
\end{aligned}$$

where in going from the fourth to the fifth line, Eq. (A.12) was used.

Appendix B

Variation of the Einstein tensor: the multipole expansion

We list the first and second-order covariant derivatives of the perturbation field $h_{\mu\nu}$, given the metric of Eq. (2.1) in Chapter 2. The three covariant derivatives ";", ":", and "|" are defined with respect to $g_{\alpha\beta}$, g_{ab}, and Ω_{AB}, respectively (see Sec. 2.1). We stress that capital roman indices are raised and lowered with Ω_{AB} or its inverse, so that no factors of r are introduced. In this context the covariant derivatives of g_{ab} and Ω_{AB} commute freely.

The covariant derivatives are calculated in Sec. B.1. The multipole expansion for the metric perturbations, in the Regge-Wheeler gauge, are then used to obtain a multipole expansion for the covariant derivatives. This is done in Sec. B.2, where, for the metric perturbations, we use Eq. (2.20) and Eq. (2.21), specialized to the Regge-Wheeler gauge. Finally, in Sec. B.3, we compute the perturbation of the Einstein tensor.

B.1 Covariant derivatives of the perturbation tensor of a general spherically symmetric spacetime

First-order covariant derivatives are not needed explicitly to calculate the perturbation equations, but we do use them to compute the second-order derivatives given below. They are easily calculated with the help of the Christoffel symbols found in Eq. (2.3). They are

$$\begin{aligned}
h_{ab;c} &= h_{ab:c} \ , \\
h_{ab;A} &= h_{ab|A} - \frac{2}{r} r_{(,a} h_{b)A} \ , \\
h_{aA;b} &= h_{aA:b} - \frac{r_{,b}}{r} h_{aA} \ , \\
h_{aA;B} &= h_{aA|B} - \frac{r_{,a}}{r} h_{AB} + r r^{,b} h_{ab} \Omega_{AB} \ , \\
h_{AB;a} &= h_{AB:a} - \frac{2}{r} r_{,a} h_{AB} \ , \\
h_{AB;C} &= h_{AB|C} + 2 r r^{,a} \Omega_{C(A} h_{B)a} \ .
\end{aligned} \tag{B.1}$$

Second-order covariant derivatives require more work but are easily calculated from the first-order derivatives. Taking one more derivative, Eq. (B.1) yields

- For h_{ab}:

$$\begin{aligned}
h_{ab;cd} &= h_{ab:cd} \ , \\
h_{ab;cA} &= h_{ab:c|A} - \frac{r_{,c}}{r} \left(h_{ab|A} - \frac{4}{r} r_{(,a} h_{b)A} \right) - \frac{2}{r} r_{(,a} h_{b)A:c} \ , \\
h_{ab;Ac} &= h_{ab;cA} - \frac{2}{r} r_{:c(a} h_{b)A} \ , \\
h_{ab;AB} &= h_{ab|AB} - \frac{4}{r} r_{(,a} h_{b)(A|B)} + \frac{2}{r^2} r_{,a} r_{,b} h_{AB} \\
&\quad + r r^{,c} \Omega_{AB} \left(h_{ab:c} - \frac{2}{r} r_{(,a} h_{b)c} \right) \ ;
\end{aligned} \tag{B.2}$$

- For h_{aA}:

$$
\begin{aligned}
h_{aA;bc} &= h_{aA:bc} - \frac{2}{r} h_{aA:(b} r_{,c)} - \left(r_{:bc} - \frac{2}{r} r_{,b} r_{,c} \right) \frac{h_{aA}}{r} \,, \\
h_{aA;bB} &= h_{aA:b|B} - \frac{2}{r} r_{,b} h_{aA|B} - \frac{r_{,a}}{r} \left(h_{AB:b} - \frac{3}{r} r_{,b} h_{AB} \right) \\
&+ r r^{,c} \Omega_{AB} \left(h_{ac:b} - \frac{r_{,b}}{r} h_{ac} \right) \,, \\
h_{aA;Bb} &= h_{aA;bB} - \frac{r_{:ab}}{r} h_{AB} + r \Omega_{AB} r_{:cb} h_a{}^c \,, \\
h_{aA;BC} &= h_{aA|BC} - \frac{2}{r} r_{,a} h_{A(B|C)} + r r^{,b} \left(\Omega_{BC} h_{aA:b} - \frac{r_{,a}}{r} \Omega_{AB} h_{bC} \right) \\
&+ r r^{,b} \left(2 h_{ab|(B} \Omega_{C)A} - \frac{4}{r} r_{(,a} h_{b)(A} \Omega_{B)C} \right) \,;
\end{aligned}
\tag{B.3}
$$

- For h_{AB}:

$$
\begin{aligned}
h_{AB;ab} &= h_{AB:ab} - \frac{4}{r} h_{AB:(a} r_{,b)} + \frac{6}{r^2} r_{,a} r_{,b} h_{AB} - \frac{2}{r} r_{:ab} h_{AB} \,, \\
h_{AB;aC} &= h_{AB:a|C} - \frac{3}{r} r_{,a} h_{AB|C} + 2 r r^{,b} \Omega_{C(A} \left(h_{B)b:a} - 2 h_{B)b} \frac{r_{,a}}{r} \right) \,, \\
h_{AB;Ca} &= h_{AB;aC} + 2 r r_{:ba} \Omega_{C(A} h_{B)}{}^b \,, \\
h_{AB;CD} &= h_{AB|CD} + 2 r r^{,a} \left(\Omega_{C(A} h_{B)a|D} + \Omega_{D(A} h_{B)a|C} \right) \\
&- 2 r^{,a} r_{,a} \left(\Omega_{D(A} h_{B)C} + \Omega_{CD} h_{AB} \right) \\
&+ 2 r^2 r^{,a} r^{,b} h_{ab} \Omega_{D(A} \Omega_{B)C} + r r^{,a} \Omega_{CD} h_{AB:a} .
\end{aligned}
\tag{B.4}
$$

We recall that parentheses around a group of indices is used to denote symmetrization with respect to this group of indices.

B.2 Multipole expansion of covariant derivatives

We now use the multipole expansion, Eq. (2.20) and Eq. (2.21), to express the covariant derivatives as multipole expansions. We work here in the Regge-Wheeler gauge and the only non-vanishing multipole moments for the expansion of $h_{\mu\nu}$ are p_{ab}, K, and h_a.

The multipole expansion of the first-order covariant derivatives are:

$$\begin{aligned}
h_{ab;c} &= p_{ab:c}\, Y^{lm} \,, \\
h_{ab;A} &= p_{ab}\, Z^{lm}_A - \frac{2}{r} r_{(,a} h_{b)} X^{lm}_A \,, \\
h_{aA;b} &= \left(h_{a:b} - \frac{r_{,b}}{r} h_a \right) X^{lm}_A \,, \\
h_{aA;B} &= h_a\, X^{lm}_{A|B} + r r^{,b} \left(p_{ab} - g_{ab} K \right) U_{AB} \,, \\
h_{AB;a} &= r^2 K_{,a} U^{lm}_{AB} \,, \\
h_{AB;C} &= r^2 K U^{lm}_{AB|C} + 2 r r^{,a} h_a X^{lm}_{(A} \Omega_{B)C} \,.
\end{aligned} \tag{B.5}$$

Substituting the multipole expansions into Eq. (B.2), Eq. (B.3), and Eq. (B.4), yields, for the second-order covariant derivatives,

- For h_{ab}:

$$\begin{aligned}
h_{ab;cd} &= p_{ab:cd} Y^{lm} \,, \\
h_{ab;cA} &= \left(p_{ab:c} - \frac{r_{,c}}{r} p_{ab} \right) Z^{lm}_A \\
&- \frac{2}{r} \left(r_{(,a} h_{b):c} - \frac{2}{r} r_{,c} r_{(,a} h_{b)} \right) X^{lm}_A \\
h_{ab;Ac} &= \left(p_{ab:c} - \frac{r_{,c}}{r} p_{ab} \right) Z^{lm}_A \,, \\
&- \frac{2}{r} \left(r_{(,a} h_{b):c} + r_{:c(a} h_{b)} - \frac{2}{r} r_{,c} r_{(,a} h_{b)} \right) X^{lm}_A \,, \\
h_{ab;AB} &= \left(r r^{,c} p_{ab:c} - 2 r^{,c} r_{(,a} p_{b)c} - \frac{l(l+1)}{2} p_{ab} + 2 r_{,a} r_{,b} K \right) U^{lm}_{AB} \\
&+ p_{ab} V^{lm}_{AB} - \frac{4}{r} r_{(,a} h_{b)} W^{lm}_{AB} \,;
\end{aligned} \tag{B.6}$$

- For h_{aA}:

$$\begin{aligned}
h_{aA;bc} &= \left[h_{a:bc} - \frac{2}{r} h_{a:(b} r_{,c)} - \left(r_{:bc} - \frac{2}{r} r_{,b} r_{,c} \right) \frac{h_a}{r} \right] X^{lm}_A \,, \\
h_{aA;bB} &= \left(r r^{,c} p_{ac:b} - r^{,c} r_{,b} p_{ac} - r r_{,a} K_{,b} + r_{,a} r_{,b} K \right) U^{lm}_{AB} \\
&+ \left(h_{a:b} - \frac{2}{r} r_{,b} h_a \right) X^{lm}_{A|B} \,,
\end{aligned}$$

$$
\begin{aligned}
h_{aA;Bb} &= \left(rr^{,c}p_{ac:b} + rr_{:cb}p_a{}^c - r^{,c}r_{,b}p_{ac} - rr_{,a}K_{,b} + r_{,a}r_{,b}K - rr_{:ab}K\right) U^{lm}_{AB} \\
&+ \left(h_{a:b} - \frac{2}{r}r_{,b}h_a\right) X^{lm}_{A|B} \ , \\
h_{aA;BC} &= 2rr^{,b}p_{ab}\Omega_{A(B}Z^{lm}_{C)} - 2rr_{,a}KU^{lm}_{A(B|C)} + h_a X^{lm}_{A|BC} \\
&+ \left(rr^{,b}h_{a:b} - 2r^{,b}r_{(,a}h_{b)}\right)\Omega_{BC}X^{lm}_A - r_{,a}r^{,b}h_b\Omega_{AB}X^{lm}_C \\
&- 2r^{,b}r_{(,a}h_{b)}\Omega_{AC}X^{lm}_B \ ;
\end{aligned}
\tag{B.7}
$$

- For h_{AB}:

$$
\begin{aligned}
h_{AB;ab} &= r^2 K_{:ab}U^{lm}_{AB} \\
h_{AB;aC} &= r^2\left(K_{,a} - \frac{r_{,a}}{r}K\right)U^{lm}_{AB|C} + 2rr^{,b}\left(h_{b:a} - \frac{2}{r}r_{,a}h_b\right)\Omega_{C(A}X^{lm}_{B)} \ , \\
h_{AB;Ca} &= \left(2rr^{,b}h_{b:a} - 4r_{,a}r^{,b}h_b + 2rr_{:ab}h^b\right)\Omega_{C(A}X^{lm}_{B)} \\
&+ r^2\left(K_{,a} - \frac{r_{,a}}{r}K\right)U^{lm}_{AB|C} \ , \\
h_{AB;CD} &= r^3 r^{,a}K_{,a}\Omega_{CD}U^{lm}_{AB} + 2r^2 r^{,a}r^{,b}\left(p_{ab} - g_{ab}K\right)\Omega_{D(A}U^{lm}_{B)C} \\
&+ r^2 K U^{lm}_{AB|CD} + 2rr^{,a}h_a\left(\Omega_{C(A}X^{lm}_{B)|D} + \Omega_{D(A}X^{lm}_{B)|C}\right) \ .
\end{aligned}
\tag{B.8}
$$

It is now a simple task to compute the multipole expansion of the various quantities appearing in Eq. (2.15). For the wave operator, we get

$$
\begin{aligned}
\Box h_{ab} &= \left(\tilde{\Box}p_{ab} + \frac{2}{r}r^{,c}p_{ab:c} - \frac{4}{r^2}r^{,c}r_{(,a}p_{b)c}\right. \\
&- \left.\frac{l(l+1)}{r^2}p_{ab} + \frac{4}{r^2}r_{,a}r_{,b}K\right)Y^{lm} \ , \\
\Box h_{aA} &= \frac{2}{r}r^{,b}\left(p_{ab} - g_{ab}K\right)Z^{lm}_A \\
&+ \left(\tilde{\Box}h_a + \left(1 - r\tilde{\Box}r - r^{,b}r_{,b} - l(l+1)\right)\frac{h_a}{r^2} - \frac{4}{r^2}r_{,a}r^{,b}h_b\right)X^{lm}_A \ , \\
\Box h_{AB} &= \left(r^2\tilde{\Box}K + 2rr^{,a}K_{,a} + 2r^{,a}r^{,b}\left(p_{ab} - g_{ab}K\right) - l(l+1)K\right)U^{lm}_{AB} \\
&+ \frac{4}{r}r^{,a}h_a W^{lm}_{AB} \ ,
\end{aligned}
\tag{B.9}
$$

where we used $\Omega^{BC}X^{lm}_{A|BC} = \left[1 - l(l+1)\right]X^{lm}_A$ found in Eq. (A.12), and $\Omega^{BC}U^{lm}_{AB|C} =$

Z^{lm}_A to simplify the appearance of $\Box h_{aA}$ and $\Omega^{CD}U^{lm}_{AB|CD} = -l(l+1)U^{lm}_{AB}$ to simplify that of $\Box h_{AB}$; both relations can be found in Eq. (A.13).

Similarly for $h^{\alpha}{}_{\alpha;\mu\nu}$:

$$\begin{aligned}
h^{\alpha}{}_{\alpha;ab} &= \left(p^{c}{}_{c:ab} + 2K_{:ab}\right)Y^{lm} \\
h^{\alpha}{}_{\alpha;aA} &= \left(p^{b}{}_{b:a} - \frac{r_{,a}}{r}p^{b}{}_{b} + 2K_{,a} - \frac{2}{r}r_{,a}K\right)Z^{lm}_{A}\,, \\
h^{\alpha}{}_{\alpha;AB} &= \left(rr^{,b}p^{a}{}_{a:b} - \frac{l(l+1)}{2}p^{a}{}_{a} + 2rr^{,a}K_{,a} - l(l+1)K\right)U^{lm}_{AB} \\
&+ \left(p^{a}{}_{a} + 2K\right)V^{lm}_{AB}\,,
\end{aligned} \tag{B.10}$$

where, in deriving $h^{\alpha}{}_{\alpha;aA}$, we used $\Omega^{BC}U^{lm}_{BC|A} = 2Z^{lm}_{A}$, and for $h^{\alpha}{}_{\alpha;AB}$, we used $\Omega^{CD}U^{lm}_{CD|AB} = 2V^{lm}_{AB} - l(l+1)U^{lm}_{AB}$ (see Eq. (A.13)).

To expand the perturbation equations, we also need $h_{\alpha(\mu;\nu)}{}^{\alpha}$:

$$\begin{aligned}
h_{\alpha(a;b)}{}^{\alpha} &= \left[p^{c}{}_{(a:b)c} + \frac{2}{r}r^{,c}\left(p_{c(a:b)} - \frac{1}{r}r_{(,b}p_{a)c}\right) - \frac{2}{r}r_{(,a}K_{,b)} + \frac{2}{r^2}r_{,a}r_{,b}K\right]Y^{lm}\,, \\
h_{\alpha(a;A)}{}^{\alpha} &= \frac{1}{2}\left[p^{b}{}_{a:b} + \frac{2}{r}r^{,b}p_{ab} + K_{,a} - \frac{4}{r}r_{,a}K\right]Z^{lm}_{A} \\
&+ \frac{1}{2}\left[h^{b}{}_{:ab} + \frac{2}{r}\left(r^{,b}h_{b:a} - r_{,a}h^{b}{}_{:b} - r_{:ab}h^{b}\right)\right. \\
&+ \left.\left(1 - r\tilde{\Box}r - r^{,b}r_{,b}\right)\frac{h_a}{r^2} - \frac{6}{r^2}r_{,a}r^{,b}h_b\right]X^{lm}_{A}\,, \\
h_{\alpha(A;B)}{}^{\alpha} &= \left[rr^{,b}p^{a}{}_{b:a} + rr_{:ab}p^{ab} + 2r^{,a}r^{,b}\left(p_{ab} - g_{ab}K\right) - \left(r\tilde{\Box}r + \frac{l(l+1)}{2}\right)K\right]U^{lm}_{AB} \\
&+ KV^{lm}_{AB} + \left(h^{a}{}_{:a} + \frac{2}{r}r^{,a}h_a\right)W^{lm}_{AB}\,,
\end{aligned} \tag{B.11}$$

and, finally, for $h_{\alpha\beta}{}^{;\alpha\beta} - \Box h^{\alpha}{}_{\alpha}$:

$$\begin{aligned}
h_{\alpha\beta}{}^{;\alpha\beta} - \Box h^{\alpha}{}_{\alpha} &= \left[p^{ab}{}_{:ab} - \tilde{\Box}p^{a}{}_{a} + \frac{2}{r}r^{,a}\left(2p^{b}{}_{a:b} - p^{b}{}_{b:a}\right)\right. \\
&+ \frac{2}{r}r_{:ab}p^{ab} + \frac{l(l+1)}{r^2}p^{a}{}_{a} + \frac{2}{r^2}r^{,a}r^{,b}\left(p_{ab} - g_{ab}K\right) \\
&- \left.2\tilde{\Box}K - \frac{6}{r}r^{,a}K_{,a} - \frac{2}{r^2}\left(r\tilde{\Box}r - \frac{l(l+1)}{2}\right)K\right]Y^{lm}.
\end{aligned} \tag{B.12}$$

It is clear from the presence of Y^{lm} only, that this term contributes only to even parity modes.

B.3 Covariant perturbations of the Einstein tensor for a Schwarzschild spacetime

Combining the previous results, we can calculate $\delta G_{\mu\nu}$ found in Eq. (2.19):

$$\begin{aligned}
\delta G_{ab} &= \Bigg[p^{c}{}_{(a:b)c} - \frac{1}{2} g_{ab} p^{cd}{}_{:cd} - \frac{1}{2} p^{c}{}_{c:ab} - \frac{1}{2} \left(\tilde{\Box} p_{ab} - g_{ab} \tilde{\Box} p^{c}{}_{c} \right) \\
&+ \frac{2}{r} r_{,c} \left(p^{c}{}_{(a:b)} - g_{ab} p^{cd}{}_{:d} \right) - \frac{r^{,c}}{r} \left(p_{ab:c} - g_{ab} p^{d}{}_{d:c} \right) + \frac{l(l+1)}{2r^2} p_{ab} \\
&- \frac{1}{2} g_{ab} \left(\frac{2}{r^2} r^{c} r^{d} p_{cd} + \frac{2}{r} r_{:cd} p^{cd} + \frac{l(l+1)}{r^2} p^{c}{}_{c} \right) - K_{:ab} + g_{ab} \tilde{\Box} K \\
&- \frac{2}{r} r_{(,a} K_{,b)} + \frac{3}{r} g_{ab} r^{,c} K_{,c} - \frac{1}{2} g_{ab} \left(-\frac{2}{r^2} (r \tilde{\Box} r + r^{,c} r_{,c}) + \frac{l(l+1)}{r^2} \right) K \Bigg] Y^{lm} \qquad \text{(B.13)} \\
\delta G_{aA} &= \frac{1}{2} \left(p^{b}{}_{a:b} - p^{b}{}_{b:a} + \frac{r_{,a}}{r} p^{b}{}_{b} - K_{,a} \right) Z^{lm}_{A} \\
&+ \frac{1}{2} \Bigg(- \tilde{\Box} h_a + h^{b}{}_{:ab} + \frac{2}{r} \left(r^{,b} h_{b:a} - r_{,a} h^{b}{}_{:b} \right) \\
&- \frac{2}{r} r_{:ab} h^{b} + \frac{l(l+1)}{r^2} h_a - \frac{2}{r^2} r_{,a} r^{,b} h_b \Bigg) X^{lm}_{A} \ , \qquad \text{(B.14)} \\
\delta G_{AB} &= \frac{1}{2} r^2 \left(\tilde{\Box} p^{a}{}_{a} - p^{ab}{}_{:ab} - \frac{2}{r} r^{,b} p^{a}{}_{b:a} + \frac{r^{,a}}{r} p^{b}{}_{b:a} - \frac{l(l+1)}{2r^2} p^{a}{}_{a} + \frac{2}{r} r^{,a} K_{,a} + \tilde{\Box} K \right) U^{lm}_{AB} \\
&- \frac{1}{2} p^{a}{}_{a} V^{lm}_{AB} + h^{a}{}_{:a} W^{lm}_{AB} \ . \qquad \text{(B.15)}
\end{aligned}$$

As discussed in Sec. 2.3.1, gauge invariance can now be restored in the equations by substituting $p_{ab} \to \tilde{p}_{ab}$, $K \to \tilde{K}$, $h_a \to \tilde{h}_a$, where the gauge invariant functions are defined in Eq. (2.29) and Eq. (2.30).

This completes the derivation of the perturbation of the Einstein tensor for a vacuum spherically symmetric background spacetime. These are used, combined with expressions for $r^{,a} r_{,a}$, $r_{:ab}$ and $\mathcal{R}$ appropriate to the Schwarzschild spacetime, to give the complete covariant and gauge invariant equations describing the metric perturbations of a Schwarzschild black hole.

Appendix C

Numerical integration of the one-dimensional wave equation: the corrected Lousto-Price algorithm

We describe the method used to numerically integrate the Zerilli-Moncrief and Regge-Wheeler equations, in Schwarzschild coordinates, given by Eq. (2.59) and Eq. (2.67). The method we use is based on an algorithm first developed by C.O. Lousto and R.H. Price [54]. Below, we retrace the steps involved in the derivation of their numerical algorithm. The essence of the derivation is unaltered, but we carefully keep track of the discretization errors and provide a quadratically convergent version of their algorithm (instead of linearly convergent). This general method is employed in Chapter 4 and Chapter 5.

In Sec. C.2, we present a convergence test of the algorithm. Numerical results

show that the algorithm is indeed converging quadratically with the stepsize. For the purpose of the demonstration, we display a convergence test of the solutions for the case of the radial infall of a point particle, starting from rest at a radius r_o, into a Schwarzschild black hole. This case was studied in detail in Sec. 4.3.

C.1 Numerical algorithm

We present a numerical algorithm to integrate

$$\left[-\frac{\partial^2}{\partial t^2}+\frac{\partial^2}{\partial r^{*2}}-V(r)\right]\psi(r,t)=S(r,t), \tag{C.1}$$

where $V(r)$ is a smooth potential, and the singular source term $S(r,t)$ is of the form

$$S(r,t)=G(r,t)\delta(r-r_p(t))+F(r,t)\delta'(r-r_p(t)), \tag{C.2}$$

where a prime denotes an r-derivative, r^* is the tortoise coordinate, $r_p(t)$ denotes the radial position of the particle as a function of time, and $G(r,t)$ and $F(r,t)$ are known functions of r and t once the motion of the particle is specified.

The numerical domain is a staggered grid in r^* and t, with a stepsize $\Delta \equiv \Delta r^*/4M = \Delta t/2M$, over the region of spacetime bounded from below by the spacelike hypersurface $t=t_o$ (time at which the numerical integration begins). The numerical grid is divided into cells of area $4\Delta^2$. (Instead of using the physical area $2\Delta^2$, we found it convenient, following C.O. Lousto and R.H. Price [54], to define $A=\int du\,dv = 4\Delta^2$, where $u=t-r^*$ and $v=t+r^*$.) The cells can be separated into two groups. The first group corresponds to cells in which $r \neq r_p(t)$ everywhere; these cells are never traversed by the particle. The second group is such that $r=r_p(t)$ somewhere within the cell; these cells are traversed by the particle. The two types of cells are displayed in Fig. C.1; in the diagram, the particle enters the cell on the right of r_b^* and leaves on the left, but other entry and exit points are possible.

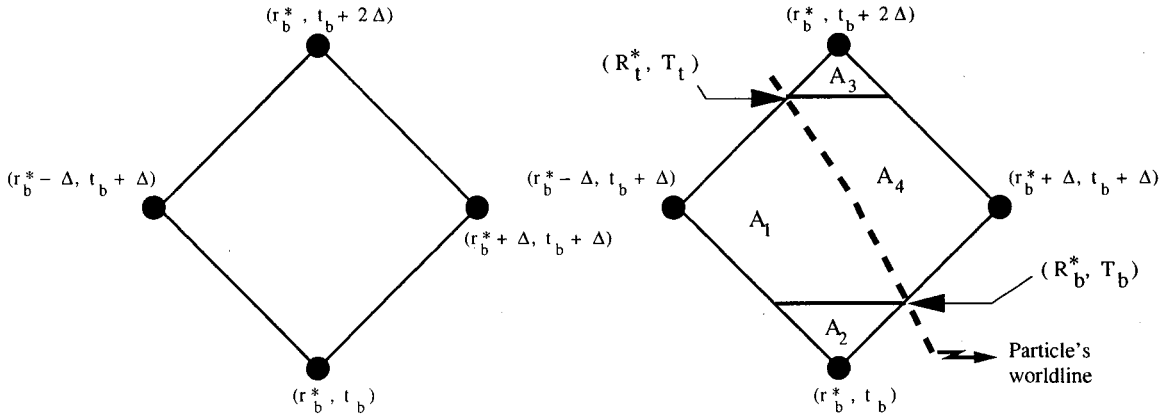

Figure C.1: The left cell is never crossed by the particle's trajectory. In such a cell the evolution of $\psi(r,t)$ is unaffected by the source term in Eq. (C.1), and Eq. (C.3) is used to evolve $\psi(t,r)$ forward in time. The right cell is traversed by the particle's world line. The areas shown in the cell are used in the numerical algorithm that incorporates the effect of the source term in Eq. (C.1). The wave function is evolved according to Eq. (C.7). The labels (R_b^*, T_b) and (R_t^*, T_t) refer to the points (r^*, t) at which the particle enters and leaves the cell, respectively.

The evolution of $\psi(r^*,t)$ across cells belonging to the first group is not affected by the source term. For these cells, we use a standard scheme, accurate to $\mathcal{O}(\Delta^4)$, for the homogeneous wave equation in the presence of a potential:

$$\begin{aligned}\psi(r_b^*, t_b + 2\Delta) \;=\; -\psi(r_b^*, t_b) \quad &+ \quad \psi(r_b^* + \Delta, t_b + \Delta)\left[1 - \frac{\Delta^2}{2} V_b\right] \\ &+ \quad \psi(r_b^* - \Delta, t_b + \Delta)\left[1 - \frac{\Delta^2}{2} V_b\right], \qquad \text{(C.3)}\end{aligned}$$

where (r_b^*, t_b) designates the bottom corner of the cell (see Fig. C.1), and $V_b = V(r_b^*)$.

The evolution of $\psi(r,t)$ across cells belonging to the second group is affected by the singular source term. To obtain the evolution of ψ across these cells, we closely follow C.O. Lousto and R.H. Price [54], carefully keeping terms up to order Δ^3. Integrating Eq. (C.1) over a grid cell, term by term, we get:

$$\begin{aligned}\int\int dA \left(-\frac{\partial^2}{\partial t^2} + \frac{\partial^2}{\partial r^{*2}}\right)\psi \;=\; &-4\left[\psi(r_b^*, t_b + 2\Delta) + \psi(r^*, t_b)\right. \\ &\left. -\psi(r_b^* - \Delta, t_b + \Delta) - \psi(r_b^* + \Delta, t_b + \Delta)\right], \qquad \text{(C.4)}\end{aligned}$$

$$\int\int dA\, V(r^*)\psi = V_b\Big[A_1\psi(r_b^*-\Delta, t_b+\Delta) + A_2\psi(r_b^*, t_b) + A_3\psi(r_b^*, t_b+2\Delta) + A_4\psi(r_b^*+\Delta, t_b+\Delta)\Big] + \mathcal{O}(\Delta^3), \tag{C.5}$$

where $dA = du\ dv$, and the A_i's are areas dividing the cell into four non-equal parts (as shown in Fig. C.1). Integration of the source term over the cell eliminates the δ-function in Eq. (C.2) and the term involving the radial derivative of the δ-function is evaluated by integrating by parts. The result is

$$\begin{aligned}\int\int dA\, S &= 2\int_{T_b}^{T_t} dt \left[\frac{G(r_p(t),t)}{1-2M/r_p(t)} - \frac{\partial}{\partial r}\left(\frac{F(r,t)}{1-2M/r}\right)\Big|_{r=r_p(t)}\right] \\ &\pm \frac{F(r_p(T_b),T_b)}{(1-2M/r_p(T_b))^2}[1\mp \dot{r}_p^*(T_b)]^{-1} \\ &\pm \frac{F(r_p(T_t),T_t)}{(1-2M/r_p(T_t))^2}[1\pm \dot{r}_p^*(T_t)]^{-1},\end{aligned} \tag{C.6}$$

where $\dot{r}_p^* = u^r/\tilde{E}$ (u^r is the radial component of the four-velocity and $\tilde{E}$ the conserved energy per unit mass), T_b is the time at which the particle enters the cell, and T_t the time at which it leaves the cell. In the previous expression, the upper (lower) sign for the first boundary term (a function of T_b) applies when the particle enters the cell on the right (left) of r_b^*. Similarly, the upper (lower) sign for the second boundary term (a function of T_t) applies when the particle leaves the cell on the right (left) of r_b^*.

Substituting the previous results in Eq. (C.1) and solving for $\psi(r_b^*, t_b+2\Delta)$, we obtain

$$\begin{aligned}\psi(r_b^*, t_b+2\Delta) &= -\psi(r_b^*, t_b)\left[1+\frac{V_b}{4}(A_2-A_3)\right] \\ &+\psi(r_b^*+\Delta, t_b+\Delta)\left[1-\frac{V_b}{4}(A_1+A_3)\right] \\ &+\psi(r_b^*-\Delta, t_b+\Delta)\left[1-\frac{Vb}{4}(A_4+A_3)\right] \\ &-\frac{1}{4}\left(1-\frac{V_b}{4}A_3\right)\int\int dA\ S(r,t).\end{aligned} \tag{C.7}$$

Notice that we have kept the factor of $(1 - V_b A_3/4)$ in front of the source term. This factor does not appear in the scheme devised by C.O. Lousto and R.H. Price[54], but is required to obtain quadratic convergence: the boundary terms appearing in Eq. (C.6) are $\mathcal{O}(1)$ in Δ and $V_b A_3/4$ represents a correction of order $\mathcal{O}(\Delta^2)$ to their contribution, which cannot be neglected when quadratic convergence is required.

The previous equations cannot be used to evolve ψ from the initial time $t = t_o$ to the next time $t = t_o + \Delta$. To get $\psi(r_b^*, t_o + \Delta)$ we need $\psi(r_b^* - \Delta, t_o)$, $\psi(r_b^* + \Delta, t_o)$, and $\psi(r_b^*, t_o - \Delta)$. By construction, $\psi(r_b^*, t_o - \Delta)$ is not known, but we can use the simple relation $\psi(r_b^*, t_o - \Delta) = \psi(r_b^*, t_o + \Delta) - 2\Delta\dot{\psi}(r^*, t_o) + \mathcal{O}(\Delta^3)$. Because we use a Taylor expansion to obtain this relation, it is valid so long as $r_p^*(t) \neq r_b^*$ everywhere in the cell; we chose $r_b^* - \Delta < r_p^*(t_o) < r_b^*$ which guarantees that this relation is satisfied if $u^r \leq 0$ on the initial hypersurface. For circular orbits, r_p^* is time independent so that choosing it in the way described above is adequate. For bound orbits, we choose the particle to be initially moving toward the black hole so that the condition $u_r \leq 0$ is satisfied. To obtain waveforms for which the particle is initially moving away from the black hole, $r_b^* - \Delta < r_p^*(t_o) < r_b^*$ should be replaced with $r_b^* < r_p^*(t_o) < r_b^* + \Delta$ with $u^r \geq 0$.

In order to numerically integrate Eq. (C.1), initial data for both $\psi(r^*, t_o)$ and $\dot{\psi}(r^*, t_o)$ must be provided as input. This issue is discussed in Chapter 4.

C.2 Convergence of the numerical code

We now describe the convergence properties of this numerical algorithm. The method described in Sec. C.1 is designed to be second-order convergent, i.e. the numerical

solution converges toward the exact solution quadratically. This means that, everything else being fixed, the field at a given spacetime point is a function of Δ described by

$$\psi_N(\Delta) = \psi_A + \Delta^2 \rho, \tag{C.8}$$

where ψ_N is the numerical field obtained with a stepsize Δ throughout the grid, ψ_A is the exact solution, and ρ is an error term independent of Δ. Note that error terms of order $\mathcal{O}(\Delta^3)$ are neglected in this equation.

The convergence of our numerical code can be tested by defining

$$\delta\psi(\Delta) = \psi_N(2\Delta) - \psi_N(\Delta) = 3\Delta^2 \rho, \tag{C.9}$$

and evaluating $\delta\psi$ for various values of Δ. This function is proportional to the error made in discretizing Eq. (C.1) and it satisfies $\delta\psi(n\Delta) = n^2 \delta\psi(\Delta)$. This later property is important as we use it to determine the convergence rate of our code.

The convergence of the method is a property of the method itself, and not of the system under study. To establish the convergence of the algorithm it is sufficient to show that it is converging quadratically for one specific system. We therefore test the convergence of the method in the instance where the point particle falls radially from rest toward a Schwarzschild black hole. This case was studied in Sec. 4.3, where a one-parameter family of time-symmetric initial data was introduced.

We construct $\delta\psi$ from ψ calculated with $\Delta = 0.005$, 0.01, 0.02, and 0.04 on the null line $v/2M = 500$, i.e. at each grid point on this ingoing null line we calculate $\delta\psi(0.005)$, $\delta\psi(0.01)$, and $\delta\psi(0.02)$. In this way, we construct $\delta\psi(\Delta)$ as a function of retarded time u. Note that for $u < -r_o^*$, we are testing the vacuum finite-difference algorithm, whereas for $u > -r_o^*$ we are testing the convergence properties of the method when cells are crossed by the particle's world line.

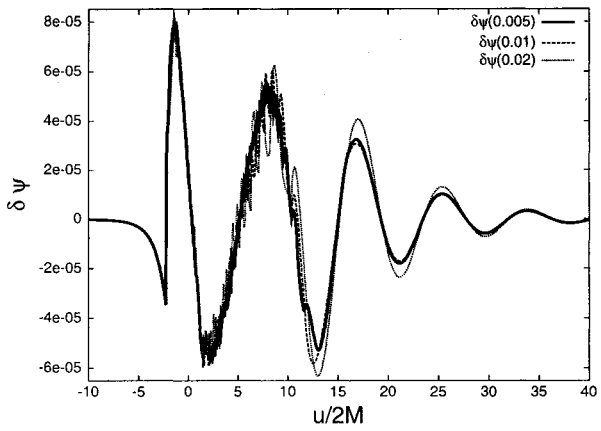

Figure C.2: Convergence properties of the numerical method. We display $\delta\psi(0.02)$, $4\delta\psi(0.01)$, and $16\delta\psi(0.005)$, for $r_o/2M = 2.1$, $\alpha = 1$, and $l = 2$. The agreement between the curves indicates that the numerical code is converging quadratically toward the exact solution. This is representative of the convergence in other cases.

From the definition of $\delta\psi$, it is obvious that they should satisfy $\delta\psi(0.02) = 4\delta\psi(0.01) = 16\delta\psi(0.005)$ at every grid point if Eq. (C.8) holds and the convergence is quadratic. In Fig. C.2, we display $\delta\psi(0.02)$, $4\delta\psi(0.01)$, and $16\delta\psi(0.005)$, for the case $r_o/2M = 2.1$, $\alpha = 1$, and $l = 2$. The fact that the three curves are close together signals quadratic convergence, with $4\delta\psi(0.01)$ and $16\delta\psi(0.005)$ being the closest. This is expected since as Δ is decreased, the approximation made in Eq. (C.8) becomes more accurate, and we get a better coincidence of the curves. The convergence rate observed in this figure is typical of the convergence obtained in our implementation of the modified C.O. Lousto and R.H. Price algorithm.